Doctoral theses at NTNU, 2020:205

Karin Fjeldstad Jusnes

Phase transformations and thermal degradation in industrial quartz

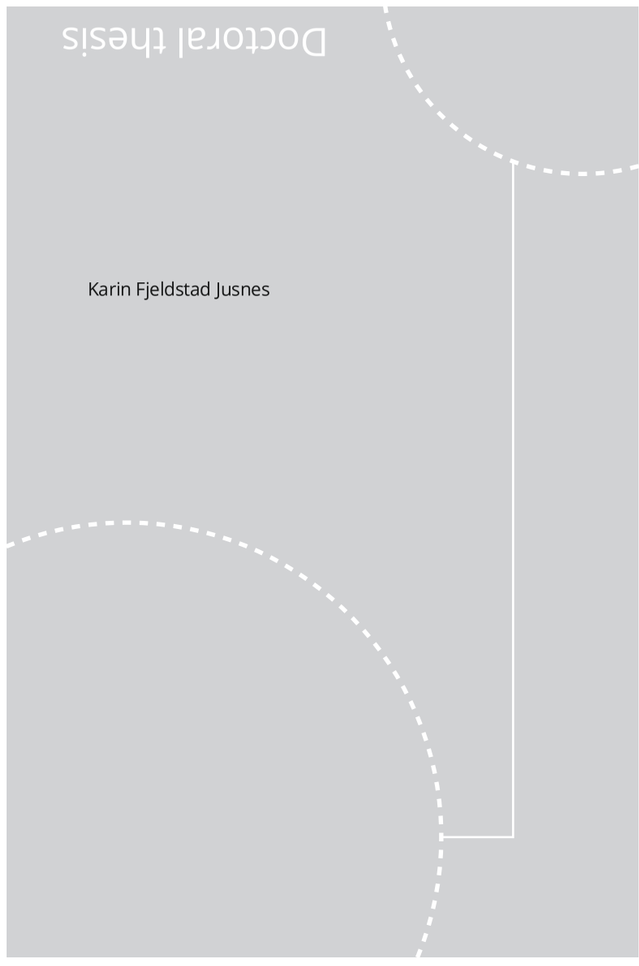

ISBN 978-82-326-4758-3 (printed ver.)
ISBN 978-82-326-4759-0 (electronic ver.)
ISSN 1503-8181

NTNU
Norwegian University of
Science and Technology

NTNU
Norwegian University of Science and Technology
Thesis for the Degree of
Philosophiae Doctor
Faculty of Natural Sciences
Department of Materials Science and Engineering

Doctoral theses at NTNU, 2020:205

NTNU
Norwegian University of
Science and Technology

Karin Fjeldstad Jusnes

Phase transformations and thermal degradation in industrial quartz

Thesis for the Degree of Philosophiae Doctor

Trondheim, June 2020

Norwegian University of Science and Technology
Faculty of Natural Sciences
Department of Materials Science and Engineering

NTNU
Norwegian University of
Science and Technology

NTNU
Norwegian University of Science and Technology

Thesis for the Degree of Philosophiae Doctor

Faculty of Natural Sciences
Department of Materials Science and Engineering

ISBN 978-82-326-4758-3 (printed ver.)
ISBN 978-82-326-4759-0 (electronic ver.)
ISSN 1503-8181

Doctoral theses at NTNU, 2020:205

Printed by NTNU Grafisk senter

Preface

This thesis has been submitted to the Norwegian University of Science and Technology as a completion of the requirements for the degree of Philosophiae Doctor. All work and modelling have been conducted by the author, if not else is stated. The work has been carried out at the Department of Materials Science and Engineering at the Norwegian University of Science and Technology. The thesis is a part of the project "High Temp Quartz" founded by Elkem and the Research Council of Norway (project number 256788).

During the work of this thesis the following scientific papers have been published or submitted:

- Jusnes, K. F., Ringdalen, E. and Tangstad, M. Shock Heating of Quartz used in Silicon and Ferrosilicon Production. Infacon XV; 2018-02-25 - 2018-02-28
- Jusnes, K. F., Ringdalen, E. and Tangstad, M. Phase Transformations from Quartz to Cristobalite. *Extraction 2018- Proceedings of the First Global Conference on Extractive Metallurgy*. Springer Nature 2018 ISBN 978-3-319-95021-1. p. 717-727
- Jusnes, K. F., Ringdalen, E. and Tangstad, M. Cracks, Disintegration and Phases Transformations in Quartz. Silicon for the Chemical and Solar Industry XIV; 2018-06-11 - 2018-06-14
- Jusnes, K. F., Ringdalen, E. and Tangstad, M. The effects of cristobalite formation on disintegration of quartz. *Materials at High Temperature* 2020 (submitted)
- Jusnes, K. F., Ringdalen, E. and Tangstad, M. Phase transformations in quartz used in silicon and ferrosilicon. *Metallurgical and materials transactions B* 2020 (submitted)

Abstract

Silicon and ferrosilicon producers worldwide are using quartz as the raw material for their production. Several types of quartz can be used, but there are some general limitations to the quartz selected. First, the lump size is important, and should ideally be 10-150 mm. The impurity content is also important for the final product. Mechanical strength is a key property that could affect the furnace operation in several ways. Even if the production of silicon and ferrosilicon has been going on since the end of the 19th century, there is still much knowledge to uncover when it comes to the behavior of the quartz inside the furnace. If the relationship between the quartz properties and their behavior at high temperature is understood, it will be very beneficial information when looking for new quartz types to mine. More knowledge could lead to more efficient furnace operations, better understanding of the process and improved selection of raw material quartz for the desired product.

In this thesis the thermal degradation and phase transformations in industrial quartz used in the Si and FeSi production are investigated to obtain a deeper understanding of the behavior of the quartz at temperature relevant for the Si and FeSi furnace. Ten different quartz types were shock heated at 1500 °C for ten minutes to determine the amount of phase created. The amount of fines below 10 mm varied from around 5 wt % up to 85 wt% between different quartz types. To explain the large differences in disintegration, the silica phases, the grain size, preexisting cracks and impurities were investigated. From these experiments it seems that grain size in the quartz type is important for the disintegration. Quartz types with smaller grains disintegrate less than quartz types with larger grains. A correlation was also seen between the amount of preexisting cracks and the amount of disintegration. The quartz types were investigated with FT-IR spectroscopy to determine the relative content of water inclusions. The method also showed to be useful for the determination of clay impurities. Based on the FT-IR results and a principal component analysis comparing the FT-IR spectra and the disintegration data, the quartz types with high muscovite ($KAl_2(Si_3AlO_{10})(OH)_2$) content disintegrated the least. The water content did not seem to have a large effect, at least the effect was overshadowed. Neither a correlation between the amount of amorphous silica or cristobalite and the disintegration could be found.

The phase composition in four different quartz types was investigated by heating 10 g and 100 g samples to 1600 °C and 1700 °C with holding time up to 120 minutes. A clear difference in the ability to transform to amorphous phase and cristobalite was seen for the types A, D, F and G. The amount of transformed quartz correlated with the alkali and alkali earth elements, but not with the Al content. A correlation with preexisting cracks was seen, and it is speculated if types with a higher amount of lattice defects will transform faster to amorphous phase and cristobalite because there are more favorable nucleation sites. No size effect was seen between the 10 g and 100 g samples. This suggests that the mechanism is independent of the size, and thus the transformation happen throughout the sample at the same time.

A model of the phase transformations from quartz to amorphous phase and cristobalite was made for the quartz type A, D, F and G. The rate constants at 1600 °C for the different types were determined to be 0.02 min^{-1}, 0.07 min^{-1}, 0.07 min^{-1} and 0.12 min^{-1} for type A, D, F and G respectively. The calculated activation energies were found to be 400 kJ/mol, 200 kJ/mol, 500 kJ/mol and 100 kJ/ mol for type A, D, F and G respectively, with accompanying pre exponential factors of 4.5×10^{10}, 3.2×10^{5}, 1.2×10^{13} and 4.1×10^{2}.

Overall, both the disintegration and phase transformation in industrial quartz vary a lot between the different types, and could therefore affect the furnace operation. The variations seen could be correlated with the properties of the quartz types.

Acknowledgement

There are many people who deserve to be thanked for helping me out during this thesis. First of all, I would like to thank my supervisor Professor Merete Tangstad (NTNU) for giving me the opportunity to perform an in-depth study regarding quartz and the silicon/ferrosilicon production, for giving me guidance in the work, and for discussions related to quartz, metallurgy, knitting and life in general. Her excellent combination of academic, metallurgical and personal skills make her supervision inspiring and learning. Small and big questions were always welcomed. I would also like to thank my always enthusiastic co-supervisor Dr. Eli Ringdalen (SINTEF). Her interest in the topic was infectious and inspiring, and she was always eager to discuss my results and theories.

I appreciate the project group in the High Temp Quartz project for their help and feedback. Thanks to Trond Brenden-Veisal and Anja Filipowicz for teaching me about geology and microscopy, and for providing useful information. Also, thanks to Aasgeir Valderhaug, Anne-Gry Messenlien, and Harald Wegge for their support and suggestions throughout this work.

At NTNU and SINTEF there are many people who I have had the pleasure of working with. Julian Tolchard has been an excellent support in XRD related problems. Dmitry Slizovskiy has helped me with experimental setup and implementation. Thanks to Bartlomiej Gawel for helping me with FT-IR and multivariate analysis. Jonas Einan Gjøvik, Tine Christin Eikevik, Berit Vinje Kramer, Sarina Bao, Kristin Høydalsvik Wells, Yingda Yu are appreciated for their technical support.

I have had the pleasure of working with intern student Jiali He for some time. Her work moral and effectiveness are very inspiring, and I am very grateful for our collaboration and the help I got from her. Erlend Lunnan Bjørnstad is highly appreciated for discussion regarding modelling of experiments and statistical support. Thanks to the people in the SiManTi-group for helpful feedback, inspirational trips and social happenings. I would also like to thank my office mates, Andrea Broggi and Marit Buhaug Folstad for keeping up with my mess in the office and not complaining when I ate their office snacks.

Throughout these years I have made some really good friends at work, who have made my work days much more enjoyable. I do not think I would have completed without your presence both at work and after work. Trine, Cathrine, Marit, Benedicte, Kamilla and Siri, I really enjoyed our coffee-breaks (even though I do not drink coffee), academic and non-academic discussions, trips and friendship. I would also like to thank my friends at Studentersamfundet, from home and from my student time in Trondheim. You have all made my years in Trondheim the best, and you have been an excellent distraction from this thesis.

Finally, I would like to thank my family. Thanks to my little sister Nora for her excellent English correcting skills and general life support, my father Sverre for being the most engaging person to this work and for his deepest compassion for me, and my mother Ann-Helen for being very supportive to my work even though she understands very little of it. Thank you for listening, discussing, helping me and encouraging me to always work hard (but not too much) and follow my own way.

Contents

List of figures

List of tables

1 Introduction

1.1 Silicon and Ferrosilicon Production

Quartz, a mineral consisting of mainly SiO_2, is the raw material used for production of silicon, Si, and ferrosilicon, FeSi. Quartz is also the low temperature, atmospheric pressure polymorph of silica. Together with energy and various carbon sources, Si and FeSi are produced in a submerged arc furnace. The simplest equation for the reaction for Si production is given in equation 1.1

$$SiO_2(s) + 2C(s) = Si(l) + 2CO\ (g) \qquad 1.1$$

Silicon has a number of applications in our everyday life. It is used as an alloying element in aluminum, in electronics and in solar cells. Also, silicon is the starting material for the chemical processing of silicones used in cosmetics, paint, coatings, medical equipment, etc. [1]. Silicon mixed with iron, ferrosilicon, is widely used in the steel industry for removing oxygen, increasing properties as strength, wear resistance and increase elasticity. Worldwide, Norway is one of the largest producers of silicon and ferrosilicon [2].

The production process of silicon and ferrosilicon is much more complex than suggested in equation 1.1. Silicon carbide and silicon monoxide gas are also stable components in a system containing silicon, carbon and oxygen. These compounds affect the production process. A more thoroughly description of the process can be found in the book *Production of High Silicon Alloys* by Schei et al. [3]. Figure 1 shows an overview of a silicon production plant. Raw materials are added to the furnace from the top. In the furnace itself, the raw materials are heated by electricity through three carbon electrodes.

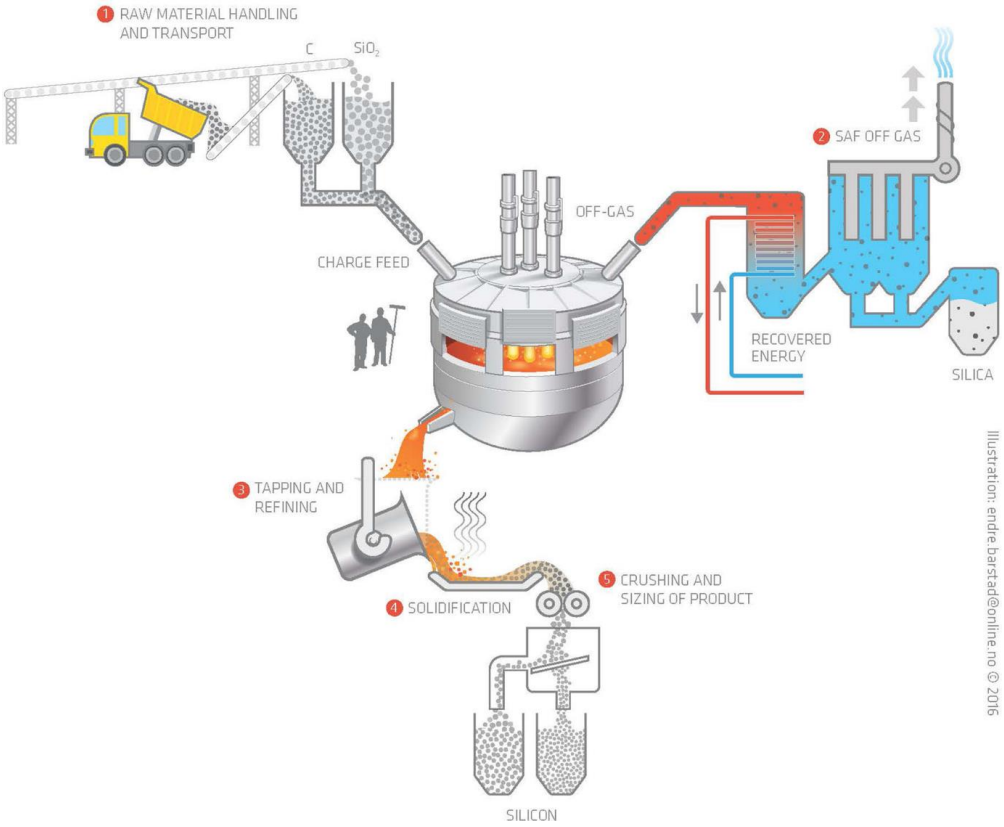

Figure 1: A typical silicon production plant, reprinted from Kero et al. [4]. Raw materials are introduced to a submerged arc furnace at the top. The product is tapped at the bottom of the furnace, and the off gas leaves the furnace at the top through an energy recovery unit and dust filters.

When the raw materials are added at the top of the furnace they will meet a charge surface which holds a temperature between 700 °C and 1300 °C [5]. This will cause the raw materials to be shock heated. The temperature will increase further as the raw materials are descending in the furnace. The upper part of the furnace is called the low temperature zone, and the lower part is called the high temperature zone due to the increasing temperature downwards in the furnace. The boundary between the zones is diffuse and could shift during operation. In Figure 2 the different zones in a furnace are illustrated together with the material flow and the reactions occurring.

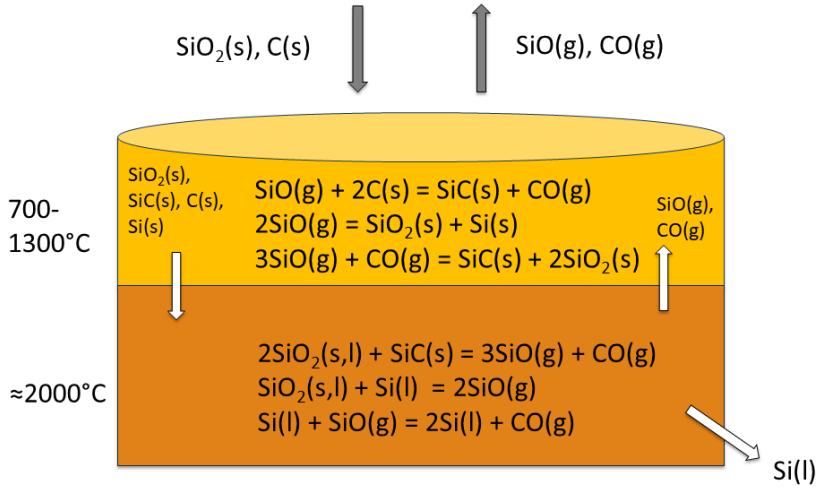

Figure 2: An overview of the reactions in a silicon furnace, the material flow and the low and high temperature zone.

Quartz can react in both solid and liquid form with either silicon carbide or liquid silicon. Both these reaction produces silicon monoxide and carbon monoxide gas, like seen in reaction 1.2 and 1.3.

$$2SiO_2(s, l) + SiC(s) = 3SiO(g) + CO(g) \quad 1.2$$

$$SiO_2(s, l) + Si(l) = 2SiO(g) \quad 1.3$$

The SiO gas produced in these reaction will ascend in the furnace, meet carbon and react according to reaction 1.4. This reaction is between a solid and a gas, and the reaction rate is affected by the SiO reactivity of the carbon. Hence, the reaction is a Si recovering reaction, since it stops the Si to leave the furnace as SiO gas.

$$SiO(g) + 2C(s) = SiC(s) + CO(g) \quad 1.4$$

Silicon will be produced in the lower part of the furnace, where the temperature is at its highest. SiC and SiO gas will react to produce Si and CO gas according to reaction 1.5. For this reaction to be thermodynamically possible, the temperature must be above 1811 °C and the partial pressure of SiO above 0.67 atm. This can be seen in the diagram in Figure 3, where the partial pressure of SiO in equilibrium with SiO_2, SiC and C is plotted as a function of temperature.

$$SiO(g) + SiC(s) = 2Si(l) + CO(g) \quad 1.5$$

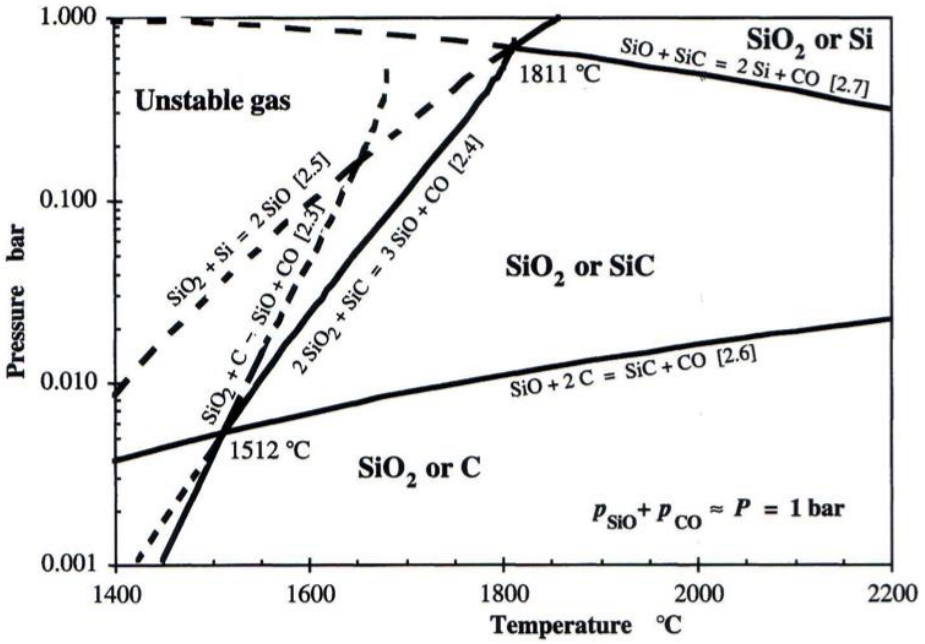

Figure 3: Partial pressure of SiO gas in equilibrium with SiO_2 , SiC and C as a function of temperature [3].

To ensure optimal furnace operation it is favorable that the SiO gas is produced in the lower part of the furnace where it is used in reaction 1.5 to produce silicon. Therefore, quartz should not start to react at too low temperatures. The SiO gas produced in the upper part of the furnace, could condensate according to reaction 1.6 and 1.7, or it could leave the furnace. This will lower the silicon yield of the process. The condensate generated will also contribute to a more compact charge and prevent gas and raw material flow.

$$2SiO(g) = Si(s) + SiO_2(s) \quad 1.6$$

$$3SiO(g) + CO(g) = 2SiO_2(s) + SiC(s) \quad 1.7$$

If the SiO or CO gases leave the charge top without condensation, they will oxidize according to reaction 1.8 and 1.9, and leave the furnace into the heat exchanger and dust filter. The filter will collect small particles of silica, called microsilica. This byproduct is sold for suitable applications such as concrete fillers.

$$2SiO(g) + O_2(g) = 2SiO_2(s) \quad 1.8$$

$$2CO(g) + O_2(g) = 2CO_2(s) \quad 1.9$$

When quartz and various carbon sources are loaded on to the top of the furnace, they will descend. The retention time for a quartz in 25 MW Si furnace is calculated to be 5.7 hours on average, but could also be as short as 1 hour [6]. After shock heating to 700 °C-1300 °C, the

retention time will give a temperature increase of approximately 200 °C per hour. The quartz will then reach a temperature around 2000 °C, and silicon will be produced. Material flow closer to the electrodes will be faster than out in the peripheral areas of the furnace because of higher temperature around the electrodes. An area in the center of the furnace will probably also have a lower temperature and hence a slower mass flow [6].

1.2 Goal and thesis outline

Different commercial quartz types are being used today. They have different chemical and physical properties which will affect the furnace operations in various ways. The relationship between a property and its effect is not fully understood, yet. It is therefore important to relate specific properties of high temperature quartz to the furnace process.

This thesis aims to investigate high temperature properties of quartz. By knowing how different quartz types will behave at high temperatures, and why, the industry could increase their knowledge base when selecting new quartz types for their production. Further, the furnace operations can be improved which means that energy consumption, raw material consumption and CO_2 emissions could decrease. Hopefully, it will also be possible to reduce interventions in nature if one can determine the behavior for a certain quartz type before full scale production is started. In more detail, this study will look into the following aspects of four different quartz types:

- The amount of fines generation, and properties enhancing fines generation
- Phase transformations from quartz to amorphous intermediate phase and cristobalite, and properties that enhance the transformations
- New methods for investigating properties of quartz that can be determining for high temperature behavior
- Summary of earlier investigations of high temperature behavior of quartz

Four different quartz types were selected to be studied thoroughly. An additional six quartz types were used in some experiments for a broader basis for comparison. The term *quartz type* is used to describe the raw material quartz, while *quartz* refers to the silica polymorph. The four main quartz types differ in geological origin as well as chemical composition. They are all suited for either silicon or ferrosilicon production. This research project is a part of High Temp Quartz, a collaboration between Elkem, Sintef and NTNU, and is financially supported by the Research Council of Norway, project number 256788.

2 Theory and Literature

This chapter is divided into two parts. The first part focuses on the silicon and ferrosilicon furnace and how the furnace operation is affected by quartz properties. The second part summarizes earlier investigations of quartz and silica, with emphasize on phase transformations, thermal degradation and quartz properties.

2.1 The furnace and its inner structure

How the inside of the furnace looks like, how the materials flow and how and where the electrical currents are moving are questions which are hard to answer. Due to aggressive surroundings and high temperatures, it is difficult to do measurements inside a furnace during operation. Several attempts to observe the furnace interior have, however, been made. Experiments were performed in the 60s by Zherdev [7], [8] and Ontani [9]. They both inserted a probe into a furnace in operation and were able to observe the areas around the electrode tip. The results from these experiments concluded a cavity existed around the electrode tip during operation. A reef-like bottom deposit of SiC crystals filled with molten silicon was observed 5-15 cm below the electrode tip. Ontani also observed an electric arc from the electrode to the bottom deposit. Further investigation from 1979 and 1982 mentioned by Schei et al.[3] confirmed that an electric arc was observed. It shifted position relatively often, but it could stay at one place for many seconds. This observation was found in a 50 kW furnace, and confirmed in a 500 kW furnace. Compared to today's industrial scale furnaces at 30-45 MW, the test furnaces were small. In the 60s the first furnace excavations also took place [3]. One of the excavations was from a 50 kW pilot furnace with one electrode with bottom contact. Based on several excavation of such kind, the drawing in Figure 4 was made of the inner structure of a furnace. For a long time, this was the accepted structure for all furnaces. Recent investigation has revealed that the inner structure of a furnace is very different from one furnace to another, and the existence of a cavity is not clear in every excavation.

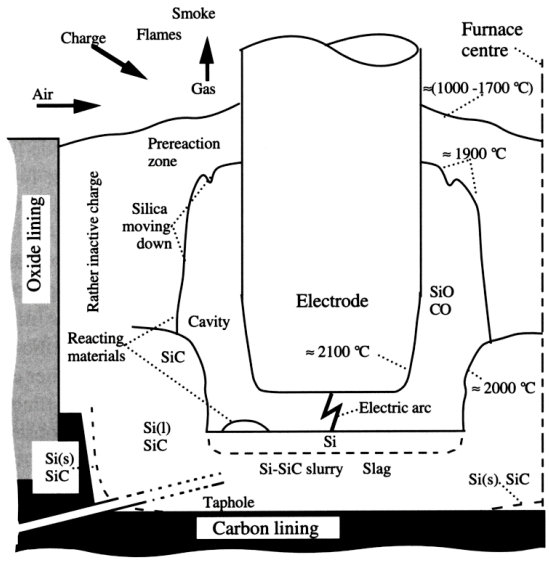

Figure 4: An illustration of furnace structure based on several pilot scale experiments in the 60s and 70s. The figure is from Schei et al. [3].

In a publication from 2016 by Ksiazek et al. [10], five different furnace excavations were compared. The result was five different stories. For the furnaces, it was possible to distinguish some main material zones:

1. Inactive zone towards the side of the furnaces. This zone mostly consisted of deposited slag and some partly or fully melted raw materials. The inactive zone was found in all the excavations, independent on the product of the furnace.
2. An electrode track zone, as the outer shell is rotating.
3. An inner zone located in the center of the furnace between the electrodes

Apart from these three common observations, the structure of the inner environment varied. For one furnace at Finnfjord producing 75 FeSi excavated in 2009, large cavities were found underneath and around the electrode tip. On the other hand, no cavities were found in the furnace at Elkem Bjølvefossen producing FeSi50. An overview of the material zones in these two furnaces can be seen in Figure 5. It must be mentioned that in the furnace from Elkem Bjølvefossen the electrodes were moved after shutting down. This could have affected the appearance of the material zones.

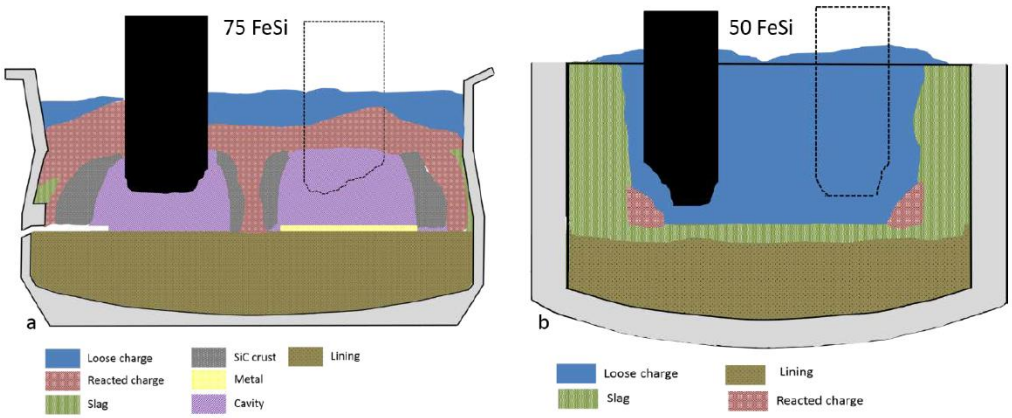

Figure 5: Material zones observed after excavations in a) 75 FeSi furnace from Finnfjord (17.5 MW), and b) 50 FeSi from Elkem Bjølvefossen [10].

For the 75 FeSi furnace excavated in 2009 at Finnfjord, the inside of the furnace can be seen in Figure 6. In the photograph, two of the electrodes can be seen. Underneath the electrodes a thin metal layer was found, and around the electrodes there were rather large cavities. A SiC crust was found outside the cavities. The furnace was operated at 17.5 MW and was about 5 m in inner diameter and 2.5 m high.

Figure 6: Overview of a 75 FeSi furnace during excavation in 2009 at Finnfjord [10].

The existence of a large cavity seen in Figure 4 around the electrode tip, is debated since it is not a common observation from all the excavations. A cavity was observed in the excavation of the Finnfjord FeSi75 furnace in 2009 [11]. The sketch in Figure 4 is based on excavation of a one-phase pilot furnace. Both the pilot furnace and the FeSi75 furnace excavated in 2009 had very high energy density, and it is speculated that such condition could cause the large cavity formations.

Ksiazek et al. [10] also compared three Si-producing furnaces. No cavities were observed underneath or around the electrode tips. For two of these furnaces, the electrodes were moved after shutting down, and it is therefore not possible to rule out any cavity existent. Also due to excavation techniques, the existence of cavities cannot be ruled out. In Figure 7 the observations from the three Si furnaces can be seen. The investigation concluded that the inner structure of a furnace is determined by the furnace operations and not by the raw materials. The reason for this conclusion is that two furnaces at the same plant were operated with the same raw material composition, but they had large differences in the inner structure.

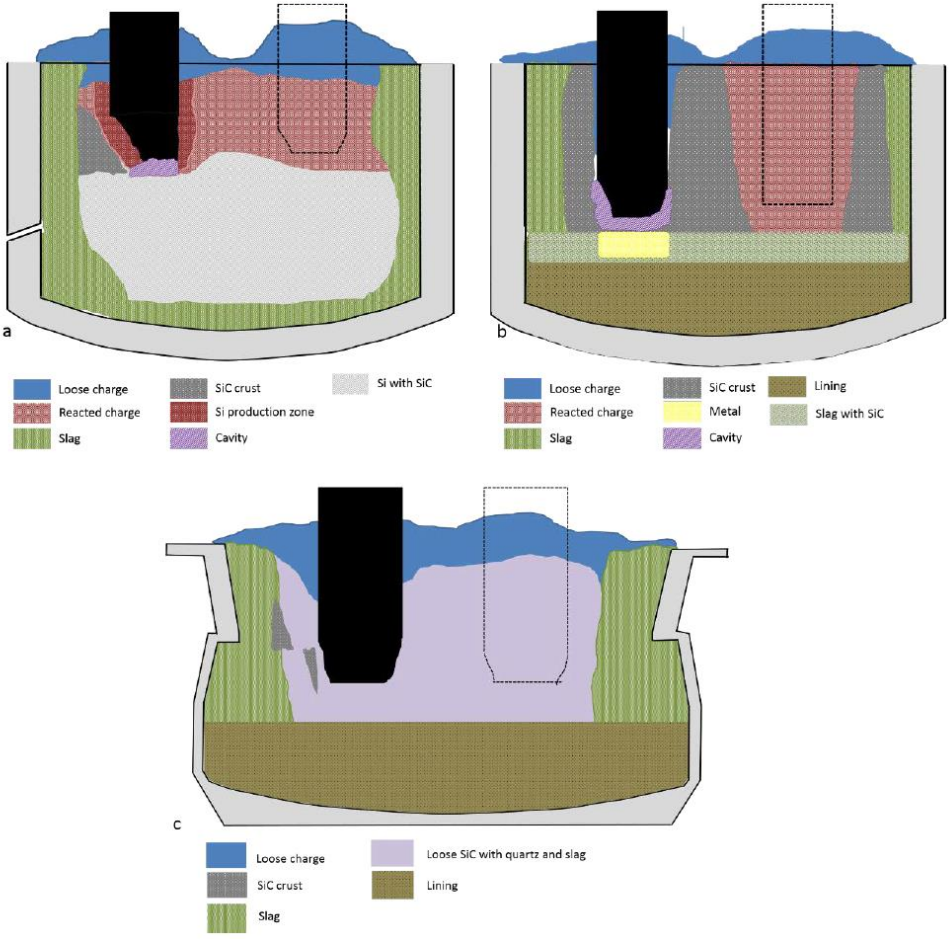

Figure 7: Material zones observed after excavation of a) Si Wacker furnace 1 (13 MW), b) Elkem Thamshavn furnace (40MW) and c) Wacker furnace 4 (33MW) [10].

2.2 Quartz in the Si and FeSi Production

The industry has put up a list where the requirements for a good quartz are given. A good raw material will give a better product, and optimize the process. The definition of furnacability can be found in Aasly's thesis [6] after Kallfelz.

> *A quartz is of good "furnacability" when all its chemical and physical criteria are such to make it an appropriate silica raw material for the production of first grade silicon metal at high rates of process performance.*

The definition is vague, and it does not give any quantitative description of what a good quartz can be. More specific requirements for quartz concerning parameters important for the operation, has been proposed by Schei et al. [3]:

- Impurity content
- Fines (dependent on mechanical and thermal strength, lump size 10-150 mm)
- Softening properties

Impurities enter the furnace through the raw materials and the electrodes. The total content of impurities determines the grade of the ferrosilicon or silicon produced. Different grades have different applications, and have different specifications when it comes to impurity levels. The lowest grade of silicon with high impurity level, is mainly used as alloying element in other metals, especially aluminum. A purer product can be used in the chemical industry to produce e.g. silicones. The highest grade with the lowest impurity level can be used for semiconductor industry. This requires a content if impurities in the ppb and ppm range for electronic devices and photovoltaic cells respectively [12]. Typical impurity content in quartz used for FeSi and Si production is given in Table 1. It can be seen that Al, Fe, Ca, K, Mn, S and Ti are the most common impurity elements in quartz used for FeSi and Si production.

Table 1: Typical content of trace elements in quartz used for Si and FeSi production. The list is made by Myrhaug [12] and is based on several raw material analysis. All units except one are in ppmw. Some analyses are below detection limit and is marked by <.

Element	Amount [ppmw]	Element	Amount [ppmw]	Element	Amount [ppmw]
Al	300-3200	Fe	100-1500	Sb	<0.1-0.9
As	<1-3	Hg	<5-10 ppbm	Se	<2-5.2
B	<10-45	K	<75-1700	Sn	<0.5-2.2
Ba	0.5-25	Mg	20-140	Sr	<0.5-12
Be	<0.5-0.6	Mn	3-600	Ti	20-200
Bi	<0.5	Mo	<2-8	V	<1-4
Ca	<75-160	Na	50-170	W	<0.5-640
Cd	<0.1-1.5	Ni	<1-9	Zn	<1-3
Co	<1-200	P	<5-50	Zr	<0.5-3.3
Cr	3-25	Pb	<0.1-9		
Cu	1-3	S	<5-1400		

Impurities that enter the silicon furnace embedded in the quartz will follow the same path as the quartz. Some elements will escape as the temperature increases, but some, for example transitions metals, will follow the quartz until it is melted and has reached the bottom of the furnace. From there, the impurities will be tapped together with the liquid product [13]. Myrhaug and Tveit [14] found that the distribution of impurities in metal, off-gas and slag was determined mainly by the boiling point of the different elements. All the impurities enter the furnace either through the raw materials or the electrodes. The impurity content of quartz is therefore crucial regarding the final silicon product. Figure 8 gives a graphic representation of the boiling points of the different impurity elements, whereas Figure 9 shows where the elements are likely to be found in the various mass flows of the furnace.

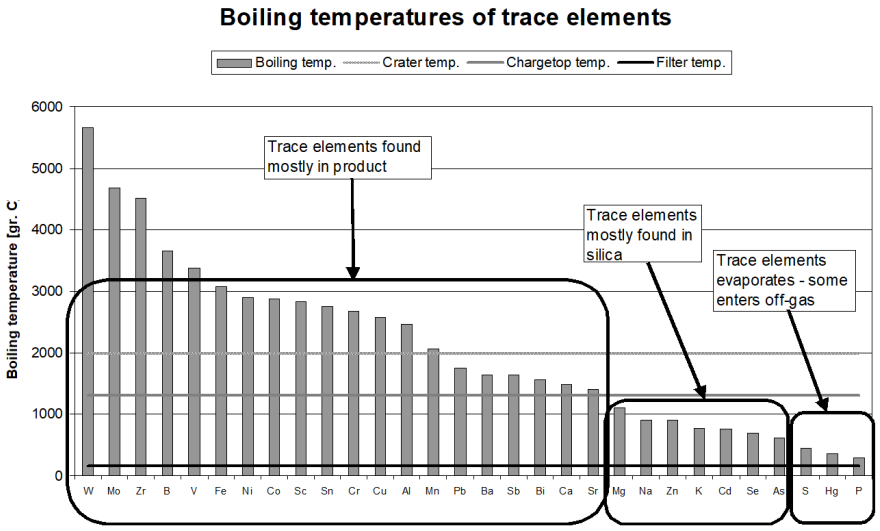

Figure 8: The boiling point of various trace elements found in the silicon and ferrosilicon process [14].

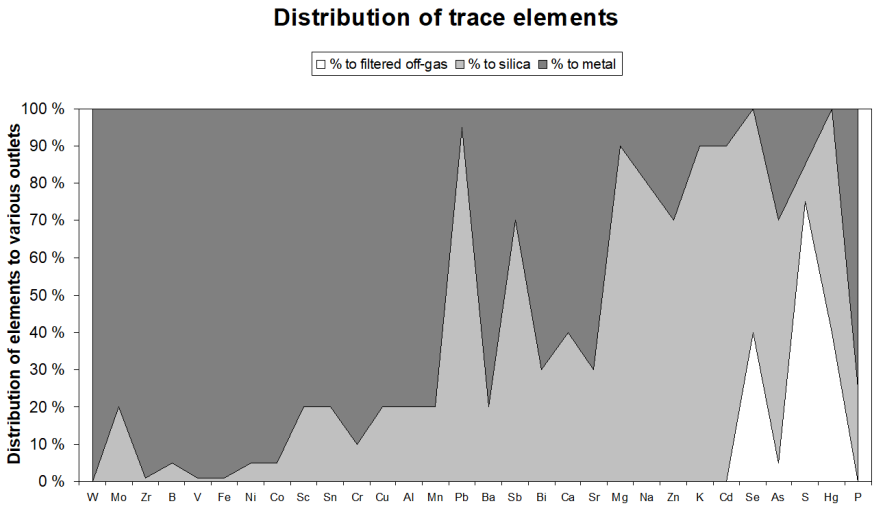

Figure 9: The distribution of trace elements as a function of the boiling point of different elements [14].

The lump size is also important for furnace operation due to clogging and decreased gas permeability with smaller particle sizes. The desired size for raw material quartz is 10-150 mm. If there are many fines in the furnace, the gas flow will be hindered. A pressure could build up in the charge and create small outbursts of gas or channeling. This will lead to decreased SiO capture through reaction 1.4. Both the mechanical and thermal strength can affect the amount of fines generated. It is also speculated if much fines can alter the reaction rates in the furnace because the reaction area will increase.

Preliminary studies of how different quartz fractions affect the pressure drop through a test cell, by Edfelt and Nordnes [15], showed that the pressure drop increased with decreasing quartz size. They tested quartz fractions from 8 mm to below 250 µm. For all experiments with quartz below 1 mm, channels were created in the charge mix due to pressure buildup. This can be seen in Figure 10.

Figure 10: Channel formation in the permeability test cell with charge materials and quartz below 1 mm [15].

Nordnes and Edfelt [15] tested both a mixed charge and a charge where some of the quartz was put in a layer in the test cell. They found that the layered setup gave a higher pressure drop since the gas permeability would increase over the quartz layer. The pressure drop for each quartz size and the different charge distributions can be seen in Figure 11. These data are scaled to the flow rate assumed to exist in an industrial furnace of 1.2 m/s.

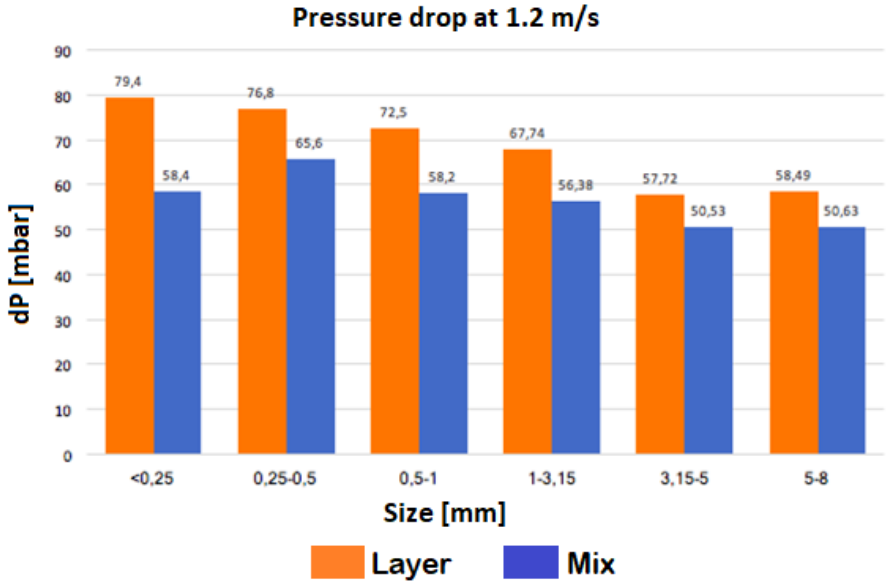

Figure 11: Pressure drop as a function of quartz size and distribution of the quartz in a test cell [15].

Further studies and improvements in the method by Edfelt [16] found that fines between 0.23-1.99 mm and 1.99-4.76 mm caused the greatest pressure drop, and hence a decrease in charge permeability. A schematic overview of the test cell and the positions of the materials and the pressure sensors can be seen in Figure 12. The results from her study can be seen in Figure 13, where the effects of size on the pressure drop is presented. Edfelt [16] suggested that the quartz fines of size 0.00-0.23 mm caused no pressure drop in the furnace, since the material was too small to clog the porous material of quartz, carbon and woodchips in her experiments. In a real furnace, this could also be the case for the 0.23-1.99 mm fraction of quartz. She also concluded that a quartz layer at a lower position in the test cell caused a higher pressure than a quartz layer at a higher position. No pattern was observed between a pure quartz layer and a charge where the quartz was blended in the carbon materials. One explanation of this could be that the size of the layer was too small to cause a noticeable difference.

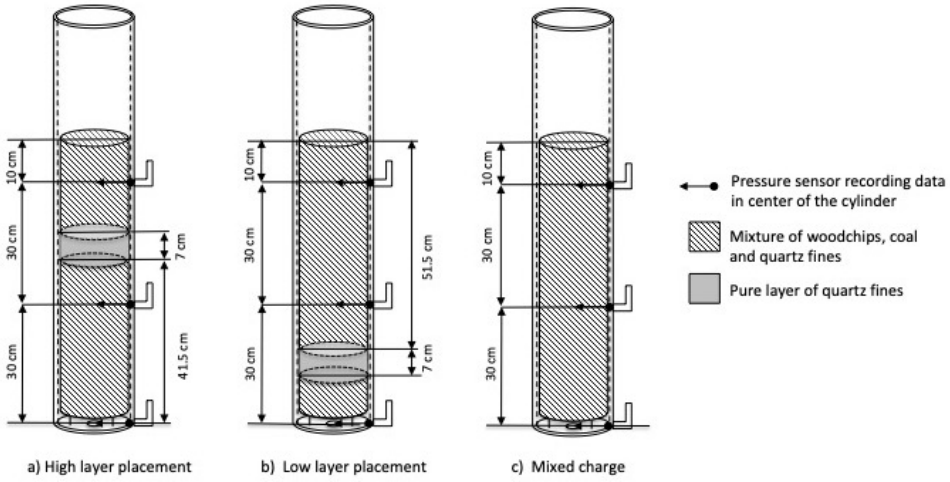

Figure 12: Schematic overview of the test cell and the layered and mixed charge positions [16].

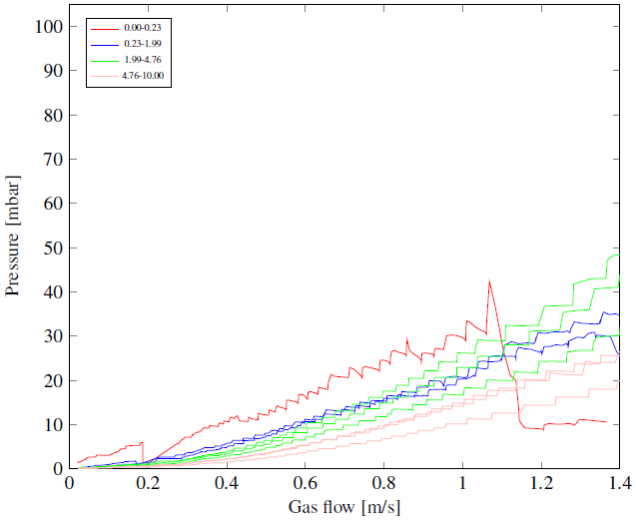

Figure 13: The pressure drop in a test cell with cold charge as a function of the gas flow [16] . Different size fractions have been investigated, and all the sizes are in mm. The smallest size group did not stay in the test tube during the experiment, so the result can be ignored as the test conditions were different. The quartz was placed in a mixed bed with 80 % carbon materials

Before melting of quartz starts, it tends to soften. In a silicon furnace, it is ideally that this softening temperature is close to the melting temperature and occur as deep in the furnace as possible. If the quartz starts to soften at a lower temperature, i.e. at a higher position in the furnace, it might cause a more compact charge and lower the gas permeability. Softened quartz might also be more reactive, and alter the reaction rates in the furnace. This could decrease the Si-yield of the process, and be economically unfavorable.

Based on data obtained from Elkem, Nordnes [17] created a temperature profile for a FeSi production furnace, where the different zones for heating, softening and melting of quartz are marked. The zones are divided based on her results from testing different softening and melting temperatures for three different quartz types A, B and C (different A, B and C than tested in this thesis). The temperature profile can be seen in Figure 14, and in Table 2 the depth of the different zones is given. The softening zone in the furnace is relatively large. This could have a negative effect on the furnace operations since the large softening zone could correspond to a low melting rate, meaning the quartz would use longer time to melt. It is also suggested by Kallfelz in the work by Nordnes [17] that charge material glued together as a consequence of softening and melting in the upper parts of the furnace would become electrically conductive and alter the electric paths in the furnace. In worst case, this will cause a reduction of the power in the arc.

Table 2: Zones in a silicon production furnace. The data are from Nordnes [17].

Zone	**Distance from charge top [m]**
Solid quartz heating zone	0 - 0.8
Softening zone	0.8 - 1.9
Melting zone	1.9 - 2.1
Molten quartz zone	2.1 - 2.4

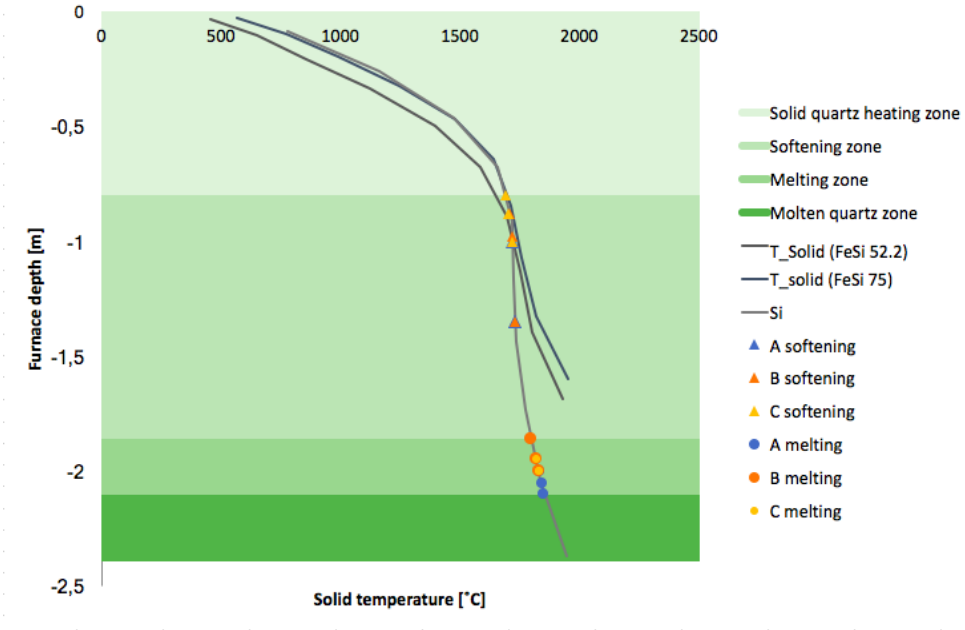

Figure 14: Temperature distribution in a production furnace based on data obtained from Elkem. The figure is from Nordnes [17]. Apparent zones for softening and melting of quartz are marked on the figure.

Nordnes [17] showed that melting of silica is a process that takes time. If the heating rate is too large, the melting will first be observed at a higher temperature than the actual melting temperature. This is further discussed in section 2.4.3. The retention time for quartz in the furnace

will affect the softening and melting of the quartz, and hence the furnace operations. Phase transformations in quartz can also be affected by the time it takes to descend. The phase transformations in quartz are discussed later in this chapter. Earlier investigation by Foss et al. mentioned by Aasly [6], gives an average retention time of approximately 5.7 hours. This is for a 25MW Si-furnace, with an inner furnace height of 2.7 m. The retention time is calculated using SiMod software. Another software tool, FeSiMod, developed for simulating furnace behavior was used in this study to calculate the retention time of quartz for a 40 MW Si furnace with inner height 3.6 m. The retention time was approximately 6 hours in this furnace as well.

2.2.1 Reaction kinetics

Silica will react with either SiC or liquid Si through reaction 1.2 and 1.3 respectively, in a Si or FeSi furnace. Tangstad et al. [18] investigated the reaction between SiO_2 and SiC pellets at temperatures between 1650 °C and 2000 °C. They found that the reaction was dependent on the reaction area either determined by the SiO_2 or the SiC. The reaction rate was also dependent on the fraction of reacted sample, hence it would be faster in the beginning. The activation energy for the reaction was reported to be between 426-464 kJ/mol for the experiments performed. Both cristobalite and quartz polymorphs were tested in the study, but no significant difference was observed in the reaction rate with varying quartz and cristobalite. The reaction rates as a function of polymorphs are discussed later in this section.

The reaction between SiO_2 and Si was investigated by Sindland [19]. She found that the reaction rate increased with temperature and time, like seen in Figure 15. The reaction rate was modelled, and as for Tangstad et al. [18] it was found that the reaction rate was dependent on the reaction area. The activation energy for the reaction between Si and SiO_2 was found to be 552 kJ/mol. Compared to the activation energy for SiO_2+SiC (426-464 kJ/mol) this number is in the same range. If the available area for reaction is very different it will determine which reaction contributes the most to formation of SiO-gas.

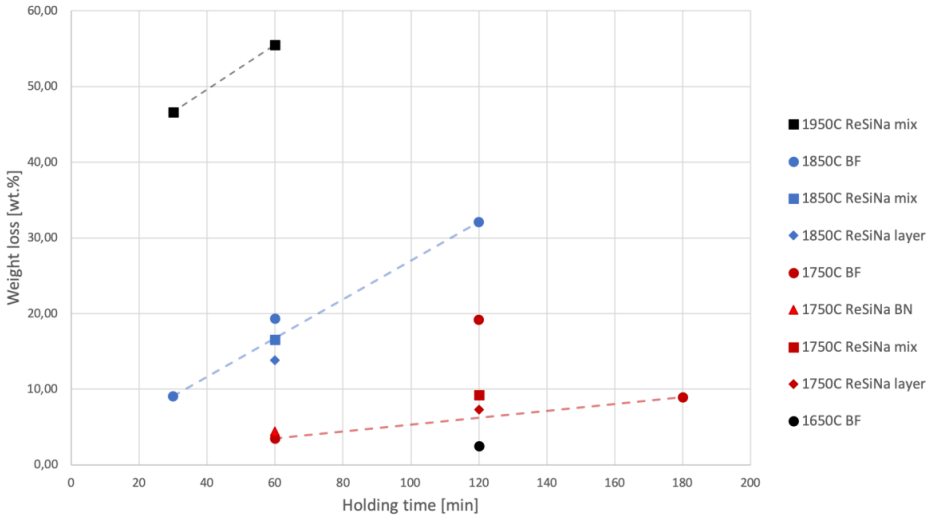

Figure 15: Weight loss as a function of time and for different temperatures for the reaction between SiO_2 and Si [19].

The effect of quartz, amorphous material and cristobalite on the reaction between SiO_2 and SiC, has been investigated by Folstad [20] and Tangstad et al. [18]. In both studies, pellets of SiC and SiO_2 were heated to an isothermal temperature, and the weight loss and gas produced recorded. As

the reaction between SiO_2 and SiC produces gases, the weight loss recorded can be related to the reaction rate. Folstad found no significant difference between 1700 °C and 1900 °C that could be related to the amount of phases of silica in the sample heated. Some of her results can be seen in Figure 16, where the weight loss is plotted as a function of amorphous silica for different heating rates, and temperatures.

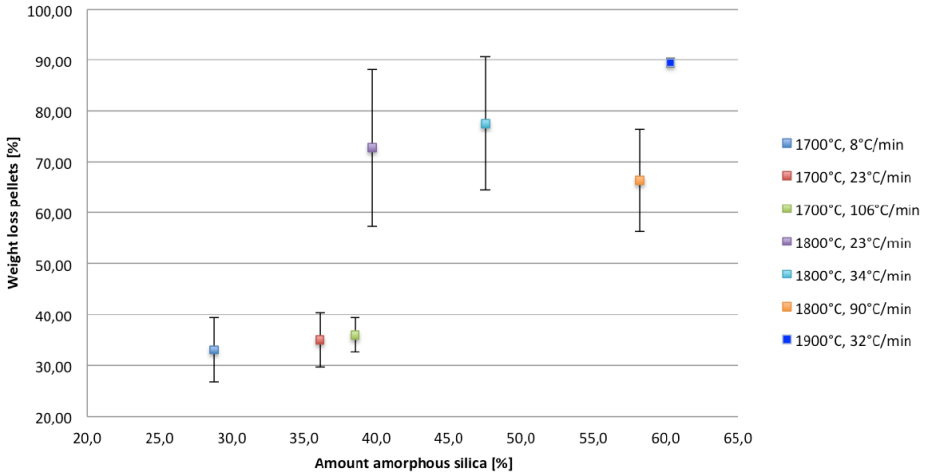

Figure 16: Weight loss recorded when heating pellets of SiO_2 and SiC to 1700-1900 °C with varying heating rate. Here the weight loss is plotted as a function of the fraction of amorphous silica [20].

No correlation between the amount of cristobalite or quartz with the weight loss of the pellets was seen [21]. This is in agreement with similar investigations by Tangstad et al. [18]. They investigated the reaction between SiO_2 and SiC for both quartz and cristobalite in the temperature range 1650-2000 °C. Based on the results, Figure 17 was made. It shows no significant difference in the weight loss between pellets containing quartz or cristobalite when reacting with SiC.

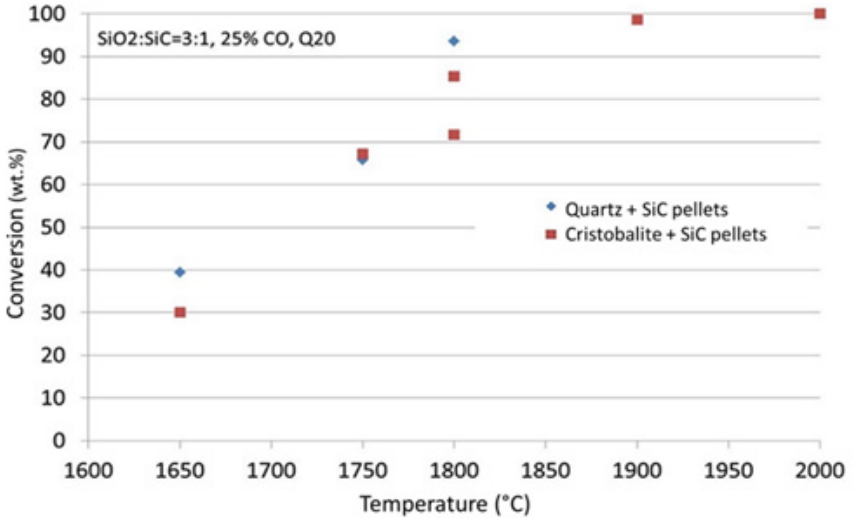

Figure 17: Weight loss after heating SiC and SiO_2 pellets to different temperatures and holding them there for 60 minutes [18].

The independence of quartz or cristobalite on the conversion rate for SiC and SiO_2 to SiO- and CO-gas, is not in agreement with Wiik [22]. He performed experiments with quartz or cristobalite together with a graphite charge at a pressure 1.066 bar CO at 1558 °C. The weight loss of the material was measured after cooling. He measured a rate almost twice as high with cristobalite versus quartz. This can be seen in Figure 18. It must be mentioned that Wiik's experiments are not directly comparable to Tangstad el al.'s [18] and Folstad's [20] since the temperature was different. Wiik explained the increased rate by the lower density and hence higher volume and surface of the cristobalite phase versus the quartz phase. He also explained that when cristobalite is cooled it will transform to its low-temperature configuration, the α-cristobalite. This transformation could have caused microcracks increasing the surface that is avaliable for reaction. In Tangstad et al.s investigations the cristobalite phase was also created in a separate heating before turned into pellets. Their results still showed no significant difference. Folstad [20] tried to take this into consideration when conducting her experiments. Both experiement where the cristobalite was formed before and during the heating experiments with the pellets were done. Still no significant difference of the reaction rate between quartz, cristobalite and amorphous phase was observed.

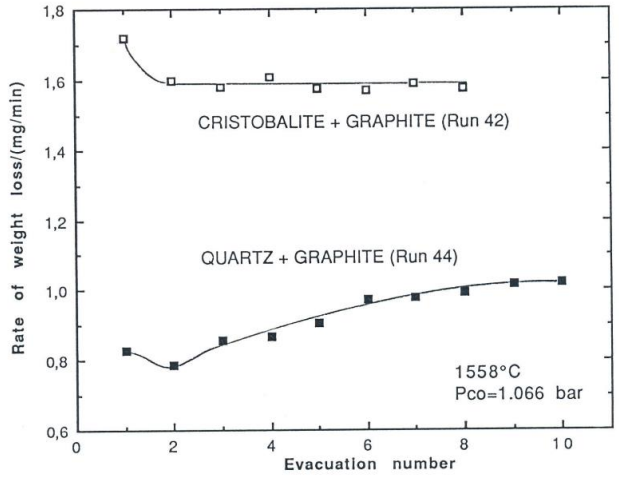

Figure 18: Rate of weight loss with use of thermogravimetry for heating different silica sources with graphite to 1558 ℃ and with 1.066 Bar CO [22].

It was shown by Hakamada et al. [23] that at 1773 K the reaction between SiO_2 and C, produced SiC at a higher rate when the silica source was amorphous silica refined from diatomaceous earth rather than quartz. As SiC is an important intermediate specie in the silicon production they concluded that amorphous silica seemed to be a good silica source for Si production. Further, it was also shown in the same study that the reaction between SiO_2 and SiC producing Si above 2073 K, had a higher yield of Si when the amorphous silica was used.

When two solids react without interaction from gas or liquid, the reaction happens at contact points. As the reaction proceeds, there will be a layer of reaction product between the two solids which slows down the reaction rate because the reactants must diffuse through a product layer. In theory, silica and carbon will react through this mechanism. Investigations by Motzfeldt and Steinmo [24] showed that the reaction between silica and carbon was more likely to happen through a gas phase. This has later been verified by Fei [25]. For silica and carbon, the reaction goes through a gas phase of CO and CO_2. This reaction mechanism is also accepted from iron oxide reduction. SiO_2 will first react with CO gas to produce SiO and CO_2 gas according to the reaction in Figure 19. Further, the CO_2 gas can react with C to produce CO gas, or after some time the CO_2 gas can react with the SiC layer. The SiO gas produced could also react with the solid carbon. Figure 19 shows an idealized sketch of the reaction between SiO_2 and C. This mechanism is more likely than a solid-solid reaction.

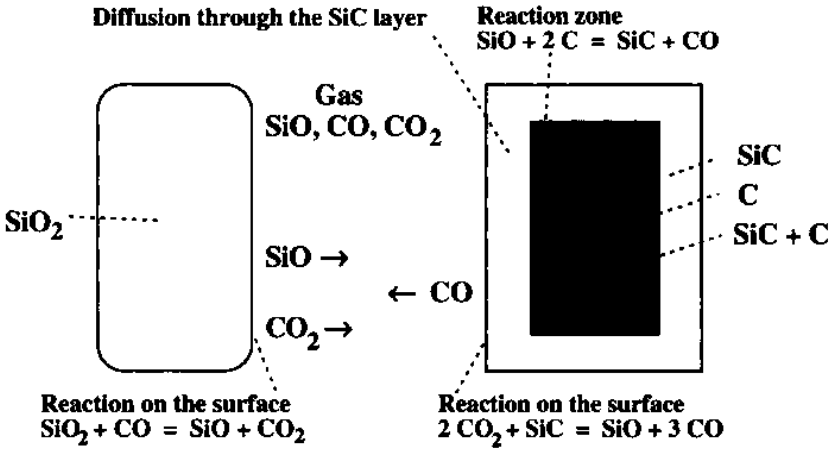

Figure 19: Mechanism for reaction between SiO_2 and C through a gas phase consisting of CO and CO_2 [3].

There has been some doubt whether the partial pressure of CO_2 gas is sufficient to explain the reaction mechanism. This has been thoroughly studied by Wiik [22], and it is shown that when heating SiO_2 with CO gas present, SiO gas and CO_2 gas will be produced. Therefore, the reaction described is likely to happen. It is also suggested by Wiik [22] that the mechanism for the reaction between SiO_2 and SiC also goes through a gas phase. Schei et al. [3] propose a reaction scheme. When equilibrium is disrupted in a system containing SiC, SiO_2, CO and SiO gas, silica will react with CO gas according to reaction 2.1, and make a gas film at the surface of the silica particle. Further, the CO_2 gas will react with SiC according to reaction 2.2.

$$SiO_2(s) + CO(g) = SiO(g) + CO_2(g) \qquad 2.1$$

$$2CO_2(g) + SiC(s) = 3CO(g) + SiO(g) \qquad 2.2$$

This mechanism has not been thoroughly tested. SiC can also react with liquid SiO_2. The contact area between the two phases will then increase, and the temperature will be above 1723 °C. This is believed to increase the reaction rate, but it has not been thoroughly tested. Results from Folstad [20] where pellets of SiO_2 and SiC were heated to different target temperatures, show that when exceeding the melting point of quartz, the SiC particles will be dispersed in a melted SiO_2 matrix. Figure 20 and Figure 21 show pellets consisting of silica and silicon carbide heated to 1700 °C and 1900 °C respectively. It is clear that the contact area between SiO_2 and SiC increases as the SiO_2 melts. The images are taken with scanning electron microscope.

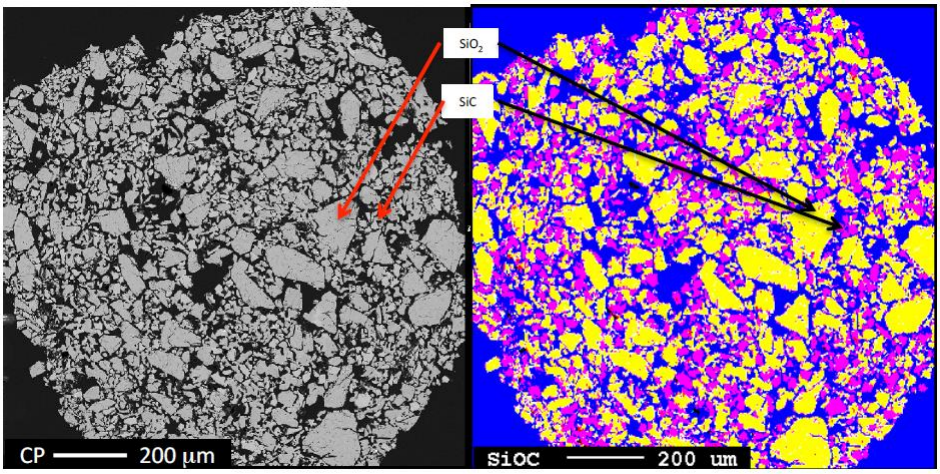

Figure 20: Backscattered image to the left and chemical composition Si-O-C to the right, for a pellet heated to 1700 °C with a heating rate of 23 °C/min. The images have magnification 80X [20].

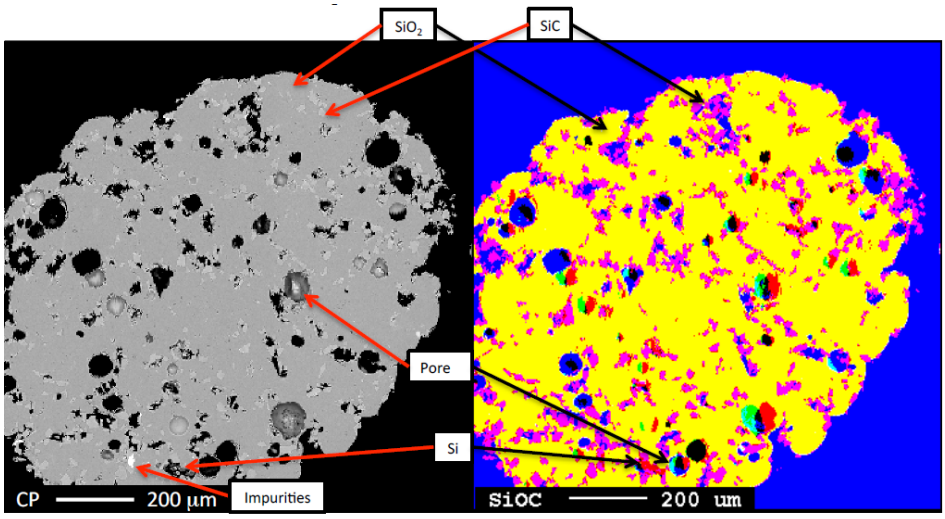

Figure 21: Backscattered image to the left and chemical composition Si-O-C to the right, for a pellet heated to 1900 °C with a heating rate of 32 °C/min. The images have magnification 80X [20].

2.3 Formation, occurrence and geological aspects of quartz

Silica is found in nature as the low temperature and low pressure polymorph quartz. It has a wide area of use from component in concrete, ceramic materials, oscillator in electric circuits, membrane in ultrasonic devices and raw material for silicon and ferrosilicon production [26]. Quartz is the second most abundant mineral in the earth's crust, and it is found around the world in various forms. This chapter will focus on the aspects of quartz considered important for metallurgical aspects.

Several types of quartz are used as raw material for the metallurgical processes. Different geological environments and the formation conditions affect the properties of the quartz. For

rocks in general, there are three types: igneous, sedimentary and metamorphic rocks. The first one, igneous, is formed when magma solidifies. This can happen at the surface of the crust or in the interior of a planetary body. Different minerals together with quartz will crystallize when the magma cools. Very pure quartz can be formed in the latest stage of recrystallization from a cooling magma. Sedimentary rocks are formed of layers or erosion products of other rocks, chemical precipitates and also organic materials. Due to its chemical and physical resistance to corrosion, quartz is concentrated under sedimentary processes. Quartz is hence relatively stable against chemical weathering. Metamorphic rocks are either igneous or sedimentary rocks that has experienced changes in temperature and /or pressure which has caused recrystallization into new rocks. Quartz can be formed as products in mineral reactions during metamorphism. In addition, hydrothermal processes play an important role in the formation of quartz. Si rich thermal fluids entering into fracture systems of the host rocks of the upper crust can crystallize quartz when temperature and pressure drops. For today's metallurgical processes lumps of quartz are used. This rule out sand as a possible source. In the future, pellets could be used as raw materials, but the method is still being investigated [25].

Different quartz deposits will contain quartz with different properties. It is important to know the origin of the quartz in order to explain its behavior and properties. The quartz deposits that are used in metallurgical industry are listed in Table 3 [6]. It also summarizes typical features of the deposits.

Table 3: Different types of quartz used for silicon and ferrosilicon production.

Type of quartz deposit	Features
Hydrothermal quartz	This type could be very pure (those are selected for silicon production). It is formed by precipitation of quartz from hot aqueous fluids which flows through fractures or other openings in rocks. A hydrothermal quartz veins is created. Such veins can be less than a cm wide with length up to several meters. It is also possible to find veins that has a width of tens of meters, and length in the km scale [6], [27].
Quartzite	This type is formed during medium to high metamorphism of quartz sandstone by recrystallization. Depending on the condition, quartzite could be very strong and uniform, but the strength will vary. The purity is high, and impurities are often mica, clay minerals, feldspar and other more durable minerals. The color is usually white, but iron or other impurities can give color to the quartzite [6], [27].
Pegmatite quartz	This type is a typically coarse grained igneous rock. High purity quartz can often be found in the core which tends to be surrounded by a zone of albite and potassium feldspar and fine-grained granitic boarder zone [28]. This type is not widely used as a raw material for Si and FeSi production, but could be a potential source in the future [6].

For metallurgical aspects, one often distinguishes between rock and gravel quartz which is quartz mined by blasting and drilling operations, and quartz taken from fluvial deposits by more gentle excavation techniques. Gravel quartz is often more resistant to size reduction because of the natural transport through fluvial deposits where only mechanical strong lumps have survived. Rock quartz on the other hand, could be weakened from the blasting and drilling operations, and is believed to disintegrate more easily [6].

The void space of quartz is fairly limited [13]. This results in a low tolerance for impurity atoms. The most common impurities in quartz are aluminum, iron, lithium, sodium and potassium. These impurities may give rise to different colors of the quartz [29]. Al^{3+} is the most general abundant impurity due to similar ionic radius to Si and common appearance in the earth's crust [28]. If the quartz contains fluid inclusions and solid inclusion, this can contribute to an increased amount of trace elements [30].

Impurities in quartz can be carried in three different forms. First, there can be structural impurities, where the Si^{4+} is replaced in the lattice structure. These are substitutional impurities. To balance the charge, interstitial impurities can also exist. These are mostly small monovalent ions, that can fit into the structure [30]. Solid inclusions are foreign minerals that grow inside of or between the quartz grains [13].

The impurity content in quartz vary with the specific geological formation. Quartzite has more impurities than pegmatite and hydrothermal quartz. Crystallization at higher temperatures will give a quartz with higher purity [31]. In general, solid solubility impurities are very low in quartz because of the strong Si-O covalent bond. Trace elements will gather at grain boundaries and make structural defects [32]. When quartz is heated, it will undergo phase transformation to a more spacious polymorph. These crystallographic configurations have shown to hold substitutional impurities more easily. The diffusivity of trace elements in high temperature polymorphs depends on the cation charge. Univalent cations are faster than divalent, and so on [13]. Since quartz has a closed crystallographic structure with limited amount of void space, impurities segregate towards grain boundaries, sub-grain boundaries and dislocations [13], [33]. These inclusions can be removed by acid leaching before carbothermic reduction of quartz. In that way, low-purity silica sources such as quartzite can be used as a raw material for solar grade silicon production [13].

The trace element composition of quartz can also be significantly influenced by fluid and mineral inclusions. Fluid inclusions could either be a liquid and/or a gas trapped in the crystal structure. These are created as the minerals grow or deform in the presence of a fluid [34]. The inclusions could give information about geological history such as temperature of formation, formation paragenesis and chemistry of mineralizing fluids [28], [35].

In the assessment of high purity quartz resources, fluid inclusions are being investigated using several techniques such as optical microscopy, micro thermometry and Raman spectroscopy to determine the orientation of the fluid inclusion (along cracks or scattered), the chemical composition and pressure. The orientation of the fluid inclusion might be important if they are aligned along tracks that will be opened during treatment [36]. All these techniques use smaller samples sizes and several samples are needed to obtain information about the bulk quartz deposits. Using optical microscopy, fluid inclusion can be imaged. An example of two-phased fluid inclusions in quartz can be seen in Figure 22.

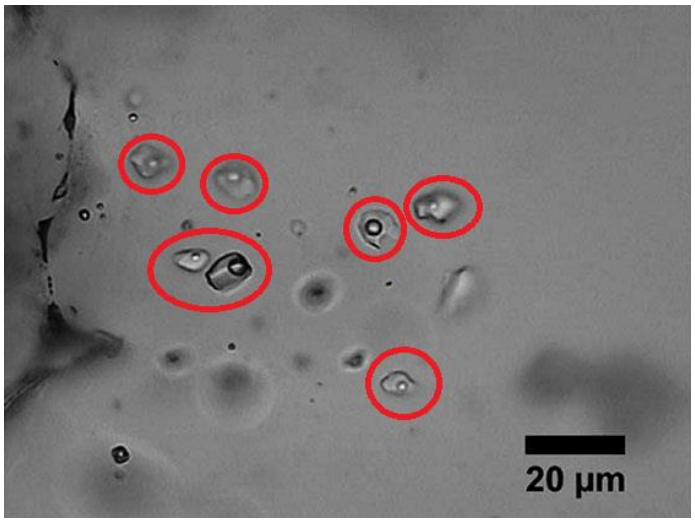

Figure 22: Secondary aqueous two-phase liquid-vapor inclusions in quartz, marked with red circles. The image is taken using plane polarized light and is retrieved from Götze et al. [36].

In general, microscopic cracks, pores, and other flaws such like inclusions will weaken a rock. Therefore, if a quartz sample has more microcracks, or solid or fluid inclusions it may weaken the strength of the sample compared to a sample with less flaws [37]. The existence of fluid inclusions in quartz can also modify the shapes and texture. When a quartz crystal experiences strain, inclusions within the crystal can deform and generate microcracks [38]. It is also suggested that if quartz is plastically deformed, fluid inclusions can migrate to grain boundaries. The consequence of this is that plastically deformed quartz grain contain fewer and smaller inclusions than adjacent undeformed crystals. If undeformed quartz crystals have primary fluid inclusions, plastic deformation can often decrepitate the primary fluid inclusions and redistribute the water into many smaller secondary inclusions. Tarantola et al. [38] investigated fluid inclusion in quartz and found that in areas where fluid inclusions were present, deformation were more frequently observed than in areas with no fluid inclusions, which seemed undeformed. The existence of fluid inclusion and especially water inclusion has been blamed for decreased thermal stability, as the fluid inclusions decrepitate during heating [6]. Investigations by Simon [39] found two H-reservoirs in quartz: fluid inclusions and structurally bounded water in small, homogeneously distributed micro-clusters. Often, such micro-clusters could be accompanied by other impurities such as Al^{3+}, K^{+}, Na^{+} and Li^{+}. An illustration of these clusters can be seen in Figure 23.

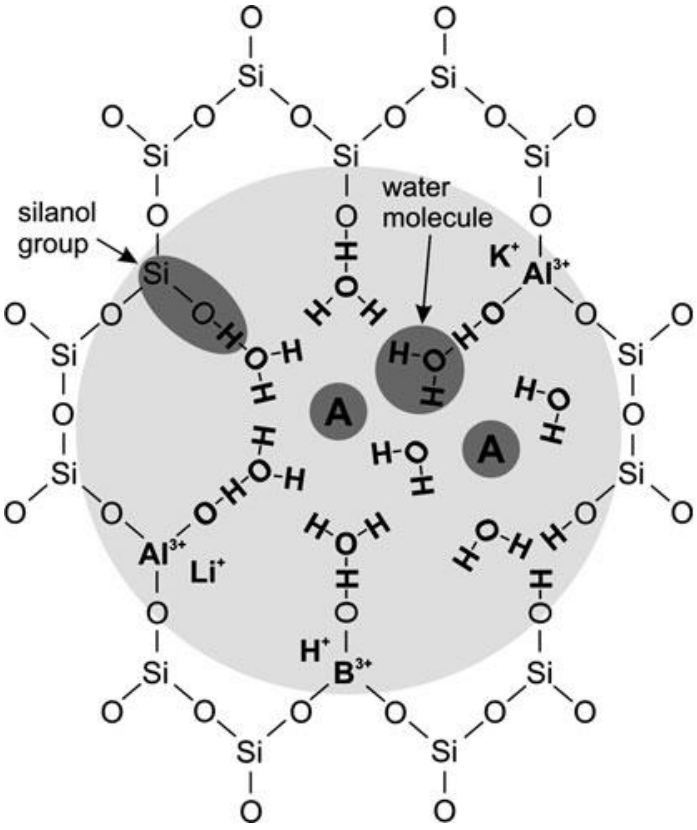

Figure 23: Theoretical arrangement of micro-clusters in quartz containing alkali ions and hydrogen, OH- groups and water [40]. The A in the illustration can represent hydroxyl-attracting ions such as P^{5+}, B^{3+} and Fe^{3+}. These sites are a transition between lattice defects and inclusions.

To measure the water content in quartz, FT-IR is the only method that can define both the quantitative distribution and the speciation. Structural water in the form of H_2O, H^+ and OH^- in quartz will give absorption band in a FT-IR spectra between 3000 and 3700 cm^{-1} [41]. In Aines' et al. [42] study it was reported that it is possible to distinguish isolated water molecules and hydroxide ions. At 1630 cm^{-1} there is an absorption due to bending of the H_2O molecule, and at 3220 cm^{-1} there is a stretching absorption with an antisymmetric stretching absorption at 3445 cm^{-1}. The presence of H_2O molecule is also confirmed by bending absorption at 5200 cm^{-1}. If the bending absorption (at 1630 cm^{-1} and 5200 cm^{-1}) is absent it indicates that the sample does not contain molecular H_2O, only OH^- groups. To distinguish between liquid water and water bounded to other molecules one can inspect the two stretching modes near 3400 cm^{-1}. If the water is bound, it produces sharper peaks around 3400 cm^{-1} than liquid water [42]. Fukuda [43] investigated the water content in chalcedonic quartz, which contained fluid water at intergranular regions and -OH groups in quartz crystal structure. He also reported that fluid water would give an asymmetric broad band ranging from 2750 to 3800 cm^{-1}, with a shoulder at around 3260 cm^{-1}. In chalcedonic quartz the -OH groups are mainly trapped as Si-OH, and at 3585 cm^{-1} the sharp band of the OH-band can be observed. A typical IR-spectrum from Fukuda [43] is shown in Figure 24. The image includes the spectrum for a thicker sample thickness (1mm), which shows combination modes of the stretching and bending modes at 5200 and 4500 cm^{-1} for fluid water and Si-OH respectively. By using the molar absorption coefficients, the contents of H_2O and Si-OH can be calculated. The

reported absorption coefficients in Fukuda's work are 0.761 and 1.141 L mol^{-1} cm^{-1} for H_2O and Si-OH, and hence the content calculated is 0.32 wt% H_2O and 0.28 wt% Si-OH.

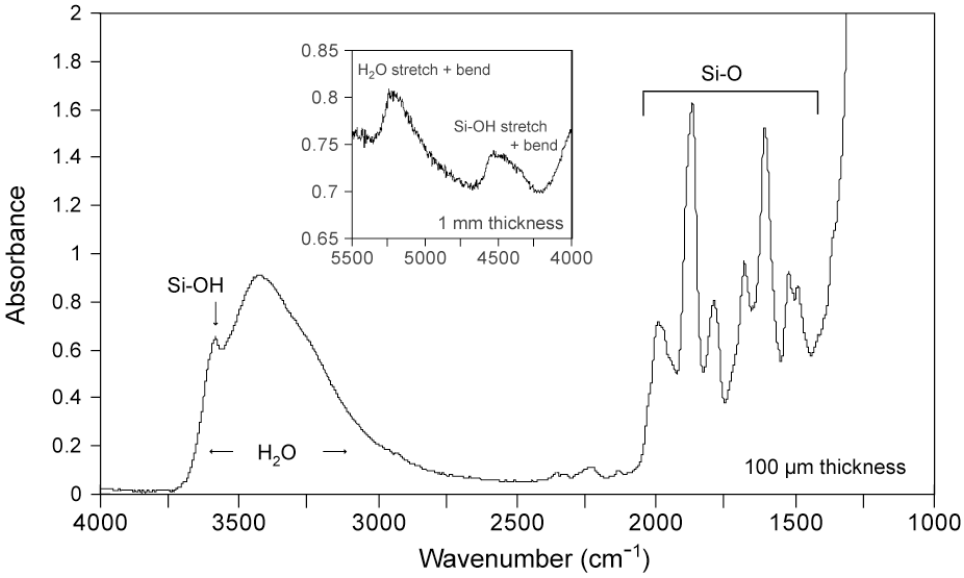

Figure 24: A typical IR-spectrum of chalcedonic quartz at room temperature [43].

Other impurities such as muscovite ($KAl_2(Si_3AlO_{10})(OH)_2$) will have a peak in the IR-spectrum at 3425 cm^{-1} and 3625 cm^{-1}, the latter due to the stretching of Al_2-OH bond [44]. Kronenberg et al. [45] investigated quartzite with FT-IR and found that mica would have a peak around 3600 cm^{-1}, while water showed a broader absorption band around 3400 cm^{-1}. These could be distinguished as seen in Figure 25. In Kronenberg study [45] they suspected the mica absorption peak to be muscovite. This could be confirmed by peaks at 3311, 3146 and 3035 cm^{-1}. These peaks are not seen in Figure 25, due to the broad OH-band from molecular water. The OH-band at around 3600 cm^{-1} could also indicate biotite ($K(Mg/Fe)_3AlSi_3O_{10})(F/OH)_2$). This is confirmed by absorption peaks at 3648, 3614, 3258, 3043 and 2829 cm^{-1}. The latter peak should be visible in the spectrum in Figure 25 if biotite was present. Broad absorption band at 3695 cm^{-1} and 3530 cm^{-1} can in general be assigned to hydroxyl stretching modes [46]. An overview of different IR-spectra of clays can be found in Madejova et al. [47].

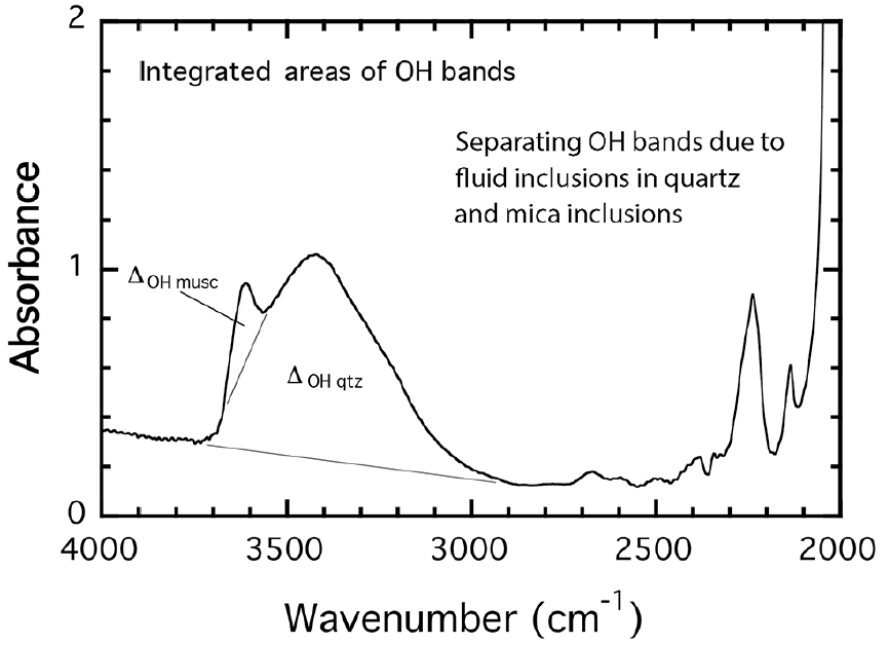

Figure 25: FT-IR spectrum of quartzite containing both molecular water and muscovite impurities. The OH-band in muscovite causes a relatively sharp absorption peak at around 3600 cm^{-1}, while the OH-band in the molecular water causes a broader absorption band around 3400 cm^{-1} [45].

2.4 Changes in quartz upon heating

As the quartz is heated in a silicon or ferrosilicon furnace, many of its properties will change. The most relevant changes are those connected to mechanical and thermal strength and to changes that could affect the reaction rates, such as melting. The bond strength might also change while the phases are changing. These changes in properties are different amongst quartz types. Therefore, the information on how much a property will change in one quartz type compared to another is important information when selecting the most suitable quartz for the silicon and ferrosilicon production.

2.4.1 Phases of silica

Silicon is mostly bounded as silicon dioxide, also called silica. The simplest building block consists of 4 oxygen atoms surrounding one silicon atom. The silicon atoms are shared with neighboring oxygen atoms, which makes the atom ratio 2:1. A drawing of this tetrahedra is seen in Figure 26. These tetrahedrons can be arranged in numerous ways to create different phases of silica. The mean Si-O-Si bond angle is 109°, and the bond has mostly a covalent character [48].

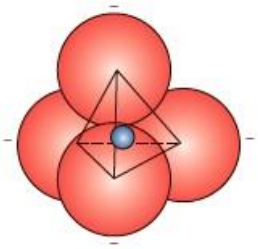

Figure 26: Silicon-oxygen tetrahedron, SiO_4^{-4} [48].

α-quartz is the predominant phase of silica, as low temperature and ambient pressure favors this configuration [29]. The most common phases of silica are shown in the phase diagram in Figure 27. α-quartz is the most stable configuration at room temperature and atmospheric pressure. At 573 °C the transformation to β-quartz will occur. This transformation is displacive, which means that no bonds are broken, only shifted, which leads to a small energy barrier for the transformations. Upon cooling, the reverse transformation will happen [29]. According to the phase diagram, β-quartz will transform to tridymite just below 900 °C. Several researchers have investigated this transformation and it is suggested that the tridymite phase is not a pure silica phase, but needs certain impurity elements to form [49], [50]. This statement is however also debated [51], [29], and a common conclusion is not accepted. Earlier investigation of the phases in quartz used for silicon and ferrosilicon production did not find any tridymite [52]. If tridymite is not considered as a pure silica phase, the next phase transformation is from β-quartz to β-cristobalite. In the phase diagram this transformation is suggested to happen at 1470 °C, but cristobalite has been detected at much lower temperatures [53]. Hence, the reaction rate may be quite slow, and in real life it is therefore more expedient to talk about a transformation interval, where an increase in temperature will increase the rate of transformation [54]. This transformation is shown to go through an amorphous intermediate phase [55], [56], [57], [58]. The transformation is reconstructive, meaning the bond between atoms are broken and rearranged. Such transformation requires more energy than a displacive transformation [13], [59]. A more detailed explanation of the transformation from β-quartz to cristobalite is given later in this chapter.

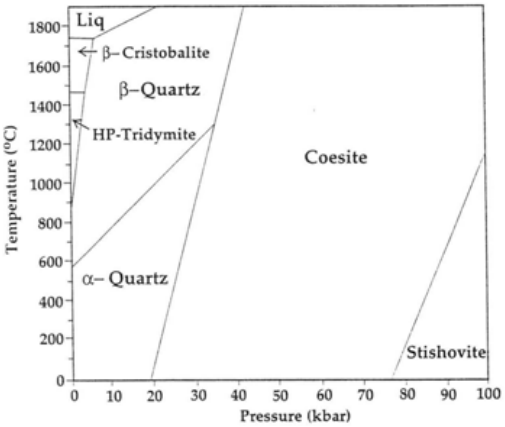

Figure 27: The phase diagram of silica [60].

A schematic representation of some phase transformations for silica is shown in Figure 28. The type of transformation is also indicated in the figure. It must be mentioned, that silica also has other configurations as the energy barrier between different phases are low. The number of silica phases is not exact, but numbers above 15 and up to 30 are mentioned in the literature [28], [61].

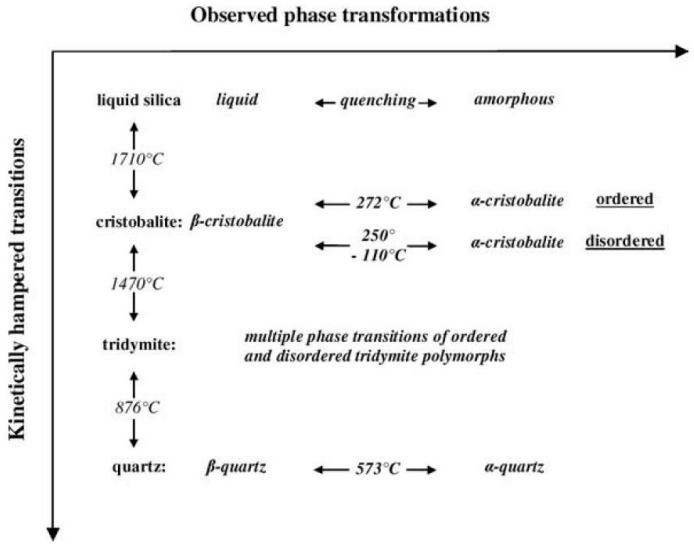

Figure 28: Phase transformations in silica [62].

In Table 4 the 15 known silica modifications are grouped and listed. The table is after Götze et al. [28], but is based on data from Mineralogical Tables by Strunz and Tennyson (1982). Trigonal α-quartz is the most common in nature. Due to its hardness (7 on Mohs scale) and its low solubility in water, α-quartz is preserved during chemical weathering, making it one of the most common minerals in sedimentary rocks [29].

Table 4: Different silica modifications and their crystal structure [28].

Group	Name	Crystal structure
Quartz-tridymite-cristobalite group (atmospheric and low pressure)	Low (α)-quartz	Trigonal
	High (β)-quartz	Hexagonal
	Tridymite	Monoclinic
	High-tridymite	Hexagonal
	(α)-Cristobalite	Tetragonal
	High (β)-cristobalite	Cubic
	Melanophlogite	Cubic
	Fibrous SiO2 (syn.)	Orthorhombic
	Moganite	Monoclinic
	Keatite (syn.)	Tetragonal

Keatite-coesite-stishovite group (high and ultra-high pressure)	Coesite	Monoclinic
	Stishovite	Tetragonal
	Seifertite	Orthorhombic
Lechatelierite-opal group (amorphous phase)	Lechatelierite	Natural silica glass
	Opal	H_2-bearing, solid SiO_2 gel

As quartz is used for the silicon and ferrosilicon production, it is further discussed together with its phase transformation products cristobalite and amorphous silica. In Table 5, the density, transformation temperature and the crystal structure of the relevant phases are given. It can be seen that the densest silica phase is α-quartz. The density is less for both tridymite, cristobalite and amorphous silica compared to quartz.

Table 5: Properties of different phases of silica which are in the same temperature and pressure area as the production of silica [29], [28].

Silica structure	Density [kg/dm^3], [29]	Transformation temperature [°C], [29]	Crystal structure, [28]
α-quartz	2.6495	573 (from α- to β-quartz)	Trigonal
β-quartz	2.5334		Hexagonal
Tridymite	2.183	970 (from β-quartz)	Monoclinic
α-cristobalite	2.333	272 (from β- to α- cristobalite)	Tetragonal
β-cristobalite	2.205	1470 (from β-quartz or tridymite)	Cubic
Amorphous	~2.0-2.2	~ 1300 [49]	

Amorphous phase

Amorphous, meaning having no fixed form or shape, categories a crystal structure (or lack of such) where there is no long-term repeatability in the positioning of the atoms. Conversely, amorphous liquids and solids may contain organized atom groups giving them a short-term order. In silica, five different amorphous states have been reported [59]. They differ in the density of the material and are sensitive to the pressure experienced. Liquid state silica also has an amorphous appearance.

One can distinguish between true amorphous solids and highly disordered nano crystalline solids. In the latter, there exists some order at the nano scale [63]. Traditionally, glassy amorphous materials are formed from a melt which is cooled at a rate that will avoid crystallization. The difference between a melt, which is also amorphous, and an amorphous solid is not distinct. There have been several ways to define the amorphous liquid-solid boundary:

- Rheological definition: As the temperature of a super cooled liquid decreases, kinetics slows down and the viscosity increases. An arbitrary viscosity limit is set, where flow is practically not observed any longer [64].
- Thermodynamic definition: the dependence of heat capacity is distinctly different for liquids and solids, with a discrete drop observed during solidification. At some point during cooling, the heat capacity of the super cooled liquid will drop down to the level of the solid, even without crystallization, entering a non-ergodic state. This can be seen in Figure 29, which shows the heat capacity as a function of temperature for Se.
- Ideal gas transition temperature: the difference in heat capacity between a liquid and a solid, results in an entropy difference between the super cooled liquid and the crystal. By extrapolation of heat capacity from stable through super cooled liquid, it is found that the system entropy at some point will drop below that of the crystal. Consequently, the melt must enter the solid glassy state at this temperature to avoid a so-called entropy crisis. The temperature where this happens is called the ideal glass transition temperature or the Kauzmann temperature [61]. Figure 30 shows the entropy of a melt as it cools and becomes a solid. At the temperature T_g, the super cooled liquid will start to form a glass.

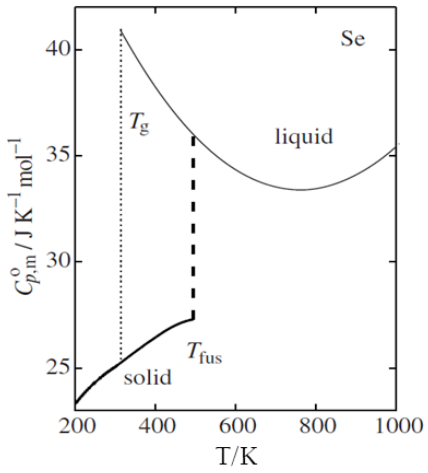

Figure 29: Heat capacity of Se as a function of temperature [61].

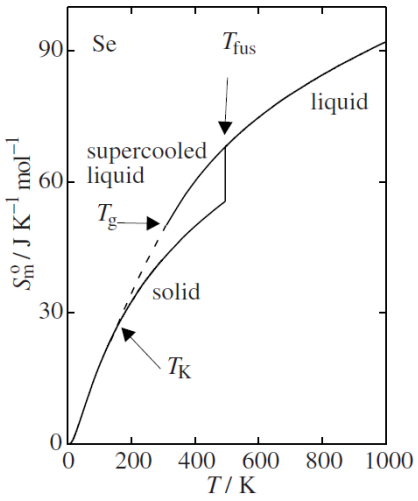

Figure 30: The entropy of a liquid as a function of temperature. The extrapolation of the entropy of the liquid will cause an entropy crisis, and an amorphous solid will form [61].

Amorphous, or non-crystalline, silica is also a stable structure of silica. The density of this phase ranges from 2000 to 2200 kg/m^3. Compared to the crystalline phase cristobalite and tridymite, which has a void space of 48.4 % and 51.7 % respectively, amorphous silica has a void space of 57 % [65]. It is therefore reasonable to believe that gas diffusion is faster in amorphous material compared to crystalline phases [62]. A possible SiO_4^- tetrahedral arrangement in amorphous silica can be seen in Figure 31 [66]. Both a random network hypothesis [67] and a microcrystalline theory of amorphous silica [68] exist. For the random network hypothesis, the SiO_4^- unit cells will have varying bond angels between the bonds. The unit cells still share one corner with each other as in crystalline phases. In the microcrystalline model, there are sub-unit-cell sized crystallites of one form of SiO_2. These two models can also converge, and both are observed by experimental data [69].

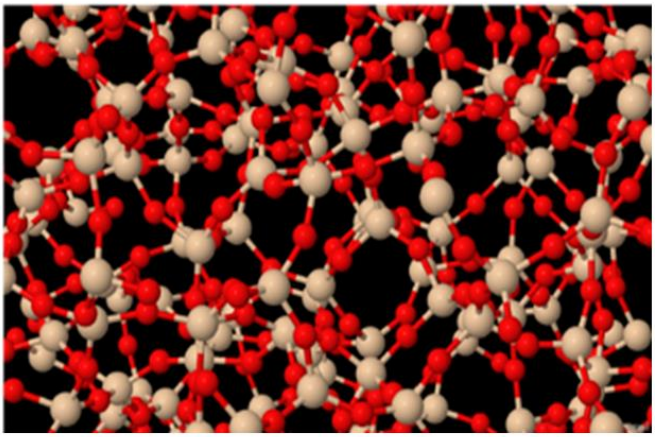

Figure 31: A possible amorphous arrangement of silica made by molecular dynamic simulations [66].

Balek et al. [70] claims that several researchers have found natural silica to have an outer layer of amorphous silica. This layer is not more than 30 nm. Grinding of silica will also contribute to an amorphous layer of up to 100 nm according to Balek et al.[70]. If a spherical particle with diameter 1 cm has an amorphous layer, this will make a negligible wt% of the total particle.

Phase transformations

The phase diagram represents the phase that are thermodynamically stable under certain conditions. In addition, there are other effects that will determine what phases are present. Energy barriers to the stable phase must be overcome. This is the case for reconstructive transformations, where energy is needed to break the bond between the atoms before a new phase can be created. The previous structure and change in surroundings could also influence the phase formed [59].

α-quartz to β-quartz

Up to 573 °C, α-quartz is the stable phase before it transforms to β-quartz. This transformation is displacive and happens rapidly. It is also reversible, so when cooled to room temperature the β-quartz will transform back to α-quartz. During this transformation there will exist an intermediate phase which is stable over a temperature interval of 1.3 °C. This phase consists of dauphine micro twins that are disproportional oriented [29].

β-quartz to β-cristobalite

At around 1400 °C, β-quartz will change to β-cristobalite. This transformation is a reconstructive type where bonds have to break and atoms have to diffuse to build the new phase [29]. A study by Marians and Hobbs [56] suggested that a third of the bonds have to break for this transformation to occur. They also found that the transformation goes through an amorphous transition phase. The following reaction equation is proposed by Stevens et al. [49] for the phase transformation from quartz to cristobalite:

approx. 1300 °C

Quartz → Transition phase → Cristobalite 2.3

Sosman [59] mentions a study that recognized the first cristobalite formed as a disordered cristobalite (called cristobalite D), but not fully amorphous. X-ray patterns indicated ordered structure in two dimensions, but not in the third. With time, the cristobalite D phase became more perfect crystalline, and did not go back to disordered cristobalite. Sosman suggests that cristobalite D could be a version of the amorphous transition phase that was observed around the same time by Chaklader and Roberts [55].

Initially the transformation from quartz to cristobalite will be slow due to a nucleation period. A more rapid nucleation will follow as the nucleated zones propagate [55]. The nucleation from amorphous phase to cristobalite has been found to reach its maximum at 1677 °C. Schneider et al. [71] also investigated the quartz to cristobalite transformation between 1100 and 1600 °C by firing 3 g samples to different temperatures in a tube furnace. They also found that the transformation proceeds through an amorphous intermediate state. New research has also investigated the phase transformation. Kjelstadli [57] measured the amount of quartz, cristobalite and amorphous phase in several silica samples heated to selected temperatures and with varying holding times at maximum temperature. Different sizes were also tested in her study, to see if there were any considerable effect of size on the phase transformation. At 1600 °C no size effect was found, but when the temperature was raised to 1700 °C, an effect was seen. Kjelstadli explains this with thermal diffusion being a limiting factor as the temperature is raised to 1700 °C. Results from the study also showed that the transformation from β-quartz to amorphous phase was rapid, while the limiting step was the last conversion from amorphous state to cristobalite. This can be seen in Figure 32, where quartz samples are heated to 1700 °C. The size effect is existing from 0 to 30 minutes.

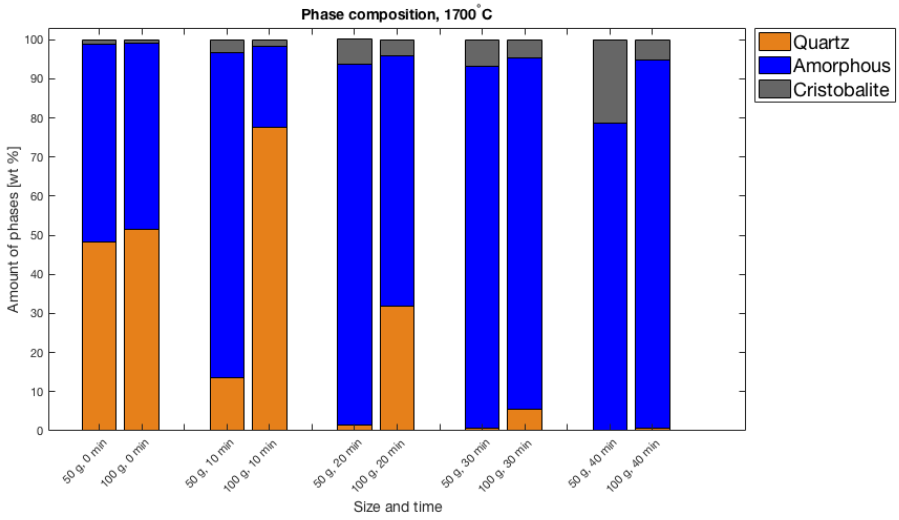

Figure 32: Amount of phases after heating an industrial quartz to 1700 °C, and held at this temperature for increased time. The figure is based on data from Kjelstadli [57].

Another study by Kjelstadli [72], investigated the amount of phases for different quartz types. She found that the ability to transform into amorphous state and cristobalite was highly dependent on the type of quartz. This can be seen for the amorphous amount in Figure 33 where the amount of amorphous content is measured for three different quartz types, at three different holding times and for two different sizes at 1600 °C. The largest variation is seen between the different types of quartz, no trend is seen in the sizes of the samples. For many of the samples the highest amount of amorphous content is found after 10 minutes, indicating that the phase is been created and then consumed as cristobalite is created.

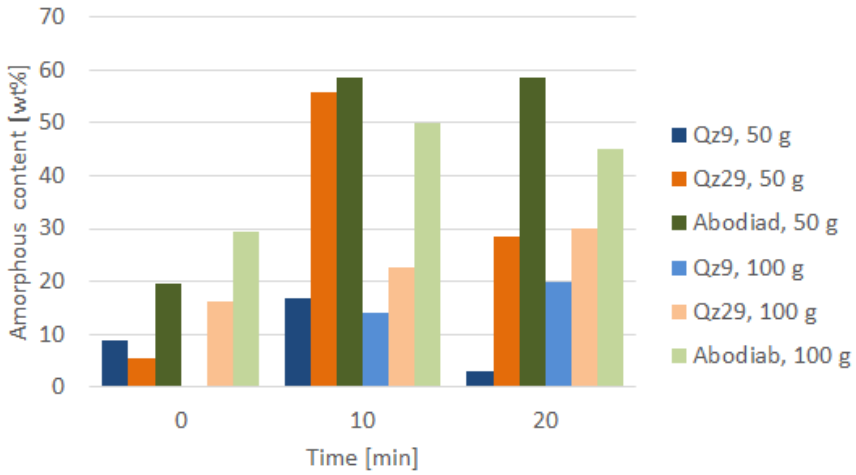

Figure 33: The amorphous content as a function of holding time at a temperature of 1600 °C for the three quartz types Qz9, Qz29 and Abodiab. The figure is based on results from Kjelstadli [72].

It is debated if the phase transformation from quartz to cristobalite starts at the surface of a quartz sample, or if it happens throughout the sample. Wiik [22] suggested that the phase transformation from quartz to cristobalite is homogeneous, and does not start at the surface. The phase transformation to cristobalite origins from nucleation sites evenly spread through the sample. Because quartz is of higher density than the transition phase between quartz and cristobalite, the transition phase will occupy a larger volume. This causes tension in the sample that will cause cracks in the parts still being quartz. The reconstructive transformation involving breaking of the Si-O bonds will result in an extensive fragmentation of the transition phase. It is mentioned by Wiik [22] that partially converted quartz samples, containing large portions of transition phase but no cristobalite, easily crumbled under pressure from the fingers. This supports the theory that the transition phase is fragmented, and therefore nucleation and growth of cristobalite would be available. The formation of cristobalite would then occur throughout the whole volume of the transition phase, not only at the outer surfaces as suggested by Ainslie et al. [73]. They reported that a glassy silica phase formed on the external surface of a quartz crystal. After heating several samples to 1570 °C and 1740 °C, they measured the thickness of any glassy silica layer on top of the quartz substrate. An example of their samples can be seen in Figure 34, where the glassy silica phase G covers the surface of the quartz substrate Q. This was the observation for all their samples, except the samples where cracks were present in the crystals. As the viscosity of the glass phase is still very high at 1740 °C, the shape of the heated sample is not considerably altered during heating, and a relationship between time and thickness could be constructed. The thickness as a function of time at 1570 °C and 1740 °C is presented in Figure 35. From the graph, it can be

seen that the thickness of the glassy layer increases with both time and temperature. The relationship is, within reasonable uncertainty limits, linear.

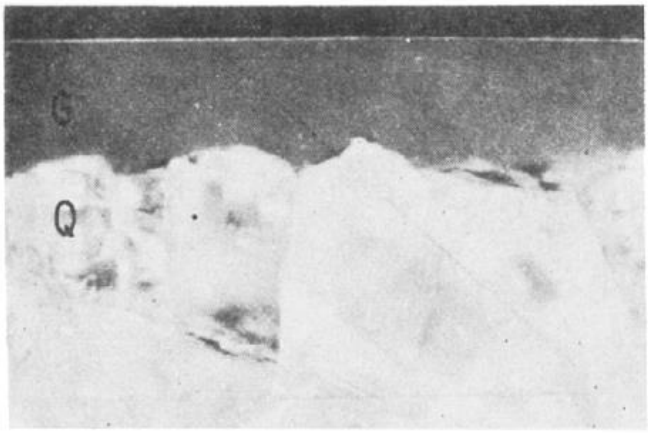

Figure 34: Section of quartz crystal heated to 1740 °C for 15 minutes in air. The formation of glass phase, G, is over the quartz substrate, Q [73].

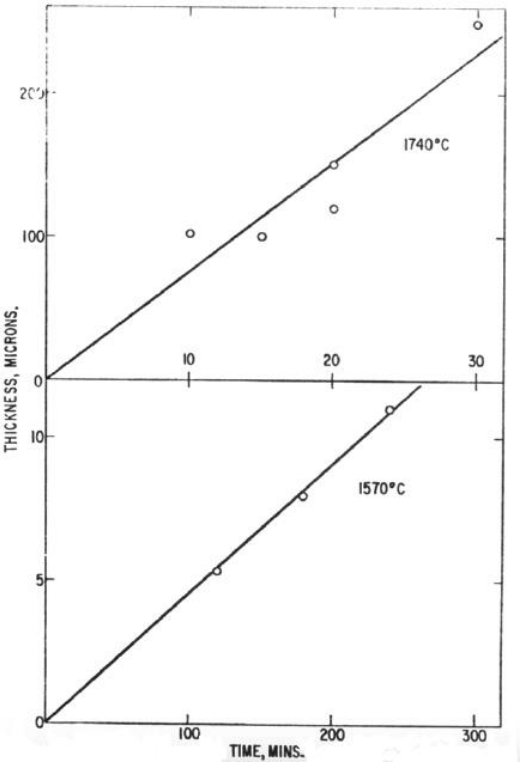

Figure 35: The thickness of glassy silica layer as a function of time for two temperatures, 1570 °C and 1740 °C.

According to Breneman et al. [74] the nucleation of cristobalite from amorphous silica starts at the surface. A cristobalite shell layer forms around an amorphous core. Cristobalite will nucleate

at internal free surfaces, and leave an amorphous core as seen in Figure 36 where backscattered electron images are seen of epoxy-impregnated specimens polished to 0.05 µm finish. These samples are heated to the temperature interval 1200 °C -1350 °C where the densification is minimal.

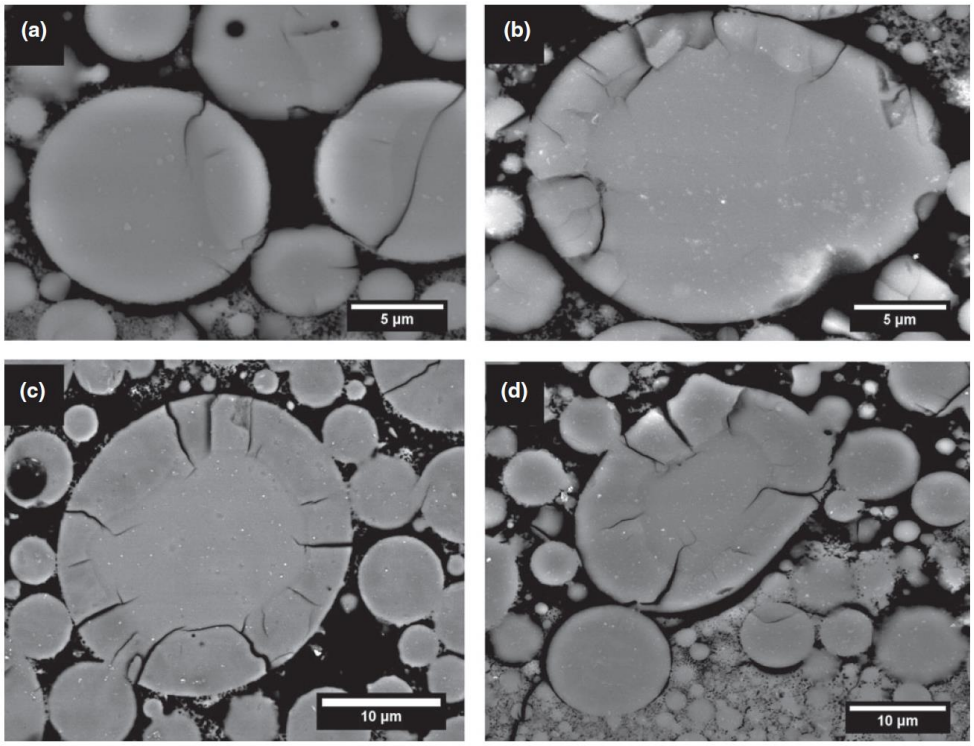

Figure 36: Backscattered electron imaging of silica samples with 11 %, 25 %, 55 % and 84 % cristobalite for a,b,c and d respectively.

Effect of particle size on µ-scale

Pagliari et al. [75] investigated the effect of particle size on the formation of cristobalite. Quartz powder was tested with XRD after heating to 1200 °C and 1300 °C. It was found that 4.135 µm powder converted more easily to cristobalite than powder with an average particle size of 15.78 µm and more. The difference is very clear from 4.135 to 15.78 µm, but from 15.78 to 28.38 µm the effect is smaller. It could therefore be proposed that the effect decreases as the particle size increases, and that the size effect is only significant for particle sizes under 15.78 µm. The effect of particle size seems to decrease as the average particle size increases. In the same study it was also found that if the powder was wet, it would enhance the formation of cristobalite at 1200 °C. Pagliari et al. [75] explained this with increased particle contact for wet powder compared to dry. In addition, the heat transmission between particles would be better.

The effect of particle size on the amount of phases formed during heating was also investigated by Dapiaggi et al. [76]. Quartz powder with a grain size of 4, 16 and 28 µm were heated to temperatures of 1000 °C and 1200 °C. No clear trend was seen between the amount of phases and the size of the particles. All samples were soaked in either KOH or NaOH prior to heating in order to see the effect of selected impurities and the amount of them. Na favored the formation of

high temperature silica phases compared to K at 1000 °C. Increasing the temperature to 1200 °C seemed to eliminate the difference. Due to the amount of impurities, tridymite was also formed in these experiments. The effects of particle size and mineralizers can be seen in Figure 37 and Figure 38 for 1000 °C and 1200 °C respectively.

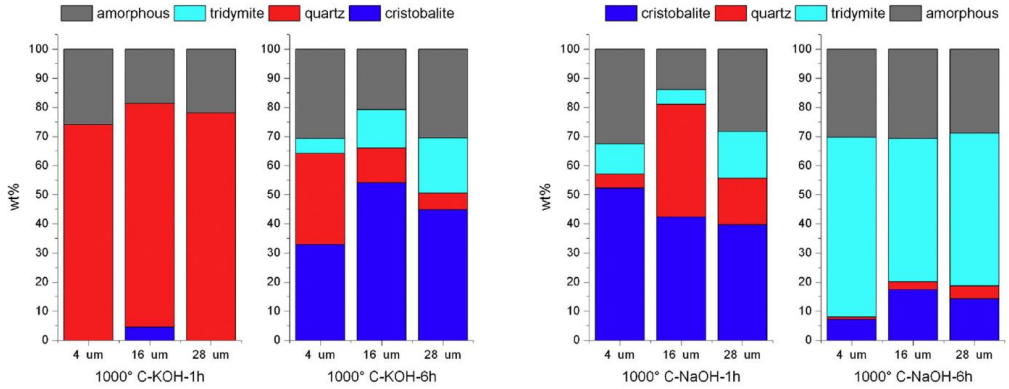

Figure 37: The effects of particle size on the formation of high temperature silica phases for two different mineralizers and two different soaking times for each mineral. All samples were heated to 1000 °C [76].

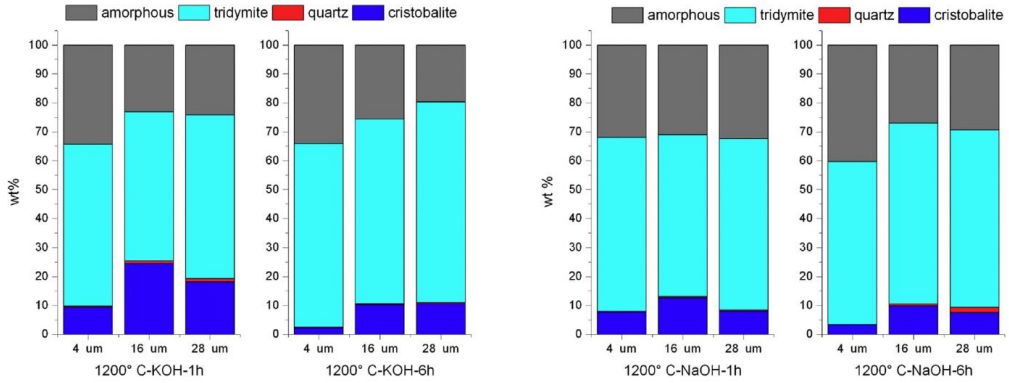

Figure 38: The effects of particle size on the formation of high temperature silica phases for two different mineralizers and two different soaking times for each mineral. All samples were heated to 1200 °C [76].

Effect of crystallinity on kinetics

Wahl et.al [77] investigated the phase transformations in silica by XRD and found that the higher the crystallinity of the starting material the higher was the conversion temperature to cristobalite. Six different silica samples with varying degree of crystallinity were heated to 1400°C with a heating rate of 5 °C/min inside an x-ray diffraction unit. The samples were rock crystal quartz, chalcedony, opal, silica gel 42 and silicic acid. The conclusions from Wahl et al.'s study [77] was that there was a correlation between the structural perfection of the α-quartz and the crystallite size of β-quartz. They suggested that larger crystallite sizes were capable to withstand a higher temperature before transformation to cristobalite, hence a more perfect α-quartz, would have the

slowest transformation to cristobalite. It was also reported that no tridymite formation was observed. The findings are listed in Table 6.

Table 6: Reported cristobalite formation temperature of different quartz types [77].

Silica source	**Crystallinity**	**Cristobalite formed at [°C]**	**Comments**
Rock crystal quartz (Hot Springs Arkansas)	Very good	1200	
Chert (Dover, England)	Medium	1050	
Chalcedony (Middle Park, Colorado)	Medium	950	
Opal (Guanajuato, Mexico)	Medium	1000	Only diffraction effects for cristobalite
Silica gel grade 42(Davison Chemical company)	Amorphous	900	No quartz observed
Silicic acid, 100 mesh (Mallinckrodt Chemical Works)	Amorphous	900	No quartz observed

The effect of impurities

It has been shown by several researchers that impurities in quartz also affect the kinetics of the phase transformation. As mentioned earlier Dapiaggi et al. [76] showed that increased amount of KOH and NaOH would speed up the transformation from quartz to other silica phases. Schneider et al. [58] also investigated the effect of alkali and alkali earth element impurities on the transformation speed. They found that the mentioned impurities would speed up the nucleation and the growth of cristobalite. In fact, the formation could be so fast that no amorphous phase would be detected if the sample was quenched. The proposed mechanism is explained as formation of liquids of low viscosity below the melting point of silica. Such liquids would easily spread throughout the sample and favor the dissolution of quartz. They would also increase the mobility of diffusion species. It is also possible that the impurities themselves break up Si-O bonds also in the solid state, making the structure more plastic and easier to rearrange to other phases.

Chaklader [50] investigated the effect of Al_2O_3. It was found that a content of Al_2O_3 up to 0.44 % would speed up the transformation, but addition beyond this amount would slow down the transformation again. The mechanism proposed was that the catalyst Al_2O_3 would first nucleate on the quartz grains, thereafter a diffusion layer produced by the penetrating catalyst would propagate. Brown et al. [78] also reported that Al_2O_3 would speed up the transformation from amorphous phase to cristobalite. They also argued that up to a certain limit Al^{3+} would increase the growth rate rapidly. This is shown in Figure 39.

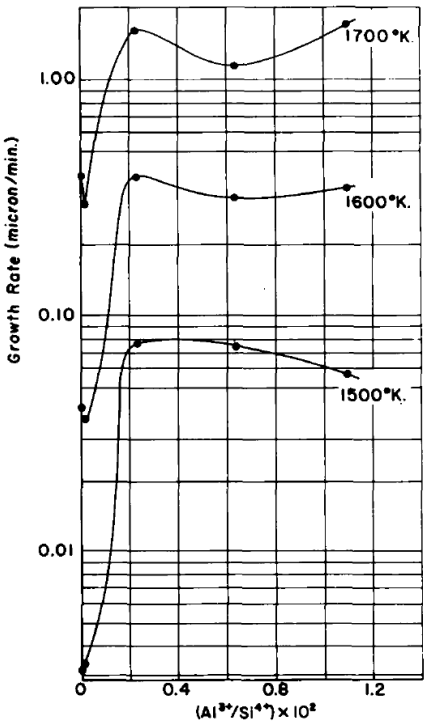

Figure 39: Growth rate of cristobalite layer from SiO_2 glass samples as a function of Al^{3+} content in the silica sample [78].

Table 7 summarizes the main results from some studies on phase transformations in silica and what affects them. Based on the information in the table, phase transformations could be affected by size, impurities and crystallinity. The size effect is not clear, and its significance is therefore believed to be small. Impurities and crystallinity seem to influence the formation of high temperature silica phases.

Table 7: Summary of studies regarding high temperature phase transformations of silica, and what affects them.

Study/paper	**Any size effect on formation of HT silica phases**	**Effects of impurities**	**Other effects on amount of phase or other phase related issues**
Pagliari et al. [75]	Very small, and decreasing with increasing particle size		
Wahl et al. [77]	No size effects		Higher crystallinity, higher transformation temperature to cristobalite

Dapiaggi et al. [76]	No clear effect	Longer soaking time, more high temperature phases. NaOH compared to KOH enhances the formation of high temperature phases at 1000 °C. The effect is not seen at 1200 °C	
Kjelstadli [57]	Effect at 1700 °C, no at 1600 °C		Different quartz types have the largest variation
Chaklader [50]		Al_2O_3 up to 0.44 % increase amorphous phase and cristobalite formation	
Schneider et al. [58]		Alkali and alkali earth elements would increase nucleation and growth of cristobalite	

Models of phase transformations

Breneman et al. [74] studied the kinetics of cristobalite formation from sintered silica glass from 1200 °C to 1650 °C. They found that from 1200 °C up to 1350 °C the formation from fused silica to cristobalite followed a Johnson-Mehl-Avrami-Kolmogorov (JMAK) model, and could be expressed by the following expression:

$$Y = 1 - \exp\left((4.7 \times 10^{-17}) e^{-\frac{555\frac{kJ}{mol}}{RT}} (t)^3\right) \quad 2.4$$

Where *Y* is the amount of cristobalite formed after time *t*. The calculations and modeled value for Y can be seen in Figure 40. At temperatures higher than 1350 °C the densification of the silica has to be taken into account, and complicates the picture. According to Breneman et al. [74] the formation of cristobalite is favored at surfaces. When the samples become more dense, the surface area decreases, and the crystallization rate at temperatures where densification is significant, might not be directly comparable to crystallization rates at lower temperatures. Other findings from the study showed that fully amorphous silica powder without cristobalite seed required the highest temperature to transform in a 1 hour annealing. Also, amorphous silica seeded with quartz increased the crystallization rate more than cristobalite seeds.

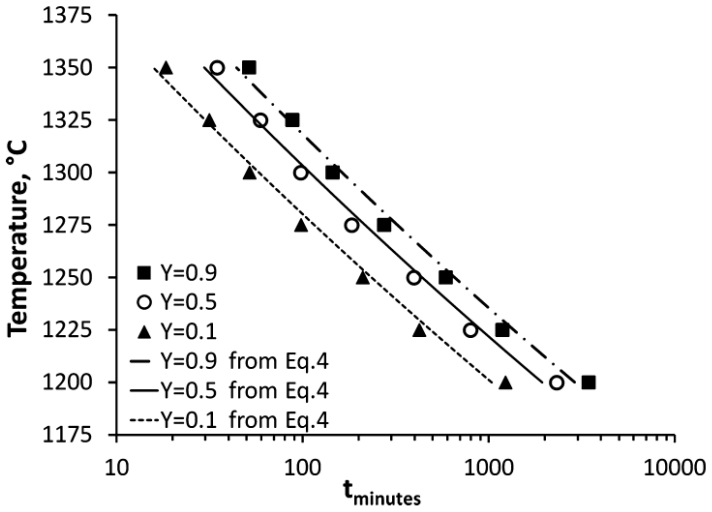

Figure 40: Low-temperature leg of the Time-Temperature-Transformation (TTT) plot for Y 10 %, Y 50 % and Y 90 %. Individual points are interpolated, and the lines are plotted from 2.4*. The figure is reprinted from Breneman et al. [74].*

In an earlier study by Mitra [79] a rate expression for the transformation from quartz to amorphous phase was suggested. It was based on firing 20-40 µm particles at 1400 °C for up to 5 days. By using DTA and the α-β-quartz inversion peaks, the amount of quartz and amorphous phase was determined by assuming the total amount to be 100 %, and estimating the amorphous content. The rate expression was as follows:

$$A_f = \left(1 - \frac{ut}{r_0}\right)^3 \qquad 2.5$$

A_f is the amount of remaining quartz after a time t, u is the linear rate of propagation of quartz-amorphous phase boundary and r_0 is the initial radius of the particle. Mitra had calculated u and r_0 earlier. He found the transformation from quartz to amorphous phase to be a phase boundary controlled process, and the transformation from amorphous phase to cristobalite to follow a first order concentration controlled process. The rate constant for the latter transformation was found to be 0.03122 h^{-1} and 0.02925 h^{-1} for two types of quartz, Jagdishpur quartz and rock crystal, respectively. Figure 41 shows the experimental values of Mitra's experiments and the estimated amount of transition phase and cristobalite based on his models.

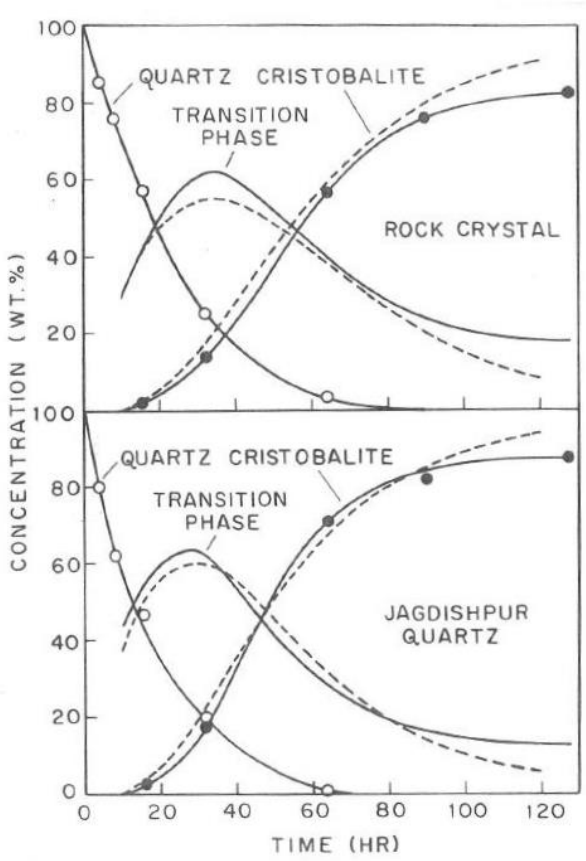

Figure 41: The amount of phases after firing 20-40 μm quartz particles at 1400 °C for up to 5 days. The solid lines with dots are experimental values, while the dotted lines are the modelled amount of phase. The figure is retrieved from Mitra [79].

Another researcher who assumed a first order reaction for the phase transformation from quartz to cristobalite was Chaklader [80]. He viewed the transformation as a twostep reaction with amorphous phase as an intermediate state, and thus had two rate constants k_1 and k_2 for the transformation from quartz to amorphous phase and from amorphous phase to cristobalite respectively. At 1560 °C these rate constants were 2.20×10^{-5} s^{-1} and 4.88×10^{-5} s^{-1} for k_1 and k_2 respectively. Mitra's k_2 value was 5-6 times lower. The values are not directly comparable since the temperature at which they were calculated for was different. Also, the quartz types were not the same, and it is likely to assume that different quartz types have different rate constants. But the values can give an indication of the temperature dependence of k. Chaklader's modelled amount of phases and his experimental values are shown in Figure 42.

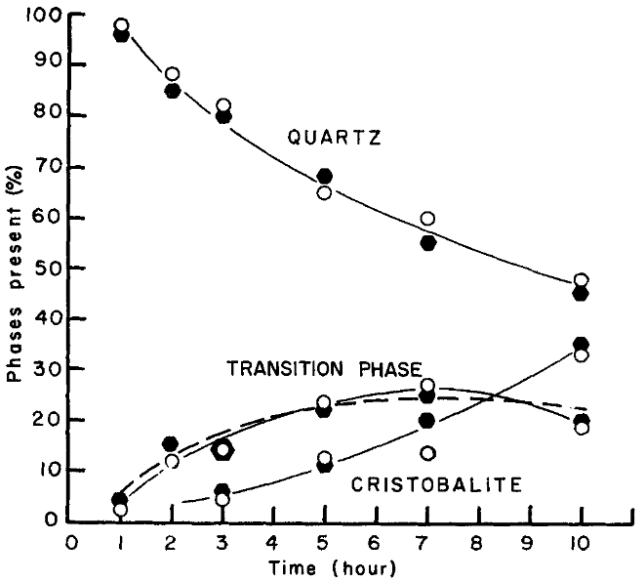

Figure 42: The amount of phases after heating a brazilian quartz type to 1560 °C. The dotted line is the modelled amount of amorphous transition phase [80].

Another study [78] on the kinetics of the phase transformations in silica suggested that the transformation from amorphous phase to cristobalite was following a zero-order rate law, i.e. the growth rate is linear and independent of concentration [81]. Brown et al. [78] found an expression for the growth rate, $\dot{g}$, in the temperature interval 1288-1457 °C, dependent on the temperature, T, and two constant A and B, related to the concentration of trace Al_2O_3. The expression can be seen in Equation 2.6.

$$\dot{g} = ATe^{\frac{-B}{T}} \qquad 2.6$$

2.4.2 Disintegration of Quartz

As the raw materials are fed to a silicon or ferrosilicon furnace, they will meet a charge top which is 700 °C -1300 °C [5]. Because of this steep temperature increase from room temperature, the quartz get shock heated and might disintegrate. Several studies [6], [52], [82], [83] have shown that different quartz types will disintegrate in various amounts. The reason for this is not clear. Ideal lump size for quartz used in a furnace is 10-150 mm [6], and if the amount of too much fine particles becomes too large it will have negative effects on the furnace performance.

Shock heating experiments have been performed as an attempt to measure the degree of disintegration for various quartz types. In Figure 43 the results from Ringdalen [52] and Paulsen and Bakken [82] are combined. They used the same experimental setup. A sample of approximately 200 g was inserted to a preheated carbon crucible at 1500 °C and held for ten minutes. The sample was taken out and sieved. Figure 43 shows the large variation amongst quartz types. If fines are defined as material below 10 mm, the amount of fines varies from 2-3 % to 85 %. Considering that the production plant often sieves away fines below e.g. 10 mm before adding the quartz the furnace, the furnace will still get a huge amount of fines if certain quartz types are used.

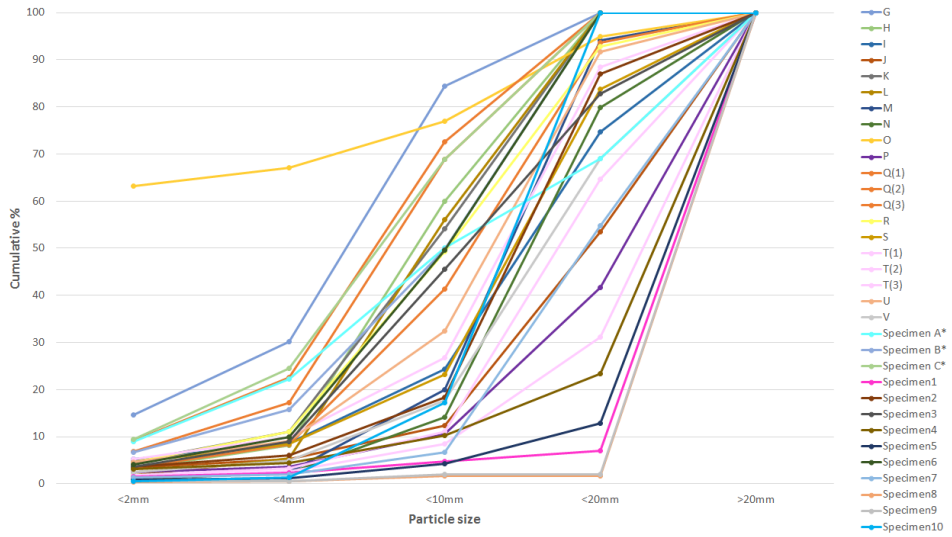

Figure 43: Cumulative percentage of different size fractions of quartz that have been shock heated to 1500 °C. The figure includes results from both Ringdalen [52] and Paulsen and Bakken [82].

Paulsen and Bakken also shock heated quartz samples at 1300 °C, and compared it to tests at 1500 °C. They observed that disintegration was greater at 1500 °C than at 1300 °C. There were some exceptions from this trend. Paulsen and Bakken suggested that different sample size for the 1300 °C and 1500 °C experiment could have affected the results. Figure 44 shows the graphic representation of the results. The dotted lines are the 1300 °C experiments, while the solid lines represent the 1500 °C experiments.

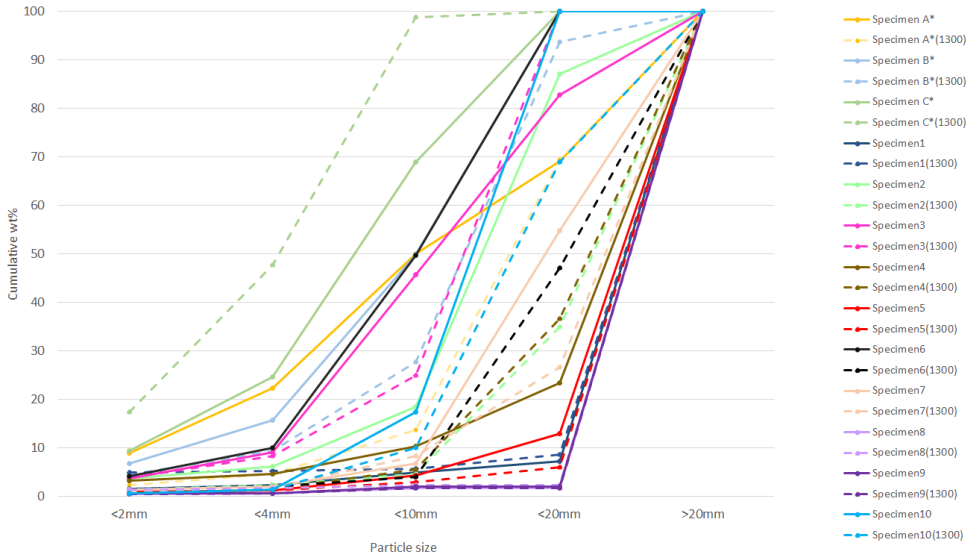

Figure 44: Cumulative percentage from shock heating quartz to 1300 °C and 1500 °C. The dotted lines represent 1300 °C, while the solid line represents experiments at 1500 °C. The graph is based on results by Paulsen and Bakken [82].

Shock heating has also been tested by Aasly [6]. He had a slightly different experimental setup than Ringdalen and Paulsen and Bakken. Aasly sliced his samples into cubes of approximately 40 mm x 40 mm x 40 mm. He also investigated unheated and heated samples of each quartz type in polarized light microscope, also with fluorescent light. It showed some significant differences in unheated and heated samples. Fluorescent epoxy were used to prepare samples. It will fill micro cracks, grain boundaries and cavities in the samples, which are visualized when fluorescent light hits the sample surface. An increase in the intensity of the light reflected by the epoxy in the grain boundaries was found in the heated samples, meaning that the grain boundaries were more open after heating. The intensity of the micro cracks also increased in most samples. For sample Aa.F, the intensity from the micro cracks suppressed the intensity from the grain boundaries. This can be seen in Figure 45.

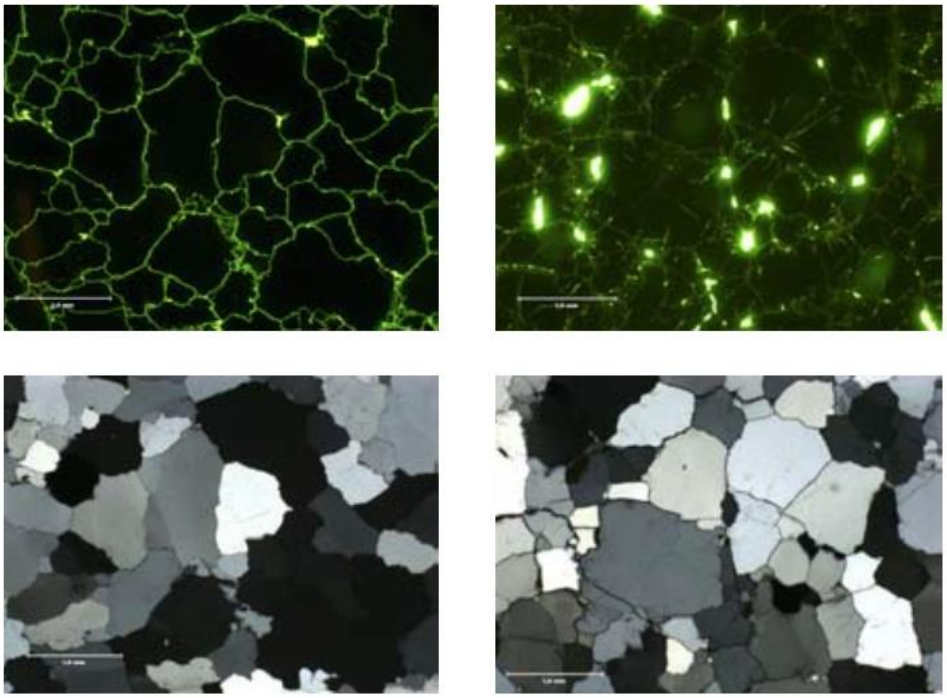

Figure 45: Images of quartz type Aa.F from fluorescent light microscopy and optical light microscope. The images to the left show unheated samples, while the images to the right are taken of material shock heated to 1300 °C [6].

In Table 8 the results from Aasly's [6] shock heating experiments and other observations are summarized. The amount of fines produced during shock heating varied. Further investigation by microscopic methods showed that during heating the grain boundaries opened, and micro cracks developed. They were grouped either in network of connected micro cracks or as short disconnected cracks in a dense pattern. Micro cracks also seemed to develop in the fluid inclusion planes, and this suggests that the micro cracks are a results of fluid inclusions escaping and causing tension in the material around it. This is not in agreement with Birkeland et al., sited by Aasly [6], which suggested that fluid inclusion planes were insignificant for the disintegration of quartz samples. Another factor that Malvik et al. [84], [85] claimed as important for the thermal strength of quartz was the grain size. They argued that there would be larger expansion in one direction, than the others when quartzite were heated. This difference would cause stresses on the grain boundaries, and the strength were therefore directly proportional to the grain size.

Table 8: Results and observations from Aasly from shock heating experiments and other test done prior to heating and after heating [6].

Quartz type	Type	Rel. grain size	Other minerals	Pos. of trace minerals	Wt% fines below 1.651 mm
Aa.A	Hydrothermal	Very coarse	None	-	1.41
Aa.B	Hydrothermal	Very coarse	Chlorite/mica	Grain boundaries	1.00
Aa.C	Hydrothermal	Very coarse	(mica)	Scattered	1.05
Aa.D	Pegmatite	Fine-coarse	(mica)	Scattered	0.71
Aa.E	Quartzite	Medium coarse	Zircon, monazite, mica, (tourmaline?)	Scattered	1.10
Aa.F	Hydrothermal	Medium coarse	Mica (or tourmaline)	Grain boundaries	1.14

On the microscopic scale, Griggs and Balcic [86] investigated the strength of synthetic and natural quartz as a function of strain rate and temperature. They found that quartz retains its hardness and strength at least to 800 °C-1000 °C. The strength becomes considerably lower at 800 °C and above if water is present. The suggested mechanism for the weakening is diffusion of water throughout the crystal hydrolyzing the Si-O bonds. This causes weaker hydrogen bonding between some of the atoms in the crystal, thus a weaker structure.

2.4.3 Softening and melting

Softening

Softening is described by Ringdalen et al. [87] as when the shape of a quartz sample starts to lose its sharp edges. The border between softened and melted quartz is diffuse. Jusnes [88] presented some examples of both conditions in her master thesis. The examples can be seen in Figure 46, and the criteria used to determine the difference were as follows:

- Melted particles have more round shape than softened.
- Melted particles have adjusted themselves to the surroundings, softened have not.
- Melted particles may have melted together, forming larger particles. If there still exists a boundary between the particles, they are softened.

Figure 46: Examples clarifying the difference between softened (left) and melted (right) silica. The silica pieces are surrounded by solid SiC particles and epoxy. The images are retrieved from Jusnes [88].

Several researchers have tried to explain the softening mechanism, since the phenomena is not thoroughly understood. According to Dash et al. [89], the disorder and mobility of atoms at the surface of a bulk sample will increase as the temperature approaches the melting temperature, and hence a material can start to melt at the surface before bulk-melting starts. At the start, the disorder region will be very thin and possess the solid bulk properties. As the region becomes thicker, the outer surface will change its properties to liquid properties more and more. It is suggested that the systems free energy could be lowered as a consequence of the wetting of an initially dry surface on a bulk solid below its melting temperature. There will be an energy cost of converting a small amount of material from solid to liquid, but this is not prohibitive. This energy cost of this conversion also determines the theoretical thickness of the pre melted layer.

Another explanation of the softening or wetting of the surface is that silica becomes more and more fluid-like at temperatures above 1677 ℃ [62], i.e. more amorphous. Kuhlmann-Wilsdorf [90] suggested that amorphous substances are understood as liquids of high viscosity. This is explained by high frictional stress on the dislocation cores in the structure. When the free energy of a dislocation core becomes negative, it will enter the molten phase. Several of these dislocation cores with negative or zero free energy will build up the liquid phase of a structure. Thermal motion reduces the frictional stress on dislocations core for a solid, as well as helps to overcome it. This can explain gradually softening of amorphous substances on heating.

Different methods have been used to test how much different materials soften. An earlier test method for investigating softening temperatures of refractory materials was the Seger cone test. Materials with unknown softening temperature was compared with other materials with known softening temperature. The cones were geometrical identical with a triangular base and a height of about 4 cm. The cones were heated together, and afterwards it was possible to measure the amount of bending in the cone from the material with unknown softening temperature compared to the known materials [91]. In Figure 47, Seger cones heated to 1400 ℃ are shown. Normally, the material that is being tested is in the middle between cones with assumed higher and lower softening temperature. For the test to be precise, the experiments setup must be as identical as possible. With this method, it is also possible to teste the same material, but with slightly different compositions, to see how certain impurities might affect the softening of the material.

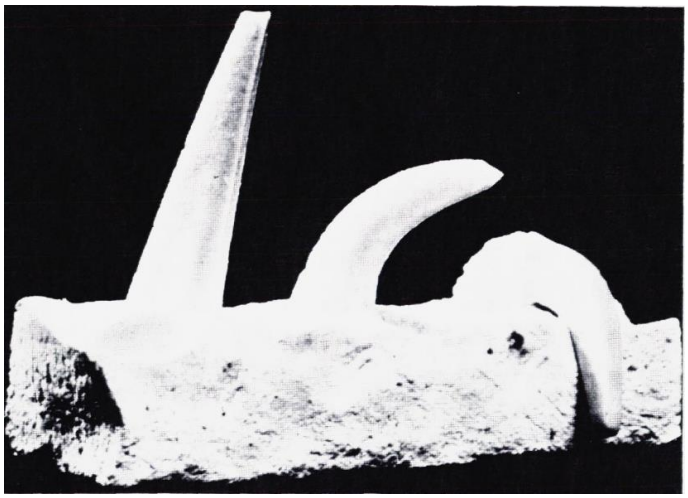

Figure 47:Seger cones that have been heated to 1400 ℃ to investigate the softening properties of a material [91].

Recent studies on softening are performed by Jusnes [88], Nordnes [17], [92] Ringdalen and Tangstad [93], Ringdalen [94], Bao et al. [95] and Andersen [96]. One of the key challenges was to determine the softening and melting temperature of different quartz types, if the heating rate of the experiments was affecting the determination of the softening and melting temperature, and how the volume changed as the quartz samples were heated. Results from Andersen [96], Ringdalen [94] and Ringdalen and Tangstad [93] can be seen in Figure 48, where it can be seen that the quartz heated with a slower heating rate, 5.5 °C/min , has a lower softening point than the ones heated with the highest heating rate, 20 °C/min. It also shows that there are variations in the softening temperature between different quartz sources.

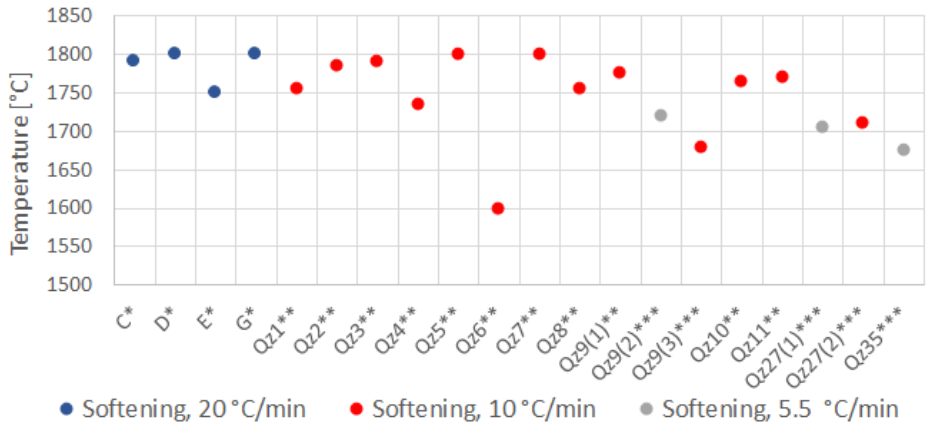

Figure 48: Softening temperatures of different quartz types, heated with different rates. The figure is based on data from Andersen[96], Ringdalen [94]** and Ringdalen and Tangstad [93]***. Parallel of the same type are marked with a number in parenthesis.*

The majority of the experiments performed by Ringdalen [94], Nordnes [17], Andersen [96], Ringdalen and Tangstad [93] and Bao et al. [95] was performed in a sessile drop furnace,

illustrated in Figure 49. Quartz samples drilled out from a larger lump were placed on a carbon substrate and placed inside the furnace chamber surrounded by graphite heating elements. Both a pyrometer and a thermocouple were used to check the temperature as the heating started. The heating rate and atmosphere in the heating chamber could be altered. A video camera was mounted in front of a window in the heating chamber, and allowed for digital recording of the melting process. Based on qualitative observations in the images recorded, the softening and melting temperature could be determined. The number is rounded to the nearest 10 °C to adjust for inaccurate observations. Images of a quartz sample at softening temperature and complete melting are seen in Figure 50. These are retrieved from Nordnes [17], and is one of four quartz types she investigated. She found that the heating rate affected the softening and melting temperature. This was in agreement with earlier suggestion by Ringdalen et al. [93], that softening and melting temperature would increase with increasing heating rate. Nordnes explained this by the high viscosity of silica at its melting point. Due to this, the sample could behave nearly as a solid at the melting temperature and a change in the shape would be difficult to observe. When samples were held at a lower temperature than the first observed softening and melting temperature, the samples would soft and melt eventually, at a lower temperature. This is illustrated in Figure 51 where multiple experiments of each quartz type with different holding temperature are shown.

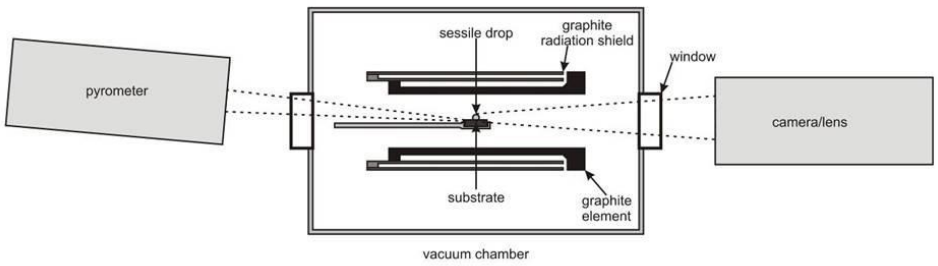

Figure 49: Schematic overview of sessile drop furnace used to investigate softening and melting behavior of quartz. The image is retrieved from Bao et al. [95].

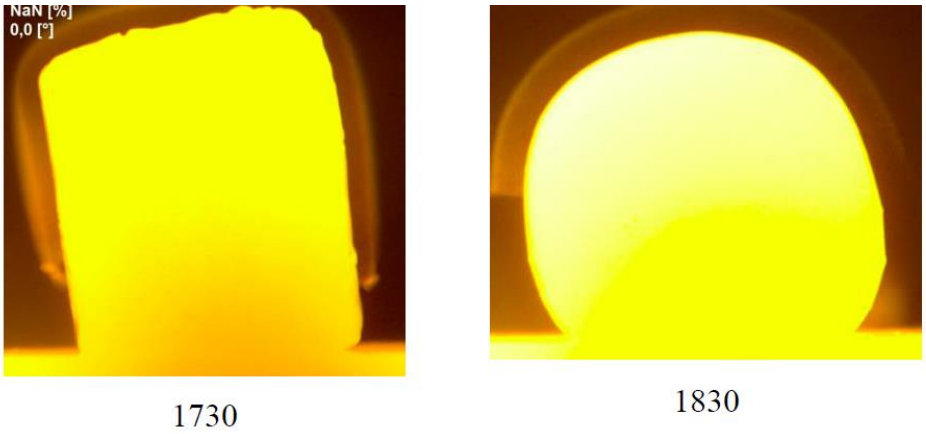

Figure 50: Images of quartz samples in the sessile drop furnace at softening temperature (left) and complete melting (right). The images are retrieved from Nordnes and the temperature is given in °C [17].

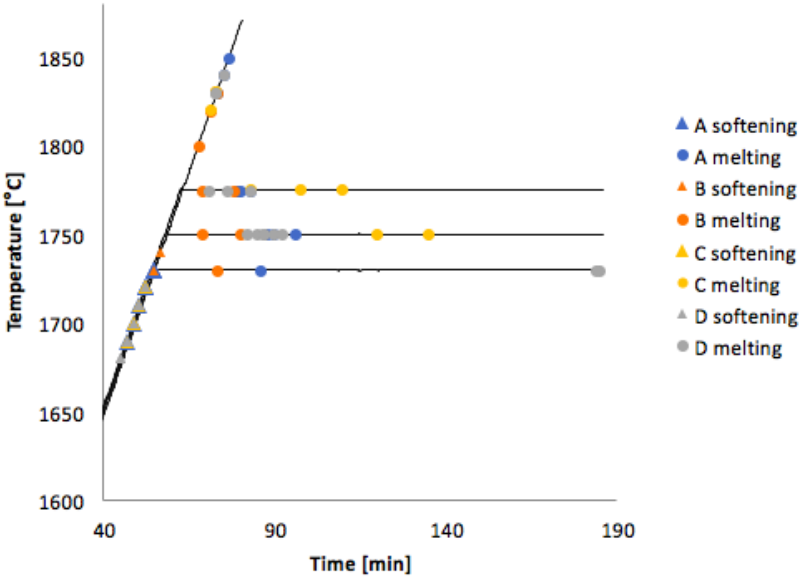

Figure 51: Apparent softening and melting temperature for four different quartz types qualitatively determined. The figure shows that increased heating rate will increase the observed softening and melting temperature [17].

Nordnes [17] also investigated the effect of impurities on the melting rate. Calculations of melting rate showed a relatively linear increase as a function of the impurity concentration. Earlier, Ringdalen et al. [93] have investigated the effect of FeO impurities on the softening temperature. They found the same trend that the softening point will decrease as the content of FeO increases, as seen in Figure 52. Andersen [96] suggested that alkali impurities also would lower the softening point. Jusnes [88] studied the softening and melting temperature of two quartz types with different impurity level. She found that increasing amount of impurity would have a

decreasing effect on the softening and melting point of the quartz types tested. Earlier it has also been suggested that the softening phase could be related to the intermediate amorphous phase in the phase transformation from quartz to cristobalite. Nordnes investigated the amount of phases for the same quartz types she determined the softening and melting temperatures for. No correlation was found between the amount of amorphous material and the holding time before complete melting at 1750 °C. This can be seen in Figure 53.

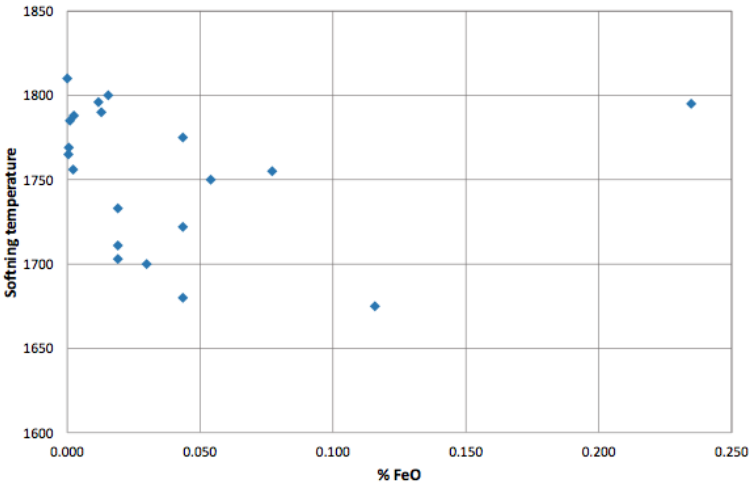

Figure 52: The effect of FeO impurities on the softening temperature of different quartz samples [93].

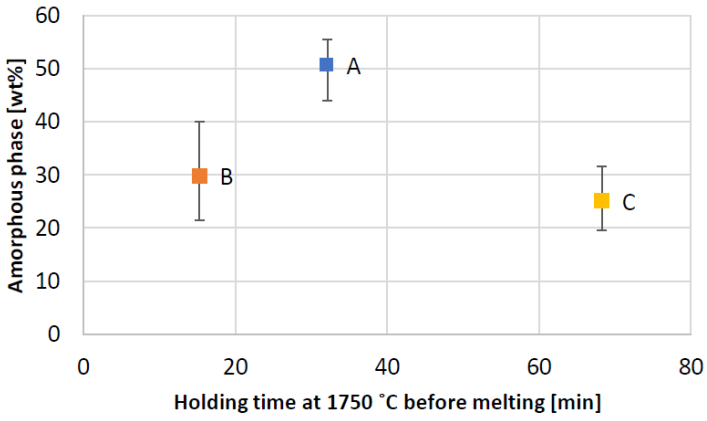

Figure 53: The amount of amorphous phase in heat treated quartz as a function of the holding time at 1750 °C before complete melting [17].

Melting

For a substance to melt the chemical potential, μ, must be the same for the liquid and the solid phase as described in Equation 2.7 [61].

$$\mu^s = \mu^l \qquad 2.7$$

The macroscopic and thermodynamical aspects of melting are well established, but the mechanism at microscopic level is not fully understood. Several researchers have tried to explain the mechanism, including Lindemann (as mentioned by Ainslie et al. [73]), Kuhlmann-Wilsdorf [90], Cotterill [97], and Thompson et al. [98]. A more recent study by Samanta et al. [99] claims that the earlier theories contain too many simplifications. Melting is a complex process that contain multiple and competing pathways involving formation and migrations of dislocations and other defects. The pathways are results of different barrier crossing events arising from several metastable states. Because atoms at the surface are more fluid-like, it is more likely that a liquid nucleus will form here rather than inside a solid. The liquid nucleus will expand until the solid phase becomes smaller and smaller. This is confirmed by Ainslie et al. [73] which claims that all observations so far (up to 1961) indicate that melting is a heterogeneous process and will start at surfaces. A liquid film will form, often at slight superheating, and propagate inwards. Melting kinetics will be affected by the viscosity of the solid. A melt of high viscosity, like silica, the heat absorbance will be slower and the solid can withstand high superheating. Mackenzie [100] showed that quartz can sustain superheating of 300 °C for a considerable amount of time. For silica, which is so viscous, it is observed, at 1730 °C, that the shape is not considerably altered despite being 20 °C above the melting point [73].

If the quartz contains impurities, they can alter the melting temperature. The effect depend on the impurity, and a mix of several impurities can have a complex impact [61]. It is argued that in a dilute crystal of an alloy, the energy will be less than in a pure crystal. This is explained by the bonding between dislocation cores and substitutional and interstitial atoms, which will decrease the system energy and thus lower the melting temperature [90]. Others have also argued that impurities will catalyze the movement of the crystal-liquid interface, when the crystal is covalently bonded [101]. In addition the melting behavior of SiO_2 can be influenced by the type and amount of fluid inclusions [28].

The melting of quartz has lately been investigated by Nordnes [17]. She found melting temperatures varying between 1730 °C and 1840 °C for the same quartz type. The samples were in mg order, and parameters such as the holding time at different temperatures was varied. The conclusion of her work showed that when quartz was held at a temperature sufficient for melting, the sample did melt in the end. It could take up to two hours. When a constant heating rate was used until the sample was melted, the recorded melting temperature was higher. This indicated that the quartz samples were superheated before melting, and the melting rate increased with increasing temperature above the theoretical melting temperature.

Viscosity

Silica is highly viscous with a viscosity of 2×10^7 Poise around its melting point [102]. The viscosity can influence a number of properties in a silica such as melting conditions, temperature of working and annealing, rate of removal of bubbles, the maximum temperature of use and the crystallization rate [103]. Urbain et al. [102] showed that the viscosity of pure amorphous silica from 1200 °C to 2400 °C followed an Arrhenius - type relationship, and found the activation energy to be 515.4 kJ/mol. Viscosity is thus highly dependent on temperature, which can be seen in Figure 54 [104]. When other oxides are added to pure silica melt, the viscosity decreases. Water is also known to increase the flow in crystalline silica [105]. It is suggested that the reason

for this is water diffusing throughout the crystal and hydrolyzing the Si-O bonds. Hydrogen bonding will then replace some of the Si-O bonds and the crystal will appear weaker [86].

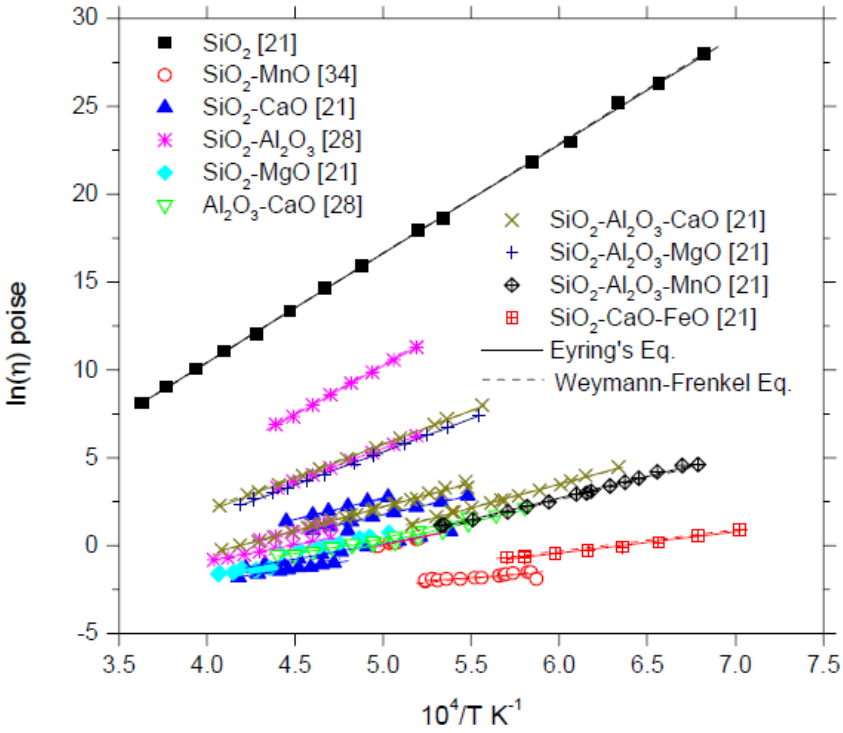

Figure 54: Temperature dependence of different silica melts. The figure is reprinted from Tang et al. [104].

2.4.4 Temperature models of quartz

A piece of quartz in the silicon or ferrosilicon furnace will instantly not have a homogeneous temperature throughout the sample. The temperature difference will be at its largest when the quartz is meeting the charge top which is 700 °C-1300 °C [5]. Nordnes [17] modelled the heat distribution in different sized quartz samples. She found that for a sample with a diameter of 40 mm and varying height from 10 to 100 mm that the temperature difference from surface to center varied from 0.05 °C to 30 °C after 1 hour at 1765 °C. Her results can be seen in Figure 55, and they give an idea of how fast a sample of quartz is heated both in experiments and in a real furnace.

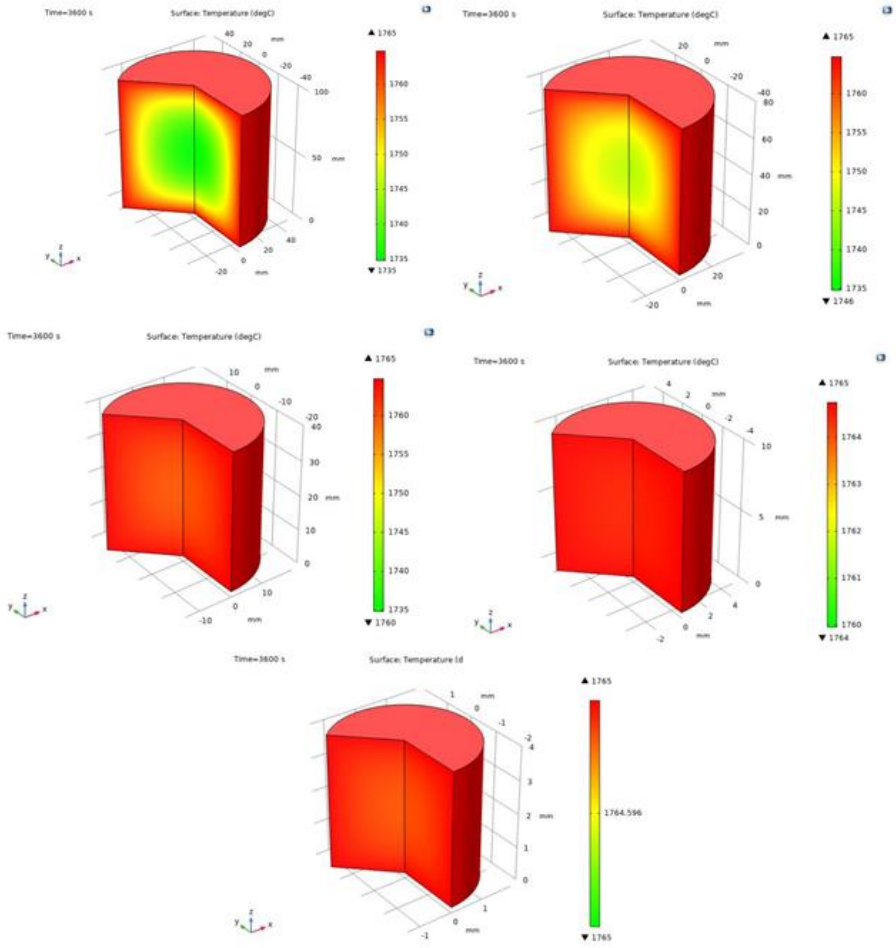

Figure 55: Temperature distribution in different quartz cylinders with diameter and height of 100, 80, 40, 10 and 4 mm [17].

Ksiazek et al. [106] modelled the temperature distribution in two different quartz particles as a function of radius. In a particle with radius 4 cm the external temperature was 1000 °C, while the temperature in the middle of the particle was 980 °C - 990 °C after 8 minutes. This is illustrated in Figure 56 together with the temperature distribution for different ferromanganese ores.

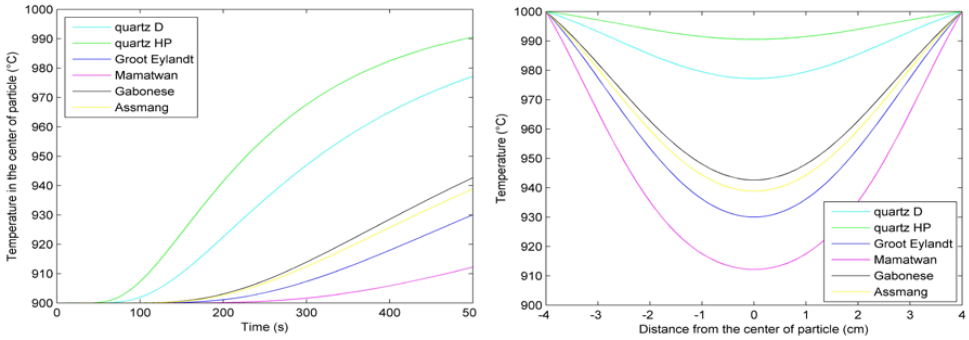

Figure 56: Temperature distribution as a function of time, and distance from the center for different ferromanganese ores and quartz [106].

Kjelstadli [57] with assistance from Ksiazek modelled the temperature distribution for various quartz sizes when heated from room temperature up to 1700 °C in a furnace. In this model it is assumed that the thermal diffusivity coefficient of quartz is constant above 573 °C. It must also be accounted for the 30 minutes it took to heat up the furnace to 1700 °C. In Figure 57, the temperature in the center of quartz samples with different size can be seen. The dotted line is the furnace temperature. As the furnace was heated together with the quartz samples it is difficult to draw a conclusion regarding the temperature diffusivity when the heating rate is less than in this model. For similar heating rates, it can be seen that the size of the particle only gives small variations in the center temperature of a quartz particle for spherical pieces from 2 to 5 cm in diameter. When the samples increase in size, the time before the center is the same temperature as the surroundings will also increases. More specific, it takes about 3 minutes longer for a 5 cm sample to reach 1700 °C in the center of a particle compared to a 2 cm particle. This holds when the heating rate is around 1°C/s.

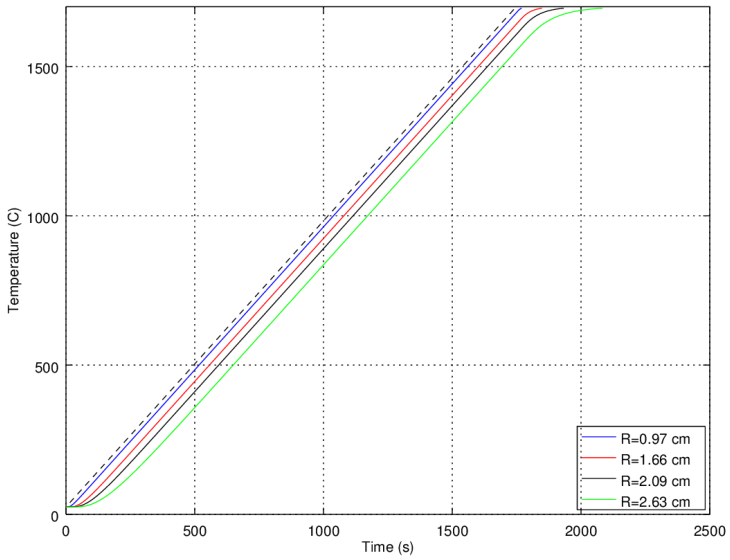

Figure 57: Temperature in the center of quartz samples with different size. It took 30 minutes for the furnace to reach 1700 °C [57].

3 Characterization of quartz types

In this chapter a thorough characterization of the four main quartz types used in this study are presented. The most important geological parameters of each quartz type are identified, and images from microscopic investigations are given. The information is gathered from different sources, both internal information from Elkem, earlier reports and theses. A major part of the characterizations is done as a part of the High Temperature Quartz project by Trond Brenden-Veisal and Anja Filipowicz. This work is found in an internal Elkem report [107].

Four different types of quartz were selected by the project group for thorough investigation. 200 kg of material were sent from different mines around the world to Trondheim. The treatment or selection of quartz before arrival in Trondheim is not known. All four quartz types were split into bathes of approximately 15 kg each upon arrival. This was done to ensure a random selection when taking samples for further analysis. For additional experiments, other quartz types were also used to obtain a broader basis for comparison. A chemical analysis was done on all the quartz types in this study. The analysis was performed by Erimsa, and the result can be seen in Table 9 for the main quartz types A, D, F and G. The quartz names are anonymized, and are therefore labelled with random letters. The method used for chemical analysis is inductively coupled plasma – optical emission spectrometry (ICP-OES).

Table 9: Chemical analysis of the quartz types investigated. The analysis is performed by Erimsa, and given in wt% if not else is stated.

Quartz type	Al [wt%]	Fe [wt%]	Ti [ppm]	Ca [wt%]	Na [wt%]	K [wt%]	Mg [wt%]	Mn [ppm]	P [ppm]	SiO_2 [wt%]
A	0.0106	0.0020	4.2	0.0003	0.001	0.0023	0.0009	0.3	<2.6	99.982
D	0.2603	0.2443	145.8	0.0033	0.0028	0.0626	0.0042	<0.1	25.6	99.405
F	0.009	0.0020	4.1	0.0010	0.0050	0.0040	0.0010	1.184	<2.6	99.977
G	0.0078	0.0024	3.8	0.0031	0.002	0.0013	0.0007	0.3	<2.6	99.982

3.1 Quartz type A

Quartz type A is a gravel quartz originating from a hydrothermal metamorphic vein. In Figure 58, a batch and a single sample of quartz type A can be seen. Type A has two domains where the texture is considerably different. Domain 1 has medium to coarse grained quartz in the mm and µm scale. In the second domain, the grains are 10-200µm thick and a few mm long. Grains found in this domain are stretched and deformed [107]. Layers of recrystallized material is found in between these grains, like seen in Figure 59 [107]. A recrystallized zone is seen from the upper right to the lower left corner. Another recrystallized area is observed in the upper left corner in Figure 59b. Contaminants such as muscovite ($KAl_2(Si_3AlO_{10})(OH)_2$) and iron hydroxide are also observed by microscopic investigations. These are mainly found along grain boundaries of recrystallized grains and grains between coarse-grained and fine-grained quartz. The contaminants vary in size, but the ones observed are smaller than 25 µm and up to 175 µm [107]. Figure 60 shows four images from microscopic investigations done by Brenden-Veisal and Filipowicz [107]. Here, the inclusions can clearly be seen. Fluid inclusion occur along healed cracks crossing several grains in a network and at the grain boundaries of recrystallized grains [107]. This can be seen in Figure 61 [107]. In general, the amount of fluid inclusions and cracks are low in quartz type A [107]. From one selected lump of quartz type A, a thin section suitable for microscopic investigations was taken. Another part of the same lump was shock heated. From

the shock heated material another thin section was prepared for microscopic investigation. In that way it was possible to compare the images from microscopic investigation of material original close to each other. The microscopic investigation of the thin sections can be seen in Figure 62 [107]. No major differences can be observed from the thin section before and after heating. The fracturing seems to have occurred at random positions in the material.

Figure 58: A batch and a separate sample of quartz type A.

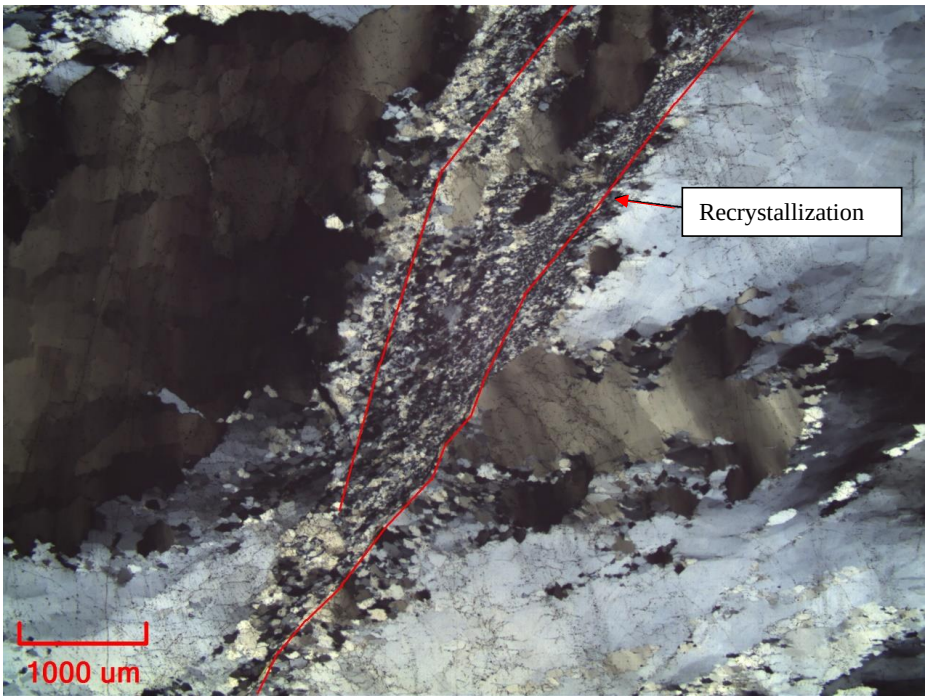

a) *Area of recrystallized quartz in between coarser quartz grains.*

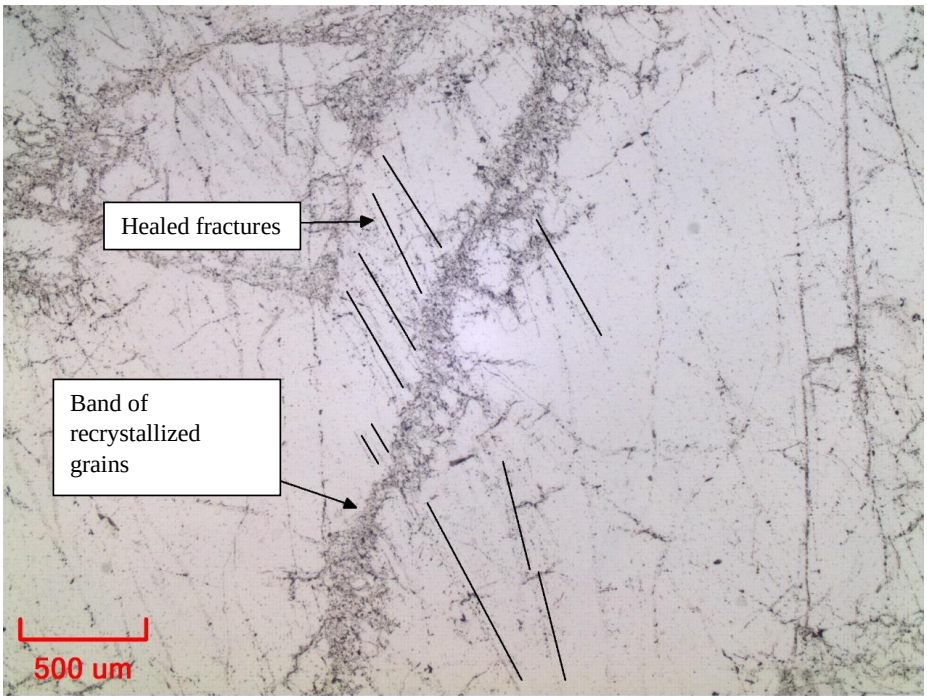

b) Band of recrystallized quartz grains and healed fractures inside coarser quartz grains.

Figure 59: Images from microscopic investigation of quartz type A showing the different domains observed, and also healed fractures. The images are obtained from Brenden-Veisal and Filipowicz [107].

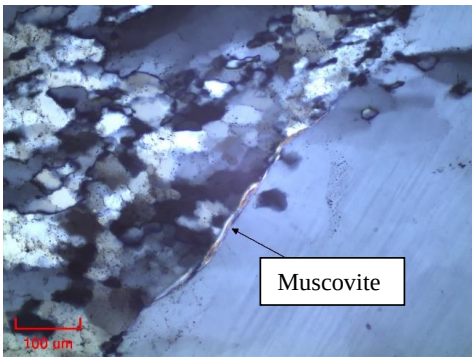

a) Muscovite contaminant on quartz grain boundary.

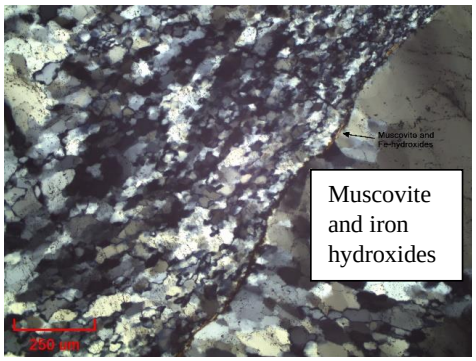

b) Muscovite and iron hydroxides on quartz grain boundary.

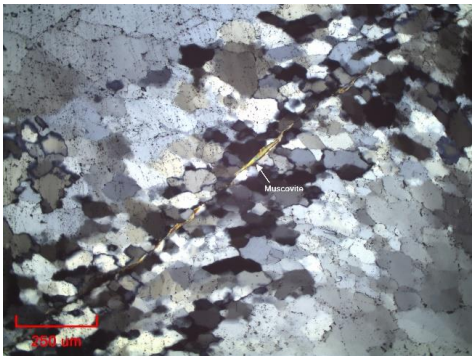

c) Muscovite contaminant along quartz grain boundary in recrystallized quartz domain.

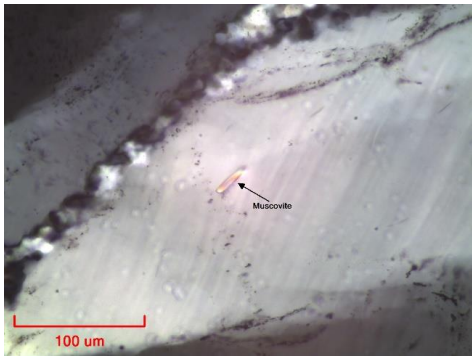

d) Muscovite contaminant embedded in elongated quartz crystal.

Figure 60: Images from optical microscope of quartz type A showing different contaminants. The images are obtained from Brenden-Veisal and Filipowicz [107].

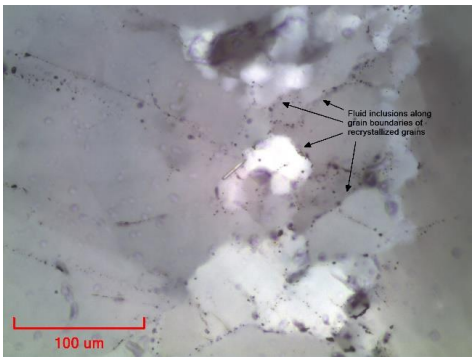

a) *Fluid inclusions along grain boundary of recrystallized quartz grains*

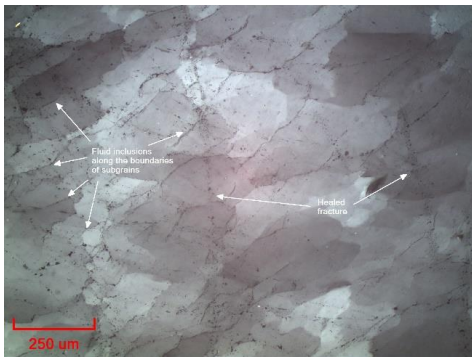

b) *Fluid inclusions along the boundaries of sub grains.*

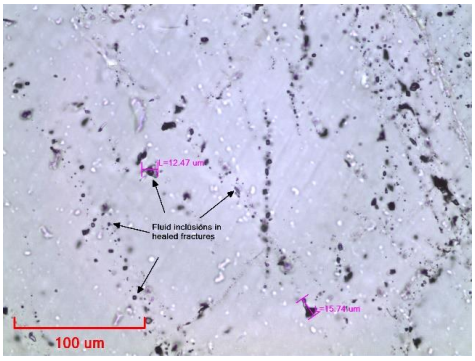

c) *Fluid inclusions in healed fractures. The inclusions are up to 15.7 μm.*

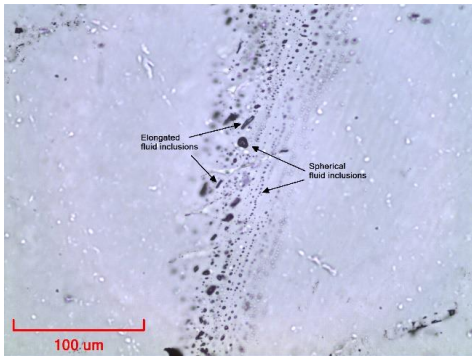

d) *Elongated and spherical fluid inclusions*

Figure 61: Fluid inclusions found by microscopic investigations of quartz type A. They are found both at grain boundaries and sub grain boundaries and at healed fractures. The shape can be both elongated and spherical. The images are obtained from Brenden-Veisal and Filipowicz [107].

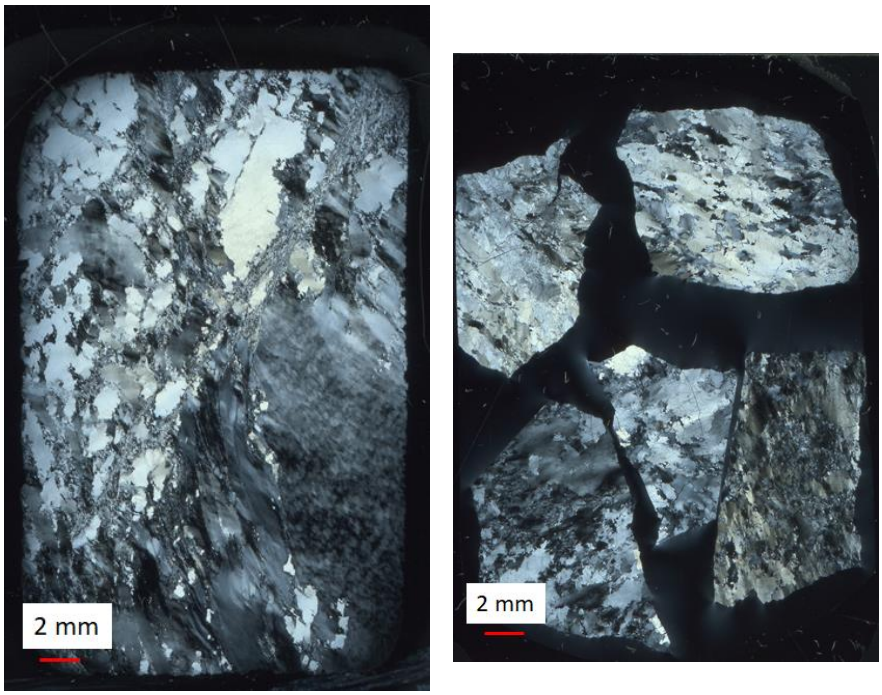

a) Thin section of unheated quartz type A b) Thin section of shock heated quartz type A.

Figure 62: Microscopic images of thin sections of quartz type A, before and after shock heating. The images are obtained from Brenden-Veisal and Filipowicz [107].

3.2 Quartz type D

Information about quartz type D is obtained from Aasly [6] and Pevik [108]. Figure 63 shows lumps of quartz type D and an enlarged image of one of the lumps. This quartz type is a quartzite, and it is mined by drilling and blasting operations. It is the quartz type with the highest impurity level in this study, but still around 99 % SiO_2. The bulk samples of quartz type D have a red color and appear homogeneous. Microscopic investigations of this type have shown a significant amount of pores, and that mineral inclusions often are located around these. The grains in type D are small, typically 0.2-1 mm, and the grain boundaries are relatively open. Images from microscopic investigation can be seen in Figure 64 [6]. Typical contaminants are sericite (fine-grained muscovite ($KAl_2(Si_3AlO_{10})(OH)_2$), zircon ($ZrSiO_4$), limonite (hydrated iron oxide) and rutile (TiO_2). The limonite occurs as stains between grains and frequently occur as small particles along the rims of primary quartz grains and overgrowth areas. Muscovite is also found at the grain boundaries, while rutile often appears as needle shaped inclusion inside quartz grains. Zircon appears as interstitial grains of approximately 100 μm. Some contaminants can be seen in Figure 65 [107]. Some fluid inclusions can be found inside the grains, but they can also be found in healed fractures. If the conditions under formation is optimal, a quartz sandstone will have uniform strength [6], [108]. From one selected lump of quartz type D, a thin section suitable for microscopic investigations was prepared. Another part of the same lump was shock heated. From the shock heated material another thin section was prepared for microscopic investigation. In that way it was possible to compare the images from microscopic investigation of material original close to each other. The microscopic investigation of the thin sections can be seen in Figure 66 [107]. From the image it can be seen that the samples are more or less intact after shock heating, and no major differences are observed in the material.

Figure 63: A batch and a separate lump of quartz type D.

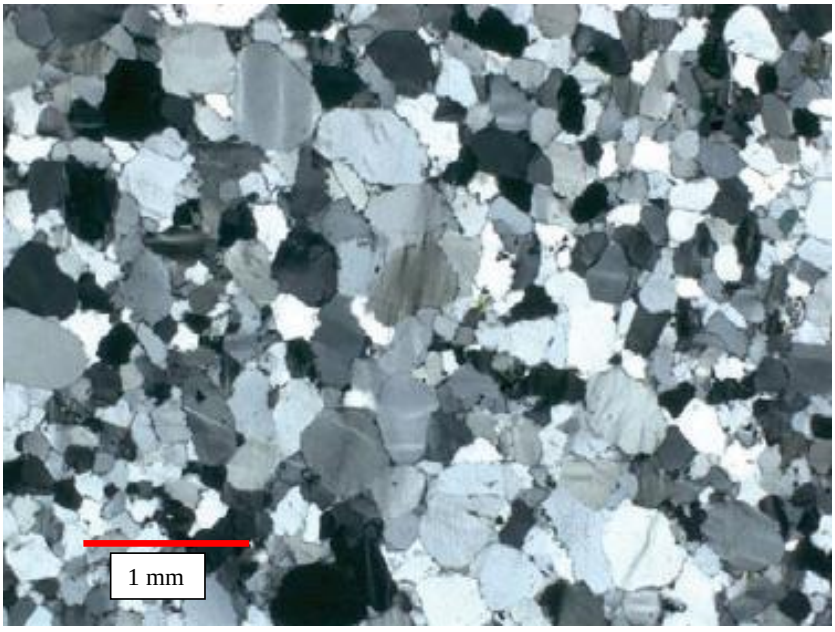

a) Image from microscopic investigation of quartz type D showing grains ranging from 0.2-1 mm.

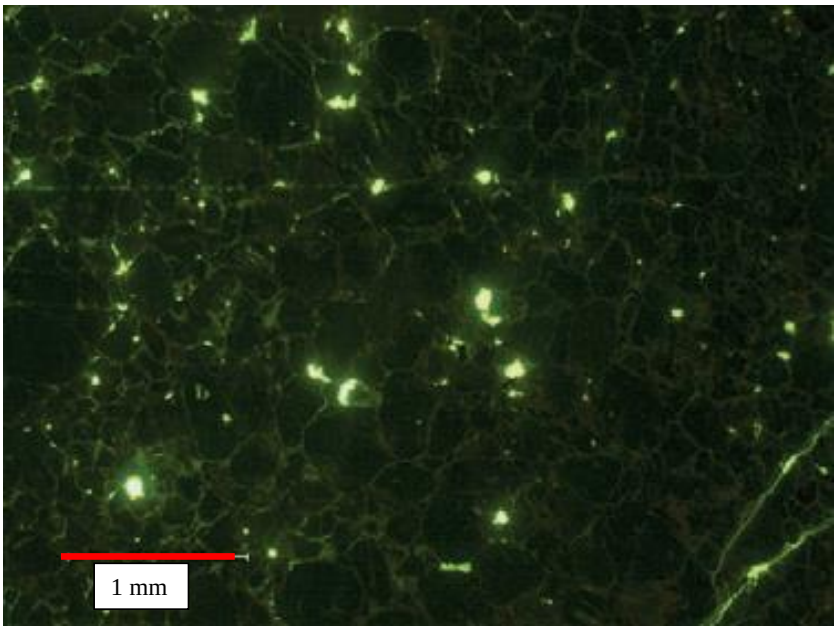

b) *Image from microscopic investigation under fluorescent light. The image shows that the grain boundaries in quartz type D are relatively open because the light is shining through the sample at these spots.*

Figure 64: Microscopic images of quartz type D [6].

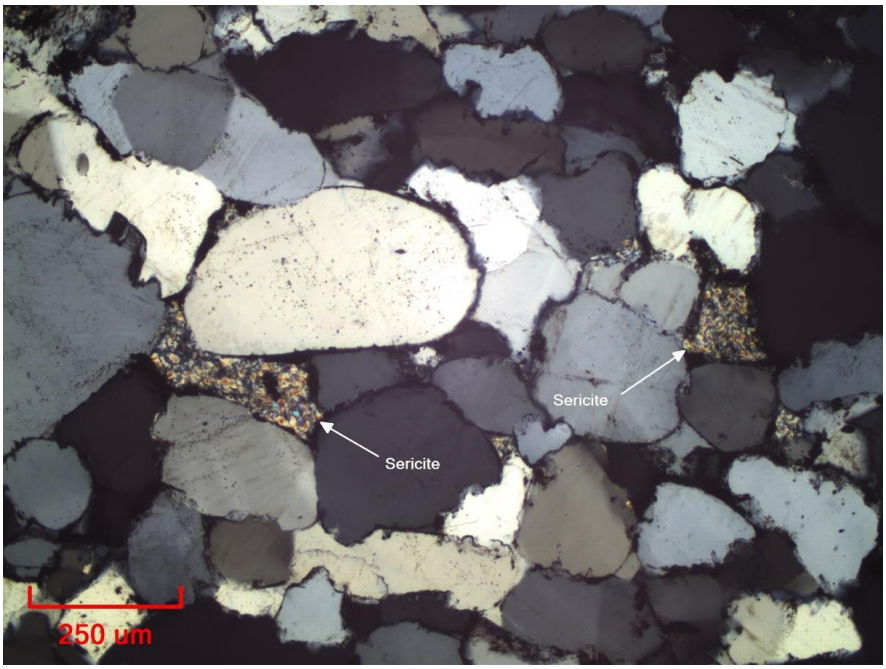

a) Sericite (fine-grained muscovite) in between quartz grains.

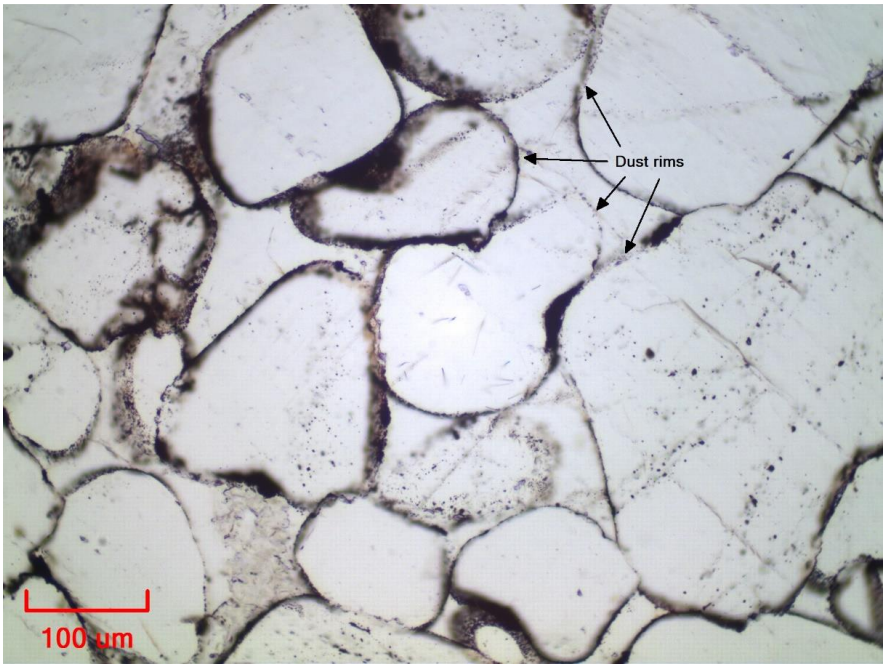

b) Dust rims around grains possibly containing iron hydroxide.

Figure 65: Images from microscopic investigations of quartz type D. The images are obtained from Brenden-Veisal and Filipowicz [107].

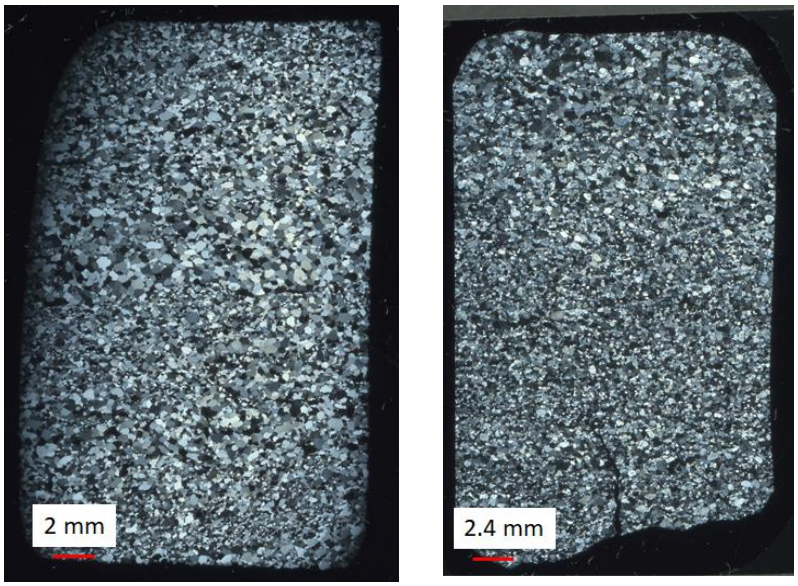

a) *Thin section of unheated quartz type D.*

b) *Thin section of shock heated quartz type D.*

Figure 66: Microscopic images of thin sections of quartz type D, before and after shock heating. The images are obtained from Brenden-Veisal and Filipowicz [107].

3.3 Quartz type F

Quartz type F is from a hydrothermal quartz vein. Images of the quartz type can be seen in Figure 67. Since the deposit is very complex, variations within a batch are expected. Microscopic investigations found large and deformed grains around and above 1 cm. The samples also contained some recrystallized grains which were 70-130 μm, and which were less deformed. Healed fractures are also observed [107]. Image form microscopic investigations can be seen in Figure 68 [109]. The most common contaminant observed is white mica, probably muscovite ($KAl_2(Si_3AlO_{10})(OH)_2$). The inclusions are relatively large, from 5 -20 μm. They are positioned both in the quartz grains, and in between quartz grain boundaries. Calcite ($CaCO_3$) contaminants are also found, and they are observed in between quartz grains. Smaller amount of apatite ($Ca_3PO_4AlO_{10}(OH)_2$), Fe-Mn oxides and ilmenite ($FeTiO_3$) is also observed [107]. Fluid inclusions are relatively abundant in quartz type F. They are often located along healed fractures, but are also observed within quartz grains. The size of the fluid inclusion are relatively large, above 10 μm [107]. Figure 69 shows images from microscopic investigation showing a single liquid-rich fluid inclusion and fluid inclusion along healed fractures [107], [109]. From one selected lump of quartz type F, a thin section suitable for microscopic investigations was prepared. Another part of the same lump where shock heated. From the shock heated material another thin section was prepared for microscopic investigation. In that way it was possible to compare the images from microscopic investigation of material original close to each other. The microscopic investigation of the thin sections can be seen in Figure 62 [107]. For this quartz types it seems like the larger grains are separated from the rest after shock heating, while the smaller grains are clustered together. This could indicate that smaller grains have higher ability to stay together during shock heating, while larger grain will split up.

Figure 67: A batch and a separate lump of quartz type F.

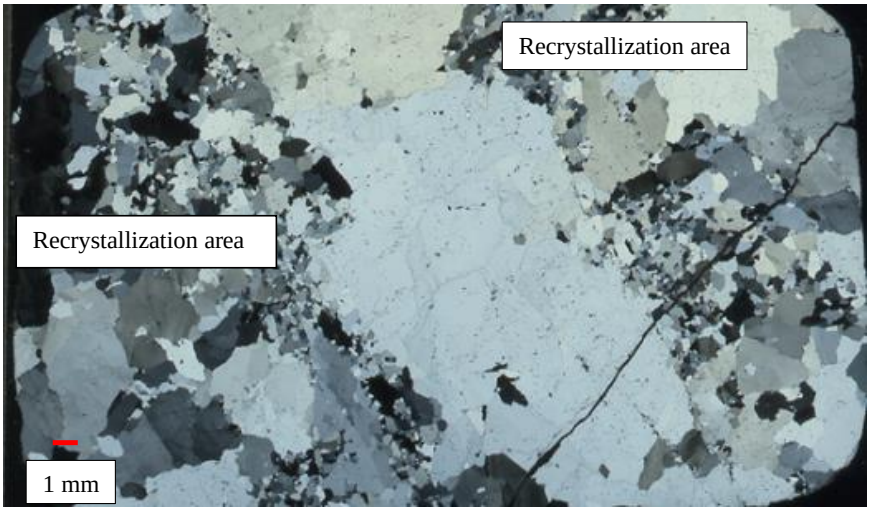

Figure 68: Image from microscopic investigations of quartz type F. The images are from Seljeset [109]. Quartz grains from regime 1 is observed in the middle and recrystallized areas with smaller grains along the sides.

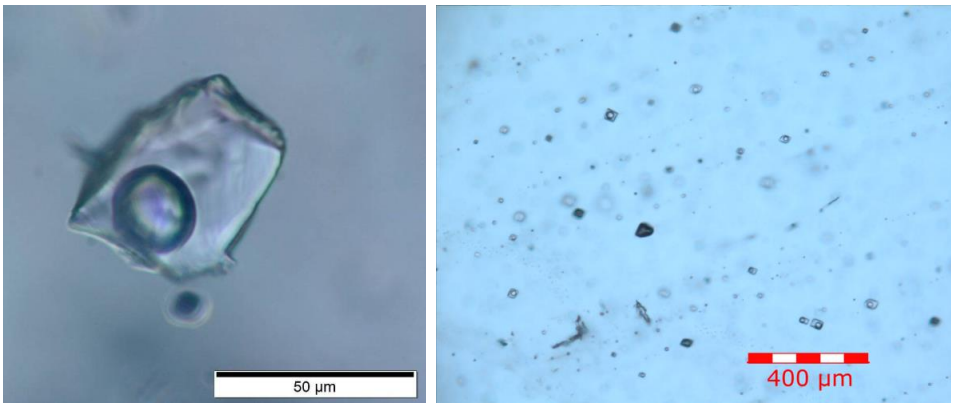

a) *Aqueous liquid-rich fluid inclusion* [107].

b) *Typical fluid inclusion trails* [109].

Figure 69: Images from microscopic investigations of fluid inclusions in quartz type F.

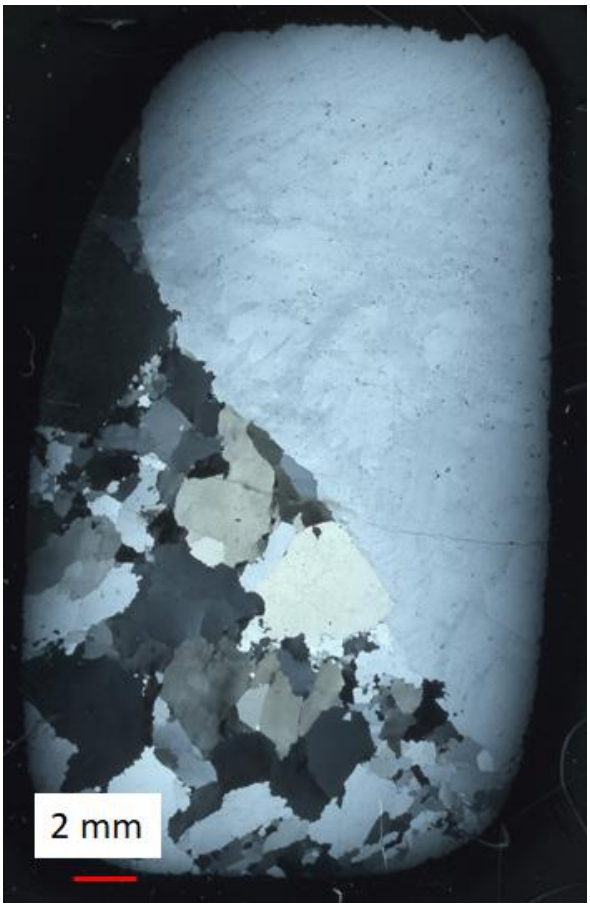

a) Thin section of unheated quartz type D.

b) *Thins section of shock heated quartz type F.*

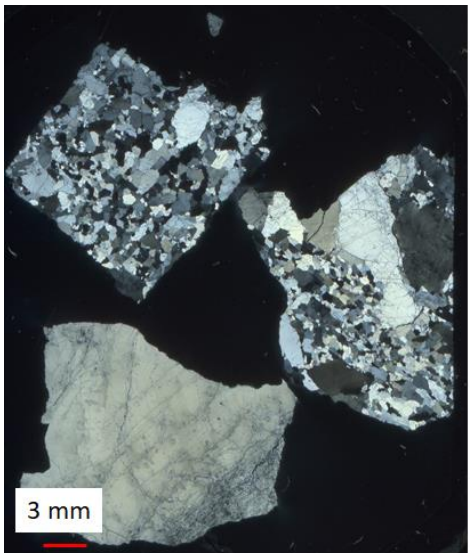

c) *Thins section of shock heated quartz type F.*

Figure 70: Microscopic images of thin sections of quartz type F, before and after shock heating. The images are obtained from Brenden-Veisal and Filipowicz [107].

3.4 Quartz type G

This quartz type is a gravel type, where erosion of surrounding mountains has deposited quartz originating from a hydrothermal vein in alluvial fans and fluvial deposits. As can be seen in Figure 71, the individual lumps have rounded edges from interaction with other material. The color is white, and there are large visual differences in the lumps.

Figure 71: A batch and a separate sample of quartz type G.

Thorough investigations of quartz type G have shown that the impurity concentration of Al, Fe and Ti is very heterogeneous. The texture of the quartz has been characterized by Filipowicz [110], and three different regimes have been identified in the samples based on the degree of deformation caused by temperature and pressure. Regime one, is the least deformed but has the largest amount of fluid inclusion and traces of such. This regime has experienced temperatures up to 400 °C. Microfractures and crosscutting fractures are also observed. Grains found in regime one is a few cm. In the second regime, the quartz is partly recrystallized, and the grain size varies from µm to cm. Regime two has been exposed to temperatures from 400 °C to 500 °C. The regime has fewer fluid inclusions than regime one, and seems strain-free. Microfractures, some crossing the entire sample, are also observed in regime two. Regime three shows dynamic recrystallization and strain-free grains. The temperature have been 500 °C to 700 °C. Few fluid inclusions are observed compared to regime one and two. The grain size in regime three varies from a few tenth of µm up to 3.5 mm. The temperatures for the regimes are based on classification of different grades of deformation and the following microstructure in quartz by Passchier et al. mentioned by Filipowicz [110]. A rough estimate is 74 % of regime 1, 22 % of regime 2 and 4 % of regime three. Figure 72 shows images of thin sections observed in microscope of each regime where the grain size is clearly seen. Other textural observations like fractures, fluid inclusions and contaminants can be seen in Figure 73 [110].

Contaminants in quartz type G, identified with microscopic methods, are mainly iron oxide and muscovite ($KAl_2(Si_3AlO_{10})(OH)_2$). The iron oxide occurs along fractures and grain boundaries as well as inclusions in quartz. Muscovite is also observed both at grain boundaries and inside grains [110]. Illite ($K_{0.65}Al_{2.0}[Al_{0.65}Si_{3.35}O_{10}](OH)_2$) and kaolinite ($Al_2(Si_2O_5)(OH)_4$) are also observed, but mainly in regime 3. An example of iron oxide impurity in a fracture can be seen in image d in Figure 73 [110].

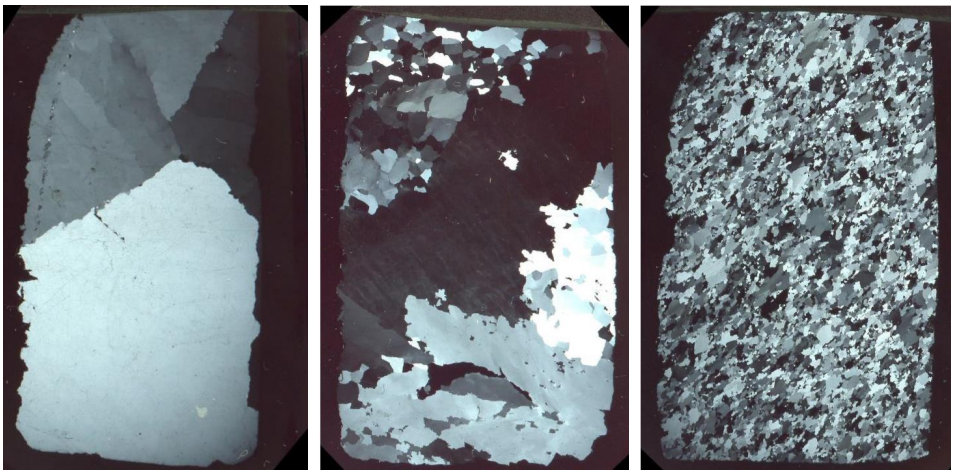

a) Regime 1 *b) Regime 2* *c) Regime 3*

Figure 72: Thin sections of the different regimes in quartz type G [110].

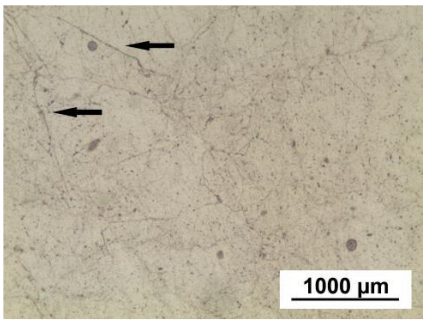

a) *Arrows pointing at micro fractures observed by light microscope.*

b) *Fractures crossing the sample from the top left corner to the bottom right.*

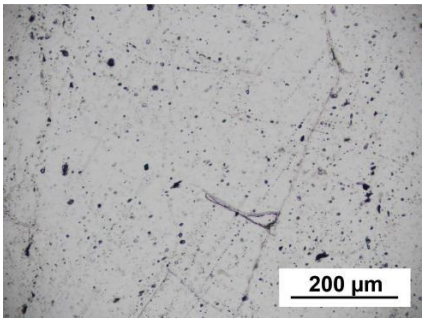

c) *Fluid inclusions and fluid inclusion trails*

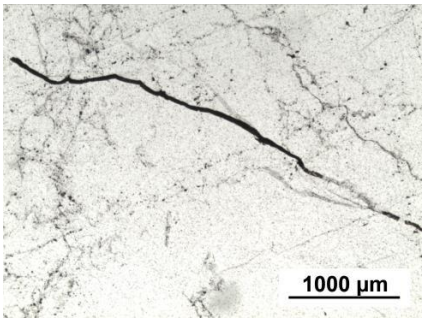

d) *Iron oxide impurities occurring in a fracture*

Figure 73: Images from microscopic investigations of quartz type G. The images show micro fractures, fluid inclusions and impurities [110].

For quartz type G, high temperature microthermometry has also been used to observe what happens to samples when they are heated to 1350 °C [110]. For samples from all regimes, decrepitation of fluid inclusions starts at low temperatures from around 100 °C to 600 °C. The decrepitation seems to cause micro fractures, and it links fractures together creating trails of fractures. At higher temperatures, 1200 °C, more severe fracturing is observed in areas where fluid inclusions are present. Samples from all the regimes behave in a similar way, but since regime 1 has the highest amount of fluid inclusion fracturing is more common in such samples. Samples with no fluid inclusions or preexisting fractures do not show any effect of heating in high temperature microthermometry [110].

3.5 Raman spectroscopy

Quartz type A, D and F were sent to Hanyang University and investigated at the Laboratory of High Temperature Physicochemical Processing of Materials. The analysis of the three quartz samples showed that mainly quartz peaks were detected in all the samples [111]. This can be seen in Figure 74. In addition, quartz type D had some additional peaks. These were determined to be due to hematite, which is expected from the chemical analysis of quartz type D since it has a higher content of Fe.

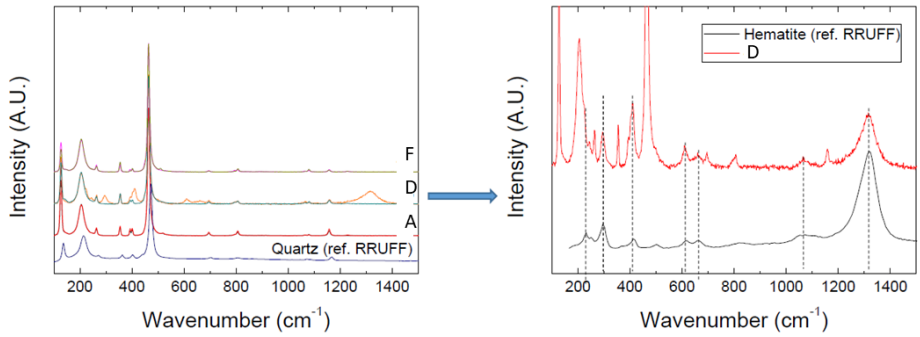

Figure 74: Raman spectra of quartz type A, D and F investigated at Hanyang University [111]. In the figure to the right quartz type D is compared with the spectra for hematite to confirm hematite is present in quartz type D.

3.6 Reference sample

For some of the tests in this study, a high purity natural crystalline quartz sand was used as a reference sample. The quartz sand, with product name NC4A, originates from quartz deposits in Spruce Pine, USA. This quartz sand has a purity level at ppm level and is used as raw material for quartz glass products for the solar and semi-conductor industries globally. The impurity level given by the supplier is given in Table 10.

Table 10: Impurity level in high purity quartz sand, NC4A, used as a pure reference sample. The impurity content is from the data sheet from the supplier.

Impurity	Typical value [ppm]	Maximum [ppm]
Al	13	18.0
B	≤0.1	0.1
Ca	0.5	1.0
Co	≤0.01	0.01
Cr	≤0.01	0.03
Cu	≤0.01	0.03
Fe	0.2	0.6
K	0.5	0.9
Li	0.4	1.0
Mg	≤0.1	0.1
Mn	≤0.1	0.2
Na	0.8	1.2
Ni	≤0.01	0.03
Ti	1.2	1.5

3.7 Additional samples

For some of the experiments, additional quartz types have been tested to get a broader foundation for comparison. In Figure 75 an image of each of these types can be seen, and the chemical analysis of each type, except type B, is given Table 11. Type B is the same type as F, but with a lower purity grade. Except for sample J, ICP-OES is used for chemical analysis, the same as for quartz type A, D, F and G.

Figure 75: Additional quartz types tested.

Table 11: Chemical analysis of additional quartz types used in this study. The analysis is performed by Erimsa and the amounts are given in wt% if nothing else is indicated.

Quartz type	Al [wt%]	Fe [wt%]	Ti [ppm]	Ca [wt%]	Na [wt%]	K [wt%]	Mg [wt%]	Mn [ppm]	P [ppm]	SiO_2 [wt%]
C	0.0509	0.0122	10.1	0.0016	0.0019	0.0098	0.0022	0.4	2.2	99.920
E	0.3012	0.0731	133.6	0.0026	0.0038	0.0924	0.0057	2.1	29.1	99.505
H	0.0329	0.0172	10.5	0.0024	0.0053	0.0075	0.0019	0.8	1.5	99.932
I	0.0608	0.0233	14.8	0.0046	0.0068	0.0267	0.0021	4.6	13.7	99.872
J*	0.0900	0.4057	-	0.0143	-	0.0166	-	-	-	<99.47

* Analysis is performed by XRD and XRF, and some impurities are below detection limit.

4 Experimental procedures

The two main experimental procedures in this study are the phase transformation experiments and the shock heating of different quartz types. In addition, different techniques have been used to see if relevant information could be obtained. These are differential thermal analysis (DTA) to measure the enthalpy change during heating, Raman spectroscopy to identify impurities, computed tomography (CT) imaging to detect cracks in quartz samples and Fourier transformed infrared spectroscopy (FT-IR) to determine possible water or OH-groups in addition to clay minerals in quartz. Multivariate analysis has also been used on some of the data obtained to detect possible correlations between variables. All these methods are presented in detail in this chapter, except the differential thermal analysis and the Raman spectroscopy since the method did not give any useful results. The results from these methods are included in Appendix A: Enthalpy change measured by differential thermal analysis (DTA) and Appendix B: Raman Spectroscopy.

4.1 Disintegration of quartz

To measure the disintegration of various quartz types, shock heating experiments were performed. Some of the samples were analyzed with CT-imaging before shock heating in order to detect the amount of crack in the sample before heating. After heating, some samples were analyzed with XRD to determine the amount of phases produced during shock heating. Each part of the experiments is described in detail later in this section. An overview of the experiment process for quartz type A can be seen in Figure 76. A similar scheme can be made for all the main quartz types A, D, F and G. In total 10 different quartz samples were shock heated, 4 samples were investigated with CT and 24 samples were investigated with XRD to determine the phase composition post shock heating.

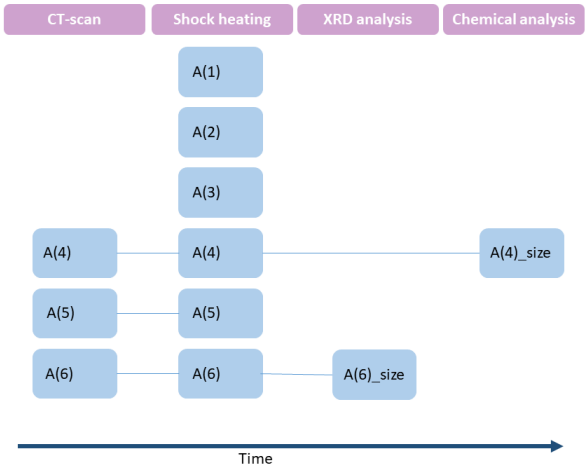

Figure 76: Overview of the experiments performed quartz type A. The term "size" means a specific size fraction obtained after shock heating.

4.1.1 Shock heating

A carbon crucible with height 38 cm and inner diameter 11 cm was heated to 1500 °C in an induction furnace, called IF75. A thermocouple of type C was used to measure the temperature. It was placed inside an alumina tube and a carbon tube to protect it. A piece of Kaowool was placed on top of the crucible to avoid heat loss from the top. Different quartz samples were placed in the crucible when 1500 °C was reached. The samples were 200 g ± 20 g, and around 5-9 cm in diameter. An image of each of the four main quartz types can be seen in Figure 77. After the

sample was placed in the crucible, the furnace temperature dropped around 100 °C, but recovered within few minutes. The sample was kept in the crucible for ten minutes. An illustration of the experimental procedure can be seen in Figure 78. The experimental temperature at 1500 °C is higher than an industrial furnace where the surface holds a temperature from 700-1300 °C for a Si producing furnace. The higher temperature for the experiments was chosen to more clearly see the differences, since disintegration is more extensive at 1500 °C than 1300 °C [82].

Figure 77: A sample from each of the four main quartz types shock heated. The samples were 200 g ± 20 g and 5-9 cm in diameter.

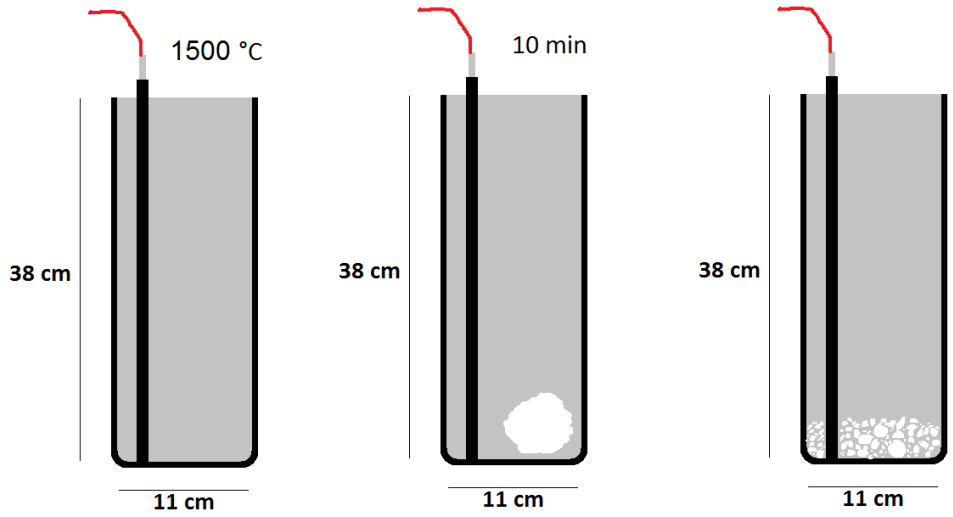

Figure 78: Shock heating of quartz samples in a carbon crucible. The samples were shock heated at 1500 °C for 10 minutes.

After 10 minutes holding time, the sample was poured into a cold carbon crucible, and cooled in air to room temperature. Each sample were carefully sieved at 2, 4, 10 and 20 mm after cooling, and each fraction weighed. For the four main quartz types in this study, several parallels were done. Some additional quartz types were also tested for a broader basis for comparison. In Table 12 all the samples are listed, and the number of parallels within each type is given. For type G, some samples named with an R indicates which geological regime they are from. These samples were selected to see any internal differences based on the geological regime. The geological regimes for type G are presented in section 3.4.

Table 12: List of samples shock heated to 1500 °C in induction furnace, and additional information of tests performed.

Quartz type	No. of samples	Sample name	Comments
A	7	A(1), A(2), A(3), A(4), A(5), A(6), A(geo)	• 3 of the samples were CT-scanned before heating • The geo-sample have thorough geological characterization • Silica phases measured
B	2	B(1), B(2)	
C	2	C(1), C(2)	
D	6	D(1), D(2), D(3), D(4), D(5), D(geo)	• 2 of the samples were CT-scanned before heating • The geo-sample have thorough geological characterization

			• Silica phases measured
E	2	E(1), E(2)	• Silica phases measured
F	7	F(1), F(2), F(3), F(4), F(5), F(6), F(geo)	• 3 of the samples were CT-scanned before heating • 1 of the samples were only 100 g, (F(2)) • The geo-sample have thorough geological characterization • Silica phases measured
G	10	G(1), G(2), G(3), G_R1a, G_R1b, G_R2a, G_R2b, G_R1-2, G_R3a, G_2-3	• 3 samples were CT-scanned before heating • The R indicated geological regime • Silica phases measured
H	3	H(1), H(2), H(3)	• Silica phases measured
I	3	I(1), I(2), I(3)	• Silica phases measured
J	1	J(geo)	• The geo-sample have thorough geological characterization

4.1.2 Computed tomography (CT-imaging)

X-ray computed tomography (CT) was done to measure cracks in the cross sections on the four quartz types A, D, F and G. The scans were performed with a Nikon XT H225 ST Instrument. To make the samples more stable, they were covered with aluminum foil before they were placed in the sample holder. The settings used during the scanning were 140 kV and 200 µA. Each sample was scanned for 1 hour. The CT imaging were done before the same samples were shock heated. The software ImageJ was used to measure the area of cracks and the total area of the sample on the images. An average crack thickness was used for each image, since the thickness of the crack could vary. The area of each crack was added to obtain a percentage of crack for that sample. For every sample, more than thousand images were created in the CT procedure. A random selection of twenty images for each scanned sample were used for further analysis, and an average was calculated. Figure 79 shows an image of quartz type F where all the cracks are marked and measured.

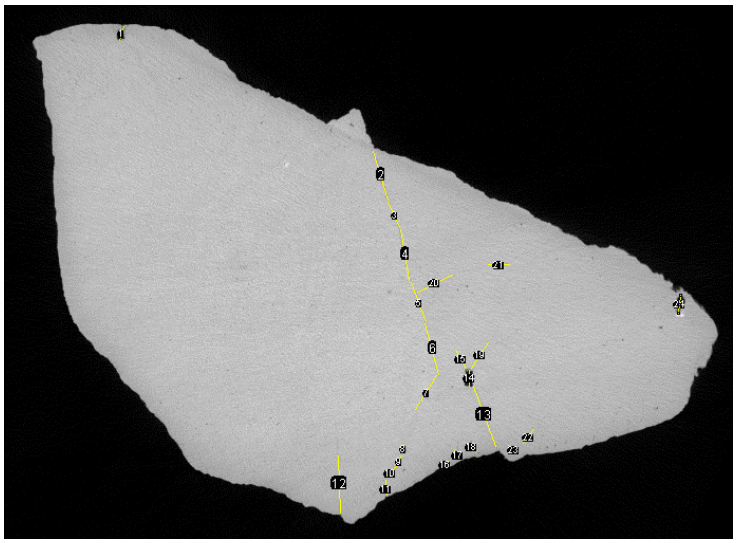

Figure 79: An image of type F quartz after labelling of all the cracks.

4.1.3 Impurity measurements in samples post shock heating

After shock heating of the quartz samples, some size fractions from the four main quartz types were sent to Erimsa for chemical analysis to check if the impurities segregated during disintegration. Erimsa did also perform the bulk analysis, thus, the uncertainty of different measuring methods is ruled out. The samples sent to chemical analysis are listed below. The smallest size fraction could not be measured since the total amount of this was too low.

- A4 10-4 mm
- A4 20-10 mm
- D5 > 20 mm
- F5 10-4 mm
- F6 10-4 mm
- G1 20-10 mm
- G1 > 20 mm

4.1.4 XRD-analysis of shock heated quartz

For 7 of the quartz types, a sample was taken from each size fraction after shock heating. These samples were analyzed with X-ray diffraction to measure the amount of different silica phases. The method used is the same as described thoroughly later in this chapter, in section 4.2.2 and 4.2.3. Samples from the following experiments were analyzed:

- A(6): > 10 mm, 10-4 mm, 4-2 mm and <2 mm
- D(4): >20 mm, 20-10 mm, 10-4 mm, 4-2 mm and <2 mm
- E(1): >10 mm
- E(2): >10mm
- F(4): >10 mm, 10-4 mm, 4-2 mm and <2 mm
- G(2): >10 mm, 10-4 mm, 4-2 mm and <2mm
- H(1): 20-10 mm
- I(1): >20mm and 10-4 mm
- I(3): > 20 mm and 10-4 mm

4.2 Analysis of phases

The pieces used for these experiments were approximately 10 or 100 g. It was difficult to obtain the exact weight for the samples, therefore ± 20 % was accepted. Larger pieces of quartz were crushed with a hammer to obtain the preferred size. Some of the samples were crushed with a jaw breaker because of their high strength.

4.2.1 Rapid heating

The quartz sample heated was placed on an alumina plate to avoid any reaction with the furnace interior at high temperatures. No reaction with the alumina plate was observed during the experiments. For some experiments at 1700 °C and long holding time, some nearly melted silica could be stuck to the alumina plate after heating. This material was not used further. The furnace chamber with a sample ready for heating can be seen in Figure 80. The furnace front can also be seen in the same figure. One sample was heated at time.

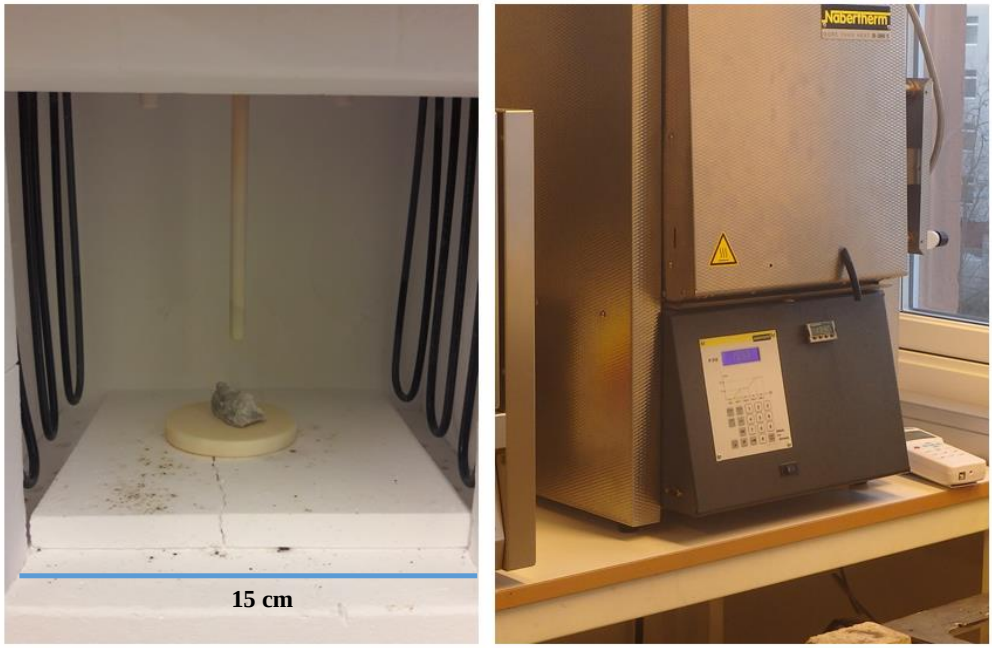

Figure 80: To the left, a 10 g sample of quartz is placed inside the rapid heating furnace. The width and the height of the furnace is approximately 15 cm. In the picture to the right, the furnace is seen from the front. The front door can be lifted, and the furnace has a programming panel at the front.

For each sample, the maximum temperature and holding time at this temperature were set for the furnace. The maximum heating rate was set, around 50 °C/min. To check the consistency and reliability of this furnace, additional tests with external thermocouple were performed. The thermocouple used for these tests was type B. This thermocouple detected a temperature difference of 5 °C - 10 °C when the temperature was at its maximum. Figure 81 show the logged temperatures from the additional thermocouple, both with empty furnace and with samples inside. The figure shows that it took approximately 30 minutes for the furnace to heat up to 1600 °C, and 36 minutes to reach 1700 °C. No significant difference was observed in the heating rate when there was a sample in the furnace compared to empty furnace. When the heating and holding time were completed, the furnace was opened and the sample taken out and placed on a cold brick to

cool in room temperature. All the samples were heated in the same furnace, a Nabertherm L04/08. In the middle of the experimental project the furnace lining was changed due to damage. After this incident, a minor increase in the heating rate was observed. This is illustrated in Figure 81 for test 5. Repeated experiments before and after relining did not give any significant difference in the phase composition.

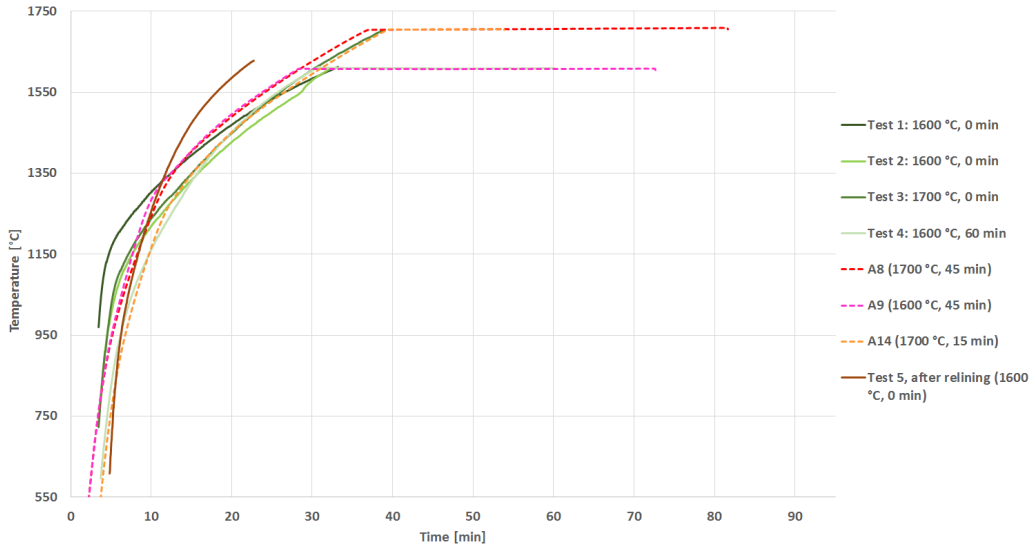

Figure 81: The heating profile for Nabertherm L04/08 furnace, tested with external thermocouple without samples inside the furnace. During some experiments the temperature were also externally logged. These results are compared in the figure with dotted lines.

The particle size, holding time and maximum temperature were varied in the experiments. In Table 13 the experiments details are given for all the four main quartz types. At the end of the table a list of additional experiments is given. These experiments were done to check the repeatability, and to redo experiments with results deviating from the trend. Up to three experiments with the same heating plan were done for some randomly selected experiments. The X in A1.X represents the different parallels for experiment A1 etc.

Table 13: Experiments details for rapid heating experiments of four quartz types of different size.

Experiment no.	**Temperature [°C]**	**Holding time [min]**	**Weight [g]**
A1, F1, G1, D1	1600	0	
A2, F2, G2, D2	1600	120	
A3, F3, G3, D3	1700	0	
A4, F4, G4, D4	1700	15	10
A5, F5, G5, D5	1600	15	
A6, F6, G6, D6	1700	30	
A7, F7, G7, D7	1600	30	
A8, F8, G8, D8	1700	45	

A9, F9, G9, D9	1600	45	
A10, F10, G10, D10	1600	60	
A11, F11, G11, D11	1700	60	
A12, F12, G12	1600	0	100
A13, F13, G13	1700	0	
A14, F14, G14	1700	15	
A15, F15, G15	1600	15	
A16, F16, G16	1600	30	
A17, F17, G17	1700	30	
A18, F18, G18	1600	45	
A19, F19, G19	1700	45	
A20, F20, G20	1700	60	
A21, F21, G21	1600	60	
Additional experiments			
A1.2	1600	0	10
A1.3	1600	0	10
A3.2	1700	0	10
A3.3	1700	0	10
A14.2	1700	15	100
A15.2	1600	15	100
A16.2	1600	30	100
A17.2	1700	30	100
Ax1	1550	0	10
Ax2	1550	30	10
Ax3	1550	60	10
Ax4	1650	0	10
Ax5	1650	30	10
Ax6	1650	60	10
F3.2	1700	0	10
F4.2	1700	15	10
F4.3	1700	15	10
F7.2	1600	30	10

F7.3	1600	30	10
G6.2	1700	30	10
G7.2	1600	30	10
G14.2	1700	15	100
G16.2	1600	30	100
G19.2	1700	45	100

4.2.2 Pre- XRD treatment

After heating, the samples were either crushed with a hammer to obtain smaller grains that were more suitable for further milling, or the samples had already disintegrated. To avoid contamination from the hammer, the samples were placed inside several plastic bags. A tungsten carbide planetary mill was used to crush the samples further into powder. Later, a stainless steel planetary disk mill was also used. The milling was done at 700 rpm for 10 s. Some samples needed to be crushed for a longer time period to obtain a fine powder suitable for XRD. Before the milling was started, the equipment was washed thoroughly with ethanol, and milling with a washing quartz was performed. After each milling the equipment was rinsed with water and ethanol to avoid contamination.

A hypothesis that the milling procedure could cause formation of amorphous silica existed. To see if the milling could cause any change in the phase composition, unheated sample of quartz type A and D was crushed for 60 s instead of 10 s. The comparison between milling time of 10 s and 60 s showed no increased amount of amorphous phase that can be related to increased milling time. In fact, an amorphous content of 12 % was observed for type D milled in 10 s, while no amorphous material was observed for the samples milled for 60 s. The initial phase content of the different quartz types is discussed later, but there is no evidence that milling causes an increase in amorphous phase. This can be seen in Figure 82. Ringdalen et al. [112] also investigated if milling could cause any amorphous phase. They milled their samples in 18 s and 5 minutes, and no significant amount of amorphous phase was created. It is therefore expected that milling time up to 5 minutes will not affect the phase composition in silica samples.

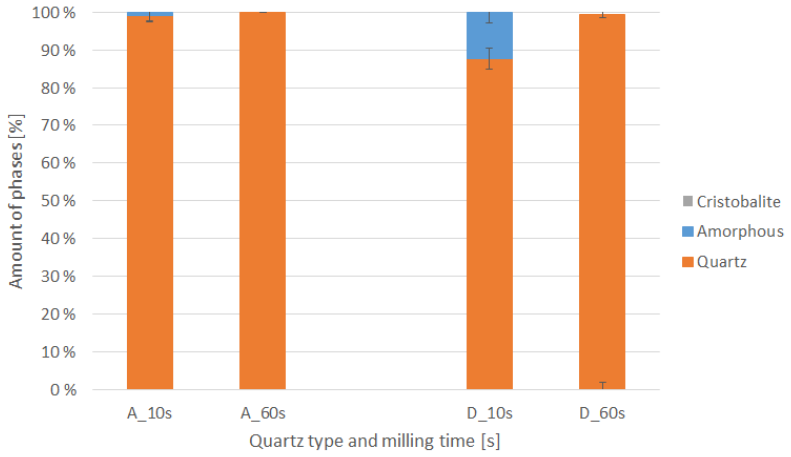

Figure 82: Amount of phases in unheated quartz type A after milling at 10 s and 60 s.

4.2.3 XRD

X-rays are electromagnetic waves, and these can be used to detect the periodicity of a crystal lattice, and determine crystal phases in a sample. X-rays with a known wavelength are emitted towards a sample. The radiation will interact with the atoms in the sample and monochromatic radiation will be reflected according to Bragg's law. Each crystalline structure gives a unique reflection pattern, and it is therefore possible to identify different phases. It is possible to quantify the amount of phases by comparing the intensity peaks of each crystalline structure [113].

For the XRD sample preparation, back loading sample holders were used to minimize preferred orientation in the powder. This could cause peak intensity errors. The samples were measured with a Bruker D8 A25 Da-Vinci X-ray Diffractometer with CuKα radiation. The detector in the instrument was a LynxEye^{TM} SuperSpeed Detector. The sample were scanned between 5° and 90° for 32 minutes each.

Internal standard method

When a sample contains some amorphous material, the quantification of phases becomes more complicated since the amorphous materials lack crystallinity and long range order. One method to do quantitative analysis of an amorphous material is the internal standard method. It is described by Madsen et al. [114]. First, the amount of crystalline phase present in each sample is estimated using the following algorithm from Hill and Howard:

$$W_a = \frac{S_a(ZMV)_a}{\sum_{j=1}^{n} S_j(ZMV)_j} \tag{4.1}$$

Where S_a is the Rietveld scale factor for phase a, ZM is the mass of the unit cell contents, V is the volume of the unit call and n is the number of phases in the analysis. The method relies on that all crystalline phases have been included in the analysis, and Equation 4.1 sums to unity.

An exact known amount of crystalline internal standard material, also called spike, is added to each sample. This allows the reported amount of phases to be corrected proportionally according to:

$$Corr(W_a) = W_a \frac{STD_{known}}{STD_{measured}} \tag{4.2}$$

Where $Corr(W_a)$ is the corrected weight present of phase a, STD_{known} is the weighted concentration of the standard in the sample and $STD_{measured}$ is the concentration derived from Equation 4.1. This calculation is done for each of the crystalline phases in the sample. Then the amount of amorphous material can be calculated using the following expression:

$$W_{amorphous} = 1 - \sum_{j=1}^{n} Corr(W_j) \tag{4.3}$$

This method is according to Madsen et al. [114] the most common for quantitative phase analysis via the Rietveld method. It relies on the assumption that all crystalline phases in the material have been included in the analysis. The crystalline standard must have similar mass and mass absorption coefficient as the sample. This is to minimize the effects of micro absorption.

The milled quartz samples and a crystalline standard (also called spike), Al_2O_3, were dried overnight in a calcination furnace at 250 °C. The aluminum oxide used, was an Al_2O_3 α-phase, also called corundum. It had a 99.9 % purity. When the temperature reached 120-150 ° C in the calcination furnace, the samples were taken out and sealed in order to prevent any humidity in the samples before weighing. For each XRD-sample approximately 80-90 mg of silica and 20-25 mg of spike was exactly measured and mixed. The weights were recorded for later calculations. Three XRD parallels were taken from each sample to check for consistency and reveal any outliers. The powders were poured into a mortar and a splash of acetone was added to ease the mixing, and the powder were mixed with a pestle until the acetone had evaporated and the powder were homogeneous. The powder was carefully poured back in the sample container, and the equipment rinsed with ethanol between each mixing.

Quantitative analysis of XRD results

To identify which phases were present in the sample, the software Diffract.Eva was used. Then the quantitative analysis of the diffraction patterns was performed using the Topas V5 software. The exact percentage of the spike was put into the program, which then can calculates the absolute amount of the crystalline phases after the peaks have been fitted. A standard file with selected settings were used for all the samples, to make sure the calculations were run with the same parameters. To make a good fit with the calculated curve, unit cell parameters and sample displacement were refined for each sample. The Chebyshev order was kept at 4 for all the measurements, and the instrument had a 2θ angular range of 3, and a fix divergent slit (FDS) angle of 0.3.

The initial phase composition of unheated quartz types

Uncertainty of the initial phase composition was a concern. Earlier findings could suggest that untreated quartz also contained some amorphous content [115]. To check this, untreated sample of A, D, F, G and NC4A were analyzed. The samples were milled in a planetary disk mill to a fine powder, and after mixing and addition of spike, back loading samples were prepared for the XRD analysis. As can be seen in Figure 83, all the samples contained some amorphous material before heating. Type A contained the least amount of amorphous material, around and below 10 % for all samples tested. All samples from quartz type F contained 15% - 19 % amorphous phase, and hence type F had the smallest internal variance between the different samples tested. A large variance between the samples within the type was observed for quartz type D and G. Samples from type D contained between 6 and 22 % amorphous phase, and in type G contained the amount of amorphous phase varied from 5 % to 20 %. Since it has been ruled out that the milling will create amorphous phase, also concluded by Ringdalen et al. [112], the original quartz samples probably contain some amorphous material. The variance observed both between the quartz types and within are believed to be a consequence of heterogeneous raw material. However, the amorphous phase is a minor phase in all samples, and does for most samples not exceed 20 %.

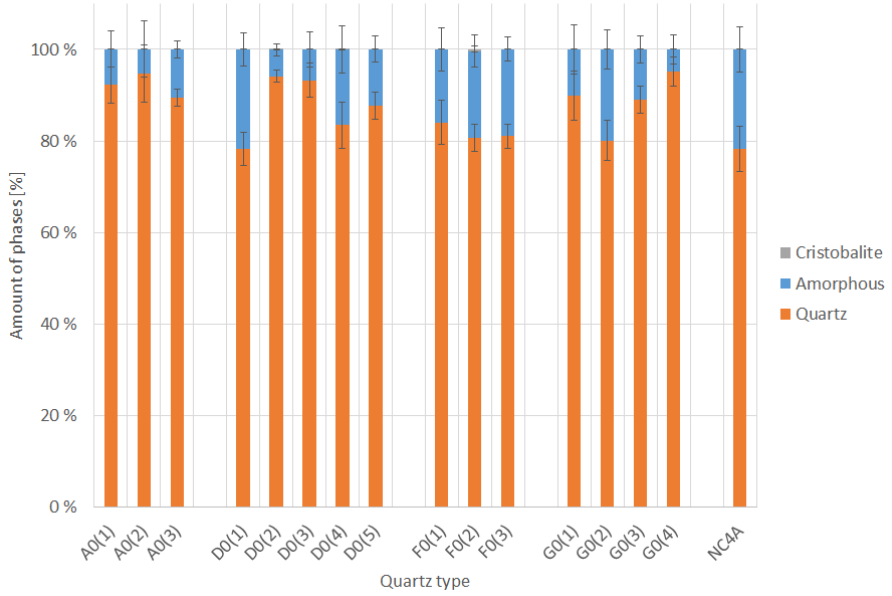

Figure 83: The amount of phases in unheated quartz. All the samples have been milled to a powder before XRD analysis.

4.3 Fourier Transformed Infrared Spectroscopy

Infrared spectroscopy is the interaction between infrared radiation and matter. Radiation with a specific energy interacts with bonds between molecules. For a molecule to be detected by IR-spectroscopy, it has to be IR-active. That means, it has to have a change in dipole moment when energy is absorbed. Therefore water, or OH-bond and other dipole bonds are easily detected compared to e.g. N_2 or other homo nuclear diatomic molecules. For IR-spectroscopy the incoming radiation is sufficient to cause molecules to rotate and, if possible, vibrate. The radiation has a certain frequency, and when the bond in a molecule vibrates at the same frequency it can absorb the radiation. The amplitude of the frequency will then increase, not the frequency itself. This makes it possible to determine the type of bond based on the frequency absorbed, since it is specific for each type of bond. An interferogram holds the spectral information collected by the spectrometer. Since all wavelengths have been incident on the sample, the output will be a wave combined of several cosine waves. A Fourier transformation is used to pick out the individual frequencies for each cosine wave in the output. From these it can be determined which bonds are present in the sample, seeing that each cosine wave corresponds to a specific frequency [116].

The most common instrument for FT-IR spectroscopy is a Michelson interferometer, illustrated in Figure 84 [117] where four optical arms with a beam splitter at their point of intersection. The incoming light is separated at the beam splitter along two perpendicular arms. At the end of these arms, a mirror is placed which reflects the light back to the beam splitter where a third mirror sends a recombined light signal to the detector. One of the mirrors can move while the other one is fixed. This changes the path length of the arm, and the recombined light hitting the detector [116].

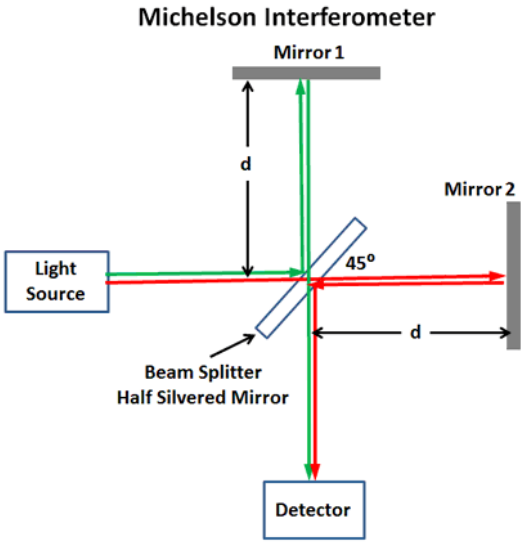

Figure 84: An illustration of a Michelson Interferometer [117].

Samples from all the quartz types A-I were analyzed with FT-IR in order to determine the different impurities with an emphasize on water inclusions (free H_2O), OH-groups and clay minerals. First, initial tests were done to see if the method could give any valuable results, and to determine the most suitable sample size. Both powders below 100 µm and between 100 and 250 µm were tested. Also, several parallels were done on some of the samples to see if the method was consistent. This is shown in Table 14, where all the samples investigated are listed. All the samples in each run had to be analyzed after each other when the instrument first was calibrated. All the samples were prepared by using a planetary disk mill. After two samples sizes had been tested, it was decided to further use the <100 µm due to better scattering of the IR-spectra compared to samples 100-250 µm.

Table 14: Samples investigated with FT-IR. The number in parenthesis gives the number of parallels above 1.

Run	Samples	Sample size
1	A, D, NC4A	< 100 µm
2	A(2), D, G	< 100 µm
3	A, D, F, G	250 µm< > 100 µm
4	A(2), B(2), C(2), D(2), E(2), F(2), G(2), H(2), I(2)	<100 µm

For the infrared spectral characterization, a Bruker Vertex 80v spectrometer fitted with Praying Mantis accessory from Harrick was used. The characterization was performed by diffuse reflectance Fourier transformed (DRIFT) spectroscopy. A potassium bromide (KBr) beam splitter and a deutroglycine sulphate (DTGS) detector was used. By averaging 100 scans at 4 cm^{-1} resolution over the range 4000-350 cm^{-1} a DRIFT spectra was acquired. Due to variation in a reflectivity of the samples, the first reflectance spectrum was divided by a KBr reference

spectrum and normalized. The baseline from KBr was then subtracted, and the spectra was concerted to absorbance. The FT-IR analysis was performed by Bartlomiej Gawel at NTNU.

4.4 Multivariate analysis

When dealing with multiple measurements on each experimental unit, multivariate analysis can be used to detect correlation between the measurements. In this work, two different techniques have been used. The first one is multivariate curve resolution (MCR). It aims to decompose a two-way data matrix **D** into two matrices **C** and $\mathbf{S}^{\mathbf{T}}$, containing concentration profiles and spectra of the *k* species investigated. The source of variation, the components and profiles contributing to the raw measurements, could be found [118]. The number of chemical species contributing to **D** which should be modelled by MCR has to be determined. An estimate for **C** or $\mathbf{S}^{\mathbf{T}}$ also has to be provided. By using alternating least squares (ALS) algorithm until convergence is reached, **C** and $\mathbf{S}^{\mathbf{T}}$ are optimized. Constraints can be used in the iteration process to obtain a meaningful solution.

In this work, MCR have been made based on the disintegration data and the different quartz types concentration of clay minerals and water to detect any possible correlation. The analysis were performed by Bartlomiej Gawel at NTNU.

Principal component analysis is another method that uses an orthogonal transformation to convert a set of observations of possibly correlated variables to a new set of values which are linearly independent. The method aims to reduce the dimension of the feature space. In other words, PCA compresses a lot of data into something that captures the essence of the original data. A technique called feature extraction creates new combination of variables based on the observed variables. The new combinations are constructed such that the first principal component has the highest likely effect on the variance in the data observed [119], [120]. In Figure 85 an illustration on how principal component 1 and principal components 2 are found from the variables, is shown. In this case the variables will be the disintegration data and the FT-IR spectra.

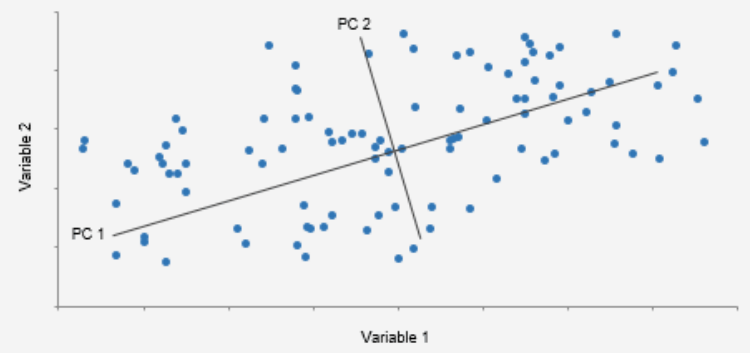

Figure 85: An illustration of how principal components 1 (PC1) and principal component 2 (PC2) are determined from two variables related to the experimental unit [121].

For the quartz types A-I a principal component analysis was done in order to find the first principal component and the second principal component when it comes to disintegration, i.e. what does the quartz types disintegrating easily have in common. The data obtained from disintegration and the spectra from FT-IR analysis were combined to create principal component 1 and 2. The principal component analysis were performed by Bartlomiej Gawel at NTNU, and the software Unscrambler was used.

5 Results

5.1 Disintegration of quartz

In total 10 different quartz types were tested by shock heating to see how much fines they produced. The four main quartzes (A, D, F and G) were tested more thoroughly. Properties that might affect the disintegration, were also tested, and are presented in the sub chapters.

5.1.1 Fines production

The amount of fines below 10 mm varied from 1 wt% to 85 wt% after shock heating to 1500 °C. All the samples were sieved at 2, 4, 10 and 20 mm, and each size fraction weighted. The wt% of each size fraction for each sample can be seen in Table 15. When the samples were poured into the cold crucible after the shock heating, no further disintegration was observed. The material had already disintegrated as a consequence of the shock heating.

Table 15: Size fractions after shock heating of different quartz types to 1500 °C

Quartz	<2 mm [wt%]	2-4 mm [wt%]	4-10 mm [wt%]	Total amount fines, <10 mm	10-20 mm [wt%]	>20 mm [wt%]
A(1)	1.38	1.97	23.18	26.53	73.47	0
A(2)	2.69	3.24	35.76	41.69	58.31	0
A(3)	2.22	3.08	17.21	22.51	67.24	10.24
A(4)	2.62	3.41	25.48	31.51	68.50	0
A(5)	2.23	2.63	15.14	20.00	63.66	16.34
A(6)	3.50	4.77	40.46	48.73	51.26	0
A(geo)	1.65	2.71	28.12	32.48	67.52	0
B(1)	5.91	9.47	50.53	65.91	34.09	0
B(2)	3.43	4.09	33.35	40.87	59.13	0
C(1)	11.90	12.83	47.97	72.7	27.30	0
C(2)	6.00	4.16	19.38	29.54	46.89	23.58
D(1)	0.49	0.36	3.09	3.94	2.77	93.29
D(2)	0.73	0.77	3.78	4.59	6.47	88.26
D(3)	0.97	0.96	4.66	6.59	10.26	83.16
D(4)	0.91	0.75	4.68	6.34	14.38	79.28
D(5)	0.71	0.74	4.28	5.73	10.73	83.54
D(geo)	0.31	0.26	0.56	1.13	7.23	91.64
E(1)	1.60	1.03	9.23	11.86	62.49	25.66

E(2)	2.08	0.95	6.32	9.35	41.36	49.29
F(1)	6.12	10.03	57.36	73.51	26.49	0
F(2)	5.76	8.74	39.84	54.34	22.71	22.95
F(3)	5.97	9.72	59.91	75.6	24.39	0
F(4)	5.31	8.66	57.70	71.67	28.34	0
F(5)	6.75	12.76	64.50	84.01	16.00	0
F(6)	8.83	15.77	59.74	84.34	15.66	0
F(geo)	9.15	10.81	41.29	61.25	38.75	0
G(1)	3.37	2.36	8.84	14.57	27.28	58.14
G(2)	6.35	10.41	55.83	72.59	27.41	0
G(3)	4.89	6.60	51.15	62.64	37.36	0
G(R1a)	3.14	4.80	45.54	53.48	46.52	0
G(R1b)	4.82	5.53	52.52	62.87	37.13	0
G(R1-2)	5.58	6.48	49.35	61.41	38.59	0
G(R2a)	2.55	2.33	9.55	14.43	35.37	50.20
G(R2b)	1.23	0.97	4.42	6.62	38.00	55.39
G(R2-3)	1.42	1.40	10.95	13.77	53.91	32.32
G(R3a)	1.80	1.51	12.94	16.25	48.89	34.87
H(1)	3.27	6.35	48.39	58.01	41.99	0
H(2)	4.18	8.06	72.48	84.72	15.27	0
H(3)	11.0	3.77	5.25	20.02	29.43	50.55
I(1)	2.56	1.39	6.08	10.03	30.92	59.06
I(2)	2.36	3.35	45.52	51.23	48.77	0
I(3)	1.73	1.63	14.25	17.61	35.67	46.72
J(geo)	2.98	2.09	13.01	18.08	41.05	40.79

Based on the size fraction a cumulative representation was constructed for the four main quartz types. It can be seen in Figure 86. In general, the difference between the quartz types are larger than the differences within the parallels for one type. Quartz type D had a low amount of fines after shock heating, and hence have a higher thermal strength than the other types. For quartz type G the largest internal variation is observed for the types tested. This is further investigated in 5.1.2. Quartz type F is the type showing the highest amount of fines after shock heating. For a simpler overview of all the different quartz types, the amount of fines below 10 mm has been

added and presented as a bar chart in Figure 87. Here it is also clear that there are variations between the quartz types that are in general larger than the differences between the parallels. From this figure it can be seen that quartz type D and E produce a considerably lower amount of fines below 10 mm. It is also clear from Figure 87 that quartz type F produces the largest amount of fines during shock heating.

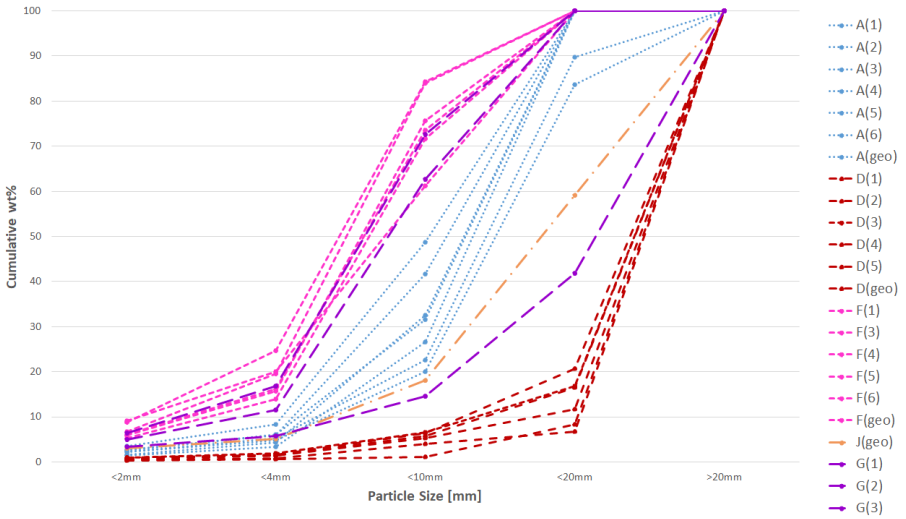

Figure 86: Cumulative representation of the wt% fractions from shock heating of different quartz samples to 1500 °C.

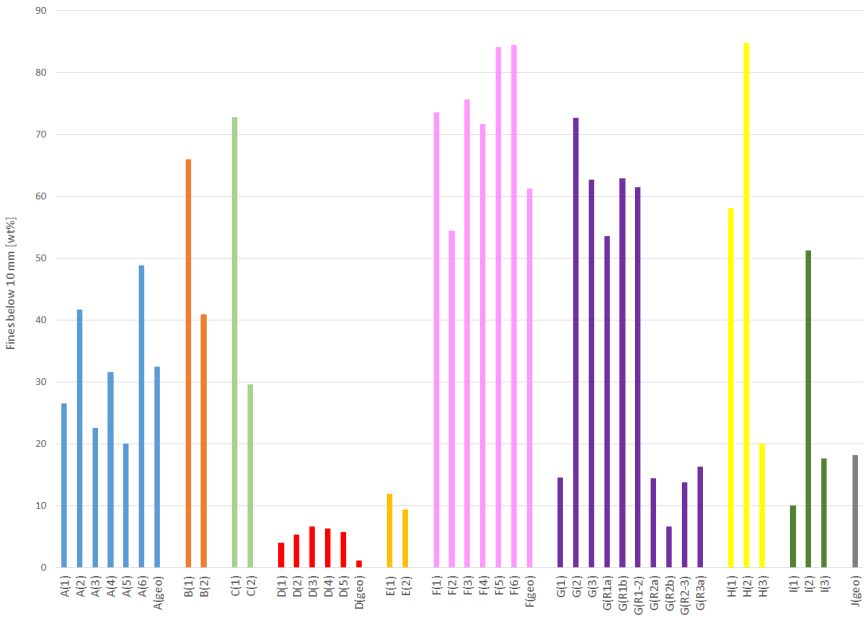

Figure 87: The amount of fines below 10 mm after shock heating different quartz types to 1500 °C. Each letter is one quartz type, and the number indicated parallel number.

The following figures, Figure 88 to Figure 96 shows each sample after sieving at 2, 4, 10 and 20 mm. From these figures, it is also clear that the amount of fines produced for each quartz type vary a lot.

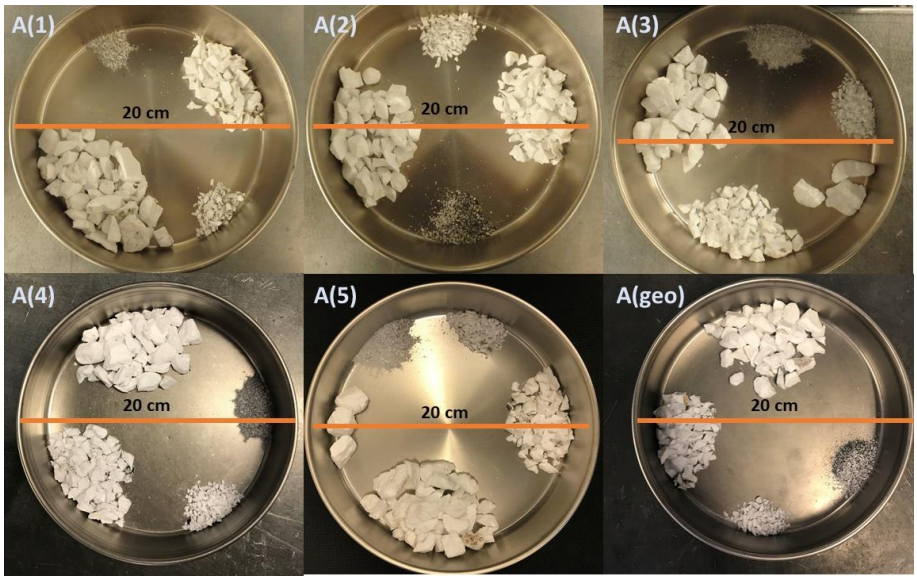

Figure 88: Sample A(1), A(2), A(3), A(4), A(5) and A(geo) after shock heating at 1500 °C and sieving.

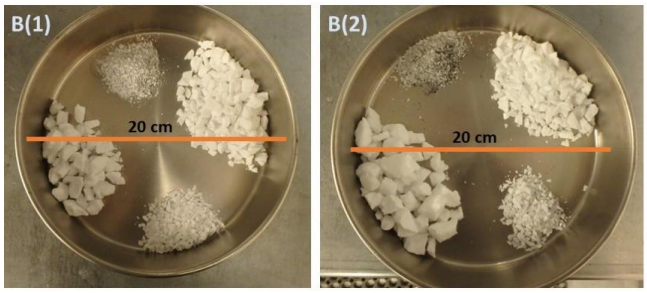

Figure 89: Sample B(1) and B(2) after shock heating at 1500 °C and sieving.

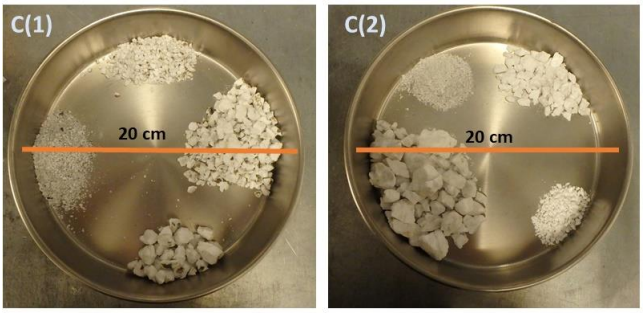

Figure 90: Sample C(1) and C(2) after shock heating at 1500 °C and sieving.

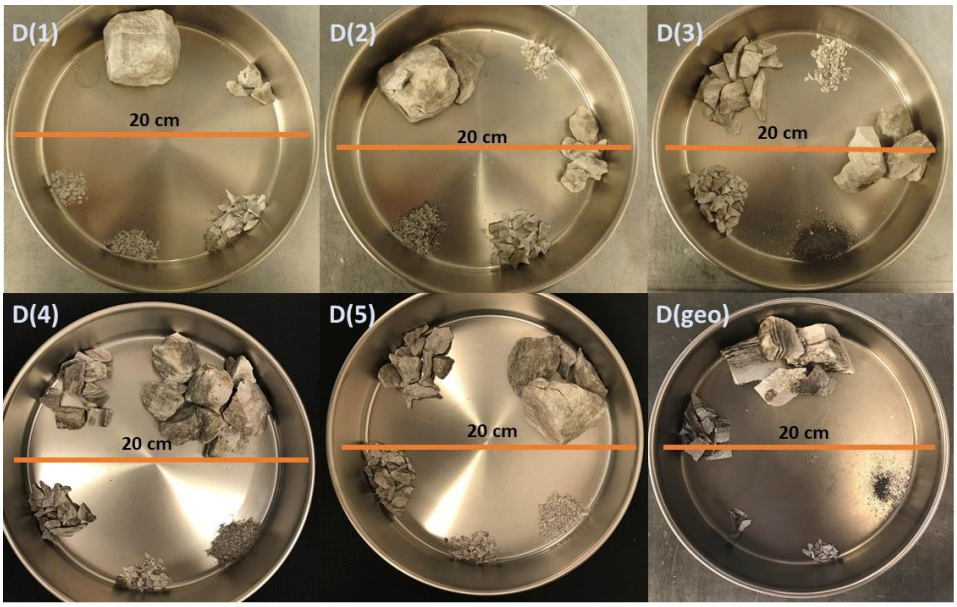

Figure 91: Sample D(1), D(2), D(3), D(4), D(5) and D(geo) after shock heating at 1500 °C and sieving.

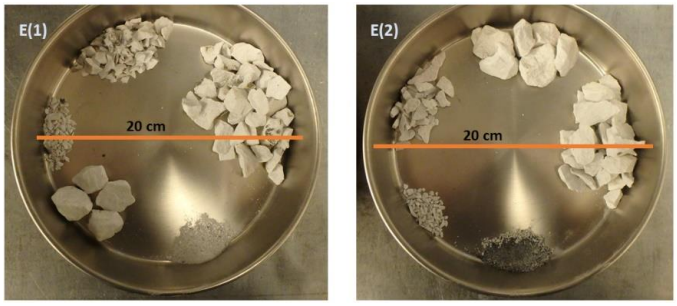

Figure 92: Sample E(1) and E(2) after shock heating at 1500 °C and sieving.

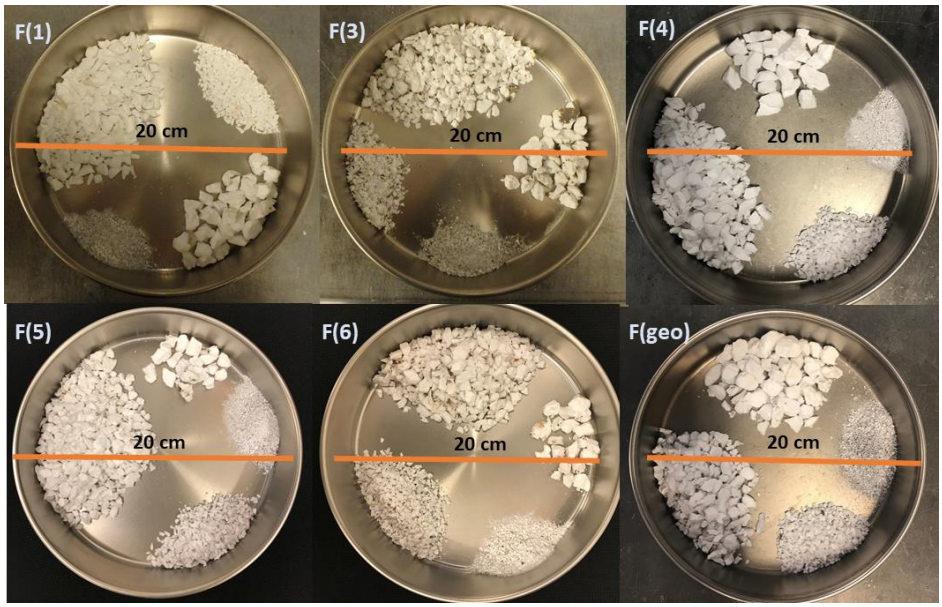

Figure 93: Sample F(1), F(3), F(4), F(5), F(6) and F(geo) after shock heating at 1500 °C and sieving.

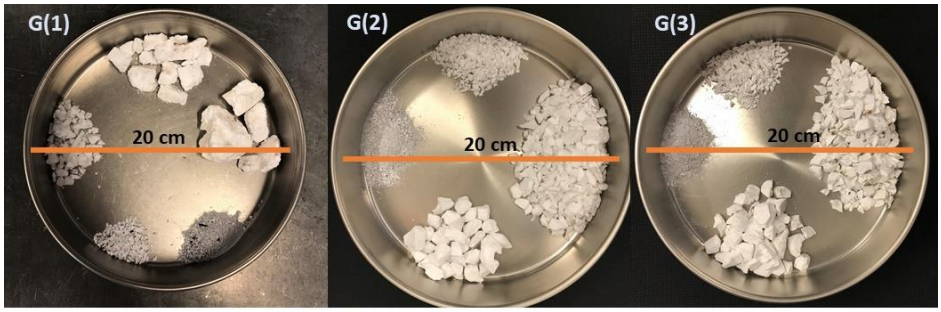

Figure 94: Quartz sample G(1), G(2) and G(3) after shock heating at 1500 °C and sieving.

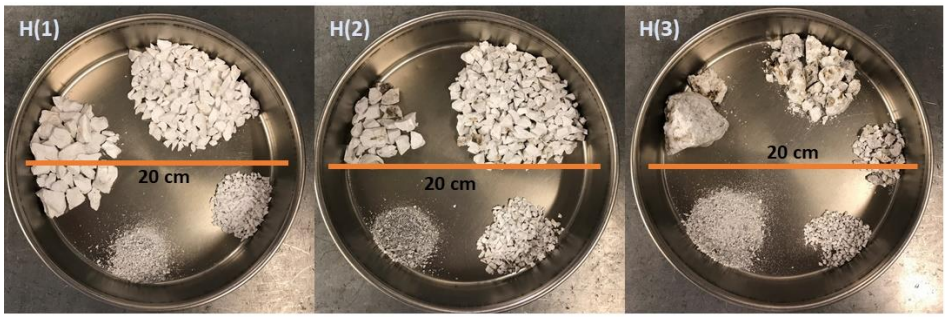

Figure 95: Quartz sample H(1), H(2) and H(3) after shock heating at 1500 °C and sieving

Figure 96: Quartz sample I(1), I(2) and I(3) after shock heating at 1500 °C and sieving.

5.1.2 Amount of fines in different regimes in quartz type G

A large internal difference was observed for quartz type G. Since the quartz type has different geological regimes, seven samples were the regime was identified before heating were selected. Three regimes were identified, and the major difference was that samples from regime 1 had much larger grains than samples from regime 2 and 3. Regime 1 also had more fluid inclusions than regime 2 and 3. The number after the letter G tells which regime the samples belongs to, e.g. sample G_R1b is type G, regime 1, parallel b. In the following Figure 97, Figure 98, and Figure 99 the samples from quartz type G with identified regime can be seen. They are sieved at 2, 4, 10 and 20 mm. A clear difference is seen between the samples from regime 1 and the samples from regime 2 in Figure 97 and Figure 98 respectively. The samples from regime 1 has a higher ability to disintegrate then the samples from regime 2 and 3. In Figure 100 the results are plotted in a graph, and also here the same trend can be seen. The purple dotted lines are the first three experiments which led to further investigation of the a large internal variation observed. When plotting the results from the different regime samples, it divides the graph into two sections. Samples from regime 1 disintegrates more than samples from regime 2 and 3. This explains the internal variation observed for the initial three experiments G(1), G(2) and G(3). The results indicate that samples with larger grains disintegrate more than smaller grains.

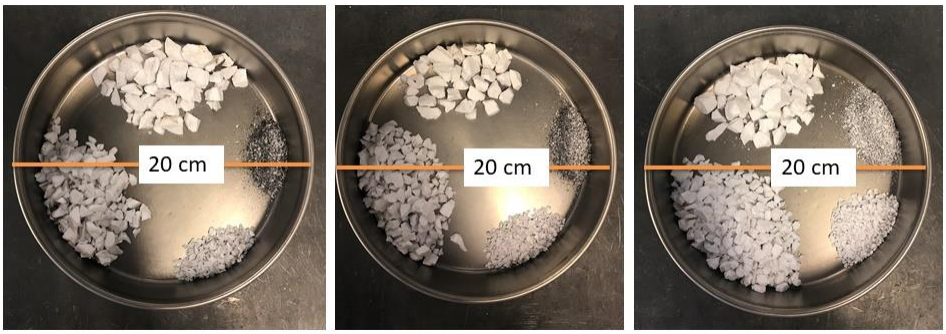

Figure 97: Samples from regime 1 and 1-2 of quartz type G post shock heating.

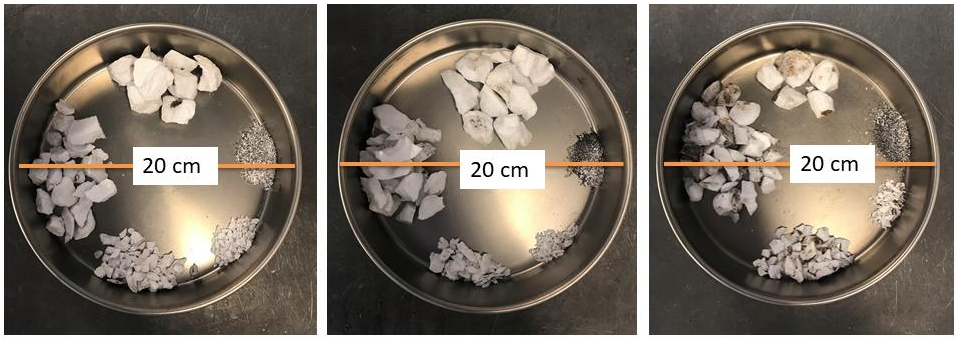

Figure 98: Samples from regime 2 and 2-3 of quartz type G post shock heating.

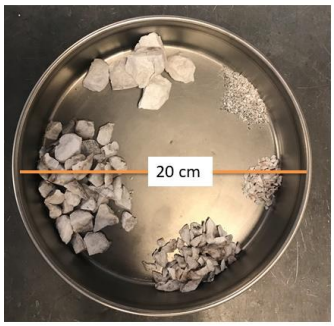

Figure 99: Sample from regime 3 of quartz type G post shock heating

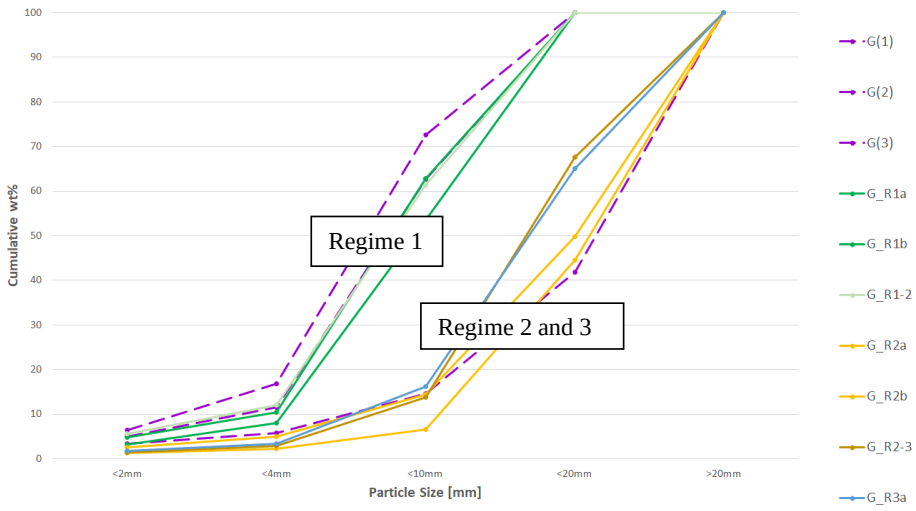

Figure 100: Cumulative wt% of different samples from different regimes of quartz type G shock heated to 1500 °C. The samples were the regime is identified before heating are labeled with an R and the regime number. The samples G(1), G(2) and G(3) were initial experiments with large internal variation leading to deeper investigations of the regimes.

5.1.3 Amount of fines and chemical compositions

For some selected fraction from the shock heating experiments, a chemical analysis identical to the analysis of the original material, was performed. In the table below, Table 16, the chemical analysis from each fraction post shock heating and the original chemical composition of the bulk sample are shown. Not all size fractions could be analyzed due to lack of material in the different size fractions. 50 g was needed to do the analysis, and all size fraction did not have this amount of material. In Figure 101 to Figure 104 the amount of impurities in the different size fractions are seen for type A, D, F and G respectively. The overall trend is that the size fractions below 20 mm contains more of the impurities than the rest of the bulk. There are some deviations from the trend but for type A, D and G almost all the impurities analyzed were larger in the small size fractions than in the bulk. For type F this is the case for certain impurities. In type D, only pieces above 20 mm were available for analysis, and these pieces had mostly a lower impurity content than the bulk. This means that the smaller size fraction must have a content above the bulk content. The uncertainty of the measurements must be taken into consideration when dealing with such small amounts.

Table 16: Impurity analysis for the different size fractions obtained after shock heating of four different quartz types. The analysis is performed by Erimsa. All the numbers are given in wt% if not ppm is indicated.

Quartz type	Al_2O_3 [wt%]	Fe_2O_3 [wt%]	TiO_2 [ppm]	CaO [wt%]	Na_2O [wt%]	K_2O [wt%]	MgO [wt%]	MnO [ppm]	P_2O_5 [ppm]
D-CT2 > 20 mm	0.3077	0.2913	175.2	0.0027	0.0081	0.0441	0.0035	2.781	<2.6
D bulk	0.492	0.3493	243.3	0.0046	0.0037	0.0754	0.007	<0.1	58.7
F-CT2 4-10 mm	0.0216	0.0057	5.71	0.0034	0.0056	0.0044	0.0009	28.30	<2.6
F-CT3 4-10 mm	0.0282	0.0068	4.129	0.0090	0.0102	0.0018	0.0009	32.713	<2.6
F bulk	0.017	0.003	6.8	0.001	0.007	0.005	0.001	1.5	<2.6
A-CT1 4-10 mm	0.1205	0.0037	53.5968	0.1163	0.0023	0.0019	0.0035	1.0257	<2.6
A-CT1 10-20 mm	0.0319	0.0039	16.9946	0.0217	0.0017	0.002	0.0012	0.3408	<2.6
A bulk	0.02	0.0029	7.0	0.0004	0.0013	0.0028	0.0014	0.3	<2.6
G-CT1 10-20 mm	0.0210	0.0101	9.3754	0.0036	0.0026	0.0025	0.0021	0.2608	<2.6

G-CT1 > 20 mm	0.0151	0.0054	7.1138	0.0025	0.0039	0.0019	0.0009	<0.1	<2.6
G bulk	0.015	0.0035	6.3	0.0044	0.0028	0.0016	0.0012	0.3	<2.6

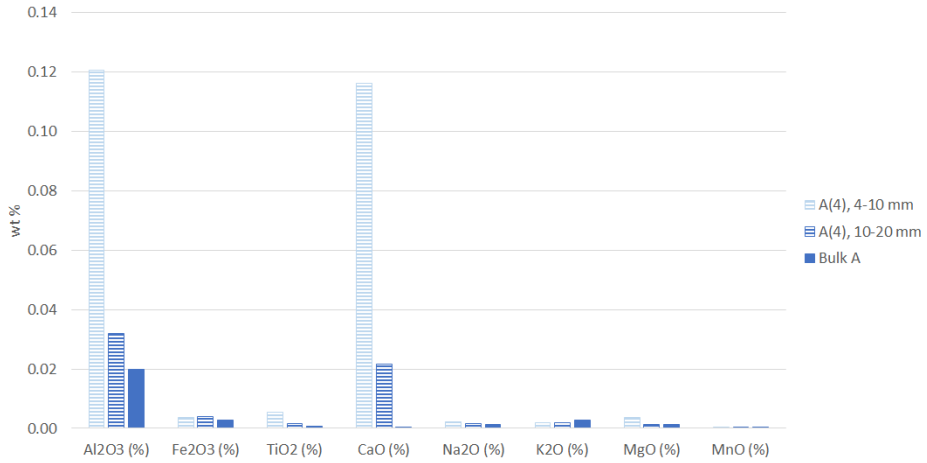

Figure 101: Chemical composition for different size fraction obtained after shock heating of quartz type A. The bulk analysis is also included for comparison.

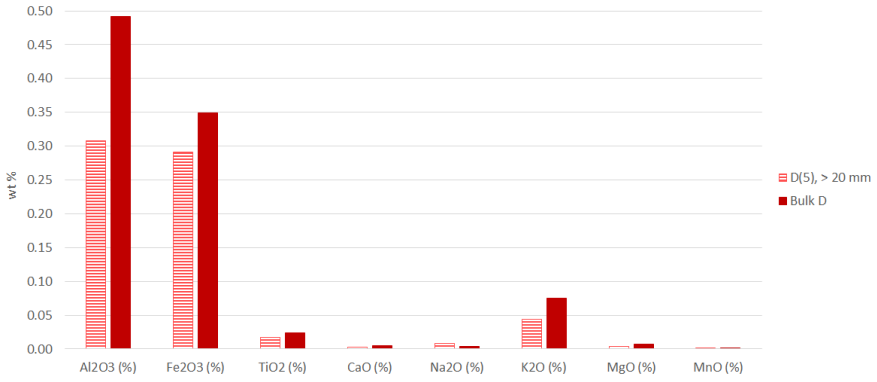

Figure 102: Chemical composition for different size fraction obtained after shock heating of quartz type D. The bulk analysis is also included for comparison.

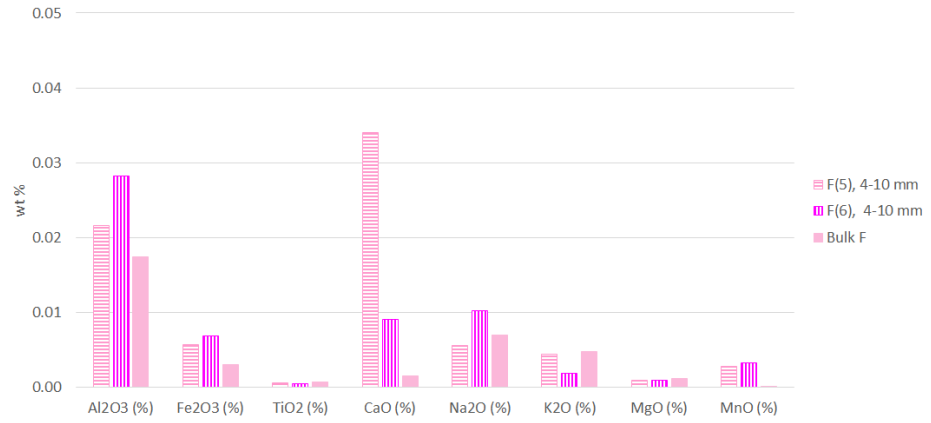

Figure 103: Chemical composition for different size fraction obtained after shock heating of quartz type F. The bulk analysis is also included for comparison.

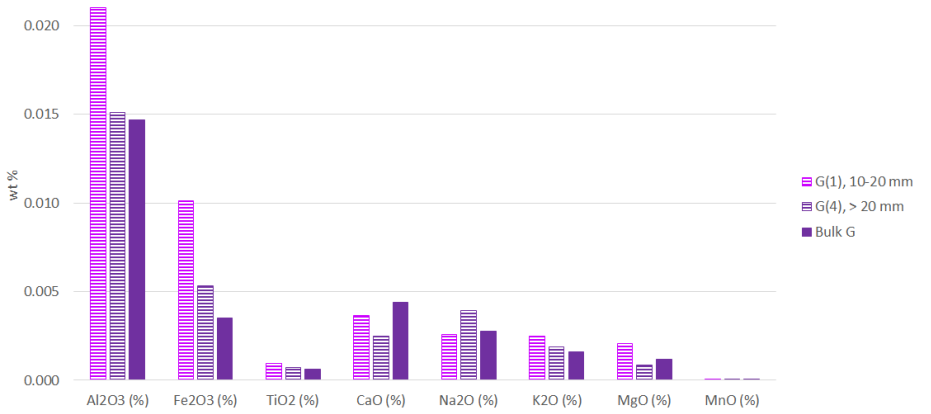

Figure 104: Chemical composition for different size fraction obtained after shock heating of quartz type G. The bulk analysis is also included for comparison.

5.1.4 Phase composition in shock heated quartz

The phase composition in the different size fractions after the shock heating were measured by X-ray diffraction. This was done in order to investigate if the smaller particles had more cristobalite and amorphous phase than the larger particles, and hence if there were a correlation in the phase composition and the ability to disintegrate. All quartz types contained between 12 and 32 % amorphous material after shock heating. The amount of cristobalite varied from 0 to 19 %. No clear trend of the different phases could be seen when comparing the different size groups.

When comparing the different types of quartz and amount of phases, some difference is observed. Type D has the largest amount of transformed quartz (amorphous + cristobalite), around 40 % for all samples. This can be seen in Figure 105. Quartz type A, H and I have the least amount of transformed quartz, around 20 %, while type G and F has approximately the same amount of transformed quartz around 30-40 %. The variation between the quartz types is not very large, and does not seem to explain the large difference observed in disintegration upon shock heating.

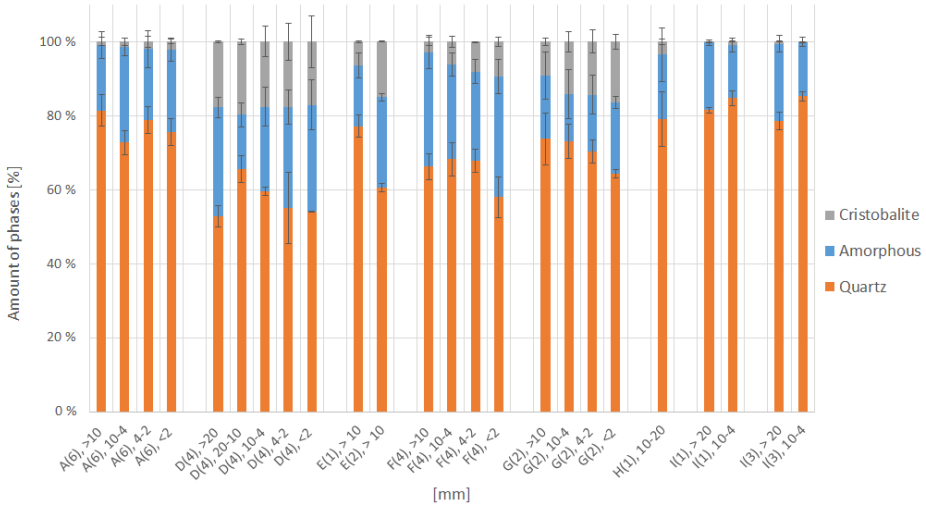

Figure 105: Amount of phases in different quartz types after shock heating at 1500 °C.

5.1.5 CT investigations pre-heating

Some of the quartz samples were investigated with X-ray computed tomography (CT) before heating, to determine if preexisting cracks in the quartz could be correlated with the disintegration. This method allows for non-destructive analysis of the interior of a sample. In Figure 106, Figure 107, Figure 108, and Figure 109 CT images from sample A, D, F and G respectively can be seen. Cracks were observed in all the sample, but in various amount and in different size. Some of the cracks are easily seen in the images below, while some are not visible without magnification in the software ImageJ. The thickness of the cracks also varied from 0.05 mm to 0.2 mm. Cavities were also observed for some of the samples. These were up to 2 mm in width. Each sample gave more than thousand images.

In Figure 106 CT images from type A is seen. The general observation for this quartz type were few cracks. Sample A(4) was very homogeneous, while sample A(5) and A(6) showed more cracks towards one end. One to two cavities were observed in the image series for sample A(4) and A(5).

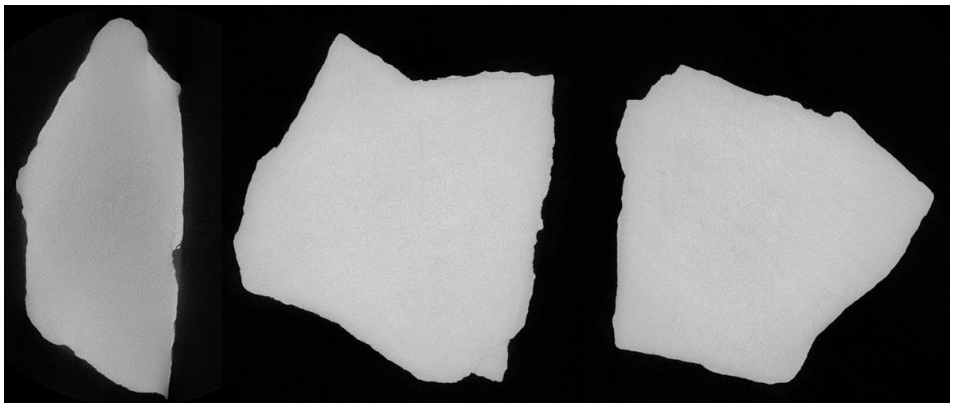

Figure 106: CT images from quartz sample A(4) (left), A(5) (middle) and A(6) (right).

Two samples from type D were analyzed, and two of the images can be seen in Figure 107. The general observations for type D were few cracks, but more than in type A. Some white small dots were also observed, and areas with porous material. The cracks in sample D(5) were clearer than in D(4).

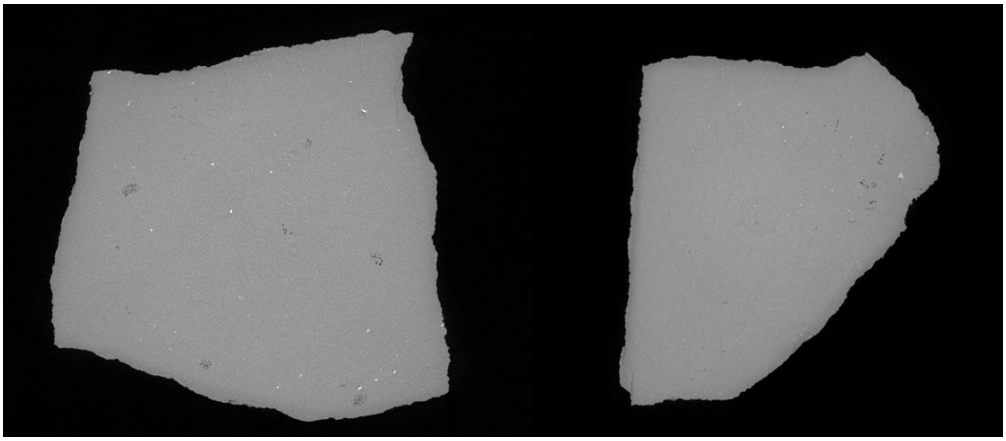

Figure 107: CT images from quartz sample D(4) (left) and D(5) (right).

In Figure 108, CT-images from type F can be seen. Type F had more cracks than type A and D. The cracks were also slightly thicker in this type. Small black cavities were also observed, also with crossing cracks. Some white areas were observed in sample F(5). This is believed to be impurities with a different density than quartz.

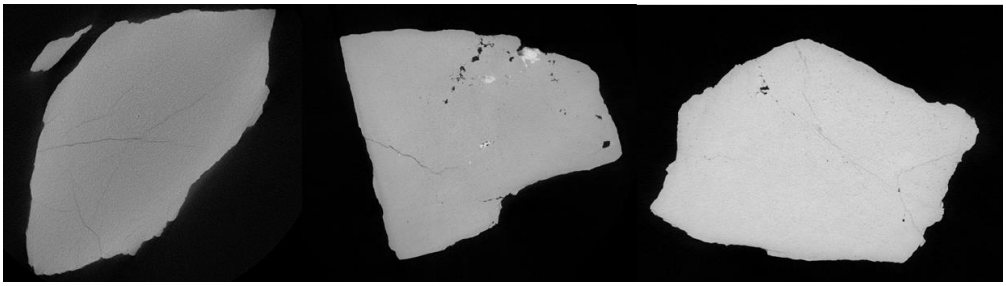

Figure 108: CT images from quartz sample F(4) (left), F(5) (middle) and F(6) (right).

CT-images from type G can be seen in Figure 109. The general observations were cracks with cavities along. Some of these cavities were elongated. Sample G(1) had many faded cracks which were not observed to the same extent in sample G(2) or G(3). Sample G(3) had some areas with a different grey tone.

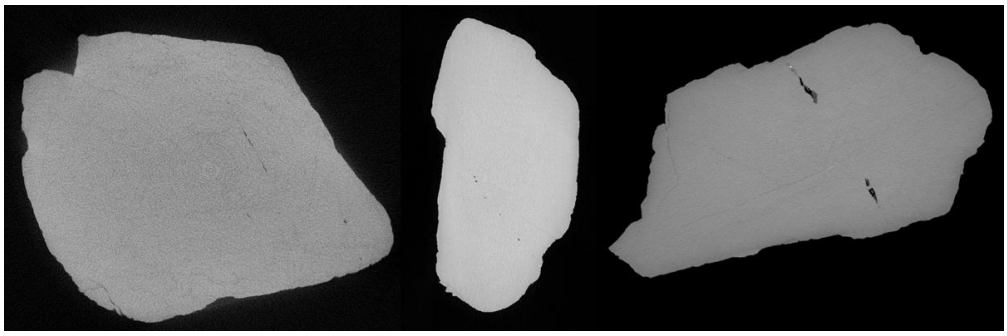

Figure 109: CT images from quartz sample G(1) (left), G(2)(middle) and G(3) (right).

Twenty images were selected from each quartz type. For all the selected images, the total area, the crack length and the average crack thickness were measured and recorded. The average crack area was calculated, and is given in Table 17. There is some variation within the same quartz type, but in general quartz type F seems to have the largest crack area, while quartz type A and D has the lowest. For quartz type G a very large internal variation is observed, but the sample G(1) is believed to be from regime 2, while sample 2 and 3 are believed to be from regime 1. This assumption is based on similar results from shock heating from other samples from regime 1 and 2. This was previously shown in section 5.1.2.

Table 17: The crack area for each quartz sample measured from 20 CT images.

Sample	**% crack**	**wt% fines < 10 mm**
A(4)	0.14	31.5
A(5)	0.26	20.0
A(6)	0.18	48.7
D(4)	0.18	6.3
D(5)	0.26	5.7
F(4)	1.29	71.7
F(5)	0.56	84.0
F(6)	1.23	84.3
G(1)	1.13	14.6
G(2)	0.30	72.6
G(3)	0.47	62.6

5.2 Phase composition

In total ninety-eight experiments with different combinations of variables were performed. The parameters varied were the quartz type, the temperature, holding time and size. For each experiment, three XRD measurements were done in order to obtain a larger certainty of the experiments, and to calculate sample variance. All samples were heated in a Nabertherm L04/08 furnace. General observations and summary of the phases found in the four main quartzes are

given in Table 18. In Figure 110 to Figure 113 an example of a sample of the quartz types before and after heating is shown.

Table 18: General observations after heating of 4 different quartz types.

Quartz type	**General observations**
Type A	In one piece after heated, but mechanically weaker.
Type F	Fractured after heating, if not, easily crumbled under light pressure.
Type G	Weaker than the A type, but not as weak as F type. Some samples fractures during heating.
Type D	In one piece after heating, but weaker.

Figure 110: Sample A11 before (left) and after (right) heating to 1700 °C and held for 60 minutes. The sample were 10.8 g, and 2-3 cm in size.

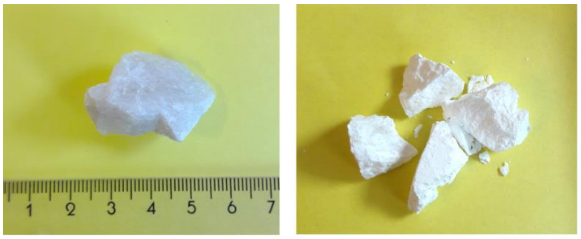

Figure 111: Sample F2 before (left) and after (right) heating 1600 °C and held for 120 minutes. The sample was 9.7 g and 2-3 cm in size.

Figure 112: Sample G3 before (left) and after (right) heating to 1700 °C and held for 0 minutes. The sample were 11.0 g, and 2-3 cm in size.

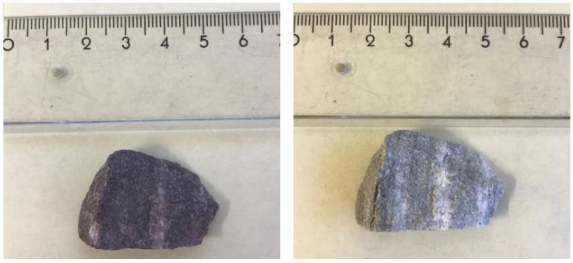

Figure 113: Sample D9 before (left) and after (right) heating to 1600 °C and held for 45 minutes. The sample were 10.8 g.

Topas software was used to determine the phase composition of quartz, amorphous phase and cristobalite. The three XRD measurements done for each sample showed that the sample variation on average were 2-3 % for all the three phases quartz, cristobalite and amorphous. Some clear outliers are left out of this calculation. These are either a natural outlier, or an incorrect measurement by the instrument. This could happen if the surface of the sample is not homogeneous or if the fitting of the data clearly is insufficient. The amount of amorphous phase is calculated based on the known amount of quartz, cristobalite and spike in each sample. An example of how a XRD spectra and the fitted calculated curve for a sample, is seen in Figure 114. This is sample A10 and contain 20 % amorphous phase, 47 % cristobalite and 33 % quartz.

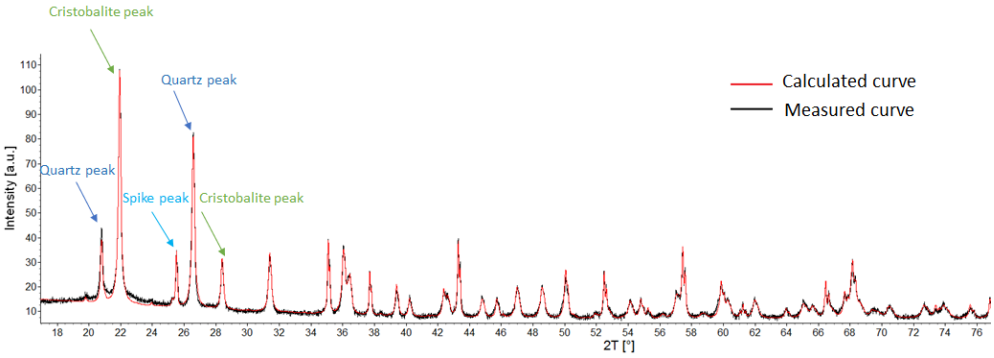

Figure 114: A XRD diffractogram for sample A10 that contains quartz, cristobalite and amorphous phase. The red line indicates how a sample containing quartz, cristobalite and spike should look like ideally.

5.2.1 Phase transformation and modelling

The general trend for the phase composition was that the amount of quartz decreases as the holding time at maximum temperature increased. This were seen for all the quartz types, but in various amounts. In Figure 115 to Figure 119 the phase composition of type A, D, F and G respectively can be seen for samples heated to 1600 °C and 1700 °C, and with size 10 and 100 g The dots, squares and triangles represents the measured amount of phases, while the dotted lines are the model of the amount of phases. For some experiments several parallels were done to check the repeatability of the experiments. It can be seen from Table 13 which experiments have been performed additional times. In Figure 115 to Figure 119, the parallel experiments can be seen as several dots at one time value. An example is in Figure 115a, where the experiment at 0 minutes has been done three times. It only looks like two, because two of the experiments showed 100 % quartz, and 0 % amorphous phase and cristobalite. The repeated experiments showed some

variation, but not more than seen between the different holding times and between the different types. Some experiments deviate from the trend. These are not taken into account of the amount of phase models later, and are marked with a red circle. Since the quartz is a natural raw material some variation is expected and unavoidable.

It can be seen for type A in Figure 115 a, b, c and d that the concentration of quartz at 0 minutes is approximately 90 and 65 wt% for the 10 g and 100 g samples heated to 1600 °C, and around 70 wt % for the samples heated to 1700 °C. The large difference at 1600 °C is believed to be because of internal variation in the quartz. The main trend for all the quartz types is similar: the wt% of quartz is higher at 1600 °C than 1700 °C. This is expected due to an increase in temperature and hence an increase in phase transformation rate. There are large variations between the different types though. If type A are considered the quartz concentration at 0 minutes are 90 wt% and 65 wt% for 10 g samples heated to 1600 °C and 1700 °C respectively, seen in Figure 115a and b. In Figure 118a and b, type F has 0 wt% and 15 wt % quartz for 10 g samples at 1600 °C and 1700 °C respectively. This shows that type F has a higher ability to transform to amorphous phase and cristobalite than type A. These are the two outermost types, hence the ability for type D and G to transform is lying in between. For type D the concentration of quartz is 55 wt% and 5 wt% for 10 g at 1600 °C and 1700 °C respectively. Type G has 20 wt% and 0 wt % quartz for the 10 g samples heated to 1600 °C and 1700 °C respectively. The ability to transform in increased order is A, D, G, F.

When comparing the difference in phase composition for the 10 g and 100 g samples no clear trend is seen. For type A, a faster transformation is seen for the 100 g samples at 1600 °C. At 1700 °C there is little difference between the 10 g and 100 g samples. In type F, the opposite is seen. At 1600 °C the samples at 100 g transformed slower than the 10 g samples, and at 1700 °C the difference is small. For type G, the 10 g samples transform faster than the 100 g samples. It does not seem that samples between 10 g and 100 g have a consistent effect on the amount of phases created in types upon heating to 1600 °C and 1700 °C. 100 g samples were not tested for type D, due to no clear trend in the other three types.

For type A, 1600 °C, 100 g samples in Figure 115c the results seem to be at two levels. In the model presented in Figure 115c, the experiments with higher cristobalite content at 0, 15 and 30 minutes were view as outliers because if compared to the 10 g samples, the cristobalite content is quite low at these two holding times. However, it is also possible that the samples showing high cristobalite content for the 100 g experiments are the most correct. This could be an effect of the grain size, fluid inclusions, degree of recrystallization etc. varying in different parts of type A. Therefore, an alternative model could be made for type A, 1600 °C, 100 g were the discarded experiments at 0, 15 and 30 minutes are used in addition to the phase composition at 0 minutes. The alternative model is seen in Figure 116, and hence give a different reaction rate and activation energy for the phase transformation. The alternative reaction rate and activation energy are given in Table 19 and Table 20 respectively.

The model for type G, 1600 °C, 100 g could also have an alternative model. It is given in Figure 120. Instead of discarding the experiments at 30 minutes as done in Figure 119c, the experiments at 15, 45 and 60 minutes are discarded. The alternative model has an alternative k_1 and k_2 and activation energy given in Table 19 and Table 20. The reason for differences in the amount of phases for type G, could be related to the different regimes in type G, and hence different texture in the sample.

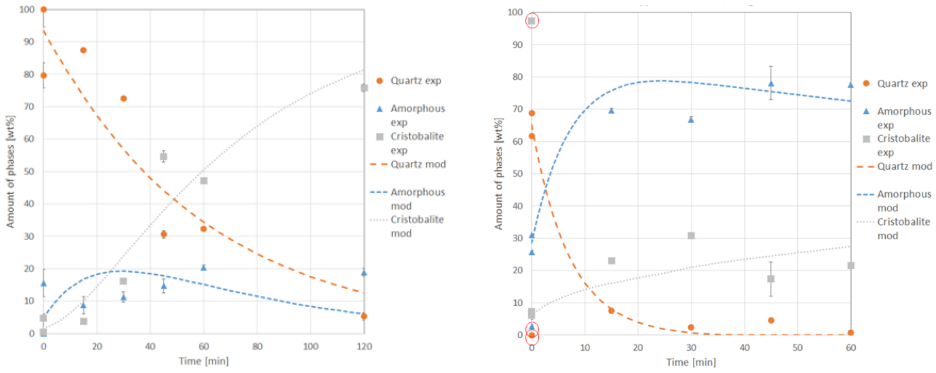

a) Quartz type A, 1600 °C, 10 g

b) Quartz type A, 1700 °C, 10 g

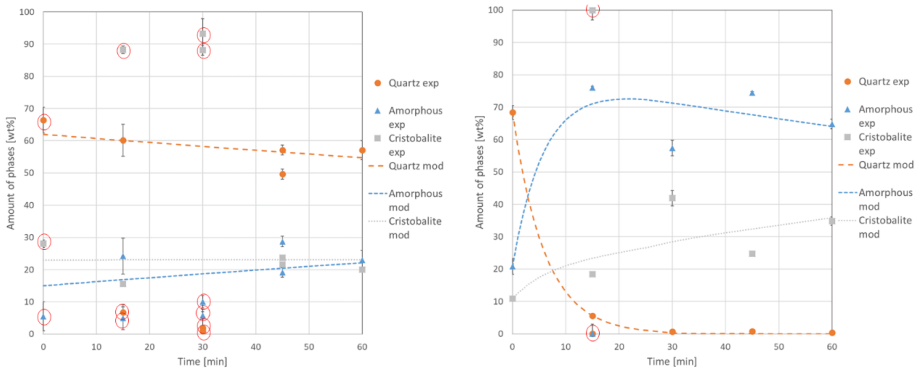

c) Quartz type A, 1600 °C, 100 g

d) Quartz type A, 1700 °C, 100 g

Figure 115: The phase composition for quartz type A for samples of 10 g and 100 g heated to 1600 °C and 1700 °C with a varying holding time from 0 up to 120 minutes at maximum temperature. The dots, squares and triangles are experimental values, while the dotted lines represent the modeled phase composition at various times. Outliers are marked with a red circle.

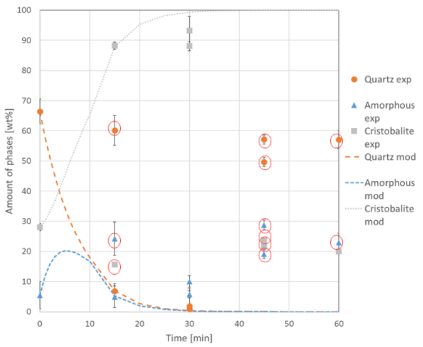

Figure 116: The amount of phases of quartz type A, 1600 °C, 100 g but with an alternative model for the phase transformations. The dots, squares and triangles are experimental values, while the dotted lines represent the modeled phase composition at various times. Outliers are marked with a red circle.

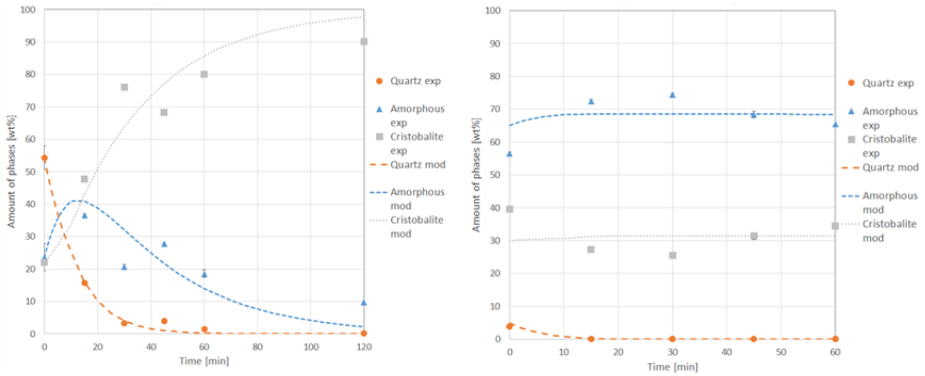

a) Quartz type D, 1600 °C, 10 g *b) Quartz type D, 1700 °C, 10 g*

Figure 117: The phase composition for quartz type D for samples of 10 g heated to 1600 °C and 1700 °C with a varying holding time from 0 up to 120 minutes at maximum temperature. The dots, squares and triangles are experimental values, while the dotted lines represent the modeled phase composition at various times.

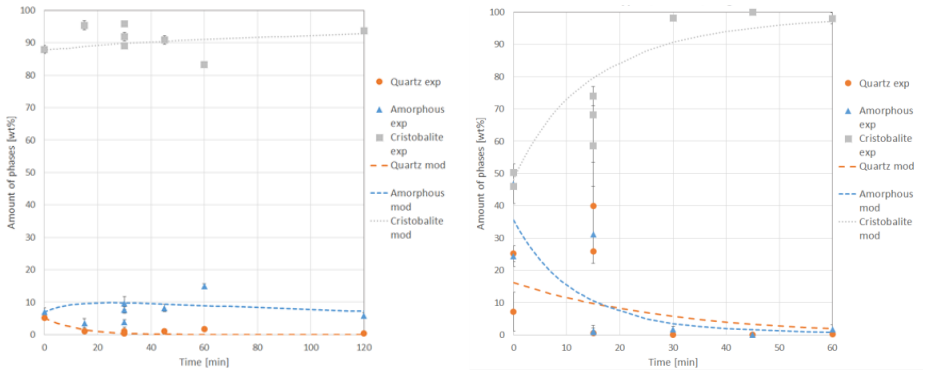

a) *Quartz type F, 1600 °C, 10 g*

b) *Quartz type F, 1700 °C, 10 g*

c) *Quartz type F, 1600 °C, 100 g*

d) *Quartz type F, 1700 °C, 100 g*

Figure 118: The phase composition for quartz type F for samples of 10 g and 100 g heated to 1600 °C and 1700 °C with a varying holding time from 0 up to 120 minutes at maximum temperature. The dots, squares and triangles are experimental values, while the dotted lines represent the modeled phase composition at various times.

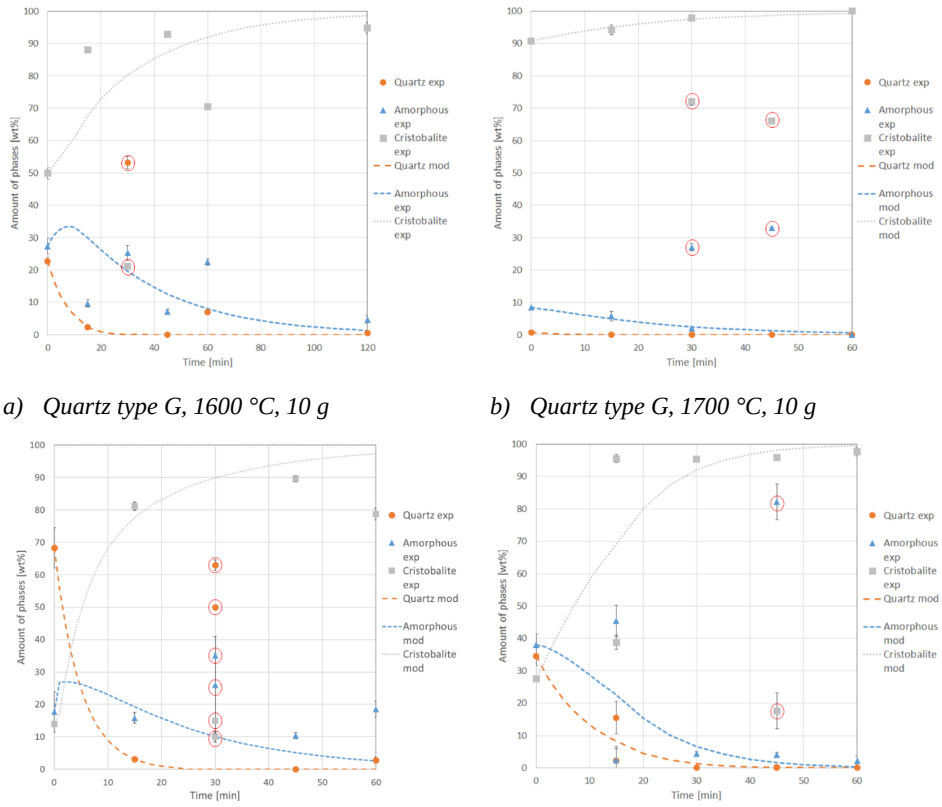

a) *Quartz type G, 1600 °C, 10 g*

b) *Quartz type G, 1700 °C, 10 g*

c) *Quartz type G, 1600 °C, 100 g*

d) *Quartz type G, 1700 °C, 100 g*

Figure 119: The phase composition for quartz type G for samples of 10 g and 100 g heated to 1600 °C and 1700 °C with a varying holding time from 0 up to 120 minutes at maximum temperature. The dots, squares and triangles are experimental values, while the dotted lines represent the modeled phase composition at various times. Outliers are marked with a red circle.

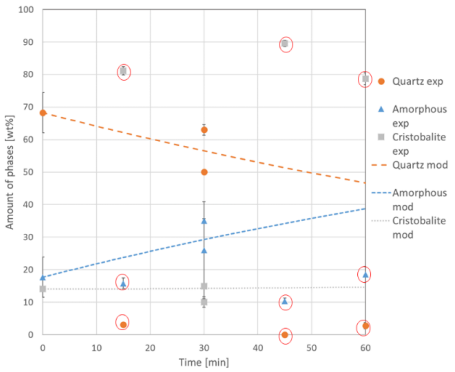

Figure 120: The amount of phases of quartz type G, 1600 °C, 100 g but with an alternative model for the phase transformations. The dots, squares and triangles are experimental values, while the dotted lines represent the modeled phase composition at various times. Outliers are marked with a red circle.

The model for the phase composition assumes a two step reaction, with two apparent rate constant k_1 and k_2 for the transformation from quartz to amorphous phase and from amorphous phase to cristobalite respectively, as seen in equation 5.1. The amorphous phase is considered as an intermediate phase, both being created and consumed at the same time. Both reaction are assumed to be first order, as Chaklader [80] also assumed, and the reaction rates can hence be described by equation 5.2, 5.3, and 5.4 for the change in concentration for quartz, amorphous phase and cristobalite respectively. Based on these expressions and a numerical method, the concentration after a time Δt can be calculated. The expressions for the phase concentration as a function of time can be seen in equation 5.5, 5.6, and 5.7 for quartz, amorphous phase and cristobalite respectively.

$$Quartz \xrightarrow{k1} Amorphous \xrightarrow{k2} Cristobalite \tag{5.1}$$

$$\frac{dQ}{dt} = -k_1[Q] \tag{5.2}$$

$$\frac{dA}{dt} = k_1[Q] - k_2[A] \tag{5.3}$$

$$\frac{dC}{dt} = k_2[A] \tag{5.4}$$

$$[Q]_{n+1} = [Q]_n - k_1[Q]_n \Delta t \tag{5.5}$$

$$[A]_{n+1} = [A]_n + k_1[Q]_{n+1} \Delta t - k_2[A]_n \Delta t \tag{5.6}$$

$$[C] = 100 - [Q] - [A] \tag{5.7}$$

The k_1 and k_2 values have been found by minimizing the difference between the measured and the calculated values. k_1 and k_2 are assumed to follow an Arrhenius relation given in 5.8. k_0 is the pre exponential factor, E is the activation energy for the transformation, T is the temperature in K and R is the gas constant. The k_1 values are given in Table 19, together with the sum of the squared difference between the measured and calculated value divided by the number of values used for the optimization. k_1 at 1600 °C is ranging from 0.002 min^{-1} to 0.184 min^{-1}, and at 1700 °C they are ranging from 0.033 min^{-1} to 0.363 min^{-1}. This means that the transformation from quartz to amorphous phase generally goes faster, which is expected with increasing temperature. The k_2 values also listed in Table 19, are in general lower than the k_1 value for the same experiment. This means that the transformation from quartz to amorphous phase goes faster than the transformation from amorphous phase to cristobalite. The deviation to experimental value for the k_2 values are in general higher than for k_1, and thus k_1 has a better fit to the experimental data than k_2.

$$k = k_0 e^{-\frac{E}{RT}} \qquad 5.8$$

The activation energy for the different types for the reaction from quartz to amorphous and amorphous to cristobalite is listed in Table 20. The activation energies are calculated from the plots in Figure 121 where ln k is plotted as a function of *1/T* for all the quartz types for both 10 g and 100 g samples. From Table 20 and Figure 121, it can be seen that some of the transformations have a negative activation energy. For the transformation from amorphous phase to cristobalite, the negative activation energy could mean that the amorphous phase is more stable at higher temperatures. This could indicate the starting of a melting phase, as silica melts at 1727 °C. The melted amorphous phase is not the same phase as the intermediate amorphous phase, but they cannot be distinguished by the XRD analyses. The negative activation energy for the quartz to amorphous phase for type F 10 g is believed to be negative due to unsuitable data to measure this. Since the measurements starts when the remaining quartz content is only 5 wt%, the transformation is almost finished. Therefore, to find the activation energy for the transformation from quartz to amorphous phase from these data are meaningless.

Type A has the highest activation energy for the transformation from quartz to amorphous phase, while F has the lowest, for 10 g samples. Compared to type A with an activation energy of 642 kJ/mol, type D and G has a considerably lower activation energy of 238 kJ/mol and 126 kJ/mol respectively. Based on the experiments for 10 g samples at 1600 °C the temperature dependence of the activation energy shows that type A needs a higher temperature for the transformation to start. The temperature dependence for the different quartz type in decreasing order are A, D, G and F. At 100 g samples, the order is A-F-G. Also, for 100 g the activation energy for quartz type A at 1317 kJ/mol are considerably higher than the activation energy for G and F at 371 kJ/mol and 510 kJ/mol respectively.

Table 19: k_1 and k_2 values for different quartz types, temperatures and sizes. The sum of the difference in measured and modelled squared value for each phase are also given in the table where x_m is the modelled value, x_e is the experimental value and n is the number of measurements used for the optimization.

Experiment series	k_1 [min^{-1}]	$\sum \frac{(x_m-x_e)^2}{n}$	k_2 [min^{-1}]	$\sum \frac{(x_m-x_e)^2}{n}$
A, 1600 °C, 10 g	0.016	*140*	0.046	*66*
A, 1600 °C, 100 g	0.002	*5*	4.54×10^{-5}	*22*
A, 1600 °C, 100 g, alt.mod.	0.123	*1*	0.188	*19*
A, 1700 °C, 10 g	0.130	*6*	0.003	*51*
A, 1700 °C, 100 g	0.153	*0*	0.004	*66*
D, 1600 °C, 10 g	0.073	*2*	0.029	*52*
D, 1700 °C, 10 g	0.159	*0*	4.54×10^{-5}	*15*
F, 1600 °C, 10 g	0.073	*1*	0.004	*12*
F, 1600 °C, 100 g	0.069	*40*	0.048	*36*
F, 1700 °C, 10 g	0.033	*46*	0.098	*1*
F, 1700 °C, 100 g	0.363	*0*	0.138	*7*
G, 1600 °C, 10 g	0.124	*13*	0.028	*174*
G, 1600 °C, 100 g	0.184	*3*	0.062	*98*
G, 1600 °C, 100 g, alt.mod	0.006	*0*	4.54×10^{-5}	*2*
G, 1700 °C, 10 g	0.187	*0*	0.039	*1*
G, 1700 °C, 100 g	0.091	*0*	0.082	*4*

Table 20: Activation energy for the different quartz types and the reaction quartz to amorphous phase, Q → A, and amorphous phase to cristobalite, A → C. The negative activation energies are written in italic, and are believed to be less reliable.

		10 g [kJ/mol]	100 g [kJ/mol]
Type A	Q→A	642	1317 (alt mod: 68)
	A→C	*-883*	1337 (alt mod: *-1223*)
Type D	Q→A	238	
	A→C	*-1983*	
Type F	Q→A	*-244*	510
	A→C	990	325
Type G	Q→A	126	*-217* (alt mod: 834)
	A→C	104	80 (alt mod: 2300)

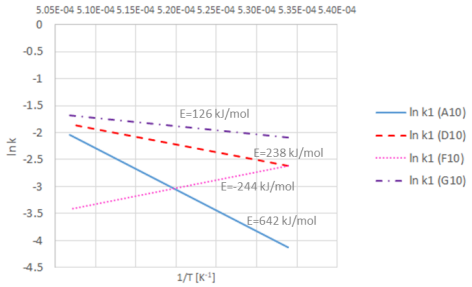

a) ln k_1 for 10 g samples for quartz type A, D, F and G.

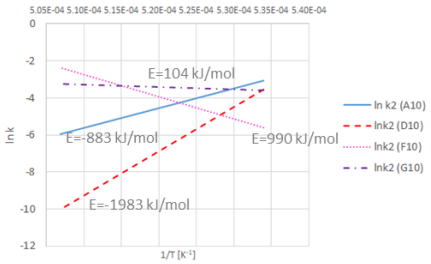

b) ln k_2 for 10 g samples for quartz type A, D, F and G.

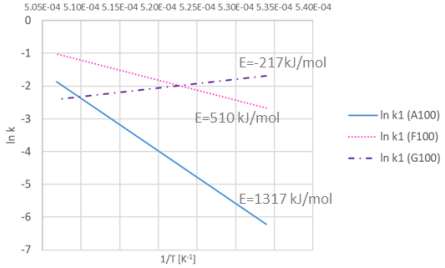

c) *ln k_1 for 100 g samples for quartz type A, F and G.*

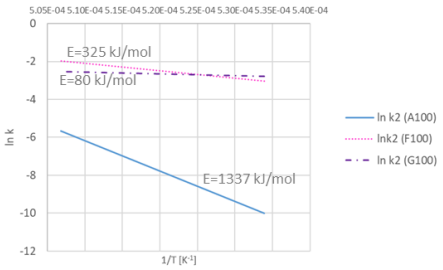

d) *ln k_2 for 100 g samples for quartz type A, F and G.*

Figure 121: Plots of ln k values for the transformation from quartz to amorphous phase (k_1) and from amorphous phase to cristobalite (k_2). Four different quartz types at 1600 °C and 1700 °C for 10 g and 100 g samples are seen.

To check if the first order model assumed were correct, additional experiments were done for type A at 1550 °C and 1650 °C. The experiments were with the same setup and with holding times at 0, 30 and 60 minutes. The results and model of the phase composition are given in Figure 122. The corresponding k_1 and k_2 values are given in Table 21.

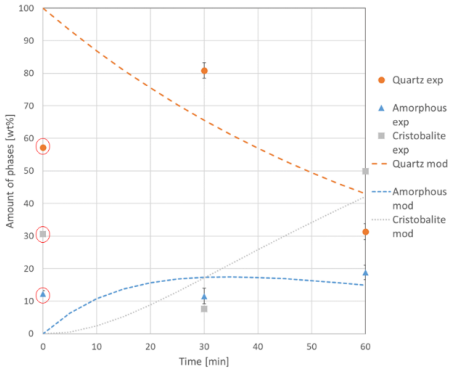

a) *Quartz type A, 1550 °C, 10 g*

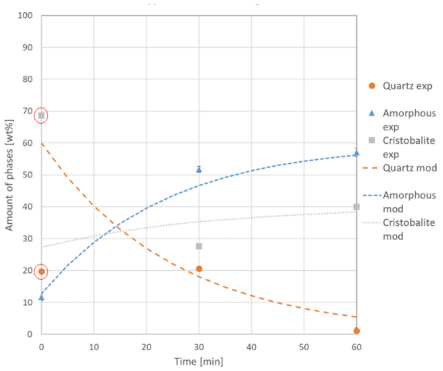

b) *Quartz type A, 1650 °C, 10 g*

Figure 122: The phase composition for quartz type A for samples of 10 g heated to 1550 °C and 1650 °C with a holding time of 0, 30 and 60 minutes. The dots, squares and triangles are experimental values, while the dotted lines represent the modeled phase composition at various times. Outliers are marked with a red circle.

Table 21: k_1 and k_2 values for extra experiments at 1550 °C and 1650 °C for type A. The sum of the difference in measured and modelled squared value for each phase are also given in the table where x_m is the modelled value, x_e is the experimental value, and n is the number of measurements used for the optimization.

Experiment series	k_1 [min^{-1}]	$\sum \frac{(x_m-x_e)^2}{n}$	k_2 [min^{-1}]	$\sum \frac{(x_m-x_e)^2}{n}$
A, 1550 °C, 10 g	0.014	*185*	0.047	*25*
A, 1650 °C, 100 g	0.034	*13*	0.0005	*14*

5.3 Fourier transformed infrared spectroscopy

In order to establish whether Fourier transformed infrared spectroscopy gave any differences in spectra for different quartz type, Type D and F in addition to the pure quartz type NC4A were tested in an initial experiment. As seen in Figure 123 a significant difference in the spectra for quartz type D and F were observed. It is likely that quartz type F is more similar to pure quartz since the spectra shows little difference. Based on this initial experiment, it is likely that quartz type D contains more water or OH-groups because of the broad band from 3000 cm^{-1} to 3600 cm^{-1} [45]. The peak at around 3625 cm^{-1} could indicate muscovite ($KAl_2(Si_3AlO_{10})(OH)_2$) in the sample [44].

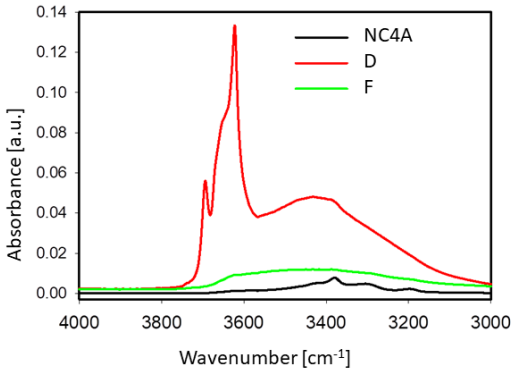

Figure 123: Spectrogram of quartz type D and F in addition to the pure quartz sample NC4A.

All the quartz types A to I were investigated with Fourier transformed infrared spectroscopy after the initial test. The spectrogram obtain from the analysis is shown in Figure 124. There are different intensities in the peaks at around 3400 cm^{-1}, 3625 cm^{-1} and 3700 cm^{-1}. Quartz type E and H have the highest intensity at the 3400 cm^{-1} peak, while quartz type D and E have the highest peak at 3625 cm^{-1}, and at 3700 cm^{-1} quartz type D and H have the highest intensities. The broad band from 3000 cm^{-1} to 3700 cm^{-1} indicates structural water in the form of H_2O, H^+ and OH^- [41]. Then Quartz type E, H and D are the types with the highest water content. To distinguish between water molecules and hydroxide ions one can look closer at the bending absorption at 5200 cm^{-1} which confirms H_2O molecule [42]. The near infrared area of the specter is shown in Figure 125. By looking at both figures it is possible to identify water molecules in both sample E and H, but the bending absorption at 5200 cm^{-1} is absent for quartz type D. The peaks at 3625 cm^{-1} for quartz type D and E could indicate the presence of muscovite ($KAl_2(Si_3AlO_{10})(OH)_2$) in the sample [44].

Quartz type B, F and A does not seem to contain either water, OH-groups or muscovite, while quartz type C, G, and I contain some but smaller amounts than Type D, E and H.

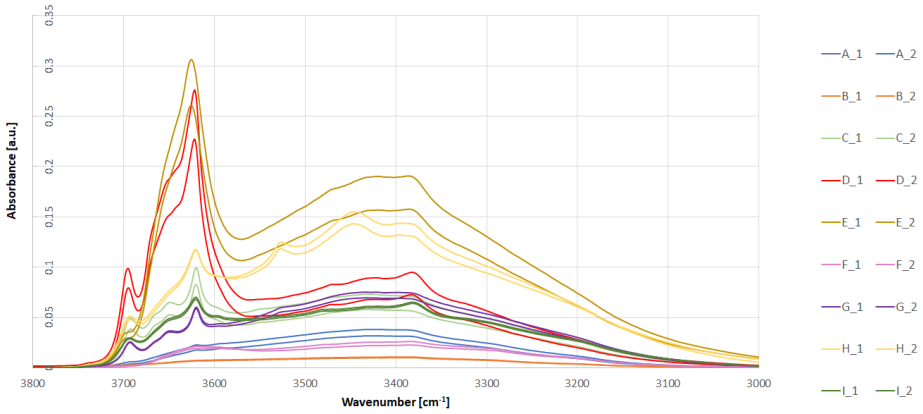

Figure 124: Spectrometer from Fourier transformed infrared spectroscopy for nine different quartz types. The size of the samples was below 100 μm.

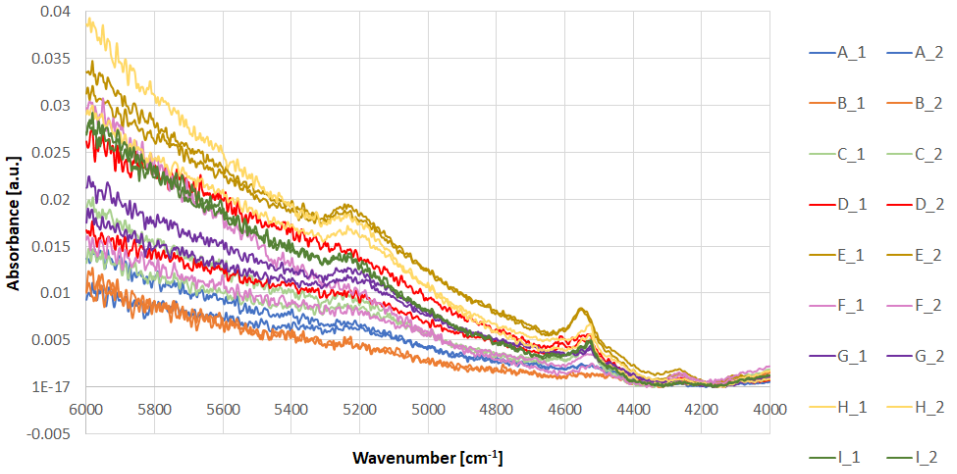

Figure 125: The near infrared region of the spectrogram for different quartz types.

To see if the different quartz types had any similarities that could determine different groups of quartz depending on the FT-IR, and hence either water content or any other impurities, a principal component analysis were done. The first principal component showed weight of 90 %, which means that this component explains 90 % of the variation seen between the IR-spectra of the quartz types. In Figure 126 the quartz types are plotted as a function of principal component 1 (PC-1) and principal component 2 (PC-2).

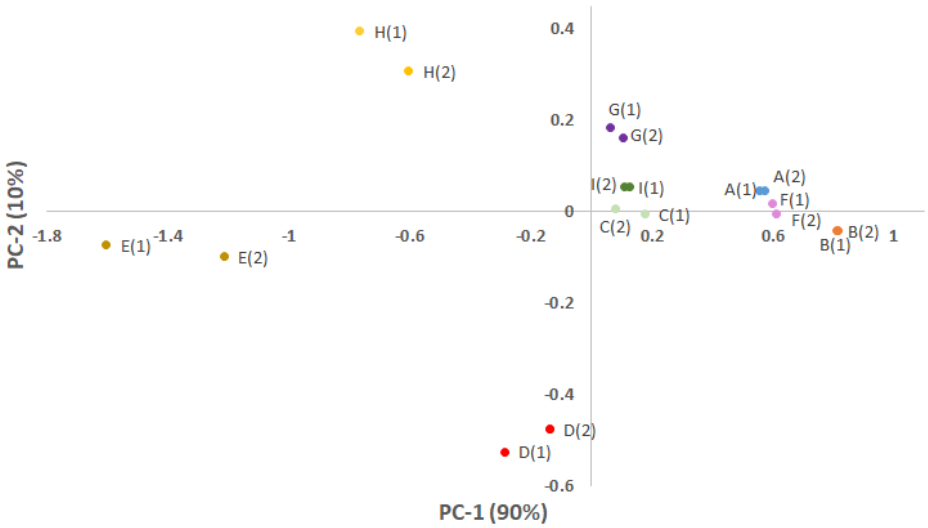

Figure 126: Principal components analysis of the FT-IR data for nine different quartz types.

The principal components are linear combination of the FT-IR spectra, so it is possible to figure out what their contributions are. The software used for the principal component analysis makes a variable contribution plot to see which wavenumbers are contributing the most to the principal component. Such a plot is seen in Figure 127. For PC-1 the major contributions are a relatively sharp negative peak around wavenumber 3625 cm^{-1}, and a broader negative band around 3400 cm^{-1}. If these wavenumbers represent muscovite ($KAl_2(Si_3AlO_{10})(OH)_2$) and water respectively, it means that quartz types having a high value for PC-1, has a lower content of muscovite and water compared to the quartz types with a negative value for PC-1, seen in Figure 126, e.g. quartz type D, E and H have a higher content of water and muscovite than quartz type B and F. For PC-2 a positive contribution is seen for the broad band at around 3400 cm^{-1}, meaning quartz with higher PC-2 value contains more water than quartz types with lower PC-2 value. Also, a sharper negative peak is seen for the 3625 cm^{-1} peak. As for PC-1, this means that higher PC-2 value means less muscovite.

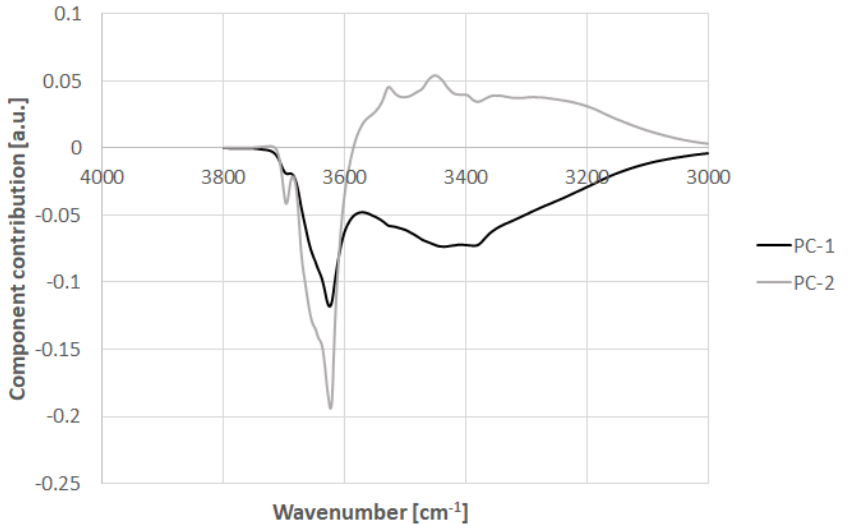

Figure 127: Loadings plot for PC-1 and PC-2, which are linear combinations of the FT-IR spectra of different quartz types.

6 Discussion

Chapter 2 presented how different quartz properties are suspected to affect the furnace operation when producing Si or FeSi. Earlier research on the high temperature properties of quartz were also summarized. In chapter 3, four selected industrial quartz types and their geological appearance as well as microscopic investigation done as a part of this project, were presented. The experimental results obtained from this thesis work were presented in chapter 5. The results showed how different quartz types behave when shock heated. Different possible reasons for disintegration were also presented. The second part of chapter 5 showed how different quartz types transform to other silica polymorphs. These phase transformations were also modelled. In the discussion chapter the results will be confronted with the literature presented, and possible correlations between properties will be investigated. Based on the results and previous literature, mechanisms for disintegration and phase transformation will be discussed. The sources of error of the main results are evaluated.

6.1 Disintegration of quartz

The disintegration of quartz upon heating is important for the furnace operation because a large amount of fine particles will clog the furnace and hinder an even flow of raw materials downwards and off gases upwards [3], [52]. Clogging of the furnace could cause small outbursts of gas or channeling in the furnace, and hence a lower Si-yield, as ascending SiO is not being captured. The generation of fines is thus one of the factors affecting the furnacability of the quartz [83]. Quartz with good furnacability have "chemical and physical criteria such to make it an appropriate silica raw material for the production of first grade silicon metal at high rates of process performance". Figure 128 illustrates what happens with the gas flow (red arrows) if the charge has much fines in it. The charge will be less permeable, and the gas will force its way up, leading to less interaction with the descending raw material and less SiO gas recovery. If there is more space around the raw material, the gas flow will even out and react with the raw materials. There is no exact limit for what size is detrimental for the furnace operation, but ideal lump size is 10 – 150 mm [3]. The fines production upon shock heating could be a consequence of both mechanical handling before heating, and thermal strength during heating. When quartz disintegrate the surface area will increase. There might be a correlation between the available surface area and the amount of condensate formed [122]. More condensate will also lead to a more compact charge. Softening properties could also enhance the clogging in the furnace, because partly melted silica will glue the charge together. The relative importance of the different properties is not known. In this thesis the disintegration upon shock heating has been investigated, and the possible enhancing properties are discussed.

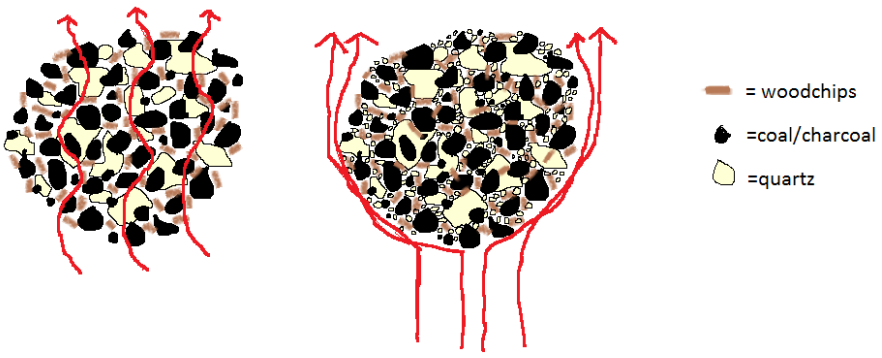

Figure 128: Illustration of gas permeability in a charge with a low amount of fines (left) and a high amount of fines (right).

The fines produced during shock heating at 1500 °C were measured for ten different industrial quartz types. For the four main quartz types A, D, F and G, six to ten parallels were done to check the repeatability and variance between the types. Lumps of 200 g ± 20 g were inserted to a carbon crucible preheated to 1500 °C. After ten minutes the sample was poured into a cold carbon crucible to cool in room temperature. Sieving of the sample was done at 2, 4, 10 and 20 mm. In Figure 129 the fines below 10 mm can be seen from all the experiments. The experiments are plotted such that the amount of fines increases for each type. Large variation can be seen between the different quartz types. The least disintegrated is type D with around 5 wt% of fines below 10 mm, while the most disintegrated is type F with up to 85 wt% of fines. There is also some internal variation within each quartz type. For type G there are two groups of results. This is likely due to different regimes, and will be discussed later. Variation within one type is also seen in some of the other types, and could be linked to differences in the samples heated, e.g. impurities, cracks, grain size and other textural properties. A quartz deposit could in general be very heterogeneous, even though some common features of each quartz type could be identified. These differences could appear in test results, such as during disintegration. In type A there are two domains where the grain size is different (medium to coarse grain in mm and µm scale in domain 1, and 10-200 µm in domain 2). This could explain the variance seen in the fines generated during shock heating for type A in Figure 129. Also in type F, different textural domains which can explain the variance are identified. Type D has a more homogeneous appearance, and it could therefore explain less divergent results than the other types. For type B, C, E, H, I and J thorough microscopic investigation of the texture and more parallels are needed to say why large variation are seen in these types, but it is likely to believe that also textural differences occur in these types.

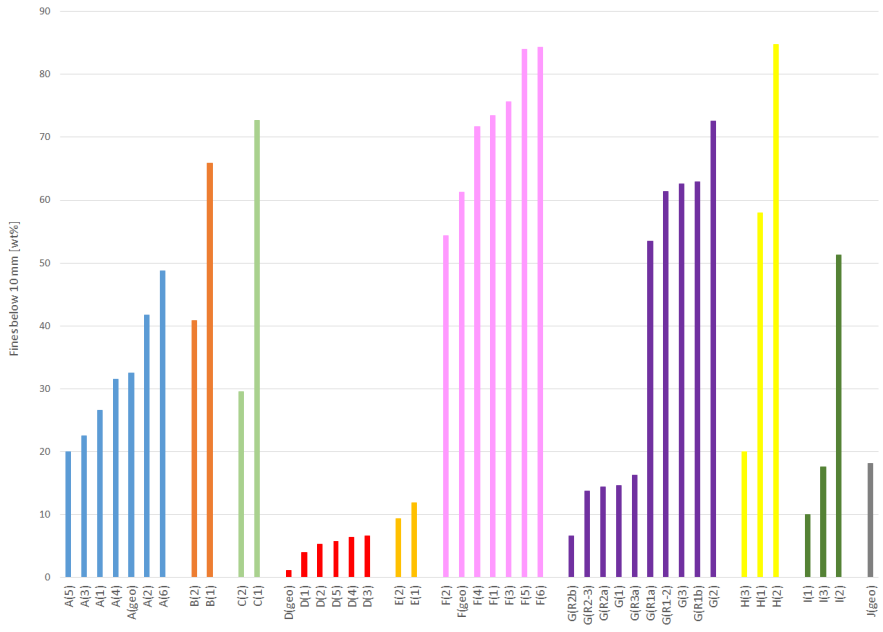

Figure 129: Fines below 10 mm after shock heating of different quartz types to 1500 °C. The number in parenthesis indicates the parallel number. For the G samples, the R gives the regime for the sample. The (geo) label indicates that these samples have had microscopic investigations before and after heating.

6.1.1 Internal differences and statistical significance

One of the important observations from Figure 129, is that the differences between the quartz types are larger than the internal differences, and hence there should exist properties in each quartz type increasing or decreasing the amount of fines. Sample G(1), G(2) and G(3) in Figure 129, showed a very large internal variation, from 15 to nearly 75 wt% fines below 10 mm. These samples led to deeper investigation where the regime for the sample was determined before heating. Type G has three regimes where the grain size, the degree of recrystallization and the temperature experienced are different. In addition, grains in regime 2 seem strain free, and grains in regime 3 are strain free [110]. Thin sections from each regime can be seen in Figure 130, and it can easily be seen that the grain size varies a lot between the regimes. With reference to Figure 129, sample G(R1a) and G(R1b) are samples with regime 1 identified. Sample G(R2a) and G(R2b) are from regime 2, and G(R3a) is from regime 3. There were two samples, G(R1-2) and G(R2-3), where the regime was difficult to distinguish. From the figure it can be seen that samples with identified regime 1 produced the largest amount, above 55 wt%, of fines below 10 mm, while samples from regime 2 and 3 all produced less than 18 wt%. This shows that there are internal variations in the quartz types, and these can be explained due to different regimes where the texture of the quartz is different. Since quartz is a natural resource there will always be natural variations in the samples collected even if they are from the same mine. For some types, e.g. type D, the variation is much less. This could be explained by a more homogeneous quartz deposit.

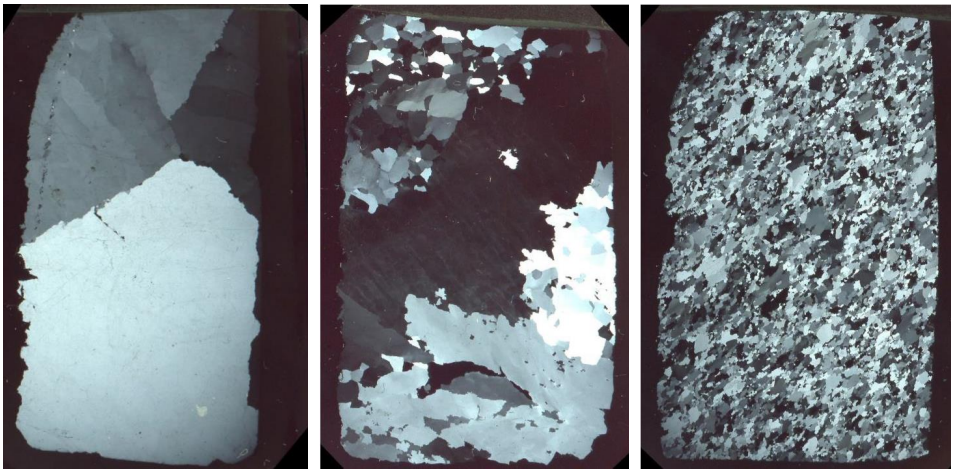

a) Regime 1, up to 400 °C. *b) Regime 2, 400-500 °C.* *c) Regime 3, 500-700 °C.*

Figure 130: Thin sections of different regimes of quartz type G, and the temperature the regime has experienced [110].

To test if the results for the different quartz types are in fact different, the statistical significance has been calculated between type D and F, the least and most disintegrated type, and between type A and F. First, the statistical significant difference between type D and F is discussed. The standard deviation for each type is calculated using Equation 6.1, where s is the standard deviation, x_i is each individual data, μ is the mean for each type and N is the number of samples tested for each type. The data for fines below 10 mm, presented in Figure 129, are used. For type D and F, the standard deviation is 2.03 and 11.10 respectively.

$$s = \sqrt{\frac{\sum(x_i - \mu)^2}{N - 1}} \quad 6.1$$

To find the standard error between each type, Equation 6.2 is used. s_d is the standard error, while s_D and s_F are the standard deviations for type D and F respectively, and N_D and N_F are the number of samples tested for type D and F, respectively.

$$s_d = \sqrt{\left(\left(\frac{s_D^2}{N_D}\right) + \left(\frac{s_F^2}{N_F}\right)\right)} \quad 6.2$$

The standard error between type D and F is calculated to 4.28. Further, a *t*-score must be calculated which allows the data sets to be compared with tabulated values for *t*, and the table gives the probability of the data sets being statistically different. The *t*-score is calculated by using Equation 6.3. To use the *t*-score table, the degrees of freedom must also be known. For type D and F, this number is 11 as there are in total 13 different measurements.

$$t = \frac{(\mu_F - \mu_D)}{s_d} \quad 6.3$$

The *t*-score is calculated to be 15.8. Compared to a *t* distribution table [123], a *t*-score of 4.44 would give a significance level of 0.05%, meaning there is a 99.95 % chance that type D and F are different when it comes to disintegration. The score calculated is way above, meaning that there is nearly 100 % statistical chance that they are different.

The same calculation was done between type A and F, as the results for them were closer. The same procedure as described above was followed, and it gave a *t*-score of 7.02. When comparing with the *t*-score table [123], the *t*-score is well above the t of 4.32 which would give a confidence level of 99.95 %. Based on these calculations, it is safe to say that despite some internal variation, there are differences in the amount of fines produced by each quartz type. Why there are differences will be further discussed.

6.1.2 Impurities

According to Griggs and Blacic [86] the strength of quartz would decrease above 800 °C if water was present in the sample. Aasly [6] also argued that fluid inclusion escaping during heating of quartz would cause tension in the material around it. For the four main quartzes, extensive microscopic characterization showed that all samples contained fluid inclusions, but in various amount. For quartz type A and D, a low amount of fluid inclusions were observed [6], [107], [108] . In quartz type F, fluid inclusions are more abundant [107], [109], while in quartz type G they are abundant in regime 1 (which counts for the majority of the samples) [110]. It is difficult to quantitatively determine the amount of fluid inclusions based on microscopic investigations because a very small area is investigated. Thus, to determine any bulk content multiple samples have to be investigated. Microscopic investigation can only give a qualitative measure on impurity elements. FT-IR is however a method that is suitable to measure the quantitative distribution of water in quartz [40]. It is also possible to distinguish between bounded water as OH-groups, and fluid molecular water [43]. In this thesis nine different quartz types were measured with FT-IR to study the amount of water. The analysis suggested that type D and E contain the highest amount of muscovite ($KAl_2(Si_3AlO_{10})(OH)_2$) and type E and H contain the

largest amount of water. This is seen in Figure 131, where the peaks for muscovite and water are marked. Another spectrogram of quartz containing water fluid inclusions and muscovite can be seen in Figure 132 [45]. When comparing the spectrograms in Figure 131 and Figure 132, some similarities are observed. It exists a broad absorption band around 3400 cm^{-1}. Several studies suggest this peak is due to water [28], [42], [43]. Based on these similarities it is likely that quartz type D and E contain muscovite and type E and H contain water. Type H, C, I and G also seem to contain muscovite, while type A, B and F shows no peak around 3625 cm^{-1}.

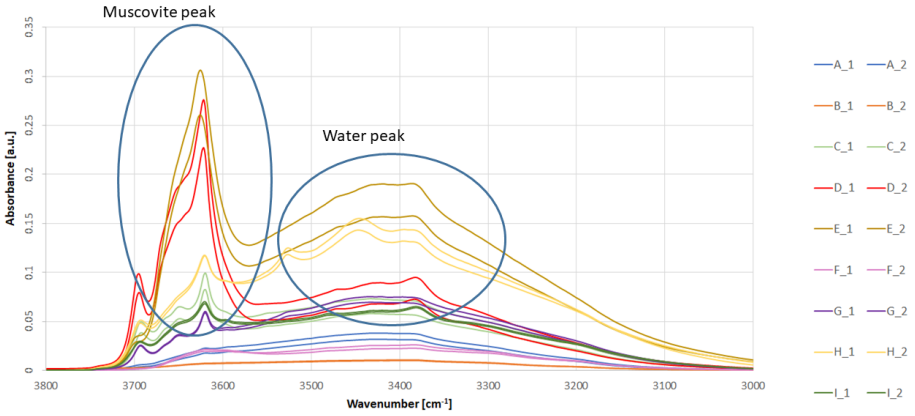

Figure 131: Spectrogram of different quartz types used for Si and FeSi production. Two parallels of each type are tested.

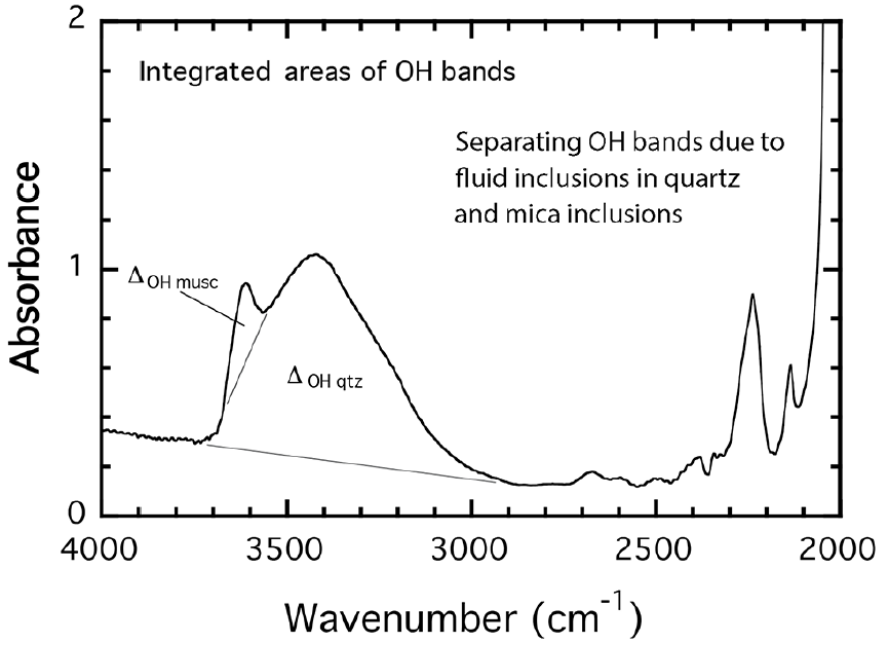

Figure 132: FT-IR spectrum of quartzite containing both molecular water and muscovite impurities. The OH-band in muscovite causes a relatively sharp absorption peak at around 3600 cm^{-1}, while the OH-band in the molecular water causes a broader absorption band around 3400 cm^{-1} [45].

The relative water content can be calculated from the spectrograms in Figure 131, and is compared to the amount of fines below 10 mm in Figure 133. The average amounts of fines below 10 mm for each quartz type are used. No clear correlation between the water content and the amount of fines can be observed. Despite this, water can still be of importance to the thermal strength of quartz. The FT-IR does not take into account whether the fluid inclusions are located inside grains or at grain boundaries. It could be possible that the location of fluid inclusions is more important than the amount. The location of the fluid inclusions cannot be determined using FT-IR. The microscopic investigations are more useful for that purpose. For quartz type A, the fluid inclusions are observed both at grain boundaries, sub grain boundaries and at healed fractures [107]. In quartz type D, some fluid inclusions can be found inside the grains, but they can also be found in healed fractures [6]. Quartz type F often has fluid inclusion along healed fractures [107]. In quartz type G the location of the fluid inclusions are along subgrain boundaries and at intergranular microfractures [110]. When considering that quartz type D and F disintegrated the least and the most respectively, and that they both have fluid inclusions in healed fractures and inside grains for quartz type D, it is difficult to draw any clear conclusion based on this information.

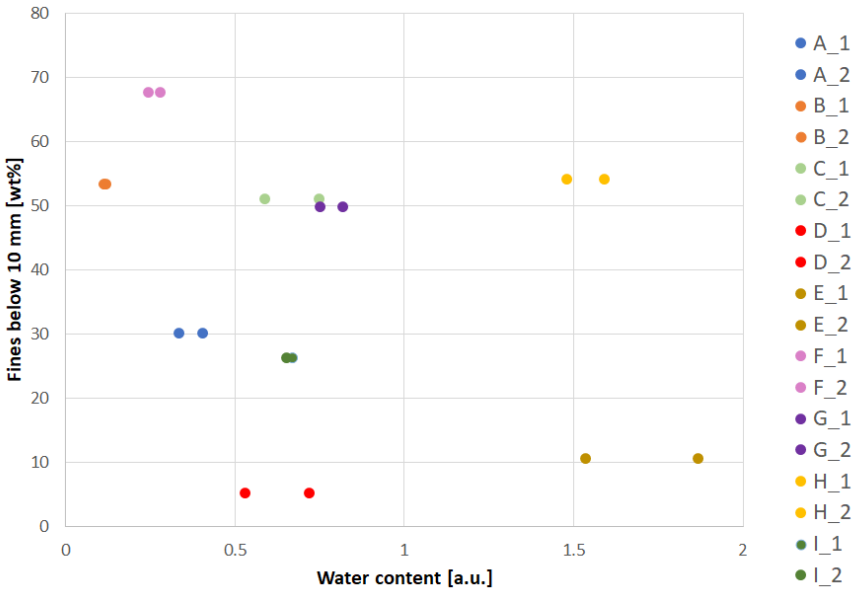

Figure 133: The average amount of fines below 10 mm for different quartz type as a function of the water content measured with FT-IR. No trend is seen between the amount of water and the disintegration of quartz samples.

Looking back at Figure 131, at 3625 cm^{-1}, six of the quartz types have a peak here. This is due to OH-vibrating groups in different clays, most likely muscovite [44], [45], [46], [47]. The peak could possibly also contain other clay types which have a vibrating OH-bond in their structures, but since muscovite is observed in microscope in all the quartz types A, D, F and G, it is likely that muscovite is present. Biotite ($K(Mg/Fe)_3AlSi_3O_{10})(F/OH)_2$) is also a possible clay with a peak in the same area. Compared to muscovite, biotite contains more magnesium while muscovite contains more potassium. As the chemical analysis of the quartz types indicates that the potassium content is higher than the magnesium content in all the quartz types tested, it is more likely that muscovite is responsible for the peak than biotite. The same quantitative measurement from the FT-IR can be done with muscovite as for water. In Figure 134 this is plotted. Despite some inconsistency in the trend in the upper left corner, an overall trend can be seen. As the clay content increases, the disintegration decreases. Compared to silica, muscovite has a sheet structure [124], which is weaker in one direction than the other. One possibility could be that the muscovite easier absorbs tension when the quartz samples experience thermal stress. Another explanation could be that the melting point of muscovite is lower than the shock heating temperature, and that muscovite melts and glues the samples together during heating. Muscovite melts at 1300 °C [125], and the samples were shock heated at 1500°C for 10 minutes.

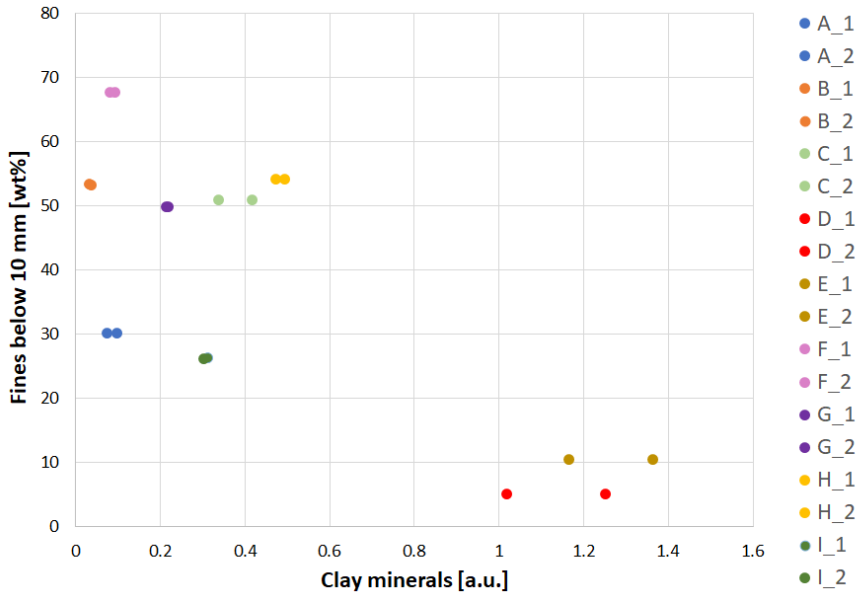

Figure 134: The average amount of fines below 10 mm for different quartz type as a function of the clay content measured with FT-IR.

To further investigate if there was any correlation between the impurities and the fines generation, Figure 135 was plotted from the disintegration data and the bulk impurity data. In Figure 135a, the main quartz types A, D, F and G, with additional types C, E, H and I can be seen. Type D and E have the highest impurity level and the lowest amount of fines produced during shock heating. For the other 6 types, Figure 135b shows the same graph but with an enlarged x-axis to see possible correlations more clearly. The trend for type A, F, G, H, I and J is not clear. This could indicate that the impurity level generally is too low for the effect of impurities to be seen, or it could be that other properties in the quartz are determining the ability to disintegrate. A combination of the two suggestions is also possible.

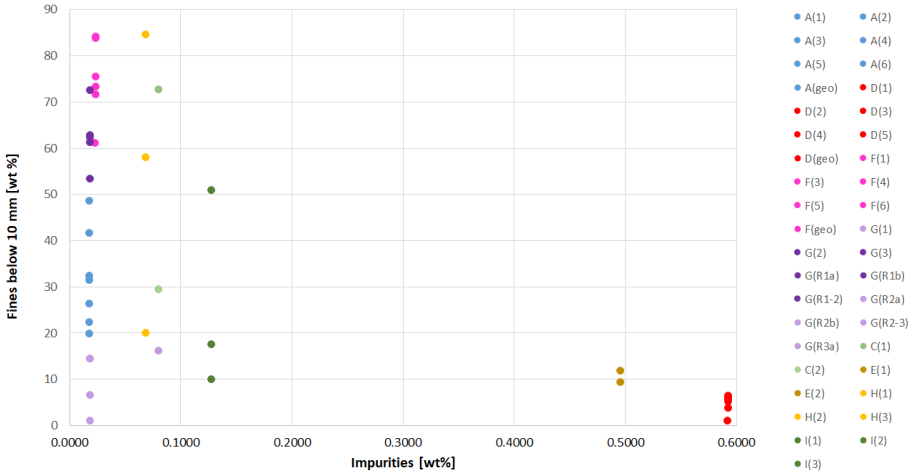

a) The total impurity content compared with the amount of fines below 10 mm.

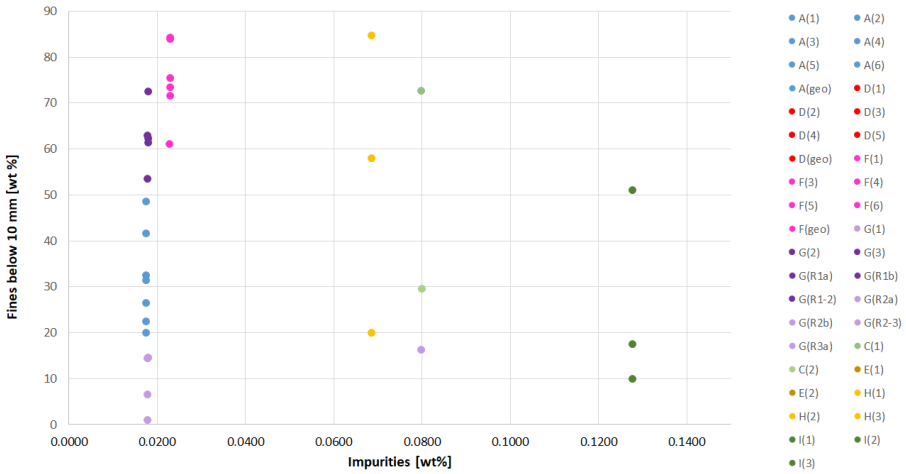

b) *The same graphs as in a) but with a different x-axis to highlight the differences at low impurity level.*

Figure 135: The impurity content measured with ICP-OES, compared with the amount of fines below 10 mm in different quartz types.

From the principal component analysis the quartz types can roughly be divided into two groups based on the content of muscovite ($KAl_2(Si_3AlO_{10})(OH)_2$) or other clay types. This is seen in Figure 136. The first group being quartz type D and E, with high muscovite content. The other group with quartz type A, B, C, F, G, H and I have a low muscovite content. When comparing the two groups with the disintegration data in Figure 87, the same grouping can be seen. Quartz type D and E have a considerably lower ability to disintegrate upon shock heating. This is supported by Figure 137a and b, where the amount of fines is plotted as a function of PC-1, and PC-2 respectively. As both PC-1 And PC-2 are increasing, the ability to disintegrate increases as well for most samples. There is some deviation from the trend, but there seems to be an overall trend.

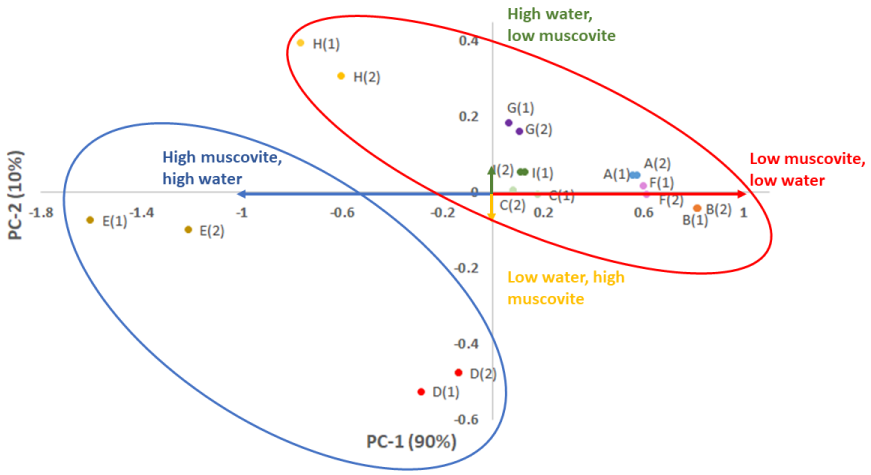

Figure 136: Principal component analysis with marked groups based on the contributions to the different components. The blue circle marks the group with quartz type D and E, having high muscovite content, and the red circle marks the group with quartz type A, B, C, F, G and I having low muscovite content.

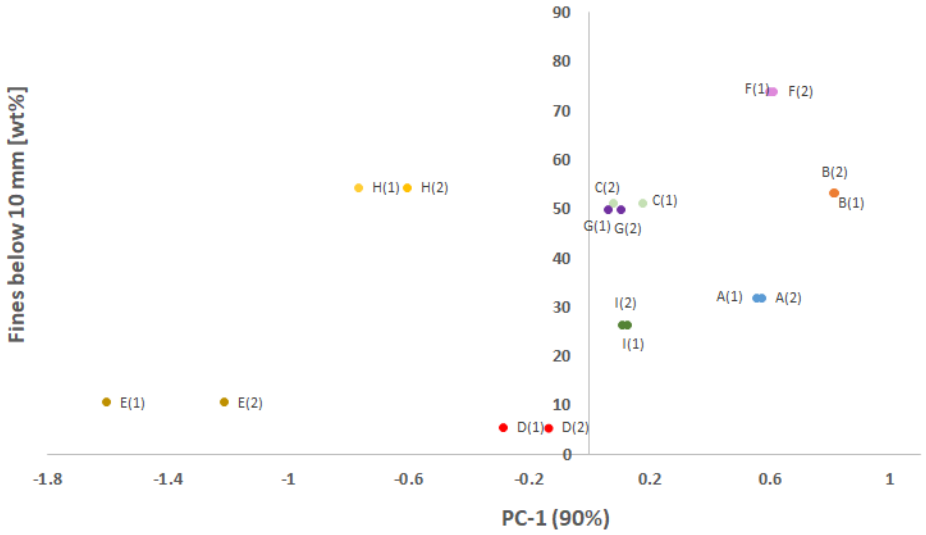

a) The amount of fines below 10 mm as a function of PC-1.

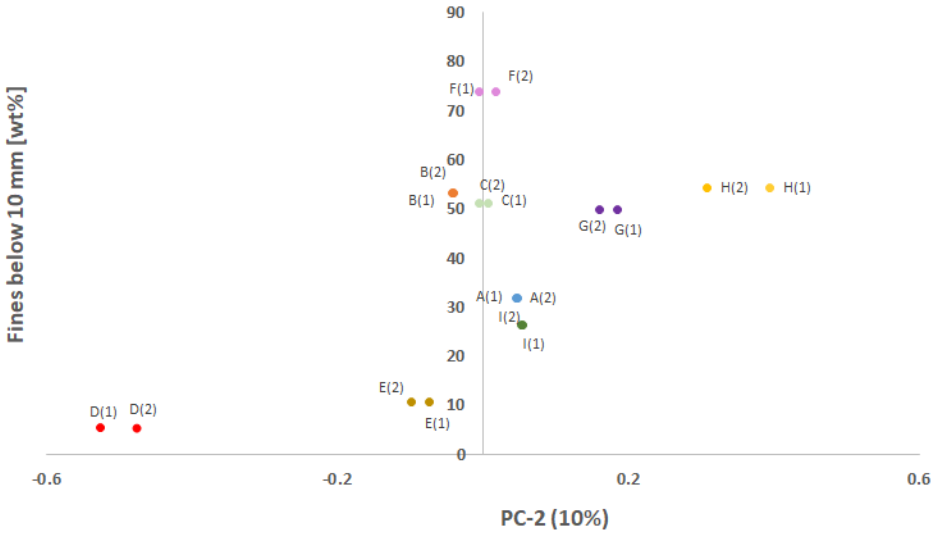

b) The amount of fines below 10 mm as a function of PC-2.

Figure 137: The amount of fines from nine different quartz types shock heated to 1500 °C plotted as a function of principal components of FT-IR data from the same quartz types.

6.1.3 Phase composition

It was suggested by Aasly et al. [83] that the amount of cristobalite would affect the amount of fines created during shock heating. This theory is often put forward as the volume change between quartz and cristobalite is 17 % and would cause tension in the sample [94]. This is illustrated in Figure 138, where the formation of amorphous phase and cristobalite causes a volume increase and hence tension and cracking of the sample. To further investigate if this theory was acceptable, the phases in shock heated material were measured.

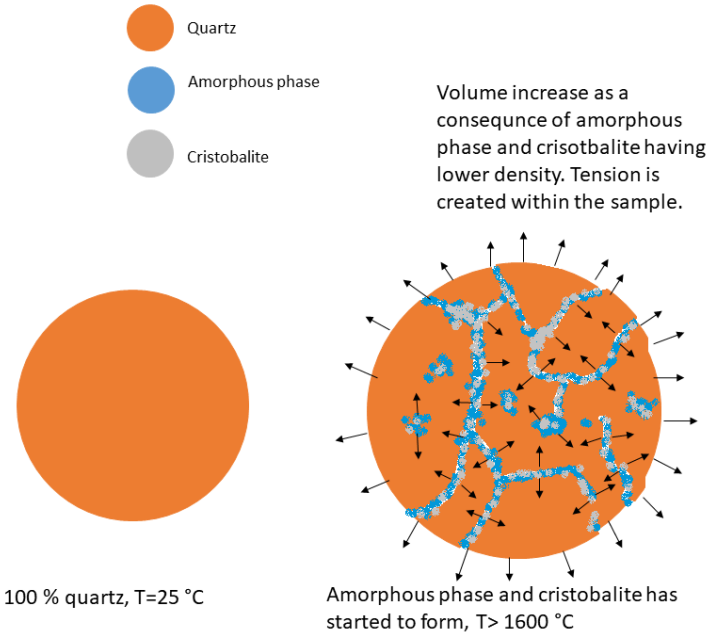

Figure 138: Illustration on how phase transformation in quartz is believed to cause tension and cracking of the sample. The figure is not to scale, only illustrative.

The phase composition was measured in selected samples for seven quartz types after shock heating. Since the material was quenched in air after the shock heating, it is believed that no further phase transformation took place after removing the sample from the warm crucible. The overall trend seems to be that 20 to 50 wt % of the material have transformed from quartz to amorphous phase and cristobalite. The amount of cristobalite is largest for quartz type D, the type with least disintegration. Also, quartz type E, which had the second least amount of fines, had up to 40 wt% amorphous and cristobalite phase. This could indicate that the disintegration happens independently of the phase transformations, or that the effect is cancelled out by other parameters. Aasly et al. [83] claim the opposite, that cristobalite formation would enhance disintegration. It can also be seen that there is no trend in the amount of phases in the different fractions of the samples. If cristobalite and amorphous phase would cause, one would possibly expect to find more of these phases in the smaller size fractions.

The amount of fines below 10 mm is plotted in Figure 139 together with the amount of transformed quartz, i.e. amorphous phase + cristobalite. For the samples where the phase composition is measured in different fraction, an average is used for the sample. In Figure 139 it is clearly seen that the amount of transformed quartz does not correlate with the amount of fines generated during shock heating. In Figure 140 and Figure 141 the amount of cristobalite and amorphous phase are plotted independently to see if one of the phases correlated with the amount of phase. None of these figures showed any correlation of the amount of fines below 10 mm and different phases. This implies that the volume increase because of phase transformation does not cause the sample to crack. The sample might increase in total volume, but in that case, it does not cause disintegration of the sample. Other properties must be responsible for the disintegration upon shock heating. Another explanation could be that the samples do crack as a consequence of the phase transformations, but some samples have other properties which equalize this effect.

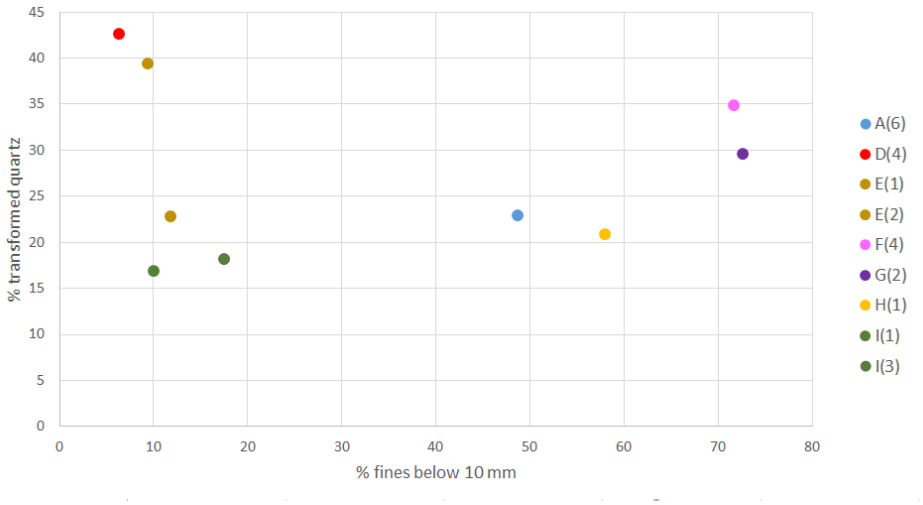

Figure 139: The amount of transformed quartz (amorphous phase + cristobalite) compared with the amount of fines below 10 mm for selected quartz samples.

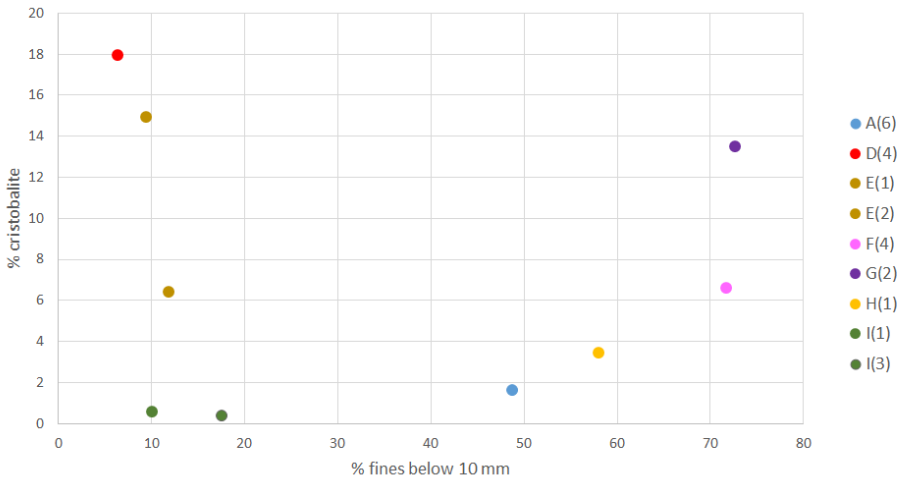

Figure 140: The amount of cristobalite in shock heated samples compared to the amount of fines below 10 mm for the same sample.

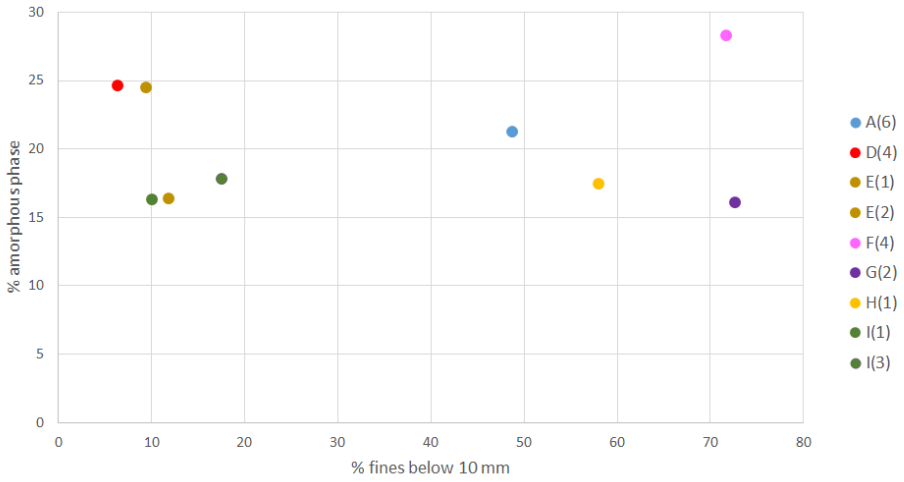

Figure 141: The amount of amorphous phase in shock heated samples compared to the amount of fines below 10 mm for the same sample.

6.1.4 Grain size

To further investigate the ability to disintegrate for different quartz types, thorough microscopic investigations were performed before and after shock heating. A piece of quartz was selected, and then divided into one part for shock heating and from the other part a thin section was prepared. In that way, the thin section is more likely to represent the quartz piece being shock heating, rather than comparing a thin section from a random quartz piece of the same type. After shock heating, the material was used to prepare another thin section. This was carried out by Anja Filipowicz, and presented in chapter 3 earlier [107]. The samples which were selected for these investigations were A(geo), D(geo), F(geo) and J(geo). The amount of fines below 10 mm for these samples can be seen in comparison with the other shock heated samples in Figure 129, and isolated in Figure 142. The variation is large, from a few wt% of fines to above 60 wt% for quartz type D and F respectively. In Figure 143, microscopic investigations before heating from the four quartz types A, D, F and J can be seen. They have very different appearances. The most different in terms of grain size would be quartz type D and F. The first has small and homogeneous grains, while quartz type F has some very large grains and some smaller recrystallized grains. Quartz type A and J are in the middle, showing some variation in the grain size but not as much as type F. Comparing the amount of fines in Figure 142 and the images in Figure 143 it could seem that larger grain size will enhance the disintegration of quartz when shock heated. When comparing the different regimes in quartz type G given in Figure 144, a difference in the grain size can also be seen. Regime 1 has larger grains, while regime 2 and 3 have smaller grains. When comparing this information with the fines generation for different regimes in Figure 145, it can be seen that samples from regime 1 with the largest grain size disintegrate more than the samples from regime 2 and 3 with smaller grain size. The samples G(1), G(2) and G(3) where the regime was initially unknown, could then be assumed to be regime 2 or 3 for sample G(1), while sample G(2) and G(3) seem to be regime 1. The theory that larger grain size would affect the amount of fines, is in agreement with Malvik et al. [85] which argued that the thermal strength would be directly proportional to the grain size. The reason for this could be that an increased amount of grain boundaries could withstand forces by dividing them on the gain boundaries. This is a known phenomenon from the manufacturing of steels where the grain size can be decreased to strengthen the steel. The effect is explained by dislocations that pile up at the grain boundaries. Thus, the more grain boundaries, the less dislocations at these pile ups and less stress on the grains [126].

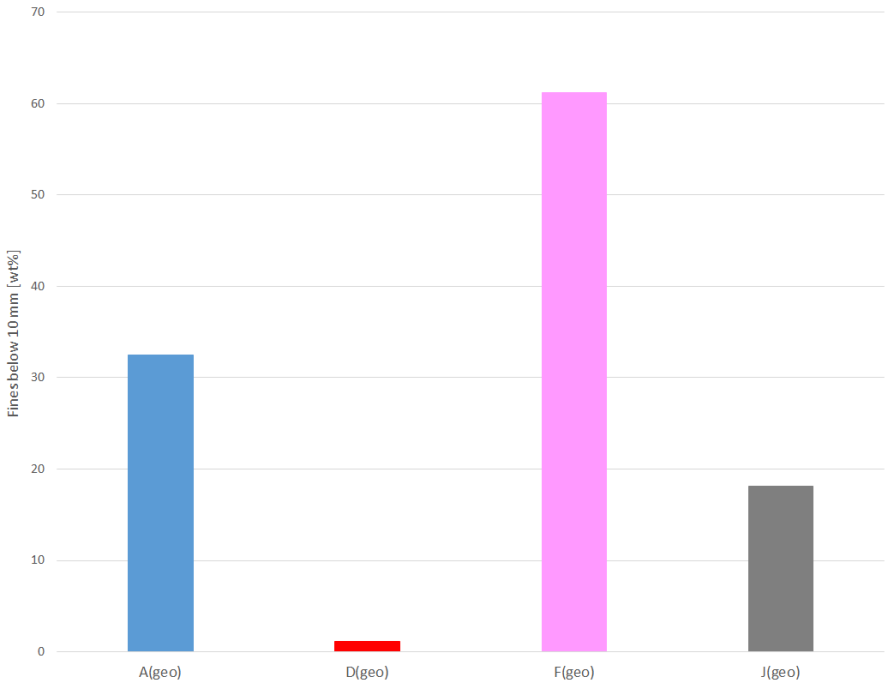

Figure 142: Amount of fines below 10 mm after shock heating to 1500 °C for four different quartz types, also with prepared thin sections for microscopic investigation.

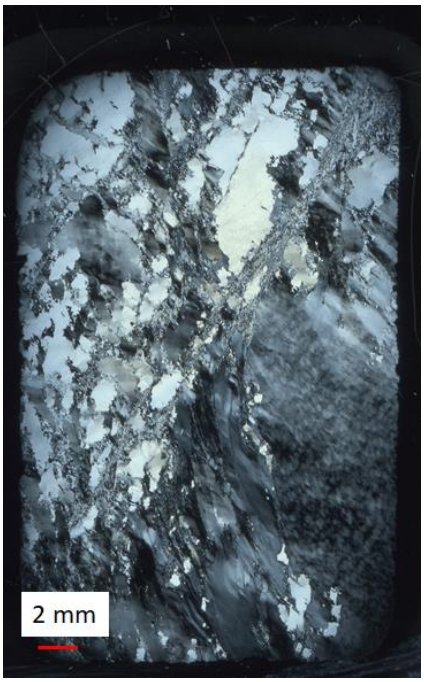

a) Thin section of quartz type A

b) Thin section of quartz type D

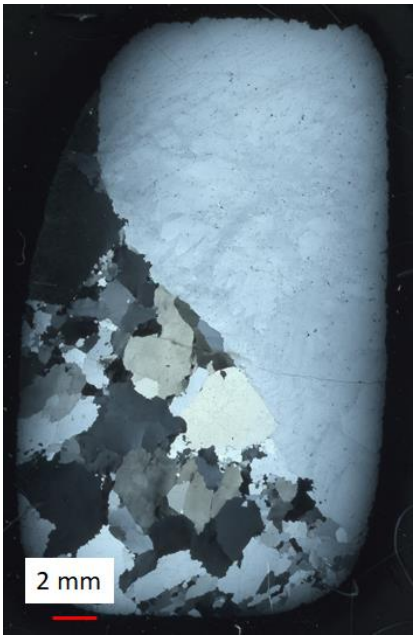

c) Thin section of quartz type F

d) Thin section of quartz type J

Figure 143: Microscopic investigation of thin sections from four different quartz types before heating. The images are obtained from Brenden-Veisal and Filipowicz [107].

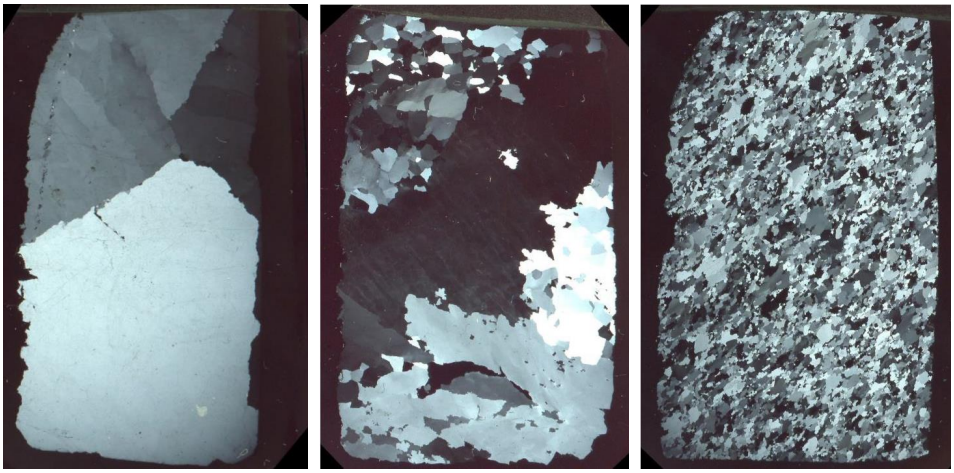

d) Regime 1 *e) Regime 2* *f) Regime 3*

Figure 144: Thin sections of the different regimes in quartz type G [110].

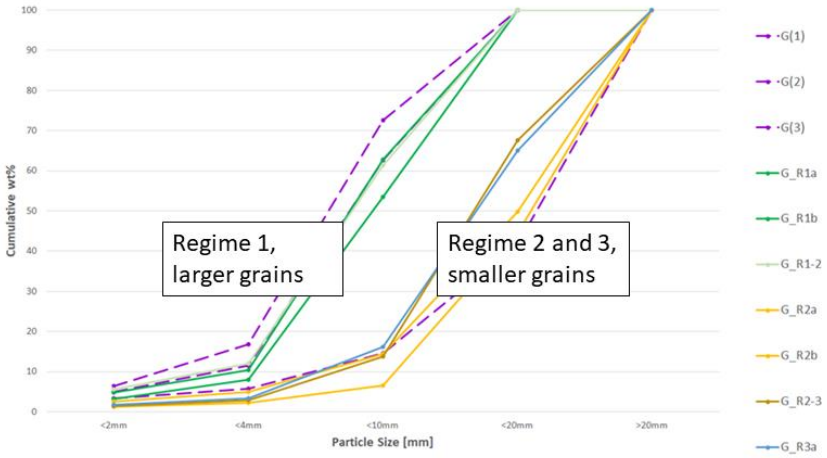

Figure 145: Cumulative representation of shock heated material in samples from different regimes of quartz type G. The number in G_R1a, means regime 1, and a and b are two different samples. For the initial samples G(1), G(2) and G(3) the regimes are now known.

When comparing the microscopic images of the thin sections in Figure 143 with the thin sections of heated material in Figure 146, small differences are observed. Quartz type A and J, which had a medium amount of fines after shock heating, have pieces crossing several grains. It could seem like quartz type F has broken at the grain boundaries around the largest grains, as these are separated in Figure 146c. This could support the theory that grain boundaries around large grain experience more stress and the quartz will therefore break at these boundaries rather than boundaries around smaller grains.

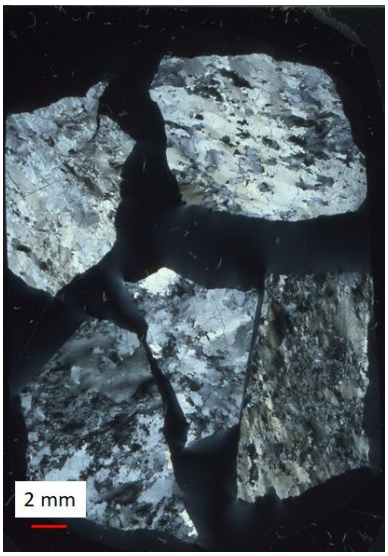

a) Thin section of quartz type A, after shock heating.

b) Thin section of quartz type D, after shock heating.

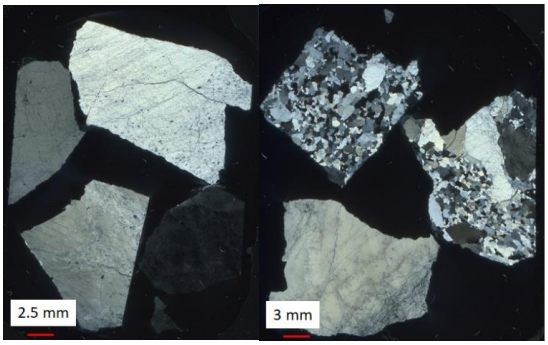

c) Thin section of quartz type F, after shock heating.

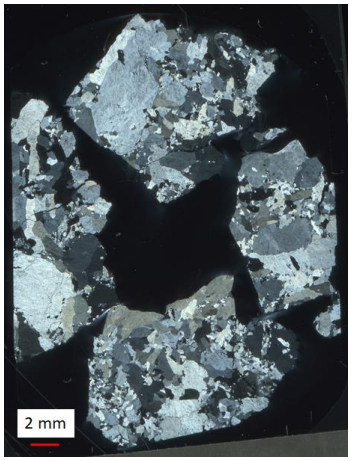

d) Thin section of quartz type J, after shock heating.

Figure 146:Microscopic investigations of thin sections made from shock heated material. The images are obtained from Brenden-Veisal and Filipowicz [107].

6.1.5 Cracks

Aasly [6] stated that micro cracks in quartz samples would reduce the mechanical strength, and probably lead to more disintegration when shock heated. By investigating samples by high-temperature microthermometry, it was observed that micro cracks would open during heating and cause fracturing of the sample. Therefore, the amount of cracks were measured using CT-scanning, before heating of the quartz samples. The images obtained were analyzed and the crack area measured. This was carried out for several parallels of quartz type A, D, F and G before shock heating to 1500 °C. Average crack area varied from 0.14 to 1.29 %. Some variation

was observed within the parallels of one type, but there is larger variance between the different types. The amount of cracks for quartz type A, D, F and G are plotted against the amount of fines below 10 mm from the same sample. This is seen in Figure 147. For each point, an average from 20 images has been analyzed. A trend is seen in the figure. As the amount of cracks increases, the amount of fines below 10 mm also increases. Thus, there is correlation between preexisting cracks and thermal stability. This confirms Aasly's observations that micro cracks would propagate to fracture when heated. There is one clear outlier, G(1). The internal difference between G(1), and G(2) and G(3) could be explained by the regimes in quartz type G. G(1) is most likely regime 2 or 3 with smaller grains, while G(2) and G(3) are from regime 1 with larger grains. G(1) is also a outlier from the general trend. It has the third largest amount of crack, but produced a very low amount of fines. This may be due to small grain size and hence more grain boundaries which can stop the propagation of cracks. It could mean that quartz with smaller grain size is better equipped to withstand cracks from blasting and handling, compared to large grains sized quartz which must be handled more delicately to avoid crack formation.

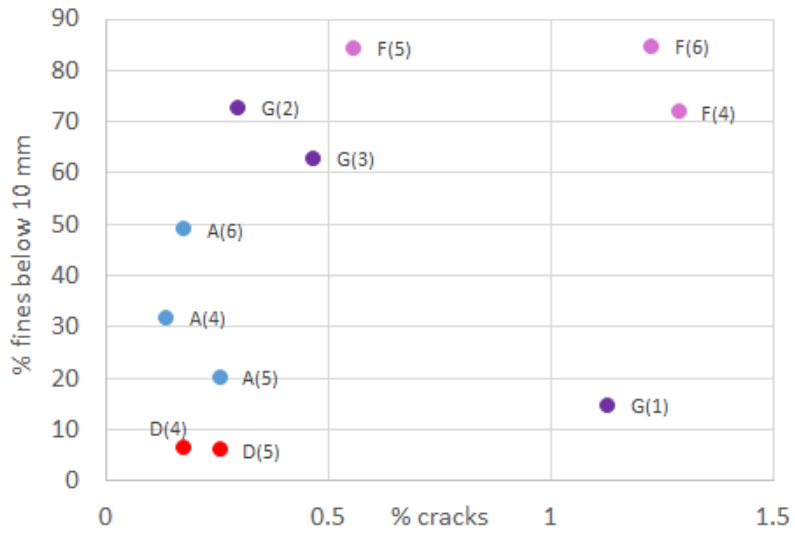

Figure 147: Amount of fines as a function of the amount of cracks in different quartz types.

There are several properties of the quartz that seems to affect the disintegration upon shock heating. A clear correlation is observed between the amount of preexisting cracks and the amount of fines below 10 mm. There is no clear trend in the total amount of impurities and the amount of fines. It could seem like muscovite prevents the sample to disintegrate, as this is seen for sample D and E in the principal component analysis. Another explanation of the low amount of fines in sample D could also be the smaller grains, and hence a larger amount of grain boundaries which makes the sample stronger. No correlation was found between the amount of phases and the amount of fines. There is also a possibility that some properties are dominating such that the effect of other properties are not seen. If the grain size is a dominant effect, it could hide the effect of fluid inclusions as no clear trend was seen for the water content based on the FT-IR analysis. It is also possible that the phase transformation and the following volume increase does enhance disintegration, but other properties equalize the effect.

6.2 Phase transformations in different quartz types

The phase transformations from quartz to amorphous phase and further to cristobalite were investigated in type A, D, F and G. Despite no correlation between the disintegration of quartz samples and the amount of transformed quartz (in Figure 139), the different silica phases could affect the furnace operations in other ways. Earlier studies [22], [23], [94] suggest that the amount of amorphous phase or cristobalite would increase the specific surface, and thus increase the rate for the reaction between SiO_2 and SiC or C. Later research [18], [19], [20] has not been able to show that the amount of amorphous phase or cristobalite would increase the reaction rates in the furnace. It is still possible that the amount of silica phases could affect the quartz behavior in other ways. Softening and melting properties are suspected to be important due to clogging in the furnace. Such properties might be affected by the silica phases. Also, the volume increase of 17 % from quartz to cristobalite could cause a more dense charge mix which will decrease the permeability in the furnace [52].

Phase transformations from quartz to amorphous phase and cristobalite are observed in all the four main quartz types A, D, F and G when heated to 1600 °C and 1700 °C. However, the different types transform at different rates. By heating to 1600 °C, type A has transformed the least, and type F the most. After 2 hours at 1600 °C, type A had almost reached the same phase composition as type F. This can be seen in Figure 148. Type A still has around 90 wt% of quartz at 0 minutes holding time, while type F has around 5 wt%. This is a considerable amount, and shows that there could be large differences in the ability to transform to other silica phases with varying the quartz type. In terms of the quartz amount measured at 0 minutes holding time, type D and G lie at 55 wt% and 20 wt% respectively. Based on the phase composition at 1600 °C and 0 minutes holding time, the ability to transform in increasing order is A, D, G and F. The different abilities to transform is in agreement with earlier studies by Ringdalen [52] and Kjelstadli [57] who also investigated quartz types used for FeSi and Si production. Mitra [79] also studied the phase transformations in two different quartz types, and found a different transformation rate into amorphous phase and cristobalite for different types of quartz raw material.

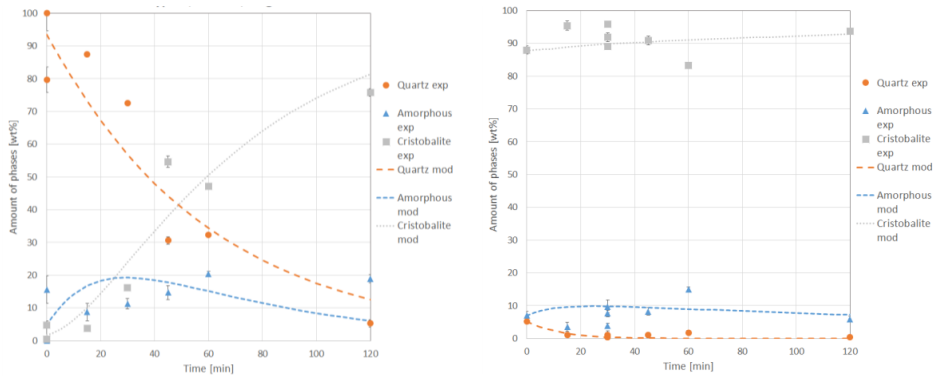

a) Quartz type A *b) Quartz type F*

Figure 148: The phase composition of quartz type A and F, after heating 10 g sample to 1600 °C with varying holding time at maximum temperature.

The initial phase composition was measured for the different types A, D, F and G before heating. All the types showed some amorphous phase in some of the unheated samples. For type A, the content was around 10 %, while for type D the amorphous content varied from 6-22%. The phase composition for unheated samples can be seen in Figure 83. Samples containing 100 % quartz before heating are also seen. In Figure 82, two parallels each of type A and D showed nearly 100

% quartz for three of the samples. This shows that there are some variations in the initial phase composition for the different types. It is also seen for two of the parallels of type A heated to 1600 °C with 0 minutes holding time that it contains 100 % quartz. It is likely to believe that this sample contained 100 % quartz before heating as well, as amorphous phase is an intermediate phase between quartz and cristobalite [49], [55], [57], [58]. The initial amorphous content measured in the different types, is still smaller than the variations between the phase composition in the different types observed after heating.

The ability to transform was in increased order A, D, G, F. Compared to the disintegration, type D created the least amount of fines followed by type A, G and F. The same trend is not seen between the ability to transform and the disintegration of the types, but the only type deviating is quartz type D. As no correlation was found between the amount of phases and the amount of fines there has to be different properties affecting the phase transformations and the disintegration. If only type A, F and G are considered, the type that disintegrated the least also had the slowest phase transformations. But, the quartz types could have other properties that affect either behavior, such as type D, which is not following the same trend. This means that some of the properties enhancing disintegration also could enhances phase transformations.

6.2.1 Impurities

The reasons for the different abilities to transform have earlier been investigated in several studies. Dapiaggi et al. [76] showed that increased amount of K and Na would speed up the transformation to high temperature silica phases, and Schneider et al. [58] claimed that alkali and alkali earth impurities would speed up the nucleation and growth of cristobalite. To investigate a possible correlation between the alkali and alkali earth elements for type A, D, F and G, the amount of alkali and alkali earth elements and the amount of remaining quartz after heating to 1600 °C and holding time 0 minutes is plotted in Figure 149. No overall trend can be seen, but if type D is discarded, a trend is seen between type A, F and G and the amount of alkali and alkali earth elements. For sample D, there could be other factors affecting the phase transformation. For type A, F and G, the amount of alkali and alkali earth elements seems to speed up the phase transformation from quartz.

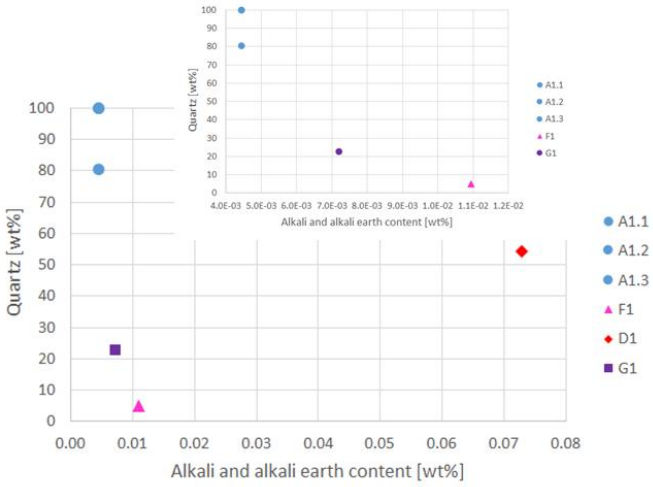

Figure 149: The amount of quartz after heating to 1600 °C as a function of the alkali and alkali earth impurity content in the different quartz types A, D, F and G. The number in the parenthesis indicates different parallels. In the top right graph, the x-axis below 0.012 is enlarged to show the differences between type A, F and G more clearly.

The amount of aluminum was also suspected to accelerate the transformation. Both Brown et al. [78] and Chaklader [50] claimed that Al_2O_3 impurities up to a certain limit would speed up the transformations from quartz to cristobalite. Chaklader [50] found this limit to be 0.44 %, while Brown et al. [78] found it to be around 0.2 %. The amount of aluminum and the amount of remaining quartz after heating to 1600 °C and no holding time is compared for type A, D, F and G. The results can be seen in Figure 150. No trend is seen between the amount of aluminum at this level and the amount of remaining quartz after heating. This does not rule out Al impurities as an accelerating factor, but there could be other affecting factors dominating.

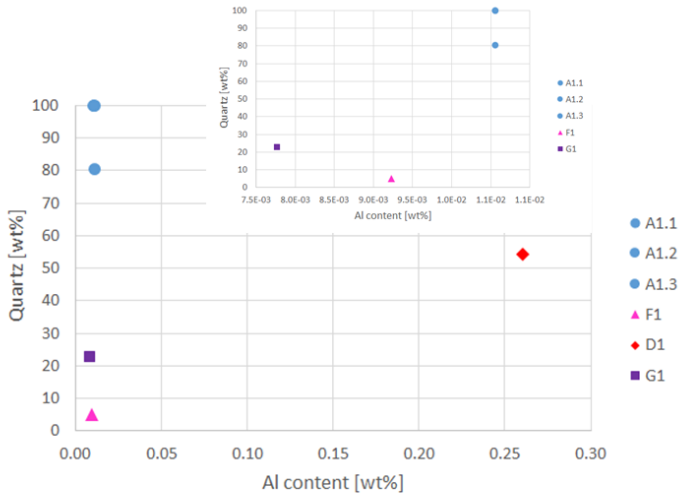

Figure 150: The amount of quartz after heating to 1600 °C as a function of the Al content in the different quartz types A, D, F and G. The number in parenthesis indicates different parallels. In the top right graph, the x-axis below 0.011 is enlarged to show the differences between type A, F and G more clearly.

6.2.2 Size effect

Different researchers have investigated whether the size of silica samples affect the transformation speed. Wahl et al. [77], Pagliari et al. [75] and Dapiaggi et al. [76] investigated the size effect at micro scale. Neither found any clear effect of the particle size. Kjelstadli [57] investigated samples sizes from 10 g to 200 g. At 1600 °C no size effect was seen, but at 1700 °C, there were results indicating that the transformations took longer time in the larger particles. This can be seen in Figure 32. Kjelstadli explained this by thermal diffusion taking longer time for the larger particles at 1700 °C. For the quartz types A, F and G in this study 10 g and 100 g samples were investigated both at 1600 °C and 1700 °C. The amount of phases in the different sizes heated to 1600 °C can be seen in Figure 151, Figure 152 and Figure 153 for type A, F and G respectively. For type A, no trend is seen in the phase composition. For 0, 15 and 30 min the 100 g samples have a larger amount of amorphous phase and cristobalite than quartz, but for 45 and 60 minutes the opposite is seen. It must be mentioned that the 100 g samples heated for 30 min at max temperature is believed to be an outlier, and should be neglected when looking at overall trends. The variation seen is believed to occur because of natural variations in the quartz type itself. For type F, a trend could be seen. At 0, 15 and 30 minutes the amount of amorphous phase and cristobalite is larger for the 10 g samples than the 100 g. For 45 and 60 minutes the phase composition is nearly the same. The variation seen could be due to slower thermal diffusion in the 100 g samples, but the variation could also be due to natural variation in the quartz. In type G, there is more amorphous phase and cristobalite in the 10 g sample at 0 minutes. For the other holding times, the phase composition is nearly the same for 10 g and 100 g. Also for this type, the results seen could indicate that the thermal diffusion is a limiting factor at the lower holding times, but as the holding time approaches 30 minutes and above this thermal diffusion barrier is negligible. The reason that this is not clearly seen in type A, could be that this type uses longer time to transform to begin with, and therefore the thermal diffusion is not a limiting step. Nordnes [17] modelled the heat distribution in quartz cylinders with diameter of 4 cm, and height varying

from 1 to 10 cm. She found that when held at 1765 °C for one hour, the temperature from surface to center would vary from 0.05 °C to 30 °C for the smallest to the largest sample. The 100 g samples tested in this thesis were approximately 5 cm large, while the 10 g samples were 1-2 cm large. Based on the model by Nordnes [17], it is likely to believe that this difference is larger below 1 hour, meaning that there is a larger thermal gradient in the 100 g samples compared to the 10 g samples. Ksiazek, as mentioned by Kjelstadli [57], modelled the temperature in the center of a spherical particle when heated to 1700 °C. He found that by heating quartz samples with varying size, it would take about three minutes longer for a 5 cm sample to reach 1700 °C in the center of the particle compared to a 2 cm particle. The heating rate in his model was around 1 °C/s, and it took about 30 minutes for the furnace to heat to 1700 °C. These are very similar conditions as used for the experiments in this thesis, and it is therefore likely to believe that the center of the 100 g samples would reach the target temperature not more than 3 minutes after the 10 g samples. Thus, a size effect might be seen for the lower holding times for type F and G, but not for the longer holding times where the temperature has reached its target throughout the sample.

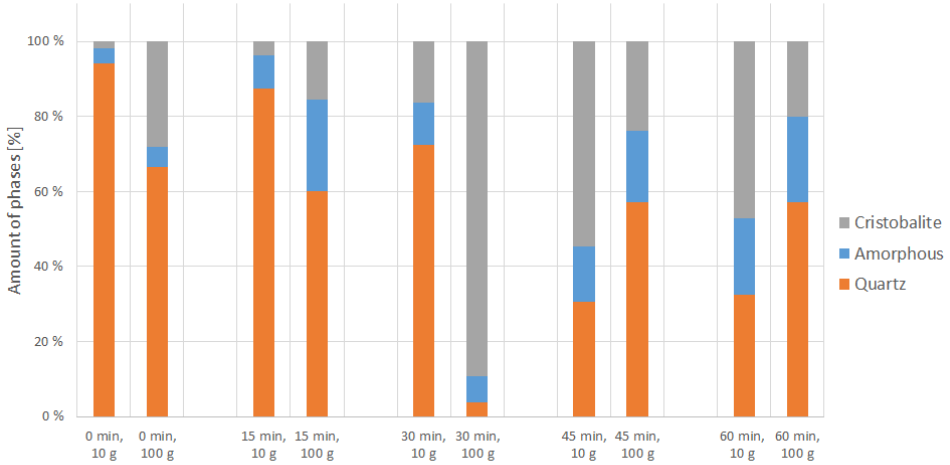

Figure 151: The amount of phases in samples from quartz type A, heated to 1600 °C.

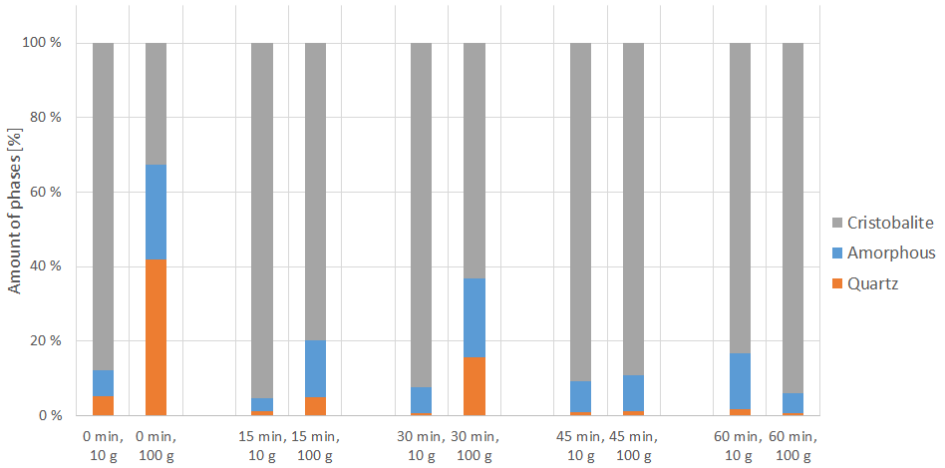

Figure 152: The amount of phases in samples from quartz type F, heated to 1600 °C.

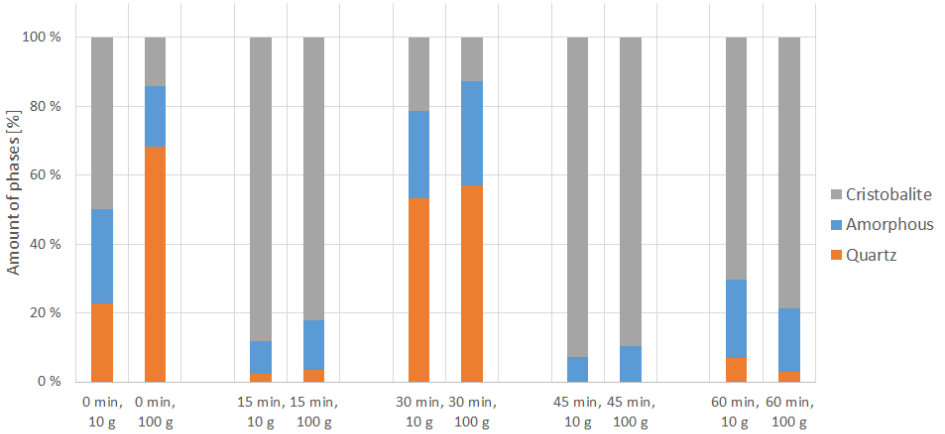

Figure 153: The amount of phases in samples from quartz type G, heated to 1600 °C.

To further investigate any possible size effect, 10 g and 100 g particles heated to 1700 °C, are compared in Figure 154, Figure 155 and Figure 156 for type A, F and G respectively. For type A, the same as samples heated to 1600 °C is seen. There is no consistent trend in the phase composition between the 10 g and 100 g samples. In fact, the phase composition is very similar for all holding times at 1700 °C. It could seem that the amorphous phase is very stable, and that the transformation to cristobalite at 1700 °C is slow. This could be due to a started melting phase, as silica melts just above 1700 °C [100], [127]. For quartz type F, in Figure 155, the phase composition is almost the same at all holding times, except 15 minutes. This could be due to natural variation in the quartz. An overall size effect is not seen. For type G, the same trend as at 1600 °C is seen. At the lower holding times, 0 and 15 minutes the 100 g samples show a slower transformation than the 10 g samples. The difference diminishes as the holding time increases.

The same argument as at 1600 °C can be used to explain this. In the beginning, the larger samples have a larger temperature gradient to the center of the particle, and therefore the reaction has not evolved as much as in the smaller samples.

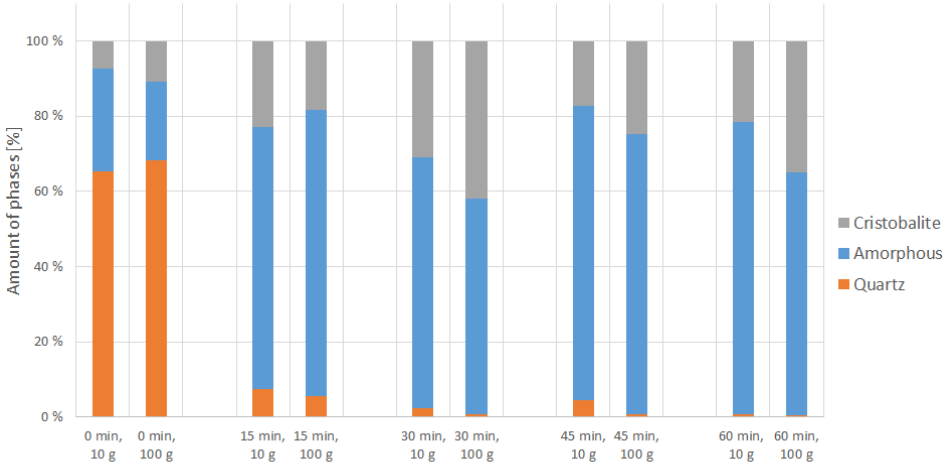

Figure 154: The amount of phases in samples from quartz type A, heated to 1700 °C.

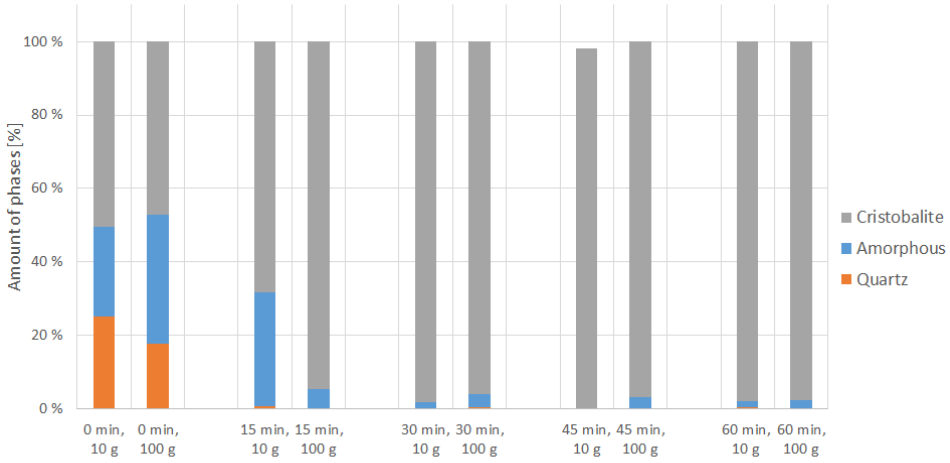

Figure 155: The amount of phases in samples from quartz type F, heated to 1700 °C.

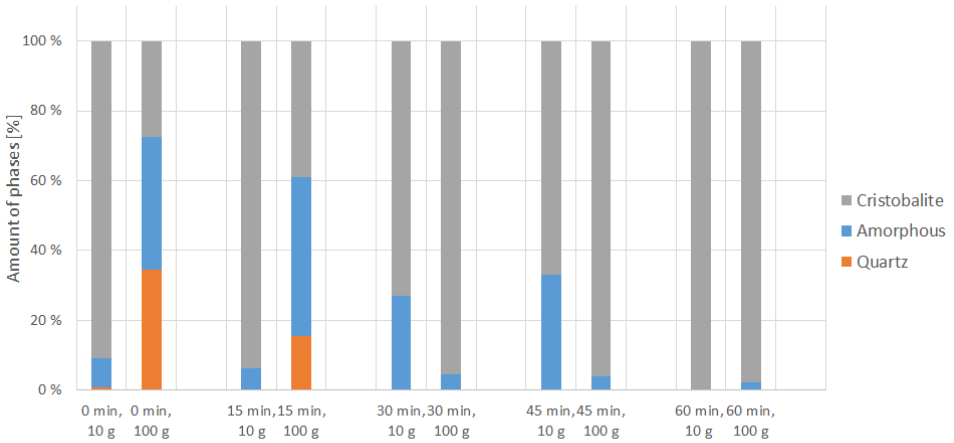

Figure 156: The amount of phases in samples from quartz type G, heated to 1700 °C.

The mechanism for phase transformations from quartz to amorphous phase and cristobalite is not clear. Wiik [22] argued that the transformation would happen throughout the sample because nucleation sites would appear evenly spread out in a sample. He also suggested that since the amorphous phase were less dense than quartz, the transformation would cause tension in the sample, and hence cause cracks in the remaining quartz. Neither Pagliari et al. [75], Dapiaggi et al. [76] or Kjelstadli [57] observed any consistent size effect in their studies. If there were a size effect and the transformation started at the surface, one should have seen a larger difference between the different sized samples. That is not observed in this study, and it is likely to assume that Wiik's [22] theory of nucleation is correct. Some researchers [73], [74] disagree, and claim that the phase transformation from quartz starts at the surface of a particle.

6.2.3 Lattice defects

Another factor that could affect the phase transformation rate is the degree of crystallinity, according to Wahl et al. [77]. They found that the higher crystallinity of a silica sample, the higher cristobalite formation temperature, i.e. amorphous silica would have the lowest cristobalite formation temperature. Fluid inclusions, cracks, impurities etc. would cause lattice defects and decrease the crystallinity. It is difficult to measure the crystallinity directly, but impurity measurements, crack measurements and microscopic investigation could give an indication of the degree of crystallinity. These properties are summarized in Table 22. The total impurity content is measured with ICP-OES. For water and clay content measured by FT-IR, only the relative amount is known, and each quartz type has achieved a score compared to the other types. The measurement of crack area was carried out using CT-scanning. The ability to transform found from the phase composition measurements is also presented in the table, also as a score from 1 to 4. When looking at the table, one can see that type A has the lowest impurity content, low score for the water and clay content and the lowest crack area, i.e. it has the lowest degree of lattice defects and hence a higher crystallinity than the other types. Type A also has the lowest ability to transform to amorphous phase and cristobalite. This is in agreement with Wahl et al.'s [77] theory that lattice defects would lower the cristobalite formation temperature. Wiik [22] suggested that nucleation sites would be created throughout the sample during heating. It could be possible that these nucleation sites easier form at defects in the sample. When looking at the other samples in Table 22, the same clear correlation is not observed. For sample F, which had the greatest ability to transform, the impurity content, and water and clay content are similar as for type A. The only

property correlating with the ability to transform is the crack area. This correlation is also seen for type D and G. If Wahl et al.'s [22] theory holds, it could indicate that cracks in the sample could initiate the creation of nucleation point throughout the sample. The impurity content could also affect, but the isolated effect is not seen in this study.

Table 22: Properties that could affect crystallinity in quartz type A, D, F and G, compared to the ability to transform to amorphous phase and cristobalite.

Quartz type	Impurity content [wt%] (1=highest, 4=lowest)	Water content (1=highest, 4= lowest)	Clay content (1=highest, 4= lowest)	Crack area [%] (1=highest, 4=lowest)	Ability to transform (1=highest, 4=lowest)
A	0.018 **3**	**3**	**4**	0.19 **4**	**4**
D	0.595 **1**	**2**	**1**	0.22 **3**	**3**
F	0.023 **2**	**4**	**3**	1.03 **1**	**1**
G	0.018 **3**	**1**	**2**	0.63 **2**	**2**

Mechanism of transformation

Wiik [22] argued that the transformations would happen throughout the sample at nucleation points evenly spread out. Ainslie et al. [73] and Breneman et al. [74] on the other hand argued that the transformation would happen from the surface of a particle and propagate inwards. If this was the case, there should have been a difference in the amount of phases between uneven sized samples. This was not observed to any large extend by Kjelstadli [57] or on the experiments in this thesis. The most probable mechanism for the transformation from quartz to cristobalite is therefore nucleation of amorphous transition phase throughout the sample. As Wahl et al. [77] showed that quartz with less defect would take the longest time to transform to cristobalite, it is presumable that the nucleation will be favored at cracks, impurities and other lattice defects. The crack area measured for type A, D, F and G compared to the ability to transform to cristobalite supports this theory. Type A had the lowest amount of cracks, while type F had the highest, and type A took the longest time to transform to cristobalite while type F took the shortest time. In Figure 157 the mechanism for the transformation is illustrated. The figure is not to scale. Amorphous phase will start to nucleate at grain boundaries, cracks, impurities and fluid inclusions, and propagate through the sample. Cristobalite will eventually start to form from the amorphous phase. Some lattice defects might be more favorable nucleation sites than other. This is not taken into account in the illustrated mechanism in Figure 157.

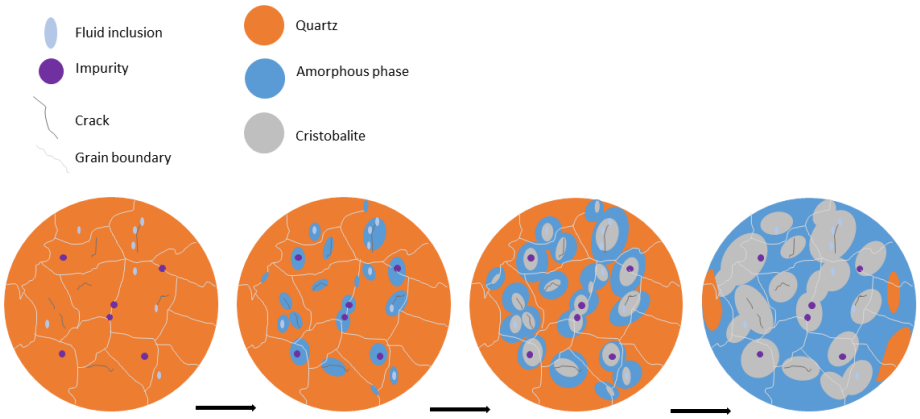

Figure 157: Illustration of the mechanism for phase transformation from quartz via amorphous phase to cristobalite. The illustration is not to scale.

6.2.4 Choice of model for phase transformation

The models for the phase transformations assumed a first order transformation both from quartz to amorphous phase and from amorphous phase to cristobalite. According to Helbæk et al. [81], if the assumption is correct, a plot of $ln(k_1)$ as a function of $1/T$, should give a straight line. In the experiments for the model only two temperatures were tested, and hence the plot will always be a straight line because there are only two points. To investigate further, experiments at 1550 °C and 1650 °C for quartz type A were performed with a holding time of 0, 30 and 60 minutes. Using the same method as for the main models presented in section 5.2.1, the k_1 and k_2 values at 1550 °C and 1650 °C were found. The k_1 and k_2 values found for 1550 °C, 1600 °C, 1650 °C and 1700 °C are shown in Table 23. k_1 is the apparent rate constant for the transformation from quartz to amorphous phase, and k_2 is the apparent rate constant for the transformation from amorphous phase to cristobalite. The k_1 values are believed to more reliable as they in general showed a lower deviation from the experimental value when optimizing the value. A plot of $ln(k_1)$ and a function of $1/T$ can be seen in Figure 158.

Table 23: k_1 and k_2 values for the transformation from quartz to amorphous phase, and amorphous phase to cristobalite respectively. The values are for quartz type A.

Temperature [°C]	1550	1600	1650	1700
k_1 [min^{-1}]	0.014	0.0161	0.034	0.1304
k_2 [min^{-1}]	0.047	0.0461	0.005	0.0026

When evaluating the regression line for the $ln(k_1)$ values in Figure 158, a rough estimate could be that the points are making a straight line, and thus confirming the first order model for the transformation from quartz to amorphous phase. There is some deviation from the straight line, but taking all the possible variations in the quartz itself and the uncertainty in the XRD measurements into account, a perfect straight line is not likely. However, it could also be possible that the most fitting model is a second order model. To get a more precise model more

experiments are needed. Based on the experiments performed for type A, and the possible variations and uncertainty taken into consideration, a first order model is the most robust and flexible model at this point. Another uncertainty in the model is the amount of amorphous phase measured close to the melting point of silica. It could be argued that the experiments at 1700 °C are too close to the melting temperature of silica. Melting and possibly softening would also create amorphous phase. For quartz type D, F and G the softening temperature has been measured at 1700 °C, 1680 °C and 1690 °C by Nordnes [17] [92]. The amorphous phase caused by softening and/or melting is not the intermediate phase, and hence it would interfere with the measured intermediate amorphous phase.

Based on the slope in the graph in Figure 158 a new activation energy for the transformation from quartz to amorphous phase for quartz type A, 10 g sample was calculated. The previous activation energy was 642 kJ/mol, while the new activation energy was 441 kJ/mol. It indicates that the activation energies calculated earlier in section 5.2.1 might be a bit high. To confirm them, the phase composition in samples heated to around 1550 °C should be measured, to be well below the melting temperature of silica.

Based on the k_2 values found in Table 23, $ln(k_2)$ is plotted as a function of 1/T in Figure 158. The values for k_2 does not make a straight line when comparing all the temperatures. There seems to be two levels of k_2 values, one for 1550 °C and 1600 °C, and one for 1650 °C and 1700 °C. At the low temperature level, the activation energy will be negative meaning that there is little variation in the formation of cristobalite at 1550 °C and 1600 °C. At the high temperature level, one can argue that the formation of amorphous phase as a consequence of softening and melting is affecting the measurements, and the k_2 values found are less reliable. This could explain the variation and the absent of a trend for the k_2 values.

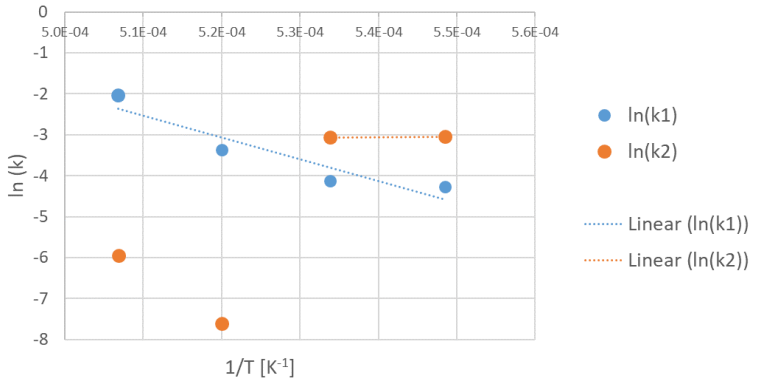

Figure 158: $ln(k_1)$ and $ln(k_2)$ as a function of 1/T for 1550 °C - 1700 °C. The dotted line connects the experiments used to find the activation energy for the transformation from quartz to amorphous phase (k_1) and from amorphous phase to cristobalite (k_2).

When considering what are the most reliable activation energies and the reaction rates for the different quartz types, one must take into consideration that to obtain them several assumptions have been made and the raw materials are natural with expected differences. Thus, the activation energies suitable to use can be rounded to the nearest hundred. For the calculations that gave a negative activation energy, it is believed that the experiments that were performed to find it, is not suitable. The activation energies that should be used for the types A, D, F and G for the transformation from quartz to amorphous phase are 400 kJ/mol, 200 kJ/mol, 500 kJ/mol and 100 kJ/mol. The calculated pre exponential factor, k_0, were 4.5×10^{10}, 3.2×10^{5} , 1.2×10^{13} and 4.1×10^{2}

for type A, D, F and G respectively. It should be taken into consideration that to determine the activation energy more precisely, experiments further away from the melting temperature of silica should be performed. As seen for type A, the activation energy decreased by 200 kJ/mol when experiments at 1550 °C and 1650 °C where considered in the calculation. The average of the k_1 values found from 10 g and 100 g experiments for 1600 °C varied from 0.02 min^{-1} to 0.12 min^{-1}. The variance in the reaction rate between the different types is not very large. For type D and F, the k_1 is 0.07 min^{-1}, while type A has the lowest reaction rate of 0.02 min^{-1} and type G the highest of 0.12 min^{-1}. At 1700 °C the average k_1 values based on the 10 g and 100 g experiments are 0.14 min^{-1} for type A and G, 0.16 min^{-1} for type D and 0.20 min^{-1} for type F. The most reliable activation energies for the transformation from amorphous phase to cristobalite for type A, F and G are 1300 kJ/mol, 300 kJ/mol and 100 kJ/mol, with preexponential factor 8.3×10^{32}, 5.5×10^{7} and 22.5 respectively.

6.2.5 Simulation of phase composition in industrial furnaces

Assuming first order phase transformations, the phase composition in an industrial furnace can be estimated. By knowing the retention time of the raw materials in the furnace, the descending speed of the raw material can be calculated, and also the temperature at this position can be estimated. For simplicity both the speed and the temperature gradient from the charge surface are assumed to be linear. By using Nordnes' [17] model in Figure 14, one can estimate that at 1.5 m depth in the furnace the temperature will reach 1700 °C. Together with the retention time of 5.7 hours [6] and an assumed furnace depth of 3.6 m, the speed will be 0.6 m/h for a quartz piece. The calculated time for the temperature increase from 1000 °C at the charge surface to 1700 °C will then be 2.5 hours. A model of the amount of phases as a function of furnace depth, temperature and time can then be made. This is done for type A and F. For type A, the calculated activation energy and pre exponential factor, k_0, for the transformation from quartz to amorphous phase found from Figure 158 are used, while the calculated activation energy and pre exponential factor from the 100 g experiments for type A are used for the transformation from amorphous phase to cristobalite. This choice is made because these experiments were the only one giving a positive activation energy for this transformation for type A. The numbers from experiments of 100 g are used for type F to calculate the amount of phases. It is also assumed that the start phase is 100 % quartz for both types. All the numbers used for the model are given in Table 24. In Figure 159 the models can be seen. Up to 1420 °C at 0.9 m depth the phase composition is very similar. The large differences are being visible at 1560 °C, where type F has a larger amount of cristobalite, around 30 %. At 1630 °C all of type F has become cristobalite while in type A there is around 35 % cristobalite and 40 % amorphous phase. The differences in the amount of phases could affect reaction rates, and the point in the furnace where the cristobalite forms might be of importance. It is also possible that volume expansion as a consequence of the cristobalite formation causes a more compact charge in the furnace, which will hinder even gas and raw material flow.

Table 24: Values used for estimating the amount of phases in an industrial furnace.

Quartz type	Quartz → Amorphous phase		Amorphous phase → Cristobalite	
	Activation energy [kJ/mol]	k_0	Activation energy [kJ/mol]	k_0
A	441	4.5×10^{10}	1337	8.3×10^{32}
F	510	1.21×10^{13}	325	5.5×10^{7}

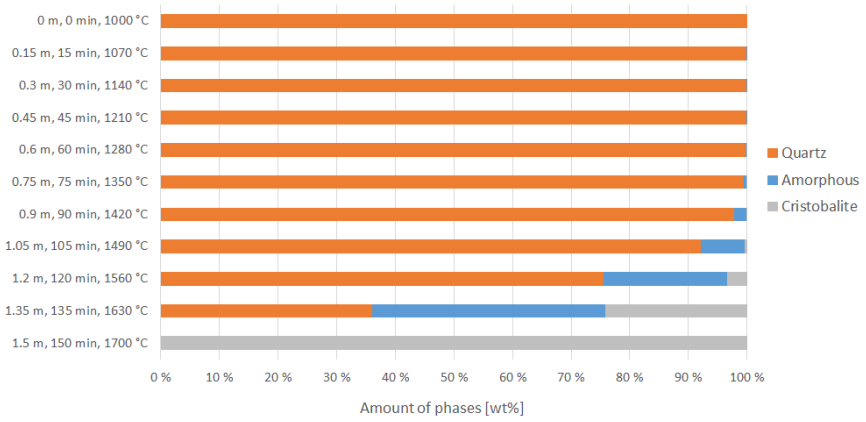

a) Modelled phase composition for quartz type A

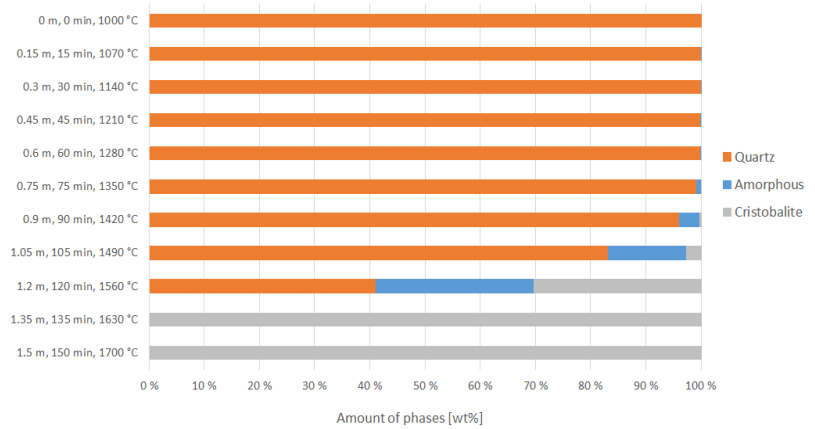

b) Modelled phase composition for quartz type F

Figure 159: Estimated phase composition of two different quartz types as a function of furnace depth, temperature and time. The models assume a linear temperature gradient and linear speed of the quartz sample.

7 Furnace excavation at Finnfjord

7.1 Observation from earlier furnace investigations

Investigations from furnace excavations have found that quartz will be altered when descending in the furnace. Aasly [6] found quartz, cristobalite and tridymite in the samples from a FeSi furnace running at 42 MW. The furnace was running on FeSi quality quartzite and a mixture of coal and coke in addition to iron pellets. The findings of tridymite were done in the inactive parts of the furnace, away from the electrodes, and possibly cavities. Aasly relates the tridymite findings to the higher impurity content on the FeSi furnace compared to a Si furnace. In the same investigation a pilot scale Si-furnace was also investigated, and here only quartz and cristobalite were found. The XRD-results also showed considerable amount of background noise, which is assumed to be amorphous silica.

To closer investigate silica samples from an industrial furnace, participation in a furnace excavation was included in this thesis work. Samples from the furnace were collected during the excavation and analyzed at NTNU. Both samples possibly containing silica and other samples were collected.

7.2 Furnace information

An excavation of a 75% FeSi furnace at Finnfjord was done in June 2018. The furnace had an inner diameter of 8.8 m, and a height of 3.7 m. Figure 160 shows an illustration of the furnace dimensions. The position of one of the electrodes are indicated. The furnace wall had a steel casing and a layer of bricks on the inside. The bottom of the furnace consisted of a thick layer of bricks with carbon paste above. Only tap hole 2 and 3 were used, and in the last period before shut down, tap hole 3 was used. The furnace was not melted down before shut down. Electrode 2 and 3 were cut off during shut down, while electrode 1 was not. Therefore, the excavation was concentrated around electrode 1.

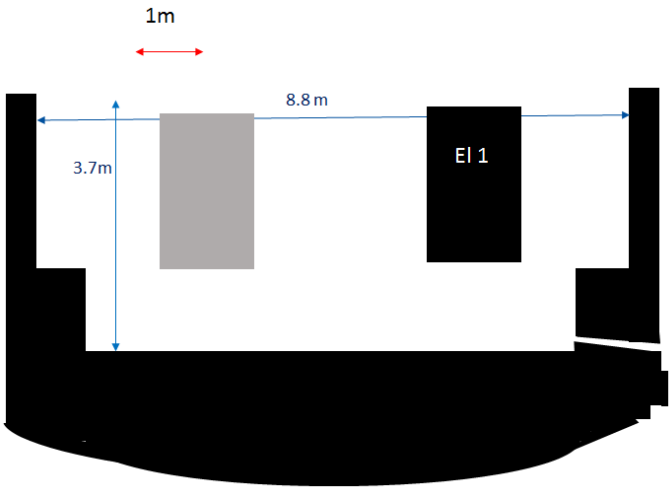

Figure 160: Overview of furnace excavated at Finnfjord.

7.3 Results and discussion

7.3.1 Overview of the excavation

The furnace was opened towards electrode 1, where the excavation was concentrated. First, the steel casing was removed before chiseling began. The material was very warm, so continuous water cooling was necessary. In photograph in Figure 161, the start of the excavation can be seen. The chiseling has just began, and glowing material can be spotted under the outer surface.

Figure 161: Photo taken during excavation of a 75% FeSi furnace at Finnfjord.

The position of samples is approximately, as it is not possible to enter the furnace and mark the exact position because of the heat and other HSE restrictions. Samples were collected from the start of the excavation until over half of the furnace was excavated. At that point the interior of the furnace had been moved around too much to be able to estimate the original position of samples. Also, electrodes 2 and 3 had been put to the bottom of the furnace before shut down. Such actions make the area around and underneath these electrodes very uncertain. It is not possible to figure out if the observations are such due to the electrode cut off or if it gives a picture of how the furnace behaved during operation. Electrode 1 was not put to the bottom of the furnace, so many samples were taken in this area and made the basis for the conclusion.

After two days of excavation, electrode 1 became visible. From this point, it was possible to distinguish different material zones in the furnace. A photograph with approximate material zones can be seen in Figure 162. The electrode is clearly seen. Around it, a thin layer of unreacted charge was found near the top of the furnace. Further away from the electrode, SiC was found. Towards the side of the furnace slag layers were observed. Underneath the electrode a very hard layer was found. This was assumed to be a mixed metal and slag layer. Samples were taken from the furnace, and analyzed with EPMA to confirm the suspected material zones.

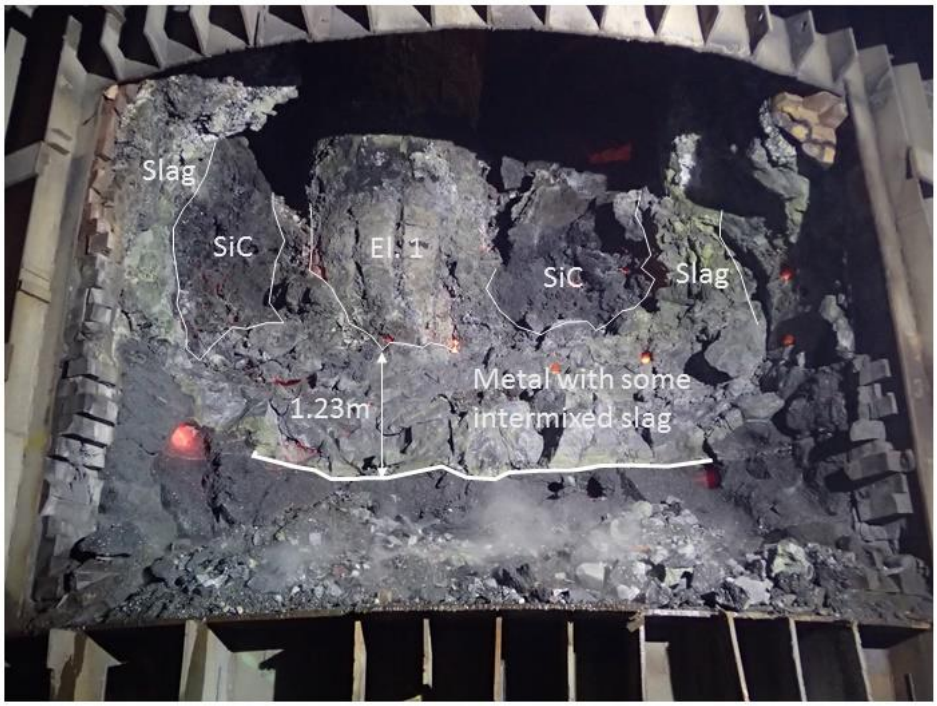

Figure 162: Material zones observed in the furnace during excavation. Electrode 1 is visible in the middle of the picture, and SiC, slag and metal zones are indicated.

Based on the observation, a drawing of a horizontal cross section of the furnace approximately 1 m under the charge surface was made. It can be seen in Figure 163. Around the electrodes and at the charge surface, loose material was found. Outside this layer and between the electrodes SiC was observed. Towards the outer shell a slag layer was found and some areas of inactive zone. The figure also shows the material zones for the whole area if it is assumed that the same materials are found around the other electrodes. A vertical cross section of the furnace through electrode 1 is illustrated in Figure 164. This figure tries to simplify what is visually observed in Figure 162.

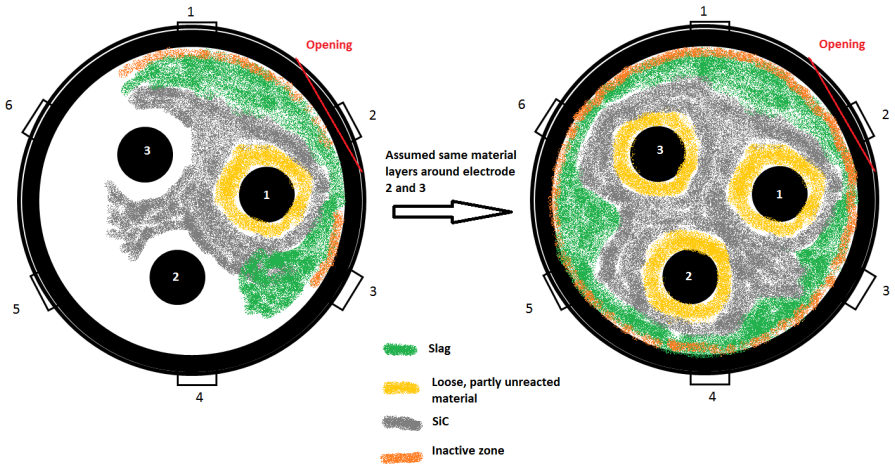

Figure 163: Overview of material zones seen from the top of the furnace. The figure to the left is visually observed, while the figure to the right is drawn based on the assumptions that the same material zones are found around the other two electrodes as well.

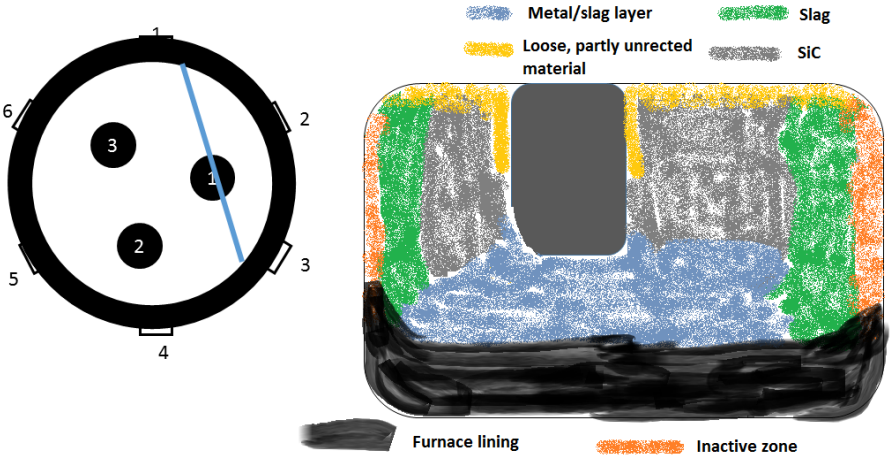

Figure 164: Cross section of the furnace seen through an excavation opening indicated in the figure to the left.

7.3.2 Collected samples and EPMA analysis

Approximately 80 samples were collected during the excavation. From these, eleven samples were picked out as representative for the zone they were collected. The approximately position of these samples can be seen in Figure 165. Some positions are better known than others. This is indicated in the figure. These samples were analyzed with electron probe micro-analyzer (EPMA) to confirm the material composition of the zone they were collected. For each material zone a representative EPMA analysis is shown in the following sections. The samples collected were crushed with a hammer to obtain a piece suitable for EPMA analysis. Samples were casted into epoxy and polished before inserted into the microscope. All the casted samples had a diameter of 3 cm.

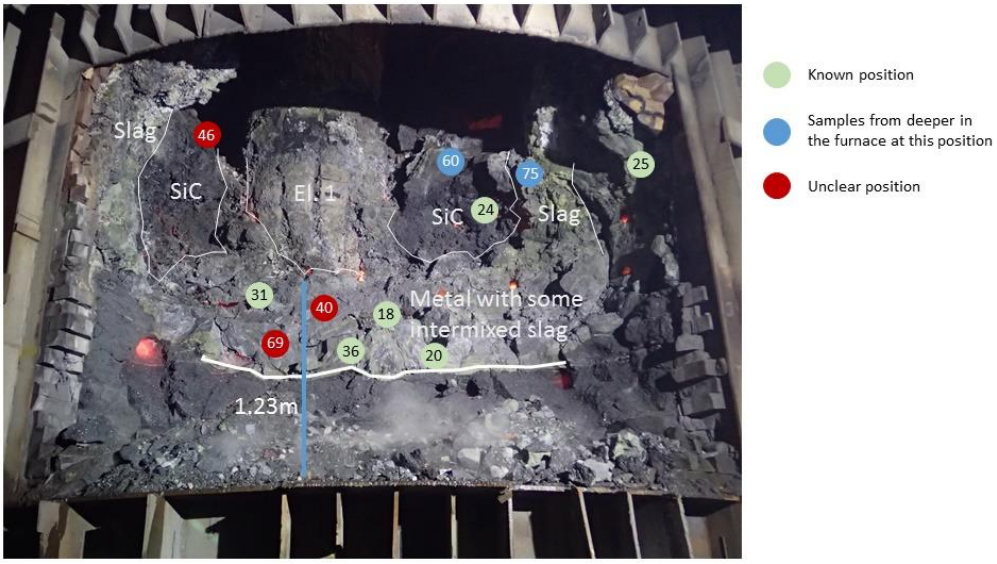

Figure 165: Approximately position of samples analyzed. The color indicates the precision of the position.

Slag/metal underneath electrode

Two EPMA analysis from sample P36 are seen in Figure 166. Both samples show a metal phase and a slag matrix with SiC particles. These analysis shows that two smaller samples from the bulk sample contains the same phases. Each point marked on the figure has been analyzed for different elements. The composition from each point is given in Table 25.

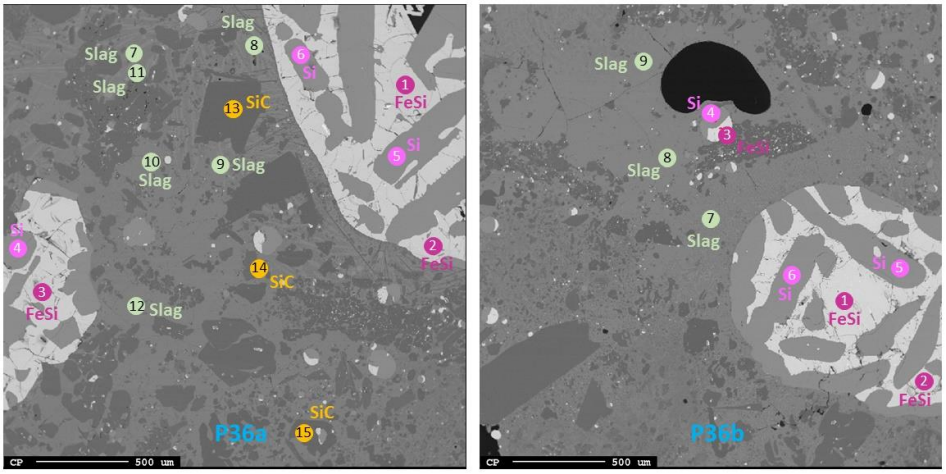

Figure 166: Two samples from the same bulk piece, P36. A slag phase with some SiC particles are present in addition to a metal phase.

Table 25: Chemical analysis of sample P36a and b collected during furnace excavation. . The table shows an average of the position numbers listed.

Position no.	Sample no.	Element analysis (wt%)									Phase
		Si	O	C	Fe	Ca	Al	K	Na	Mg	
1,2,3	P36a	56.8	0.4	1.4	44.6	0.0	0.3	0.0	0.0	0.0	FeSi
4,5,6	P36a	98.8	0.4	2.2	0.1	0.0	0.0	0.0	0.0	0.0	Si
7,8,9	P36a	14.7	36.9	0.8	0.0	19.5	20.4	0.1	0.0	0.4	Slag
10,11,12	P36a	14.8	37.0	0.9	0.0	18.8	21.4	0.1	0.0	0.4	Slag
13,14,15	P36a	70.5	0.5	33.3	0.0	0.1	0.1	0.0	0.0	0.0	SiC
1,2,3	P36b	56.2	0.4	1.2	45.1	0.0	0.1	0.0	0.0	0.0	FeSi
4,5,6	P36b	98.0	0.4	1.7	0.2	0.0	0.0	0.0	0.0	0.0	Si
7,8,9	P36b	15.8	39.4	0.7	0.0	19.6	19.6	0.2	0.0	0.3	Slag

SiC sample

A SiC sample, P60, collected in the upper part of the furnace was one of three SiC samples analyzed with EPMA. In Figure 167 the EPMA image can be seen, marked with the position where element analysis was done. The sample consist of mainly a dense SiC phase, with some small metal droplets. In Table 26 the element analysis from the EPMA can be seen.

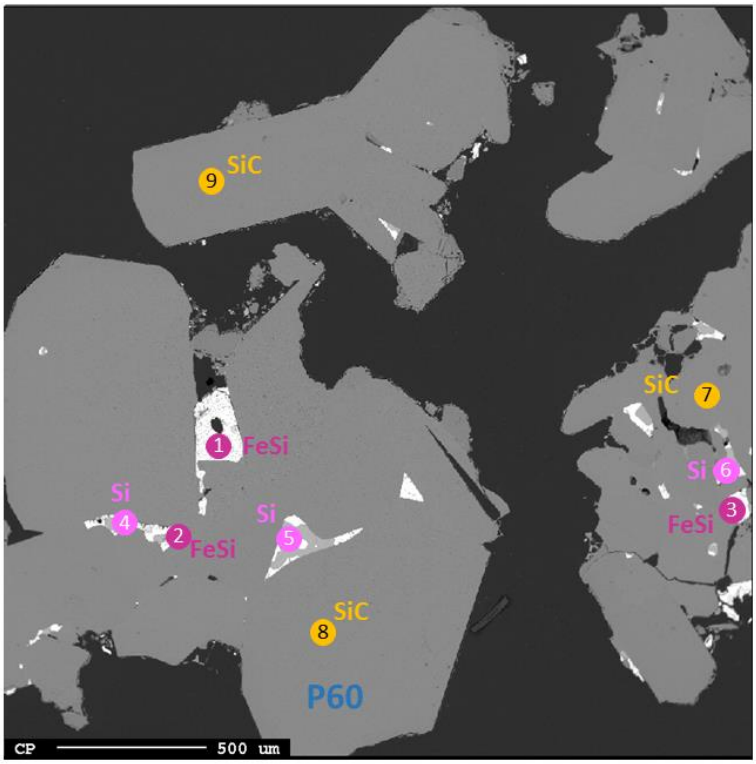

Figure 167: Sample P60 which contains a dense SiC phase with some metal droplets.

Table 26: Chemical analysis of sample P60 from furnace excavation. The table shows an average of the position numbers listed.

Position no.	Sample no.	Element analysis (wt%)									Phase
		Si	O	C	Fe	Ca	Al	K	Na	Mg	
1,2,3	P60	55.6	0.3	0.7	45.2	0.0	0.0	0.0	0.0	0.0	FeSi
4,5,6	P60	98.8	0.2	1.0	0.3	0.0	0.0	0.0	0.0	0.0	Si
7,8,9	P60	69.1	0.3	30.6	0.0	0.0	0.1	0.0	0.0	0.0	SiC

Slag phase

Two samples were collected from the assumed slag zones towards the side of the furnace. The position of the samples can be seen in Figure 165. Sample P75c is shown in Figure 168, with the chemical analysis in Table 27. The sample consist of a slag matrix with some SiC particles and some metal particles.

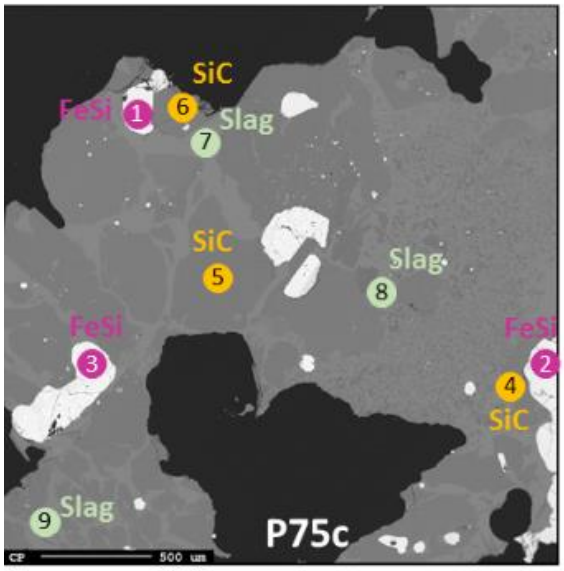

Figure 168: Sample P75c from furnace excavation. The sample has a slag matrix with some SiC particles and some metal particles.

Table 27: Chemical analysis of sample P75c from furnace excavation. The table shows an average of the position numbers listed.

Position no.	Sample no.	Element analysis (wt%)									Phase
		Si	O	C	Fe	Ca	Al	K	Na	Mg	
1,2,3	P75c	54.0	0.2	0.6	48.1	0.0	0.0	0.0	0.0	0.0	FeSi
4,5,6	P75c	68.8	0.4	29.0	0.0	0.0	0.0	0.0	0.0	0.0	SiC
7,8,9	P75c	28.7	40.2	0.5	0.0	11.0	12.0	0.4	0.0	2.2	Slag

7.3.3 Quartz in the excavation

Nine samples of silica, either quartz, or visually transformed quartz, were collected in the excavation to study how the quartz/silica is present at different positions in the furnace. The goal was to see which, and how much of the different silica phases were present where.

Samples which were assumed to contain silica based on visual inspection, were selected. The position of the samples could only be estimated very roughly. There are three places were suitable samples were collected. Most of the samples were collected around the electrode tip. Some samples were taken from a pile of material which had been dug out during excavation, and some samples were taken from the top layer in the furnace. In Table 28 an overview of the samples and their approximate position can be seen.

Table 28: Samples which contains quartz from furnace excavation in Finnfjord. The position of the samples is also indicated.

Sample	Position	Visual observations
P38	Electrode tip 1	Mainly melted quartz, pores observed.
P41	Electrode tip 1	Mainly quartz, pores observed.
P53	On electrode 1	Mainly quartz, some slag, a few metal droplets.
P67	On electrode 1	Quartz with SiC around. Some C particles and slag observed.
P70	On electrode 1	Some metal with SiC inside. A lot of quartz as well. Cracks at surface.
P54	Pile of excavation material	Mainly quartz. Canals observed.
P58	Pile of excavation material	Melted quartz, but complex sample with many materials
P61	Top layer	Mainly quartz with pores and slag defects, but more slag along side. Some metal droplets.
P79	Top layer	Carbon and quartz. More homogeneous quartz, but melted. Intrusions in the carbon and SiC around carbon, meaning the carbon has started to react at surface

Sample P38 and P41 – from electrode tip

Sample P38 was taken on the side of the electrode. Macroscopically it looked like melted silica. In Figure 169 a photograph of the sample can be seen, along with the sample prepared for EPMA. To the right in the figure the EPMA image with a magnification of 40X can be seen. The numbers in red indicate were element analysis are performed. In Table 29, the wt% of different elements at given positions can be seen. As expected, all the point analyzed showed a SiO_2 phase.

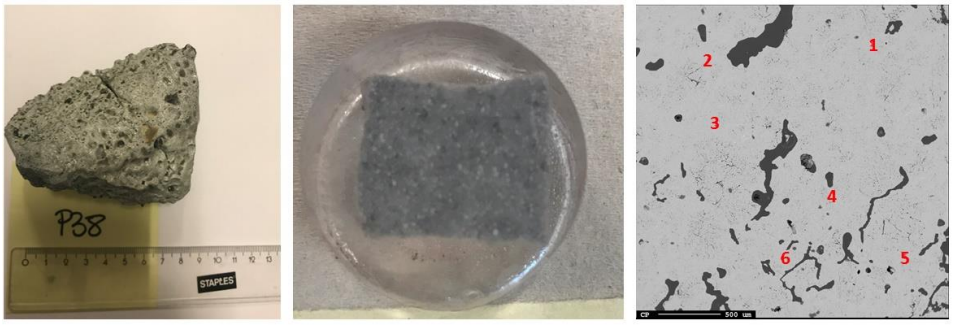

Figure 169: Sample P38

Table 29: Element analysis of sample P38. The position number refers to the right picture in Figure 169. The element analysis is an average of all the positions.

Position no.	Sample no.	Element analysis (wt%)									Phase
		Si	O	C	Fe	Ca	Al	K	Na	Mg	
1,2,3,4,5,6	P38	46.3	58.1	0.3	0.0	0.0	0.2	0.1	0.0	0.0	SiO_2

Sample P41 were also collected form the electrode tip. It had a darker appearance than sample P38 on the outside, but when comparing the casted and grinded sample they look the same. This is seen in Figure 170, were also an image from the EPMA analysis is seen. The numbers on the image refer to the point where an element analysis is done. The elements identified is listed in Table 30, and it concludes that all the point analyzed where SiO_2.

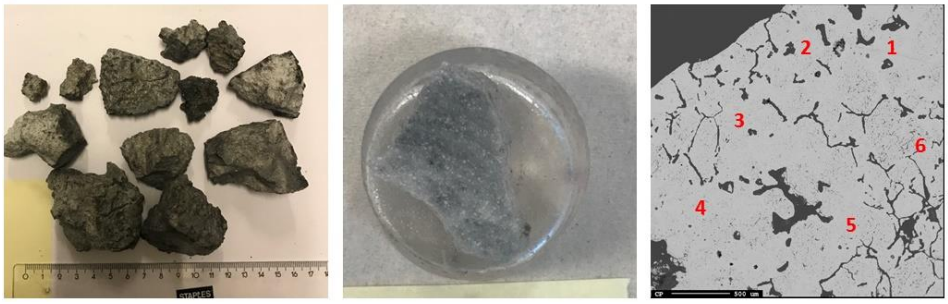

Figure 170: Sample P41

Table 30: Element analysis of sample P41. The position number refer to the right picture in Figure 170.

Position no.	Sample no.	Element analysis (wt%)									Phase
		Si	O	C	Fe	Ca	Al	K	Na	Mg	
1,2,3,4,5,6	P41	46.3	57.6	0.7	0.0	0.0	0.1	0.0	0.0	0.0	SiO_2

Sample P53, P67 and P70 - from electrode

Sample P53 were also collected from the electrode. It looked like it was mixed with some slag and other impurities. A photograph of the sample together with the sample prepared for EPMA and the EPMA image are seen in Figure 171, and in Table 31 the elements identified are listed. It suggests that the sample contained a SiO_2 rich slag together with some metal.

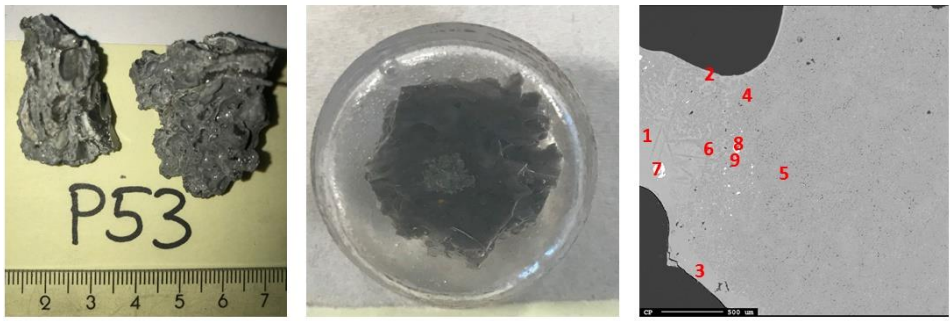

Figure 171: Sample P53

Table 31: Element analysis of sample P53. The position number refer to the right picture in Figure 171

Position no.	Sample no.	Element analysis (wt%)									Phase
		Si	O	C	Fe	Ca	Al	K	Na	Mg	
1,2,3	P53	38.4	40.1	0.5	0.0	0.2	1.8	3.8	0.1	2.2	SiO_2 rich slag
4,5,6	P53	45.9	55.3	0.7	0.0	0.0	0.1	0.4	0.0	0.1	SiO_2
7,8,9	P53	23.8	0.5	0.6	77.2	0.0	0.0	0.0	0.0	0.0	FeSi

In Figure 172, an image of sample P67 is seen together with the EPMA sample and the EPMA image. The sample contained mainly SiO_2, with some slag and metal in between. The element analysis can be seen in Table 32.

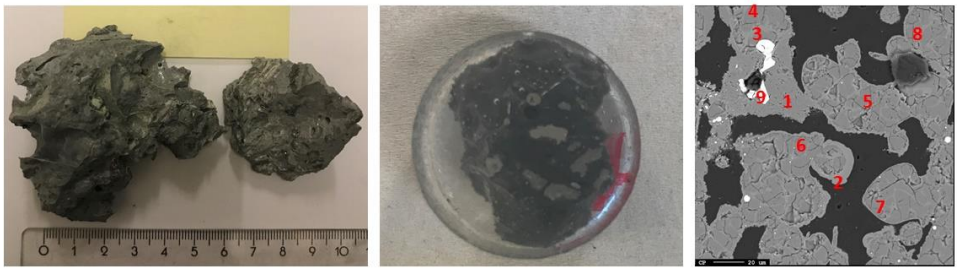

Figure 172: Sample 67

Table 32: Element analysis of sample P67.

Position no.	Sample no.	Element analysis (wt%)									Phase
		Si	O	C	Fe	Ca	Al	K	Na	Mg	
1	P67	67.3	0.8	5.9	0.1	0.0	0.0	0.0	0.0	0.0	Si*
2	P67	60.5	11.3	4.9	0.0	0.3	1.7	0.3	0.0	0.0	Si*
3	P67	35.0	44.5	0.8	0.2	1.8	9.0	2.9	0.0	0.3	SiO_2
4,5,6	P67	45.3	53.1	1.0	0.1	0.1	0.2	0.0	0.0	0.0	SiO_2
7,8	P67	36.1	46.5	0.9	0.2	1.9	8.4	2.4	0.0	0.3	SiO_2 rich slag
9	P67	35.4	0.6	0.9	66.4	0.0	0.0	0.0	0.0	0.0	FeSi

* The total mass percent does not add up to 100 %, so there could be other elements present altering the material phase.

The next sample, P70 had a glassy surface which looked like melted quartz on a more solid core. It was found on the electrode. In Figure 173 an image of the sample together with the EPMA sample and EPMA image can be seen. The element analysis for the number on the EPMA image is given in Table 31. The element analysis shows that the sample contained a SiO_2 phase with some metal with some SiC particles.

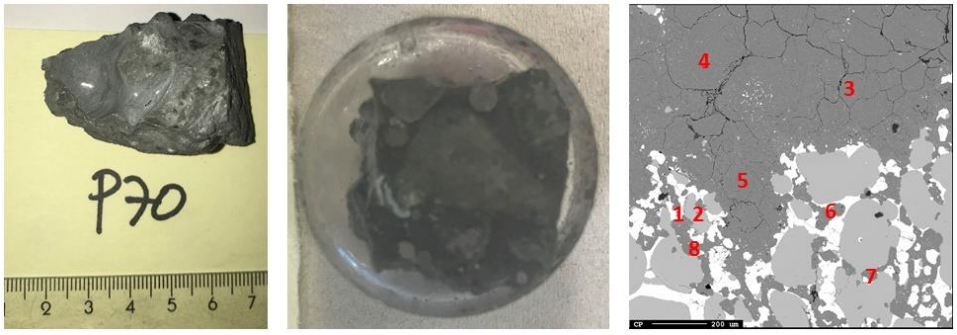

Figure 173: Sample P70

Table 33: Element analysis of sample P70

Position no.	Sample no.	Element analysis (wt%)									Phase
		Si	O	C	Fe	Ca	Al	K	Na	Mg	
1	P70	55.8	0.3	0.9	45.5	0.0	0.0	0.0	0.0	0.0	FeSi
2	P70	97.1	0.3	1.2	0.1	0.0	0.0	0.0	0.0	0.0	Si
3,4,5	P67	42.3	54.0	0.7	0.0	0.9	3.2	0.3	0.0	0.2	SiO_2
6,7,8	P67	69.0	1.0	30.5	0.5	0.0	0.0	0.0	0.0	0.0	SiC

Sample P54 and P58 from pile of excavated material

The next two samples, P54 and P58 were found in the pile of excavation material removed from the furnace. Based on the appearance of the quartz it could be possible to estimate at least the temperature it has experienced. In Figure 174 an image of the sample can be seen. It looks like a lump of quartz that has experienced some heat. When looking at the sample prepared for EPMA one can easily see that this is a solid piece of quartz. The EPMA image shows that there are areas in the quartz with lighter color. The element analysis in Table 34, shows that these areas are a SiO_2 rich slag. The rest of the sample is SiO_2.

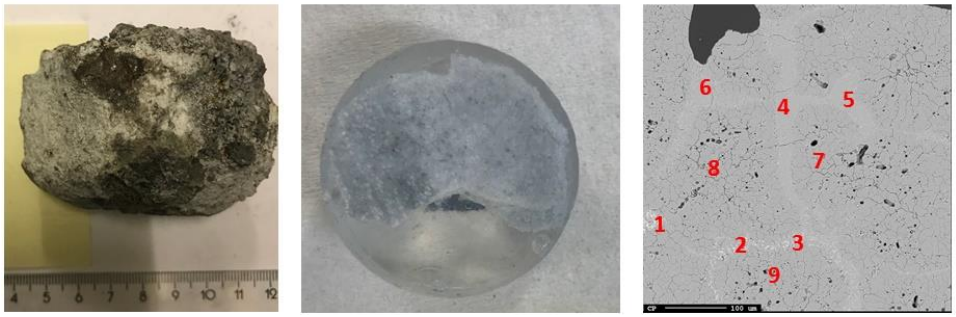

Figure 174: Sample P54

Table 34: Element analysis of sample P54

Position no.	Sample no.	Element analysis (wt%)									Phase
		Si	O	C	Fe	Ca	Al	K	Na	Mg	
1,2,3	P54	37.2	46.1	0.4	0.0	0.0	2.2	3.3	0.4	1.0	SiO_2 rich slag
4,5,6	P54	43.4	55.5	0.5	0.1	0.0	1.6	1.6	0.4	0.2	SiO_2
7,8,9	P54	46.4	59.5	0.4	0.0	0.0	0.0	0.0	0.0	0.0	SiO_2

Sample P58 was also collected from the pile of excavation material, and the original position in the furnace is therefore not known. From the image of the sample in Figure 175, the sample looks very complex with different materials partly melted into each other. The same is observed in the image of the EPMA sample. In the EPMA image a compact phase can be seen with a band of other materials. The element analysis, given in Table 35, suggests that the major phase is SiO_2, with some slag impurities in the band crossing the sample.

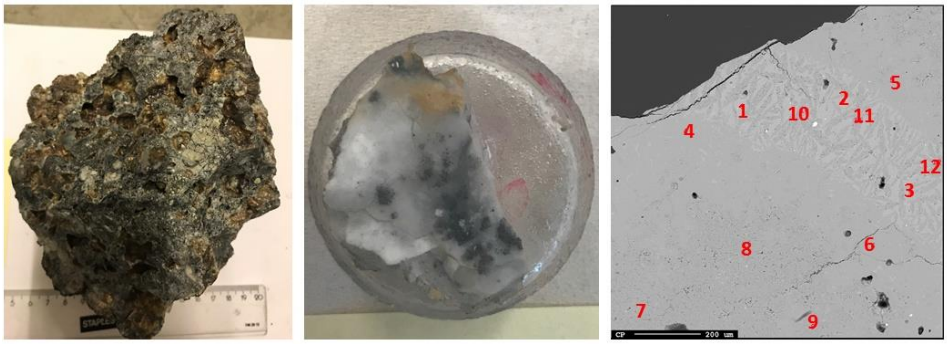

Figure 175: Sample P58

Table 35: Element analysis of sample P58

Position no.	Sample no.	Element analysis (wt%)									Phase
		Si	O	C	Fe	Ca	Al	K	Na	Mg	
1,2,3	P58	36.8	48.5	0.7	0.0	0.2	5.6	3.7	0.2	2.0	SiO_2 rich slag
4,5,6	P58	45.6	52.9	0.8	0.0	0.0	0.1	0.1	0.0	0.0	SiO_2
7,8,9	P58	45.8	53.4	1.0	0.0	0.0	0.0	0.0	0.0	0.1	SiO_2
10,11,12	P58	45.0	54.4	1.0	0.0	0.0	0.3	0.0	0.0	0.1	SiO_2

Sample P61 and P79 from top layer in furnace

The last two samples were collected from the upper part of the furnace, and could give information on how the quartz is behaving at lower temperatures before it melts. In Figure 176 sample P61 is seen. From the image it looks like a solid quartz lump with some other materials glued to it. The EPMA sample shows a grey more or less homogeneous phase. The same is observed from the EPMA image. The sample contains mostly SiO_2, with some small slag and metal impurities. Slag is also observed at surfaces, for example around analyze point 2 in Figure 176.

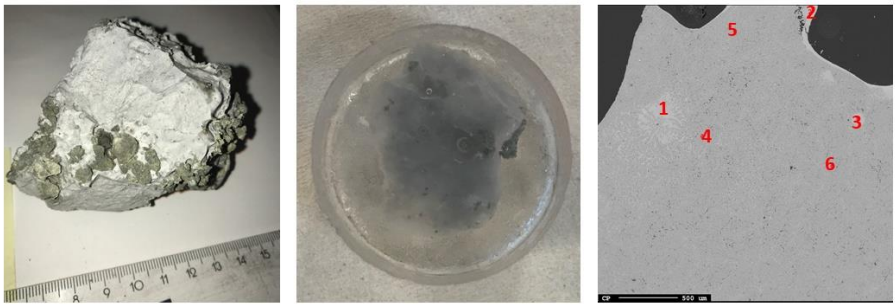

Figure 176: Sample P61

Table 36: Element analysis of sample P61

Position no.	Sample no.	Element analysis (wt%)									Phase
		Si	O	C	Fe	Ca	Al	K	Na	Mg	
1,2,3	P61	36.5	42.6	0.4	0.0	0.1	5.0	5.2	0.0	0.7	SiO_2 rich slag
4,5,6	P61	46.3	60.2	0.4	0.0	0.0	0.1	0.1	0.0	0.0	SiO_2
7,8,9	P61	20.7	0.4	0.3	81.7	0.0	0.0	0.0	0.0	0.1	FeSi

Sample P79 has a very complex appearance like seen from the sample image in Figure 177. It looks like there is some quartz mixed with carbon materials and some green condensate. The EPMA image shows a surface that is partly converted. A layer of a different material can be seen. The element analysis in Table 37 confirms this. The core of the sample is SiO_2, while there is a SiO_2 rich slag phase towards the surface.

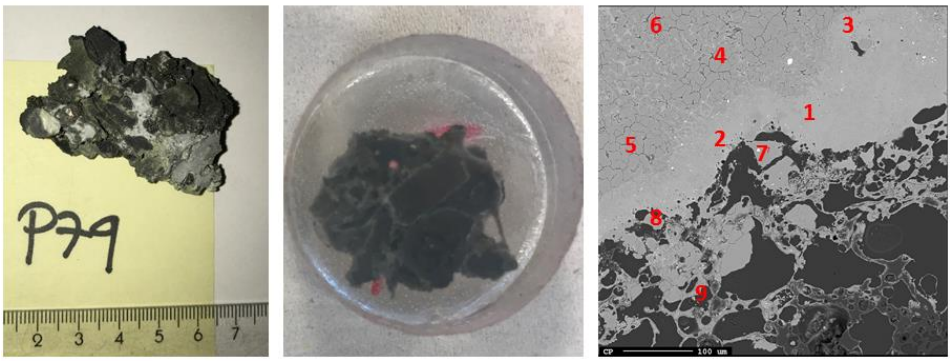

Figure 177: Sample P79

Table 37: Element analysis of sample P79

Position no.	Sample no.	Element analysis (wt%)									Phase
		Si	O	C	Fe	Ca	Al	K	Na	Mg	
1,2,3	P79	39.1	47.3	0.4	0.0	0.1	3.1	5.0	0.0	0.4	SiO_2
4,5,6	P79	46.1	56.0	0.4	0.4	0.0	0.0	0.0	0.0	0.0	SiO_2
7,8,9	P79	59.2	6.9	26.6	0.1	0.0	0.1	0.2	0.0	0.0	SiC

7.3.4 Phase composition in samples

The phase composition in the different samples was measured using XRD. Jiali He, intern student did these measurements, under my supervision. The results can be seen in Figure 178. The overall observation from the figure is that all the samples contain no or very little amount of quartz, hence amorphous phase and cristobalite is the dominating silica phases in the furnace. The samples are plotted in increasing height in the furnace along the x-axis to see any trend in the phase composition as a consequence of the position. It was expected to see a difference in the phase compositions from the samples taken from the top of the furnace and further down because of the temperature difference in the furnace. At the top the temperature is from 700 °C to 1300 °C [5] , while at the electrode tip the temperature could be around 2000 °C [3]. A clear difference is not observed, but this could be due to few samples available from the top of the furnace. Only two samples were analyzed from the top, and one of them have a higher amount of amorphous phase than the lower samples, while one has the same amount of amorphous phase. It must be taken into account that at the time of excavation of the samples, they had experienced a high temperature for up to 4 days. This could have caused any remaining quartz to transform to amorphous phase and the cristobalite phase before the furnace was cooled sufficiently to stop any phase transformations. It is also possible that some of the samples had been melted, and therefore increased the amount of amorphous phase measured. When compared to the phase composition of 10 g samples heated to 1600 °C of quartz type D tested in the laboratory, the amount of quartz after just two hours were 0 wt%. This is seen in Figure 117. Quartz type D is the same as used in the industrial furnace. It was observed during excavation that liquid metal could flow out of the excavation front. This implies that the temperature must be sufficiently high for liquid FeSi to exist. The melting point of FeSi75 is below that for Si at 1410 °C [127]. It is therefore likely to presume that phase transformation after shut down did happen in the furnace due to the high temperatures. To more accurate measure the silica phases in samples from a furnace, a different collection method where the samples can be removed more quickly from high temperature should be considered. Another source of error are other compounds present in the samples. If they are not identified, they will be counted as amorphous phase and hence give a higher amount of amorphous phase than really present. This does not affect the amount of crystalline phases, quartz, tridymite and cristobalite.

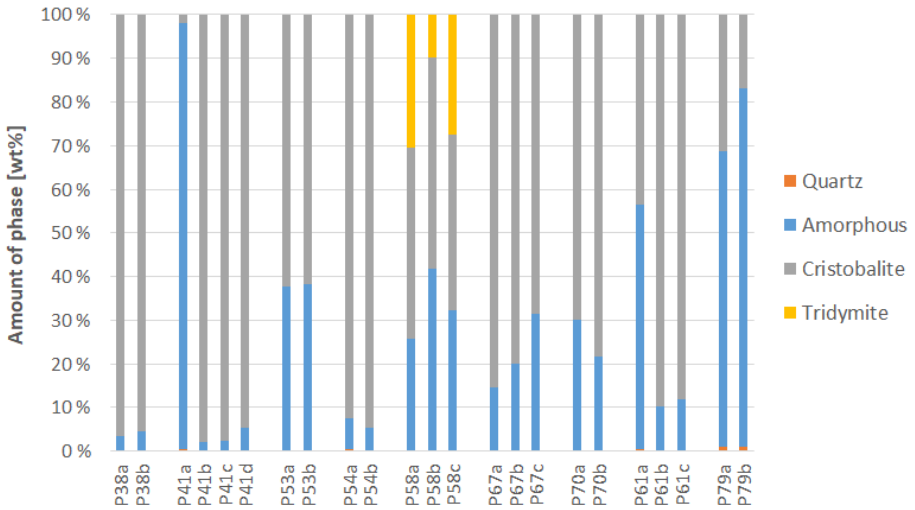

Figure 178: Phase composition in silica samples from furnace excavation of a FeSi75 furnace.

In one of the samples, P58, tridymite was also found in addition to amorphous phase and cristobalite. The formation of tridymite is believed to be dependent on certain impurity elements according to several studies [49], [50]. In sample P58 a considerably amount of Mg were found. Since both Na and K are impurities stabilizing the tridymite phase [49], it is presumed that Mg has a similar effect, and hence explains the existence of tridymite in sample P58.

8 Conclusions and future work

The high temperature behavior of quartz, used for Si or FeSi production, have been investigated. More specifically, the fines generation and the phase transformations in different quartz types have been studied. In addition, FT-IR analyses were done, and used to compare water and clay content in different quartz types, and CT-scanning were used to determine the crack area in samples before heating. The correlation between different properties in the quartz types and the behavior at high temperature were studied. Four main quartz types, A, D, F and G were thoroughly studied, and quartz type B, C, E, H, I and J were used in some experiment to obtain a broader basis for comparison.

8.1 Fines generation

Ten different quartz types used in silicon and ferrosilicon production were shock heated at 1500 °C for ten minutes. The amount of fines after heating, were measured and compared. Type D created the least amount of fines, around 5 wt% below 10 mm, while type F created the largest amount of fines, up to 85 wt%. For some of the samples CT-scans were done before heating, and the crack area were measured. A correlation was found between the measured crack and the amount of fines created during shock heating. There was some inconsistency in the trend, but due to natural variation in the quartz samples, such are expected. Statistical calculations showed that despite internal variation, it was a difference between the quartz types as well. The amount of amorphous phase and cristobalite were also measured in the shock heated material. It was earlier believed that the cristobalite formation would cause a volume increase that would lead to disintegration of the quartz samples [83]. No correlation between the amount of amorphous phase and cristobalite and the amount of fines created were found. In fact, type D which disintegrated the least had the highest amount of cristobalite after shock heating. Based on FT-IR results and the disintegration results, a principal component analysis was done to check for correlation between the two data sets. It was found that quartz type D and E contained the highest amount of muscovite, and type D and E were also the quartz types creating the least amount of fines during shock heating. It is speculated that since muscovite has a more layered structure which are compressible in one direction, quartz types with high muscovite content could absorb the tension created during shock heating. A correlation was also seen between the grain size in the different samples and the ability to disintegrate. Based on microscopic investigation, the grain size in type A, D, F and G were described. Type D had very small grains, 0.2-1 mm and disintegrated the least. Type A and G had varying grain size from the µm to cm scale. These two types had medium disintegration upon shock heating. In type F, the largest grains were observed. Some grains were several cm. Type F was the type creating around 70 wt% of fines upon shock heating. This theory is supported by investigating the ability to disintegrate for different regimes in type G as well. Three regimes were identified, and the grain size was largest in regime 1. Shock heated samples from this regime also shows the highest amount of fines after shock heating, compared to samples from regime 2 and 3 which has smaller grains. It could be possible that increased amount of grain boundaries would strengthen the quartz samples [126].

8.2 Phase transformations

The phase transformation from quartz to amorphous phase to cristobalite in the main types A, D, F and G were thoroughly investigated. Samples of 10 g and 100 g were heated to 1600 °C and 1700 °C and held up to 120 minutes for 10 g samples and 60 minutes for 100 g samples. The ability to transform for the different types was varying. By comparing the amount of remaining quartz at 1600 °C and no holding time, around 90 % of type A were still quartz, while in type F only 5 % quartz were remaining. Type D and G had 55 % and 20 % remaining quartz respectively. The phase transformations were modelled, assuming a first order reaction for both quartz to amorphous phase transformation, and from amorphous phase to cristobalite

transformation. It was found that the activation energy for the phase transformation from quartz to amorphous phase varied from 642 kJ/mol for type A to -244 kJ/mol for type F. The negative activation energy indicated that the experiments were not suitable to determine the activation energy. The 100 g samples of type F gave an activation energy of 510 kJ/mol. Additional experiments at 1550 °C and 1650 °C found a more fitting activation energy of 400 kJ/mol for type A. The most reliable activation energy, rounded to the nearest hundred, found for the quartz types A, D, F and G were 400 kJ/mol, 200 kJ/mol, 500 kJ/mol and 100 kJ/mol respectively, and the calculated pre exponential factor, k_0, were 4.5×10^{10}, 3.2×10^{5} , 1.2×10^{13} and 4.1×10^{2} for type A, D, F and G respectively. For the transformation from quartz to amorphous phase, the apparent rate constant, k_1, was varying from 0.002 min^{-1} to 0.184 min^{-1} at 1600 °C, and from 0.033 min^{-1} to 0.363 min^{-1} at 1700 °C. These values show that the transformation from quartz to amorphous phase goes faster at 1700 °C compared to 1600 °C, as expected. Based on the average of 10 g and 100 g experiments the k_1 values found for type A, D, F and G at 1600 °C were 0.02 min^{-1}, 0.07 min^{-1}, 0.07 min^{-1}, and 0.12 min^{-1} respectively. The k_2 values were in general lower than the k_1 values, meaning that the transformation from quartz to amorphous phase is faster than the transformation from amorphous phase to cristobalite. It is suspected that softening and melting of quartz will cause amorphous phase when heated near the melting point of silica. This amorphous phase will interfere with the measured intermediate amorphous phase. Hence, experiments at lower temperatures than 1700 °C and possibly 1650 °C should be used to determine rate constants and activation energies.

No clear size effect was seen between the 10 g and 100 g samples. This indicated that transformation happen throughout the samples at nucleation sites, and not from the outside an inwards.

The ability to transform for the different types were compared with the impurity content. A correlation was found between type A, F and G and the amount of alkali and alkali earth elements. No correlation was seen with the amount of Al content, as previously suggested in the literature [50], [78].

It was suggested in literature [77] that more perfect crystalline samples would have a higher transformation temperature than samples with lower crystallinity. If the crack area measured with CT is compared with the ability to transform, a correlation is seen. The type with the lowest crack amount, has the lowest ability to transform. This is type A. Type F had the highest amount of cracks, and had the highest ability to transform. It is suggested that cracks, and also other lattice defects such as impurities, creates favorable sites for nucleation of amorphous phase and hence the transformation from quartz to amorphous phase and cristobalite speeds up.

Large variations are seen in the phase composition in one quartz type. This could be explained by a natural and varying raw material. However, the differences seen between the different quartz types are larger and suggests that there are differences between the quartz types that could be significant for furnace operation. This is simulated for quartz type A and F, and the simulation shows that the down to 0.9 m in the furnace, the majority silica phase is quartz. After this point and down to 1.5 m the phase transformations happen with various speed. At 1.5 m depth all quartz will have transformed to cristobalite, and will due to the temperature at this point start to melt. Between 0.9 m and 1.5 m there is a varying phase composition depending on what quartz types is used for production. When measuring the silica phases in samples from a furnace excavation at Finnfjord, nearly no quartz phase was found. This is believed to be because of the time the raw material would have been exposed to high temperatures before excavation. Phase transformation from quartz to amorphous phase and cristobalite would have enough time to proceed up to several days before the sample is removed from the high temperatures. From the furnace excavation, no

trend was observed in the amount of phases as a function of position in the furnace, but few samples from the charge top were investigated.

8.3 Future work

To further investigate and confirm what properties of the quartz cause the behavior at high temperature, one should design experiments in such a way that only one parameter is varied each time to see the isolated effect. This could be the grain size of the quartz. One should investigate quartz types where the other parameters such as fluid inclusions and solid impurities are nearly the same. This has to be determined before high temperature experiments starts. In quartz types with large variation in the amount of fines created during shock heating, one should do a thorough geological investigation to figure out if the deposit is very heterogeneous, and hence if there are properties in a part of the quartz enhancing disintegration. This was seen for type G in this study, and explained the large variation seen. Another possibility is to perform a higher number of experiments such that the natural variations in each quartz type is easily observed.

The phase transformations in type A, D, F and G were investigated at 1600 °C and 1700 °C. In the future, experiments should be done at other temperatures, to be able to confirm the first order transformations assumed in this thesis. More than two temperatures have to be investigated, because two temperatures will always seem like first order reaction. Also, experiments below 1700 °C should be done in order to avoid melting and softening of the sample and creation of amorphous melted phase.

9 References

[1] "Elkem Silicon Materials." https:/www.elkem.com/silicon-materials/, 2016 (accessed Nov. 15, 2018).

[2] J. E. A. Maurits, "Silicon Production," in *Treatise on Process Metallurgy, Volume 3: Industrial Processes*, Burlington: Elsevier, 2013.

[3] A. Schei, J. K. Tuset, and H. Tveit, *Production of High Silicon Alloys*. Trondheim: Tapir, 1998.

[4] I. Kero, S. Grådahl, and G. Tranell, "Airborne Emissions from Si/FeSi Production," *JOM*, vol. 69, no. 2, pp. 365–380, Feb. 2017, doi: 10.1007/s11837-016-2149-x.

[5] S. Grådahl *et al.*, "Miljø og ovnsprosesser. Del III," Sintef Materials and Chemistry, Trondheim, STF24 F00600, 2000.

[6] K. Aasly, "Properties and behavior of quartz for the silicon process," Doctoral Thesis, Norwegian University of Science and Technology, Trondheim, 2008.

[7] I. T. Zherdev, D. P. Moskovtsev, and I. I. Polyakov, "Dimensions of the gas spaces in ferrosilicon furnaces," *Stal*, vol. 8, pp. 716–717, 1965.

[8] I. T. Zherdev, I. I. Polyakov, V. E. Semenov, I. I. Barashkin, and D. P. Moskovtsev, "Critical rate for rotation for ferrosilicon furnace baths," *Stal*, pp. 406–408.

[9] Y. Otani, M. Saito, K. Usui, and N. Chino, "The inner structure of the submerged arc furnace," presented at the International Congress on electro-heat, Brigthon, 1968.

[10] M. Ksiazek, M. Tangstad, and E. Ringdalen, "Five furnaces five different stories," in *Silicon for the chemical and solar industry XIII*, Kristiansand, 2016.

[11] G. Tranell, M. Andersson, E. Ringdalen, O. Ostrovski, and J. J. Steinmo, "Reaction zones in a FeSi75 furnace - results from an industrial excavation," presented at the Twelfth International Ferroalloy Congress, Finland, 2010, p. 8.

[12] E. H. Myrhaug, "Non-fossil reduction materials in the silicon process: properties and behavior," Doctoral Thesis, Department of Materials Technology, Norwegian University of Science and Technology, Trondheim, 2003.

[13] S. Bernardis, "Engineering Impurity Behavior on the micron-scale in metallurgical-grade silicon production," Doctoral Thesis, Massachusetts Institute of Technology, 2012.

[14] E. H. Myrhaug and H. Tveit, "Material balances of trace elements in the ferrosilicon and silicon processes," 2000.

[15] H. Edfelt and E. Nordnes, "Permeability Tests of Packed Bed in the Silicon Production Process," Norwegian University of Science and Technology, Summer Project Report, 2018.

[16] H. Edfelt, "The effect of fine material on gas flow in the charge for silicon production," Norwegian University of Science and Technology, Trondheim, Project report, TMT4500, 2018.

[17] E. Nordnes, "Softening and Melting Properties of Quartz," Master Thesis, Norwegian University of Science and Technology, Trondheim, 2019.

[18] M. Tangstad, J. Safarian, S. Bao, A. Valderhaug, and Ringdalen, Eli, "Reaction rates of 2SiO2 + SiC = 3SiO + CO in pellets at elevated temperatures," *Crimson Publ.*, vol. 3, no. 2, 2019, doi: 10.31031/AMMS.2019.03.000558.

[19] C. Sindland, "Reactivity of Si and SiO2 mixtures," Department of Materials Science and Engineering, Norwegian University of Science and Technology, Project report, TMT4500, 2019.

[20] M. B. Folstad, "Effect of Different Polymorphs of SiO2 on the Reaction between SiO2 and SiC in Si Production," Master Thesis, Norwegian University of Science and Technology, Trondheim, 2017.

[21] M. B. Folstad, "Effect of different polymorphs of SiO2 on the reaction between SiO2 and SiC in Si production," Norwegian University of Science and Technology, Project report, TMT5400, 2016.

[22] K. Wiik, "Kinetics of reactions between silica and carbon," Doctoral Thesis, Norwegian University of Science and Technology, Trondheim, 1990.

[23] M. Hakamada, Y. Fukunaka, T. Oishi, T. Nishiyama, and H. Kusuda, “Carbothermic Reduction of Amorphous Silica Refined from Diatomaceous Earth,” *Metall. Mater. Trans. B*, vol. 41, no. 2, pp. 350–358, Apr. 2010, doi: 10.1007/s11663-009-9332-1.
[24] K. Motzfeldt and M. Steinmo, “Kinetics of Reactions Between Carbon and Refractory Oxides,” in *Kinetics, Thermodynamics and Chemistry of High Temperature Reactions*, Denmark, 1972, vol. 2, pp. 91–109.
[25] F. Li, “SiC production using SiO_2 and C agglomerates,” Doctoral Thesis, Norwegian University of Science and Technology, Trondheim, 2017.
[26] “The Quartz Page,” 2007. http://www.quartzpage.de/intro.html (accessed May 09, 2018).
[27] James S. Monroe, *The changing earth: exploring geology and evolution*, 5th ed. Belmont, Calif: Brooks/Cole, 2009.
[28] J. Götze and R. Möckel, Eds., “Classification, Mineralogy and Industrial Potential for SiO2 Minerals and Rocks,” in *Quartz: deposits, mineralogy and analytics*, Berlin ; New York: Springer, 2012.
[29] P. J. Heaney, C. T. Prewitt, and G. V. Gibbs, *Silica - physical behavior, geochemistry and materials applications*, vol. 29. Mineralogical Society of America, 1994.
[30] B. Flem, R. B. Larsen, A. Grimstvedt, and J. Mansfeld, “In situ analysis of trace elements in quartz by using laser ablation inductively coupled plasma mass spectrometry,” *Chem. Geol.*, vol. 182, no. 2–4, pp. 237–247, Feb. 2002, doi: 10.1016/S0009-2541(01)00292-3.
[31] V. J. Hurst and S. P. Storch, “Regional variation in the cell dimensions of metamorphic quartz,” *Am. Mineral.*, vol. 66, pp. 204–212, 1981.
[32] T. Hiraga, I. M. Anderson, and D. L. Kohlstedt, “Grain boundaries as reservoirs of incompatible elements in the earth’s crust,” *Nature*, vol. 427, p. 699, 2004.
[33] R. J. Knipe, “Distribution of impurities in deformed quartz and its implications for deformation studies,” *Tectonophysics*, vol. 64, no. 1, pp. T11–T18, 1980, doi: 10.1016/0040-1951(80)90255-3.
[34] “Fluid Inclusions in Minerals,” *Institute of Geological Sciences*, Aug. 11, 2016. https://www.geo.unibe.ch/research/rockwater_interaction/research_rwi/fluid_inclusions_in_minerals/index_eng.html (accessed Mar. 11, 2020).
[35] Edwin Roedder, “Geochemistry: Uses for synthetic fluid inclusions in quartz crystals,” *Nature*, vol. 315, no. 6020, pp. 544–545, 1985, doi: 10.1038/315544b0.
[36] J. Götze and R. Möckel, Eds., “Assessment of High Purity Quartz Resources,” in *Quartz: deposits, mineralogy and analytics*, Berlin ; New York: Springer, 2012.
[37] H. Fossen, “Fracture and brittle deformation,” in *Structural geology*, 1st ed., Cambridge: Cambridge University Press, 2010.
[38] A. Tarantola, L. W. Diamond, and H. Stünitz, “Modification of fluid inclusions in quartz by deviatoric stress I: experimentally induced changes in inclusion shapes and microstructures,” *Contrib. Mineral. Petrol.*, vol. 160, no. 6, pp. 825–843, Dec. 2010, doi: 10.1007/s00410-010-0509-z.
[39] K. Simon, “Does δD from fluid inclusion in quartz reflect the original hydrothermal fluid?,” *Chem. Geol.*, vol. 177, no. 3, pp. 483–495, Jul. 2001, doi: 10.1016/S0009-2541(00)00417-4.
[40] J. Götze and R. Möckel, Eds., “Petrological and Chemical Characterization of High-Purity Quartz Deposits with Examples from Norway,” in *Quartz: deposits, mineralogy and analytics*, Berlin ; New York: Springer, 2012.
[41] A. Müller, M. Wiedenbeck, A. M. V. D. Kerkhof, A. Kronz, and K. Simon, “Trace elements in quartz - a combined electron microprobe, secondary ion mass spectrometry, laser-ablation ICP-MS, and cathodoluminescence study,” *Eur. J. Mineral.*, vol. 15, no. 4, pp. 747–763, Jul. 2003, doi: 10.1127/0935-1221/2003/0015-0747.
[42] R. D. Aines and G. R. Rossman, “Water in minerals? A peak in the infrared,” *J. Geophys. Res. Solid Earth*, vol. 89, no. B6, pp. 4059–4071, 1984, doi: 10.1029/JB089iB06p04059.
[43] J. Fukuda, “Water in Rocks and Minerals - Species, Distributions, and Temperature Dependences,” in *Infrared Spectroscopy - Materials Science, Engineering and Technology*, 2012.

[44] M. Janek, I. Bugar, D. Lorenc, V. Szocs, D. Velic, and D. Chorvat, “Terahertz Time-Domain Spectroscopy of Selected Layered Silicates,” *Clays Clay Miner.*, vol. 57, no. 4, pp. 416–424, 2009.
[45] A. K. Kronenberg, H. F. B. Hasnan, C. W. Holyoke III, R. D. Law, Z. Liu, and J. B. Thomas, “Synchrotron FTIR imaging of OH in quartz mylonites,” *Copernic. Publ.*, vol. 8, 2017.
[46] C. Navarro, M. Diaz, and M. A. Villa-Garcia, “Physico-Chemical characterization of steel slag. Study of its behavior under simulated environmental conditions,” *Environ. Sci. Technol.*, vol. 14, 2014.
[47] J. Madejova, W. P. Gates, and S. Petit, “IR Spectra of Clay Minerals,” in *Infrared and Raman Spectroscopies of Clay*, W.P. Gates et al., vol. 8, Elsevier B.V., 2017.
[48] William D. Callister, *Materials Science and Engineering:* Asia: Wiley, 2001.
[49] Stevens, S. J. and R. J. Hand, “Polymorphism of Silica,” *Chapman Hall*, vol. 32, pp. 2929–2935, 1997.
[50] A. C. D. Chaklader, “Effect of trace Al2O3 on transformation of quartz to cristobalite,” *J. Am. Ceram. Soc.*, vol. 44, pp. 175–180, 1961.
[51] T. J. Rockett, “The thermal stability of purified tridymite,” *Am. Mineral.*, vol. 52, p. 8, 1967.
[52] E. Ringdalen, “Quartz Properties in the silicon production,” presented at the Silicon for the Chemical and Solar Industry XII, Jun. 2014.
[53] D. L. Lakshtanov and S. V. Sinogeikin, “High-temperature phase transitions and elasticity of silica polymorphs,” *Phys Chem Miner.*, vol. 34, pp. 11–22, 2007, doi: 10.1007/s00269-006-0113-y.
[54] K. F. Jusnes, M. Tangstad, and E. Ringdalen, “Phase Transformations from Quartz to Cristobalite,” in *Proceedings of the First Global Conference on Extractive Metallurgy*, Ottawa, 2018.
[55] A. C. D. Chaklader and A. Roberts, “Transformation of Quartz to Cristobalite,” *J Amer Ceram Soc*, vol. 44, pp. 35–41, 1961.
[56] C. S. Marians and L. W. Hobbs, “Network properties of crystalline polymorphs of silica,” *J. Non-Cryst. Solids*, vol. 124, pp. 242–253, 1990.
[57] M. E. Kjelstadli, “Kinetics and Mechanism of Phase Transformations from Quartz to Cristobalite,” Master Thesis, Norwegian University of Science and Technology, Trondheim, 2016.
[58] H. Schneider, A. Majdic, and R. Vasudevan, “Kinetics of the Quartz-Cristobalite Transformation in Refractory-Grade Silica Materials,” *Mater. Sci. Forum*, vol. 7, pp. 91–102, 1986.
[59] R. B. Sosman, *The Phases of Silica*, 2nd ed. New Jersey: Quinn & Boden Company, Inc., 1965.
[60] C. Klein, “Mineral Stability Diagrams,” in *Manual of mineralogy*, 21st ed., New York: Wiley, 1993.
[61] S. Stølen, *Chemical thermodynamics of materials: macroscopic and microscopic aspects*. Chichester: Wiley, 2004.
[62] V. Presser and K. G. Nickel, “Silica on Silicon Carbide,” *Crit. Rev. Solid State Mater. Sci.*, vol. 33, no. 1, pp. 1–99, 2008, doi: 10.1080/10408430701718914.
[63] J. Sestak, J. J. Mares, and P. Hubik, “Glassy, Amorphous and Nano-Crystalline Materials,” *Springer*, 2011.
[64] D. Turnbull, “Under what conditions can a glass be formed?,” *Contemp. Phys.*, vol. 10, pp. 473–488, 1969.
[65] M. A. Lamkin, F. L. Riley, and R. J. Fordham, “Oxygen mobility in silicon dioxide and silicate glasses: a review,” *J. Eur. Ceram. Soc.*, vol. 10, no. 5, pp. 347–367, Jan. 1992, doi: 10.1016/0955-2219(92)90010-B.
[66] S. Andersson, “Atomic-scale modelling of structures and relative stability of different phases of silica,” Sintef Materials and Chemistry, Trondheim, 2016.
[67] W. H. Zachariasen, “The atomic arrangement in glass,” *J. Am. Chem. Soc.*, vol. 54, no. 10, pp. 3841–3851, Oct. 1932, doi: 10.1021/ja01349a006.

[68] J. T. Randall, H. P. Rooksby, and B. S. Cooper, “The Diffraction of X-rays by Vitreous Solids and its Bearing on their Constitution,” *Nature*, vol. 125, no. 3165, pp. 975–975, Jun. 1930, doi: 10.1038/125975d0.
[69] T. Bakos, “Defects in amorphous SiO2: reactions, dynamics and optical properties,” Doctoral Thesis, Vanderbilt University, Nashville, Tennesse, 2003.
[70] V. Balek, J. Fusek, J. Kříž, and M. Murat, “Differences in the thermal behaviour of natural quartz before and after mechanical grinding as observed by emanation thermal analysis,” *Thermochim. Acta*, vol. 262, pp. 209–214, Sep. 1995, doi: 10.1016/0040-6031(95)02350-B.
[71] H. Schneider and A. Majdic, “Kinetics of the quartz-cristobalite transformation in refractory-grade silica minerals,” vol. 7, pp. 91–102, 1986, doi: 10.4028/scientific.net/MSF.7.91.
[72] M. E. Kjelstadli, “Kinetics and Mechanism of Phase Transformation from Quartz to Cristobalite,” Department of Materials Science and Engineering, Norwegian University of Science and Technology, Spesialization Project, 2015.
[73] N. G. Ainslie, J. D. Mackenzie, and D. Turnbull, “Melting kinetics of quartz and cristobalite,” *J. Phys. Chem.*, vol. 65, no. 10, pp. 1718–1724, Oct. 1961, doi: 10.1021/j100827a012.
[74] R. C. Breneman and J. W. Halloran, “Kinetics of Cristobalite Formation in Sintered Silica,” *J. Am. Ceram. Soc.*, vol. 97, no. 7, pp. 2272–2278, Jul. 2014, doi: 10.1111/jace.12889.
[75] L. Pagliari, M. Dapiaggi, A. Pavese, and F. Francescon, “A kinetic study of the quartz–cristobalite phase transition,” *J. Eur. Ceram. Soc.*, vol. 33, no. 15–16, pp. 3403–3410, Dec. 2013, doi: 10.1016/j.jeurceramsoc.2013.06.014.
[76] M. Dapiaggi, L. Pagliari, A. Pavese, L. Sciascia, M. Merli, and F. Francescon, “The formation of silica high temperature polymorphs from quartz: Influence of grain size and mineralising agents,” *J. Eur. Ceram. Soc.*, vol. 35, no. 16, pp. 4547–4555, Dec. 2015, doi: 10.1016/j.jeurceramsoc.2015.08.015.
[77] F. M. Wahl, R. E. Grim, and R. B. Graf, “Phase transformations in silica as examined by continuous X-ray diffraction,” *Am. Mineral.*, vol. 46, pp. 196–208, 1961.
[78] S. D. Brown and S. S. Kistler, “Devitrification of High-SiO2 Glasses of the System Al2O3-SiO2,” *J. Am. Ceram. Soc.*, vol. 42, no. 6, pp. 263–270, 1959, doi: 10.1111/j.1151-2916.1959.tb12951.x.
[79] S. Mitra, “Kinetics of Quartz - Cristobalite Transformation,” *Trans. J. Br. Ceram. Soc.*, vol. 76, pp. 71–74, 1977.
[80] A. C. D. Chaklader, “X-Ray Study of Quartz-Cristobalite Transformation,” *J. Am. Ceram. Soc.*, vol. 46, no. 2, pp. 66–71, 1963, doi: 10.1111/j.1151-2916.1963.tb11677.x.
[81] M. Helbæk and S. Kjelstrup, *Fysikalsk kjemi*, 2. utg. Bergen: Fagbokforlag, 2006.
[82] F. O. Bakken and C. O. Paulsen, “Thermal stability of quartz for silicon process,” Department of Materials Science and Engineering, Norwegian University of Science and Technology, 2013.
[83] K. Aasly and V. Dosaj, “Assessment of production performance of quartz in the Si furnace,” in *Silicon for the chemical and solar industry XIII*, Kristiansand, 2016.
[84] T. Malvik and B. Lund, “Problems involved with quartzite as a raw material for FeSi and Si metal production,” *Miner. Met. Mater. Soc.*, 1990.
[85] T. Malvik, “Relations between mineralogical texture and comminution characteristics for rocks and ores,” Amsterdam, 1988.
[86] D. T. Griggs and J. D. Blacic, “Quartz: Anomalous Weakness of Synthetic Crystals,” *Science*, vol. 147, no. 3655, pp. 292–295, 1965.
[87] E. Ringdalen, D. Adisty, and L. Kolbeinsen, “Quartz-cristobalite tranformation and its effect on reactions in Si production: initial studies,” in *Extraction and Processing Division*, 2014.
[88] K. F. Jusnes, “Parameters Affecting Softening and Melting of Quartz,” Master Thesis, Norwegian University of Science and Technology, Trondheim, 2016.
[89] J. G. Dash, A. W. Rempel, and J. S. Wettlaufer, “The physics of premelted ice and its geophysical consequences,” *Rev. Mod. Phys.*, vol. 78, no. 3, pp. 695–741, Jul. 2006, doi: 10.1103/RevModPhys.78.695.

[90] D. Kuhlmann-Wilsdorf, “Theory of Melting,” *Phys. Rev.*, vol. 140, no. 5A, pp. A1599–A1610, Nov. 1965, doi: 10.1103/PhysRev.140.A1599.
[91] A. Seltveit, *Ildfaste materialer*, 2nd ed. Trondheim: Tapir.
[92] E. Nordnes, “Softening and Melting Properties of Quartz,” Norwegian University of Science and Technology, Department of Materials science and engineering, Project report, TMT4500, 2018.
[93] E. Ringdalen and M. Tangstad, “Softening and melting of SiO2, an important parameter for reactions with quartz in Si production,” in *Advances in Molten Slags, Fluxes, and Salts: Proceedings for The 10th International Conference on Molten Slags, Fluxes and Salts*, Seattle, USA, 2016, vol. 10.
[94] E. Ringdalen, “Changes in Quartz During Heating and the Possible Effects on Si Production,” *JOM*, vol. 67, no. 2, pp. 484–492, Feb. 2015, doi: 10.1007/s11837-014-1149-y.
[95] S. Bao and T. Anzjøn, “Volume expansion and wetting properties of Quartz,” Sintef Materials and Chemistry, 2017.
[96] V. Andersen, “Investigation of thermal properties of quartz for the silicon industry under reducing atmosphere,” Norwegian University of Science and Technology, Trondheim, Project report, TMT4500, 2009.
[97] R. M. J. Cotterill, “The physics of melting,” *J. Cryst. Growth*, vol. 48, pp. 582–588, 1980.
[98] J. M. T. Thompson and P. A. Shorrock, “Bifurcational instability of an atomic lattice,” *J. Mech. Phys. Solids*, vol. 23, no. 1, pp. 21–37, 1975.
[99] A. Samanta, M. E. Tuckerman, T.-Q. Yu, and W. E, “Microscopic mechanisms of equilibrium melting of a solid,” *Science*, vol. 346, no. 6210, pp. 729–732, Nov. 2014, doi: 10.1126/science.1253810.
[100] J. D. Mackenzie, “Fusion of Quartz and Cristobalite,” *J. Am. Ceram. Soc.*, vol. 43, no. 12, pp. 615–619, 1960, doi: 10.1111/j.1151-2916.1960.tb13629.x.
[101] D. Turnbull and M. H. Cohen, “Concerning Reconstructive Transformation and Formation of Glass,” *J. Chem. Phys.*, vol. 29, no. 5, pp. 1049–1054, Nov. 1958, doi: 10.1063/1.1744654.
[102] G. Urbain, Y. Bottinga, and P. Richet, “Viscosity of liquid silica, silicates and alumino-silicates,” *Geochim. Cosmochim. Acta*, vol. 46, no. 6, pp. 1061–1072, Jun. 1982, doi: 10.1016/0016-7037(82)90059-X.
[103] R. H. Doremus, “Viscosity of silica,” *J. Appl. Phys.*, vol. 92, no. 12, pp. 7619–7629, Dec. 2002, doi: 10.1063/1.1515132.
[104] K. Tang and M. Tangstad, “Modeling viscosities of ferromanganese slags,” in *Proceedings for Infacon XI*, New Dehli, 2007.
[105] A. Ayensu and K. H. G. Ashbee, “Plasticity of ‘wet’ quartz,” *Metallography*, vol. 11, no. 4, pp. 369–390, Oct. 1978, doi: 10.1016/0026-0800(72)90066-3.
[106] M. Ksiazek, “Heat transfer in quartz particle - modelling in Comsol Multiphysics.” .
[107] T. Brenden-Veisal and A. Filipowicz, “Develop new tools for exploration of quartz sources: Quartz textures’ significance for fines generation during handling and thermal fracturing and melting of quartz in furnace. High Temperature Quartz, WP3,” Elkem ASA, Internal project report, draft report, 2020.
[108] J. A. Pevik, “Geological and Mineralogical Characterization of the Upper Part of the Gamasfjell Quartzite at the Vaggecearu Mountain,” Master Thesis, 2015.
[109] K. Seljeset, “Trace Element Study of Quartz from Nasafjell,” Master Thesis, Norwegian University of Science and Technology, Trondheim, 2018.
[110] A. Filipowicz, “Characterization of quartz raw material for ferrosilicon and silicon alloy applications,” Master Thesis, Aarhus University, Denmark, 2018.
[111] T. Kim and J. Park, “Analysis of quartz ore samples using Raman spectroscopy,” Hanyang University, 2018.
[112] E. Ringdalen, J. Tolchard, and E. Thomassen, “Evaluation of method used to measure amount of phases in silica,” Sintef Materials and Chemistry, Trondheim, Unrestricted, Mar. 2017.

[113] V. Andersen, “Reaction mechanism and kinetics of the high temperature reactions in the silicon process,” Master Thesis, Norwegian University of Science and Technology, Trondheim, 2010.
[114] I. C. Madsen, N. V. Y. Scarlett, and A. Kern, “Description and survey of methodologies for the determination of amorphous content via X-ray powder diffraction,” *Z. Für Krist.*, vol. 226, no. 12, pp. 944–955, Dec. 2011, doi: 10.1524/zkri.2011.1437.
[115] M. B. Folstad, “Phase Transformation from Quartz to Amorphous Silica and Cristobalite,” Department of Materials Science and Engineering, Norwegian University of Science and Technology, Summer job report, 2016.
[116] J. Robinson W., E. M. S. Frame, and G. M. Frame Il, “Infrared, Near-infrared, and Raman spectroscopy,” in *Undergraduate instrumental analysis*, 7th ed., Boca Raton, FL: CRC Press, Taylor & Francis Group, 2014, pp. 243–356.
[117] B. Lawson, “Michelson Interferometer,” *Battery and Energy Technologies*, Jul. 17, 2019. https://www.mpoweruk.com/figs/Michelson-Interferometer.htm.
[118] C. Ruckebusch and L. Blanchet, “Multivariate curve resolution: A review of advanced and tailored applications and challenges,” *Anal. Chim. Acta*, vol. 765, pp. 28–36, Feb. 2013, doi: 10.1016/j.aca.2012.12.028.
[119] M. Brems, “A One-Stop Shop for Principal Component Analysis,” *Medium*, Jun. 10, 2019. https://towardsdatascience.com/a-one-stop-shop-for-principal-component-analysis-5582fb7e0a9c (accessed Jan. 27, 2020).
[120] “Principal Component Analysis (PCA) clearly explained,” Jan. 27, 2020. https://www.youtube.com/watch?v=_UVHneBUBW0 (accessed Jan. 27, 2020).
[121] “statistiXL - Principal Component Analysis.” https://www.statistixl.com/features/principal-components/ (accessed Jan. 27, 2020).
[122] A. Broggi, “Personal communication on condensation.” Aug. 04, 2020.
[123] C. Dougherty, “Statistial Tables,” 2002. https://home.ubalt.edu/ntsbarsh/Business-stat/StatistialTables.pdf (accessed Mar. 27, 2020).
[124] W. A. Deer, R. A. Howie, and J. Zussman, “Sheet Silicates,” in *An introduction to the rock-forming minerals*, 12th ed., Longman Group Limited, 1980.
[125] “Muscovite Mica Sheet,” *American Elements*. https://www.americanelements.com/muscovite-mica-sheet-12001-26-2 (accessed Mar. 27, 2020).
[126] H. K. D. H. Bhadeshia and R. W. K. Honeycomb, “The strengthening of iron and alloys,” in *Steels microstructure and properties*, 3rd ed., Oxford: Elsevier Ltd., 2006.
[127] G. H. Aylward and T. J. V. Findlay, *Si chemical data*, 6th ed. Milton: Wiley, 2008.
[128] Douglas A. Skoog, Stanley R. Crouch, and F. James. Holler, *Principles of instrumental analysis*, 6th ed., international student ed. Belmont, Calif: Thomson, 2007.
[129] “Raman || WITec Raman Imaging.” https://www.witec.de/techniques/raman (accessed Dec. 19, 2018).
[130] D. R. Neuville and D. de Ligny, “Advances in Raman Spectroscopy Applied to Earth and Material Sciences,” *Rev. Mineral. Geochem.*, vol. 78, pp. 509–541, 2014.

Appendix A: Enthalpy change measured by differential thermal analysis (DTA)

Differential thermal analysis, DTA, is a method of measuring the temperature differences between a sample and an inert reference sample during heating. The sample are placed in a crucible. A reference sample is also placed in a separate crucible. Both crucibles are heated according to a set temperature program. The furnace atmosphere can also be adjusted. The difference in output voltage from two thermocouples are recorded, and then converted to a temperature difference [128]. The heat flow is then presented as a function of time. A downwards deflection on the graph indicates an endothermic reaction, while an upward deflection indicates an exothermic reaction. To adjust for any noise, a baseline with the same settings as the experiments has to be made. Also, at the end of an experiment series a baseline is made. This is done in order to see the consistency of the furnace during time. In Figure 179 an image of the instrument setup can be seen. Two crucibles are ready to be lowered into the alumina heating tube. The crucible in the front is filled with quartz, while the other is empty for reference.

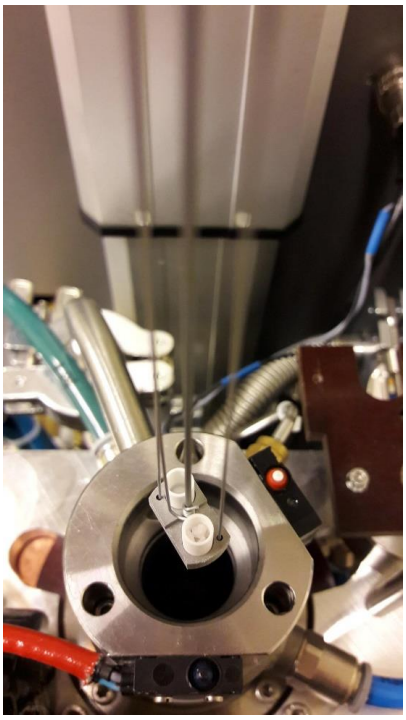

Figure 179: An image of the differential thermal analysis instrument with two crucibles ready to be lowered into the heating tube. One of the crucibles is filled with quartz, while the other one is empty for reference.

Twelve experiments were done to determine if the enthalpy change associated with a phase transformation in silica can be measured using differential thermal analysis. In addition, several baselines were recorded. A Setsys Evolution 24 instrument was used. The gas atmosphere was Argon 6.0 delivered by Aga. The order of the experiments and baseline can be seen in Figure 180. Series 1 and 2 are parallels of the same experiments, just in a different order. This was done to check the reliability of the measurements. Two samples sizes, powder and small pieces, were used for the experiments. The powder was obtained by milling in a wolfram carbide disc mill at 700

rpm for 10 s. The pieces were obtained from crushing a larger sample with a hammer, and choosing the suitable pieces that would fit in the crucible. The total amount of material used for each experiment were around 50-70 mg. A picture of the pieces and the crucible is seen in Figure 181.

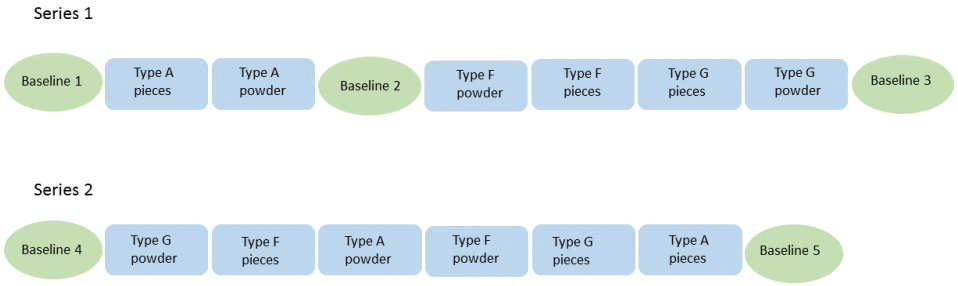

Figure 180: Order of the baselines and experiments for the differential thermal analysis of quartz.

Figure 181: Quartz samples used for DTA experiments. The total sample weight for each experiment were 50-70 mg.

All experiments in series 1 and 2 had the same heating rate to the same maximum temperature, and the same cooling rate. The crucible type and the protective gas, Argon 4.6, was also the same. The heating rate can be seen in Figure 182. The heating rate from room temperature to 1600 °C was 11 °C /min. The holding time at 1600 °C was 60 minutes.

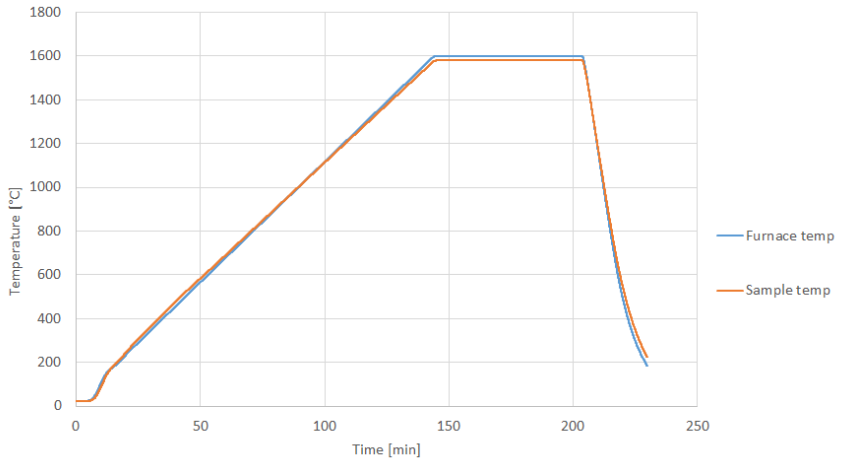

Figure 182: Heating rate for the differential thermal analysis experiments.

The mass of each sample was recorded before the experiments. Table 38 shows the mass of each sample.

Table 38: Samples analyzed with differential thermal analysis, and the mass of each sample.

Series	Sample	Sample mass [mg]
1	Type A, pieces	71.47
	Type A, powder	72.66
	Type F, powder	56.89
	Type F, pieces	59.90
	Type G, pieces	66.06
	Type G powder	49.68
2	Type G, powder	64.01
	Type F, pieces	63.58
	Type A, powder	72.21
	Type F, powder	65.16
	Type G, pieces	81.93
	Type A, pieces	69.26

In Figure 183, baseline 1,2,3 for series 1 and baseline 4,5 and 6 for series 2 are plotted. The variation is large and were the main reason for the experiments not to give any concluding results. The baselines had variations larger than the fluctuations in the heat flow from samples. More consistent and less noisy baseline must be obtained to possibly see any differences in the heat flow as a consequence of phase transformations. The heat flow for series 1 can be seen in Figure

184. These data are unaltered (the baseline is not subtracted). It is also observed that there seems to be a drift in the equipment since the heat flow is increasing as the experiments are being conducted.

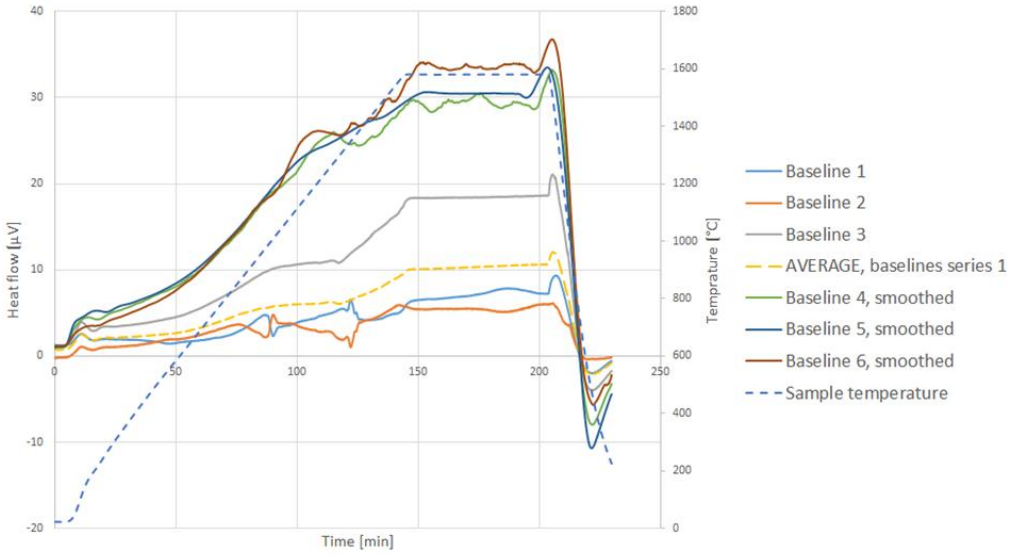

Figure 183: Baselines obtained before, in between and after series 1 and 2. The average baseline for series 1 is also included.

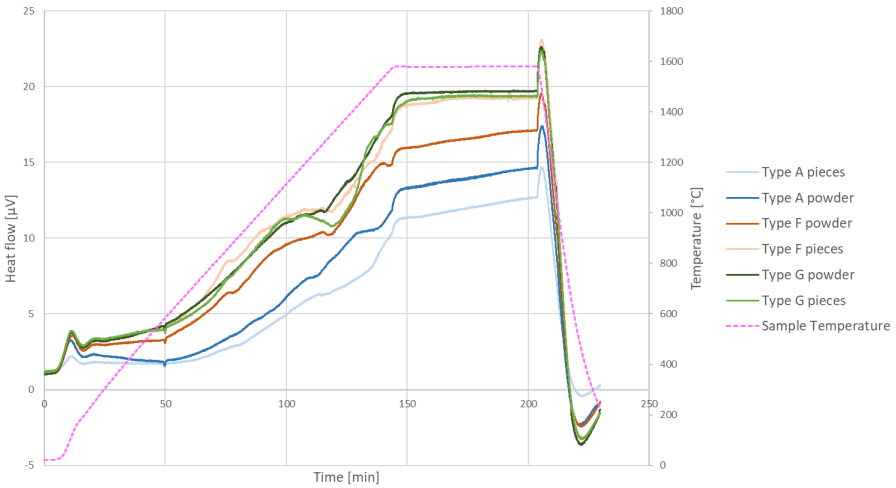

Figure 184: Measured heat flow of quartz type A, F and G measured with DTA equipment.

Appendix B: Raman Spectroscopy

Different chemical bonds vibrate with a specific frequency and hence have different energy. This information can be used to determine what kind of phases are present in a sample and impurities. Bond enthalpies can be analyzed with Raman Spectroscopy. The principle is based on light interacting with the chemical bonds of a sample. All chemical bonds are vibrating, and interacting light will cause an energy shift in the backscattered light from a sample. The Raman spectra obtained is unique for every chemical composition (as for x-ray diffraction). An advantage with the method is the non-destructive investigation [129]. Another advantage is that the instrument can switch between optical mode and laser mode, which makes it possible to first identify the position for Raman spectroscopic investigation. In Figure 185 the Raman spectrum for different silica polymorphs can be seen [130].

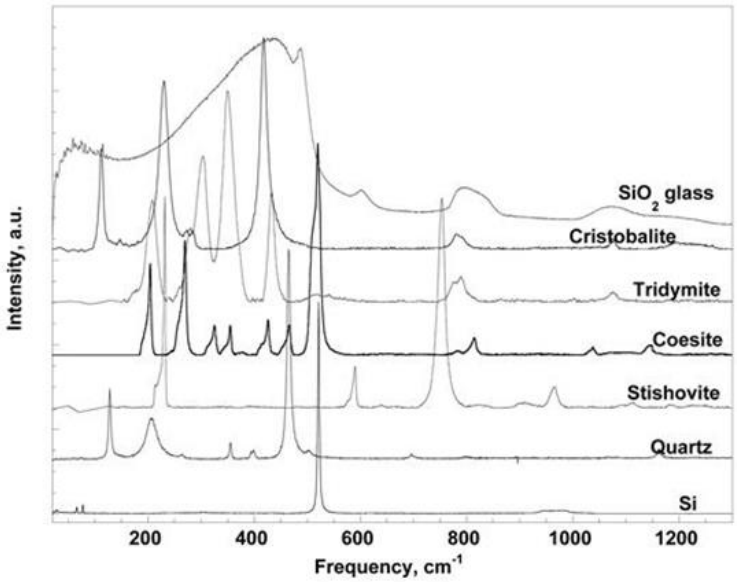

Figure 185: Raman spectrums of different SiO_2 crystalline polymorphs and amorphous state [130].

Quartz type D and G were analyzed with Raman spectroscopy. An Alpha300 R Confocal Raman Imaging equipment was used. No preparation of the samples was needed before investigations. A more or less flat surface of the sample would give better resolution of the imaging and analyses with the Raman microscope, but all the samples had this. Powder could also be investigated. The pure quartz sand reference sample NC4A was also investigated to have a reference for the other quartz types. In addition, samples of quartz type A, D and F were sent to Hanyang university and investigated at the Laboratory for High Temperature Physicochemical Processing of Materials by Taesung Kim and Joohyn Park.

Samples from quartz type D and G were more thorough investigated to see if any impurities could be detected with Raman spectroscopy. As comparison, a sample of NC4A was also investigated. An optical microscope image was taken of all the positions analyzed. The quartz matrix for each of the quartz types was also analyzed to identify the background for the specific sample. In Figure 186, optical microscope images of the positions of the Raman spectroscopic analysis are shown, and in Figure 187 the Raman spectra of the different positions can be seen. Position 005, called

“red inclusion” seems to burn of as the laser hits it. It is therefore taken out of the zoomed in image in Figure 187b.

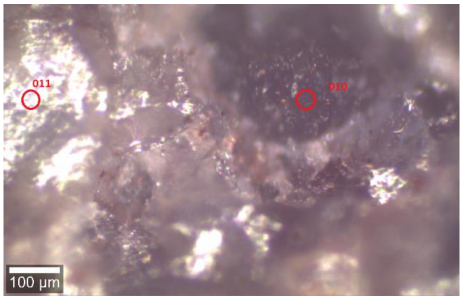

a) Position 010 and 011 were Raman analysis were done on the quartz matrix.

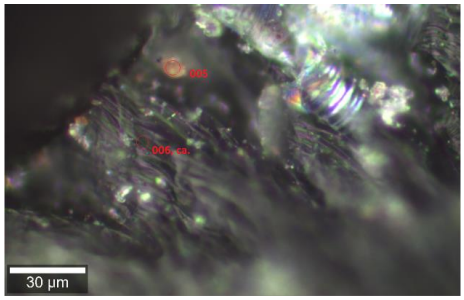

b) Position 005 and 006 analyzed with Raman spectroscopy.

Figure 186: Optical microscope images of areas in quartz type D where Raman spectroscopic analysis were performed.

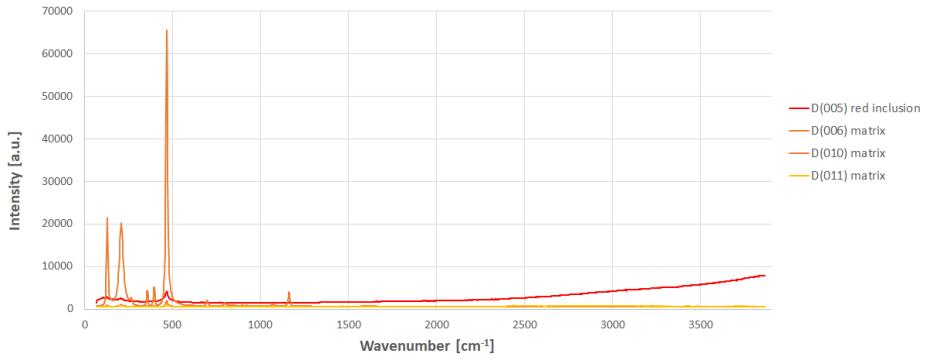

a) Raman spectra of different positions in a sample of quartz type D.

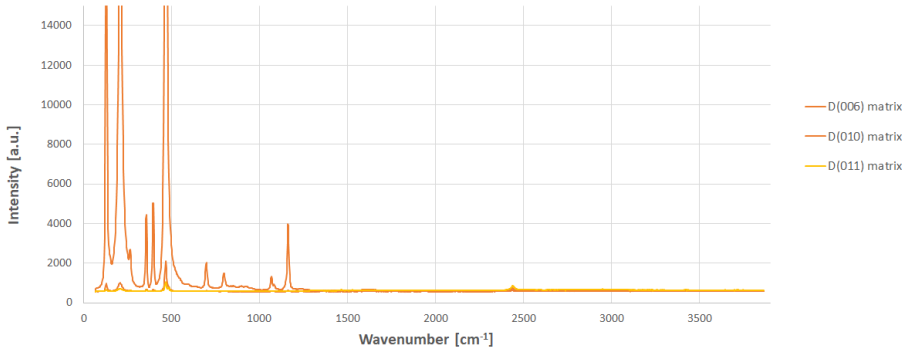

b) The same graph as in a) but with shorter range on the y-axis to more easily see the differences at lower intensity.

Figure 187: Raman spectra of different positions in quartz type D.

The positions analyzed in sample G are shown in Figure 188, and the Raman spectra are shown in Figure 189. It shows the same main trend as the spectra for sample D.

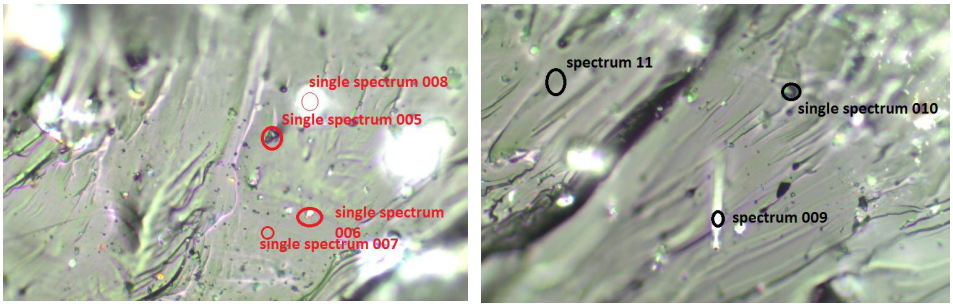

a) Position 005, 006, 007 and 008 analyzed. *b) Position 009, 010 and 011 analyzed*

Figure 188: Different positions in a sample from quartz type G.

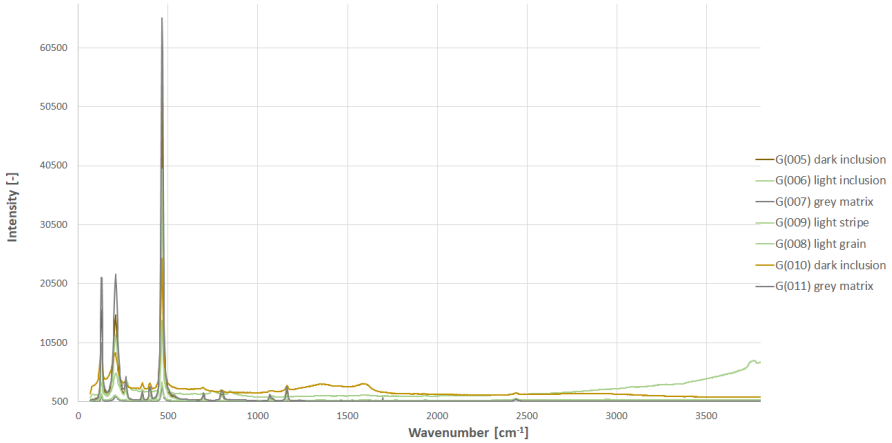

a) Raman spectra of different positions in a sample of quartz type G.

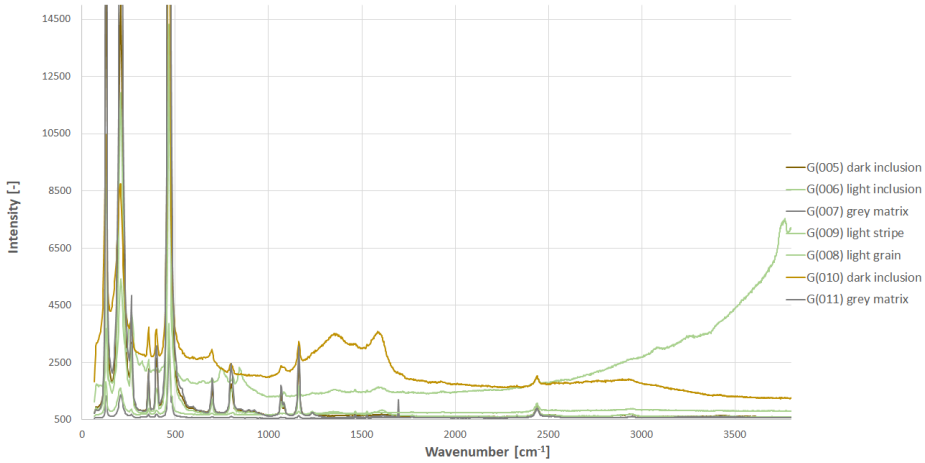

b) The same graph as in a) but with shorter range on the y-axis to more easily see the differences at lower intensity.

Figure 189: Raman spectra of different positions of quartz type G.

To compare the spectra of sample D and G with a pure quartz, sample NC4A was also analyze with Raman spectroscopy. This sample was in powder form, while sample D and G were lumps of around 10 g. The positions analyzed with Raman spectroscopy are seen in Figure 190, and the Raman spectra can be seen in Figure 191.

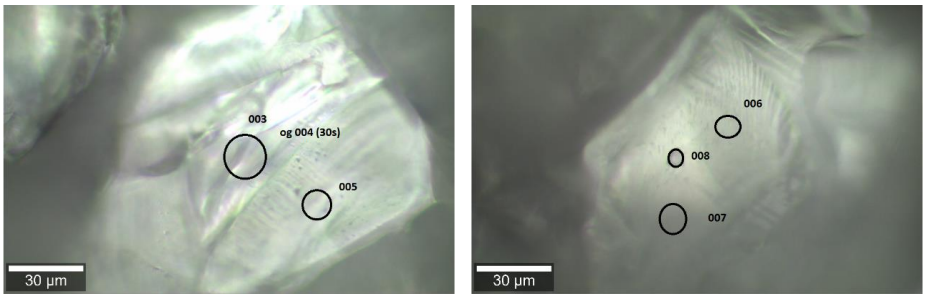

a) *Position 003, 004, and 005 in the pure sample analyzed*

b) *Position 006, 007 and 008 in the pure sample analyzed*

Figure 190: Optical microscope images of areas in pure quartz type N4CA where Raman spectroscopic analysis were performed.

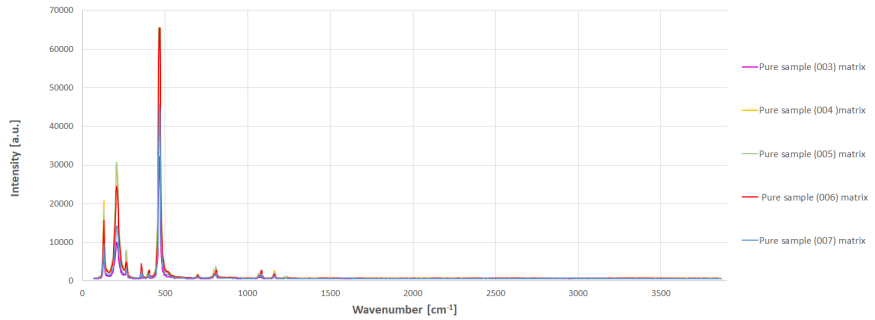

a) Raman spectra of different positions in a sample of pure quartz type N4CA.

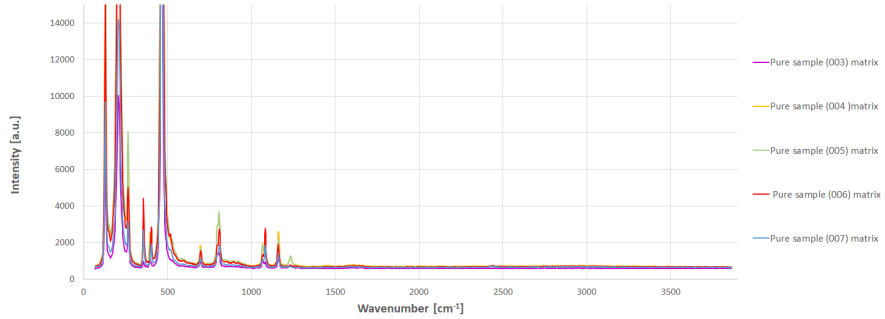

b) The same graph as in a) but with shorter range on the y-axis to more easily see the differences at lower intensity.

Figure 191: Raman spectra of different positions of pure quartz type N4CA.

Appendix C: XRD diffraction patterns

Figure 192 to Figure 265 in this section shows the diffraction patterns for all the main samples analyzed using XRD. It is stated in each figure caption what quartz type, temperature, size and holding time was used for the experiments. For all heated samples, three XRD measurement were done to limit the uncertainty. These are labelled a, b and c, and are separated in the figures to more clearly see. Extra parallels for some of the samples were also done. They are labeled A1.1 and A1.2 for parallel 1 and 2 for sample A1 e.g.

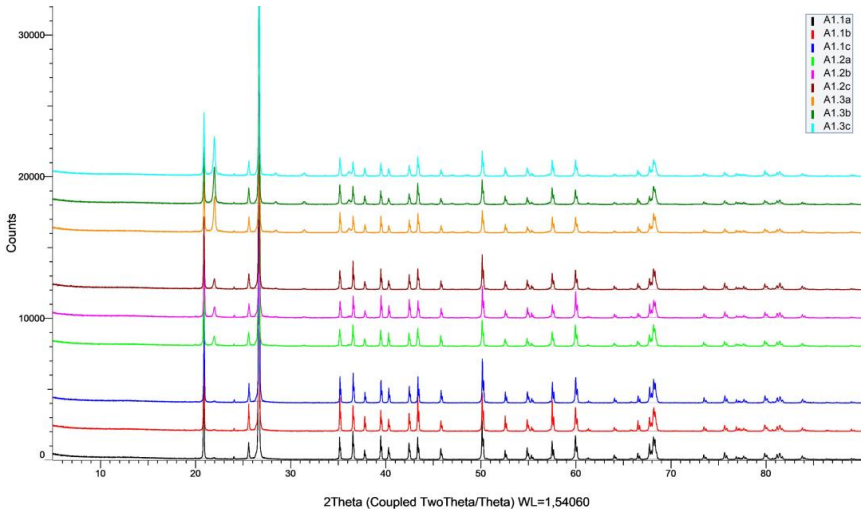

Figure 192: XRD diffraction patterns of A1 samples (10 g, 1600 °C, 0 min).

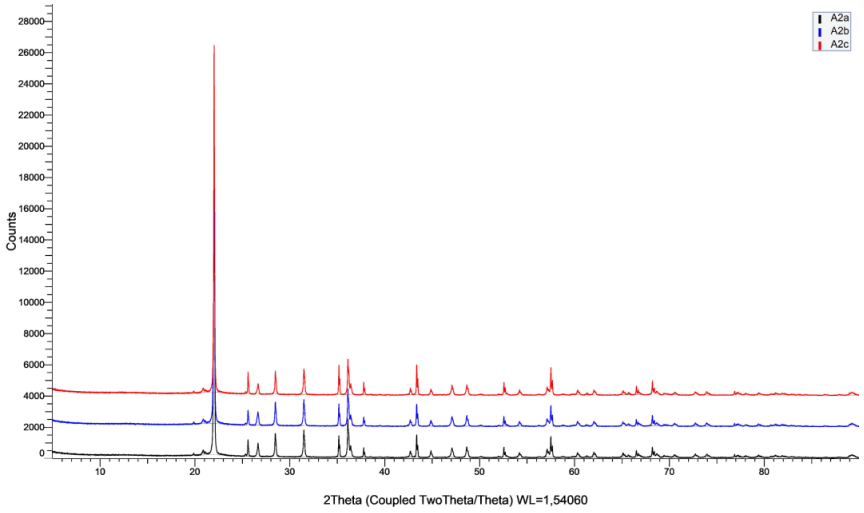

Figure 193: XRD diffraction patterns of A2 samples (10 g, 1600 °C, 120 min).

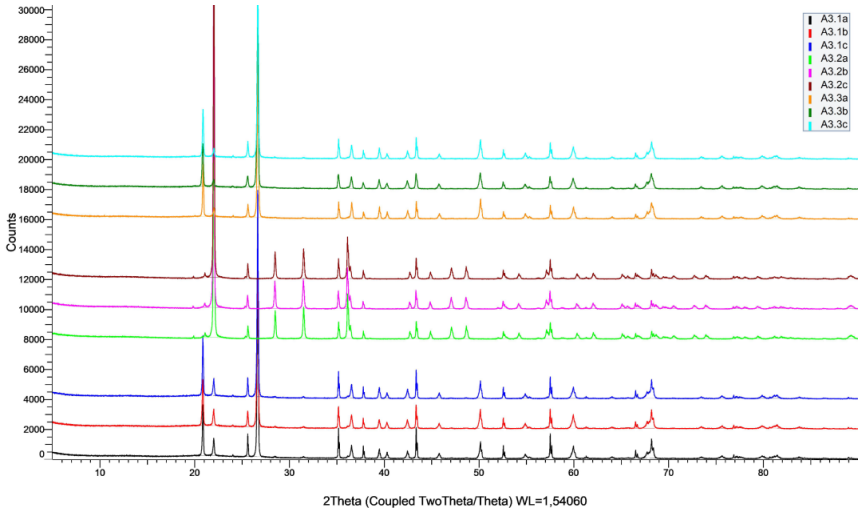

Figure 194: XRD diffraction patterns of A3 samples (10 g, 1700 °C, 0 min).

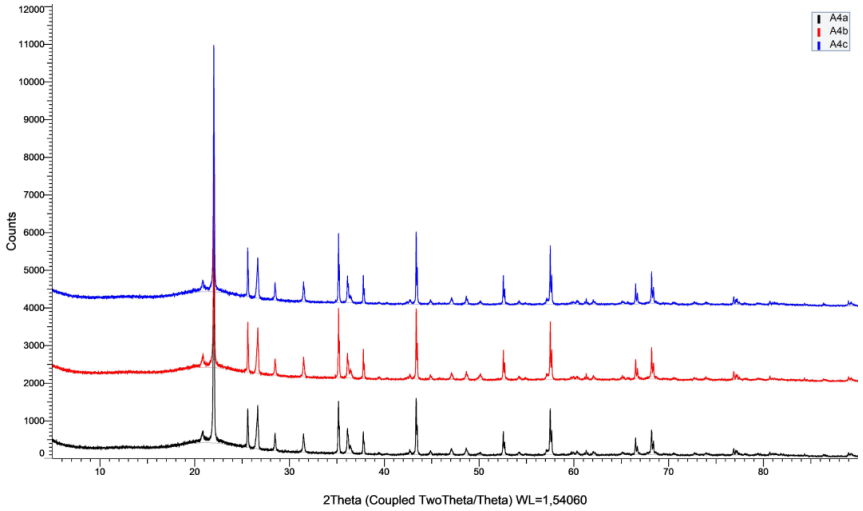

Figure 195: XRD diffraction patterns of A4 samples (10 g, 1700 °C, 15 min).

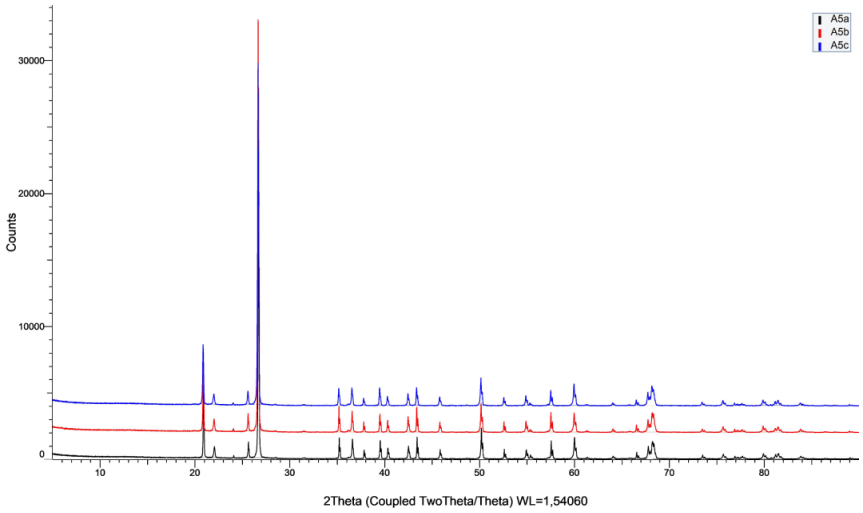

Figure 196: XRD diffraction patterns of A5 samples (10 g, 1600 °C, 15 min).

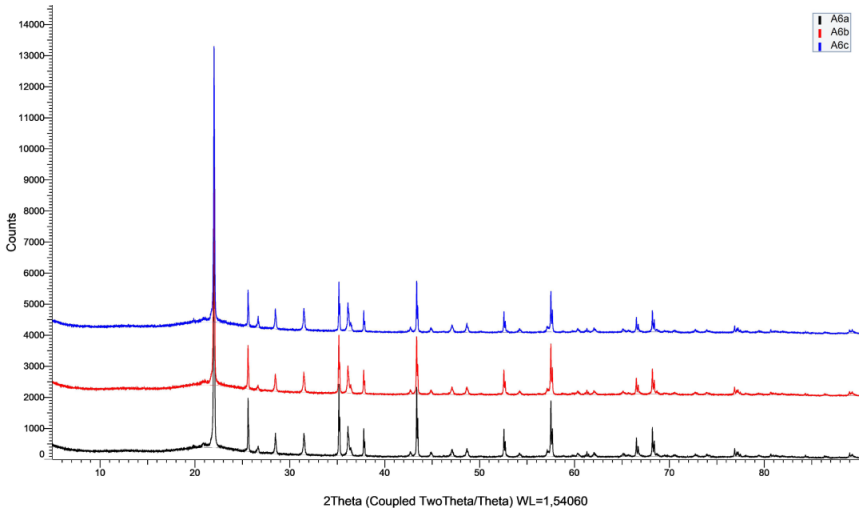

Figure 197: XRD diffraction patterns of A6 samples (10 g, 1700 °C, 30 min).

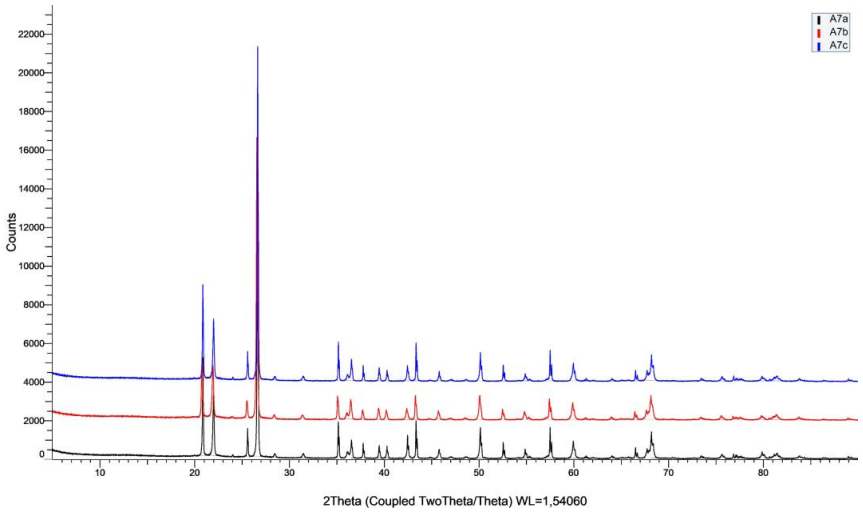

Figure 198: XRD diffraction patterns of A7 samples (10 g, 1600 °C, 30 min).

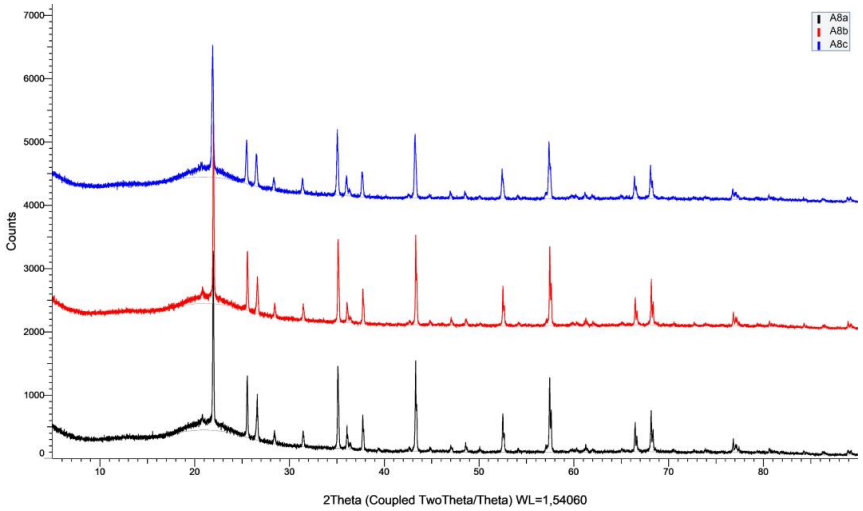

Figure 199: XRD diffraction patterns of A8 samples (10 g, 1700 °C, 45 min).

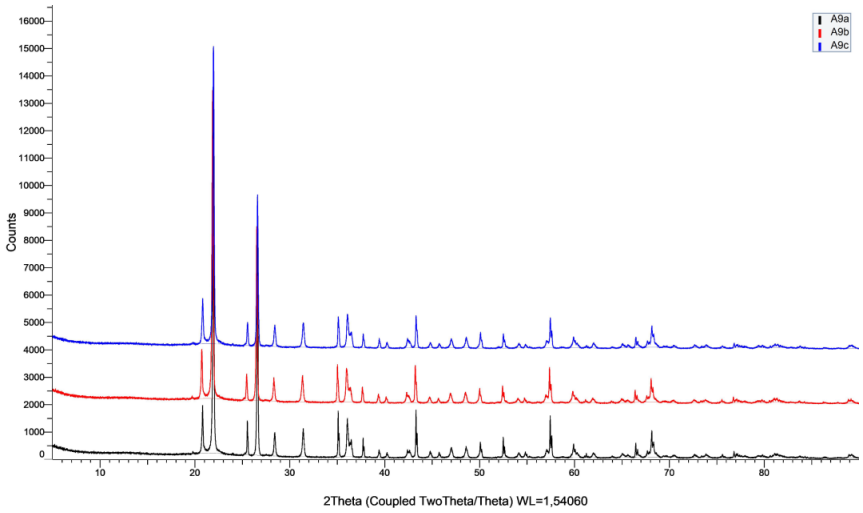

Figure 200: XRD diffraction patterns of A9 samples (10 g, 1600 °C, 45 min).

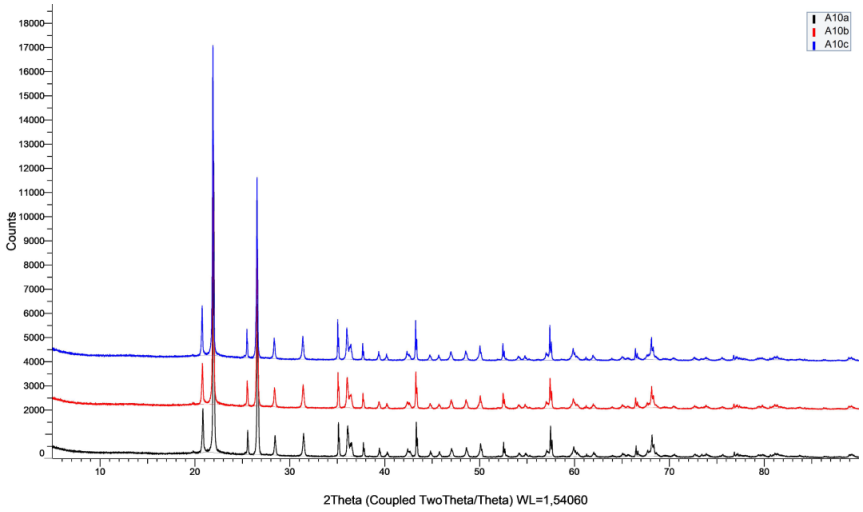

Figure 201: XRD diffraction patterns of A10 samples (10 g, 1600 °C, 60 min).

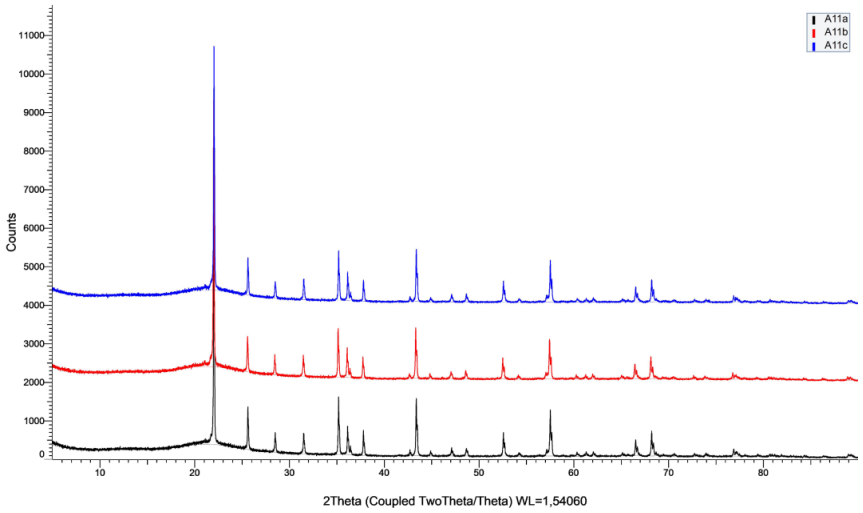

Figure 202: XRD diffraction patterns of A11 samples (10 g, 1700 °C, 60 min).

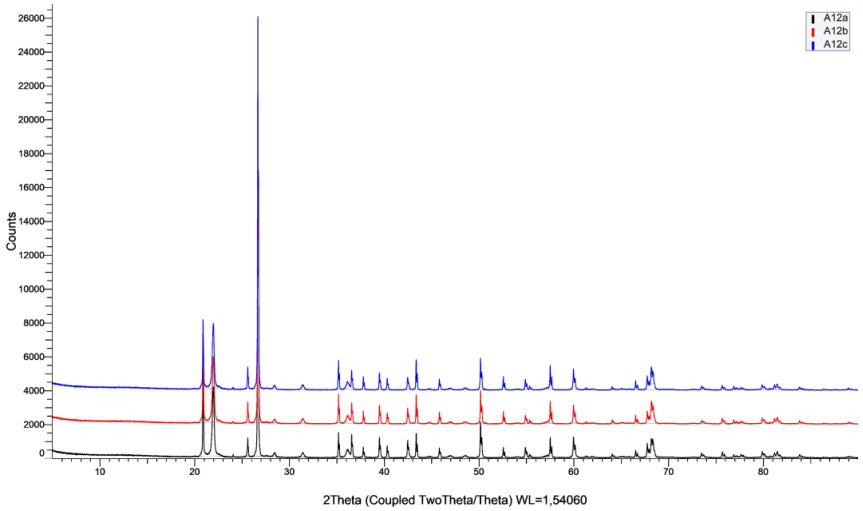

Figure 203: XRD diffraction patterns of A12 samples (100 g, 1600 °C, 0 min).

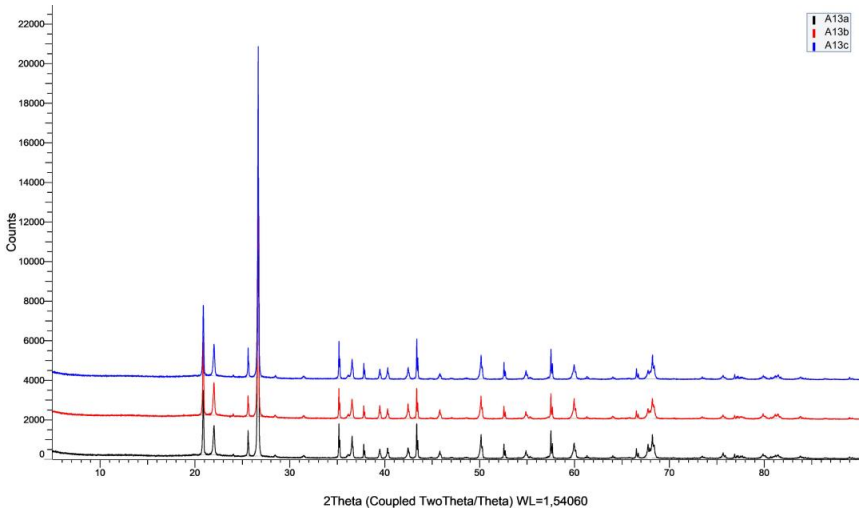

Figure 204: XRD diffraction patterns of A13 samples (100 g, 1700 °C, 0 min).

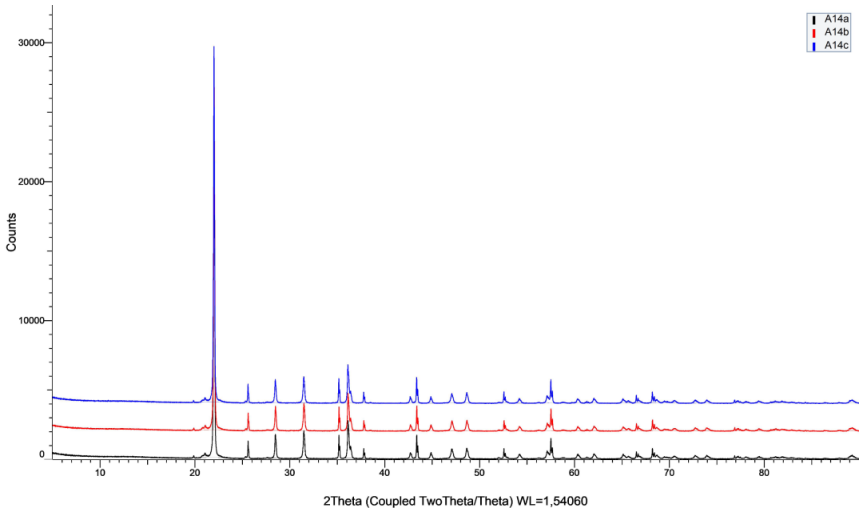

Figure 205: XRD diffraction patterns of A14 samples (100 g, 1700 °C, 15 min).

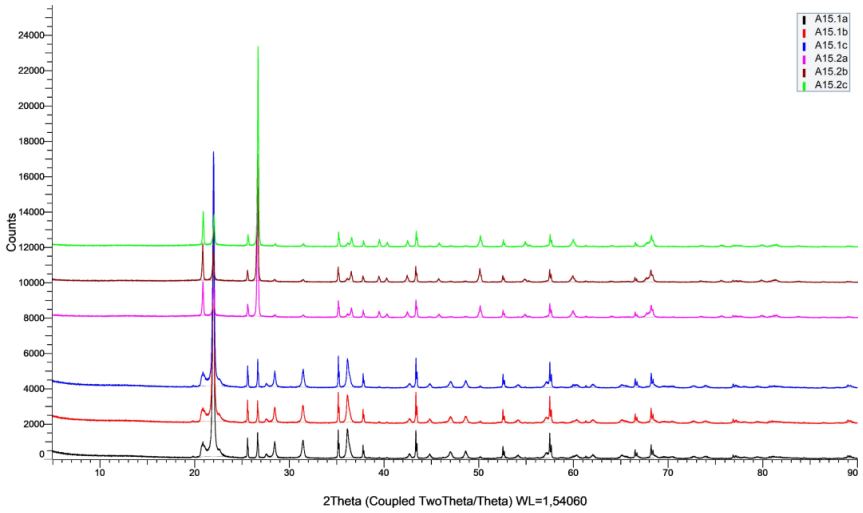

Figure 206: XRD diffraction patterns of A15 samples (100 g, 1600 °C, 15 min).

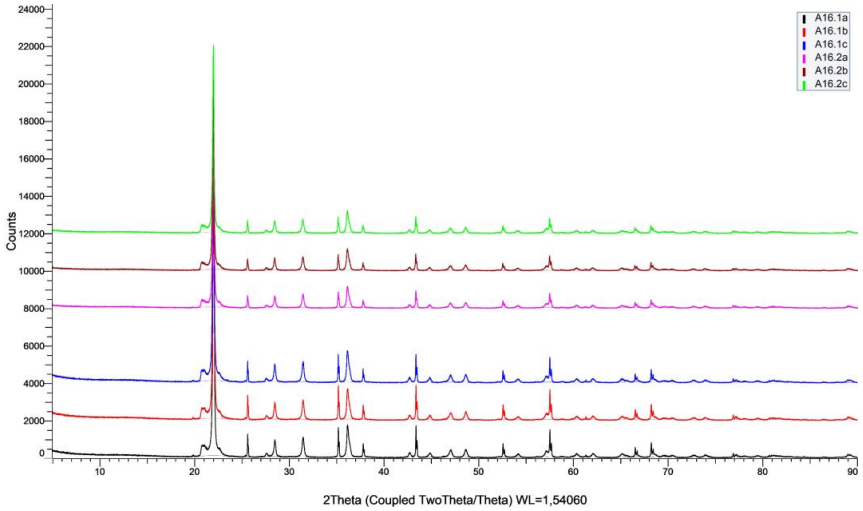

Figure 207: XRD diffraction patterns of A16 samples (100 g, 1600 °C, 30 min).

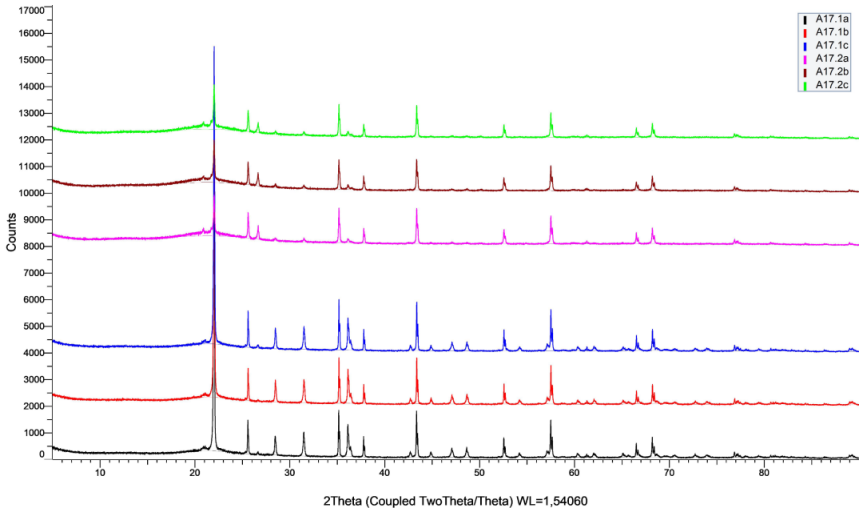

Figure 208: XRD diffraction patterns of A17 samples (100 g, 1700 °C, 30 min).

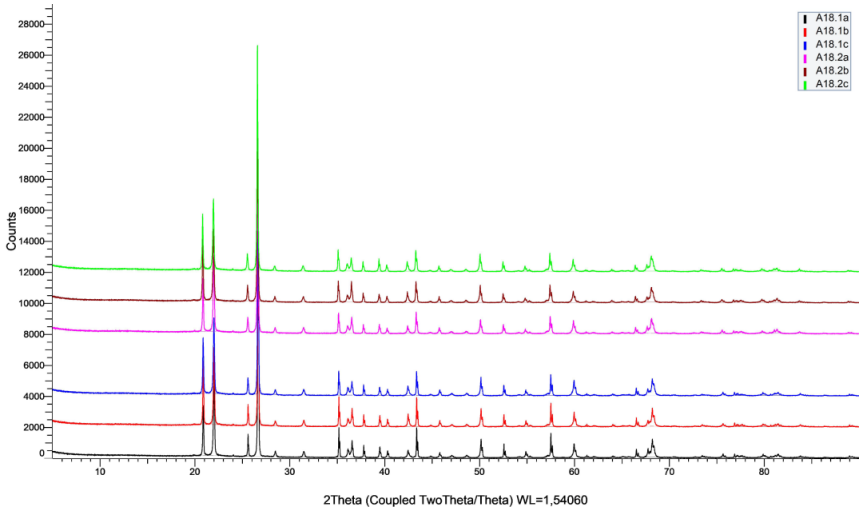

Figure 209: XRD diffraction patterns of A18 samples (100 g, 1600 °C, 45 min).

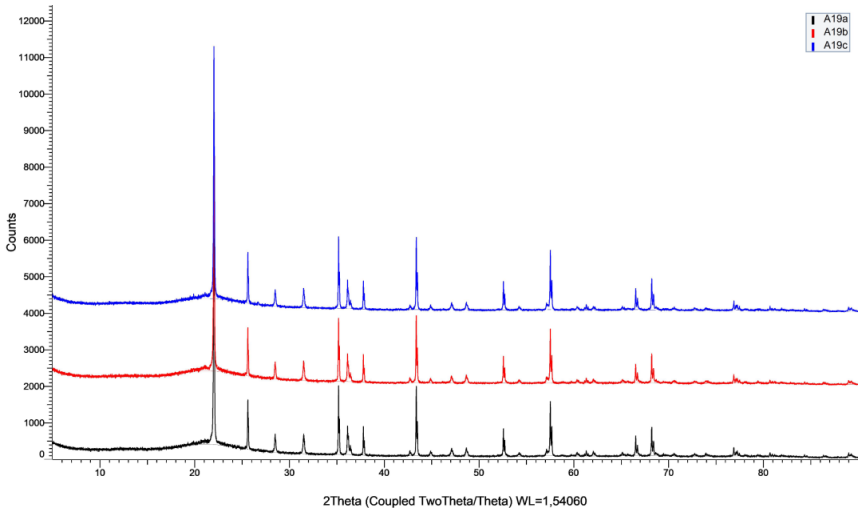

Figure 210: XRD diffraction patterns of A19 samples (100 g, 1700 °C, 45 min).

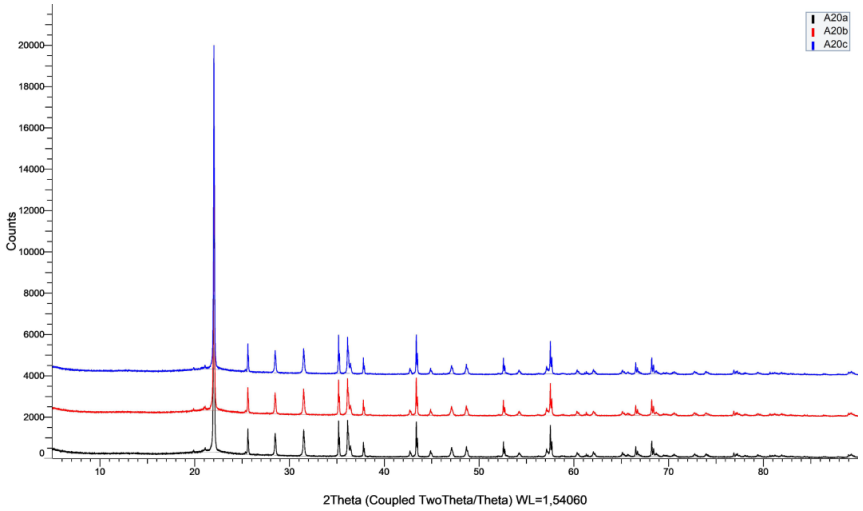

Figure 211: XRD diffraction patterns of A20 samples (100 g, 1700 °C, 60 min).

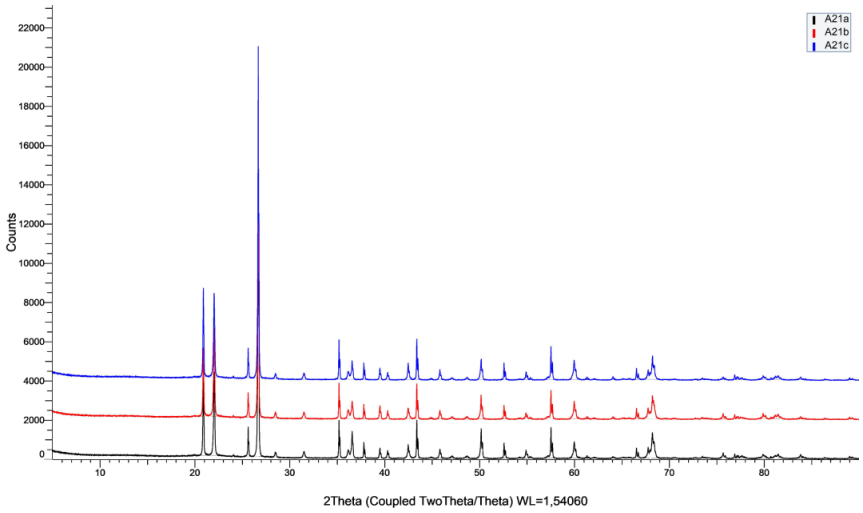

Figure 212: XRD diffraction patterns of A21 samples (100 g, 1600 °C, 60 min).

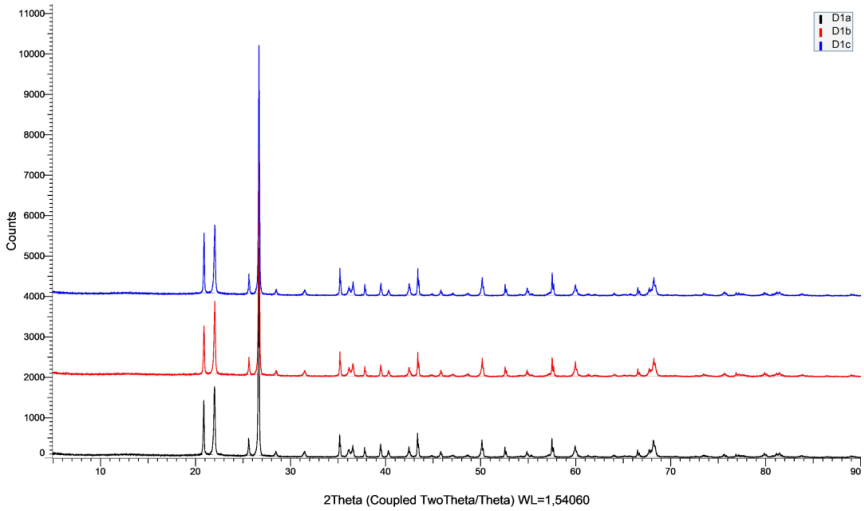

Figure 213: XRD diffraction patterns of D1 samples (10 g, 1600 °C, 0 min).

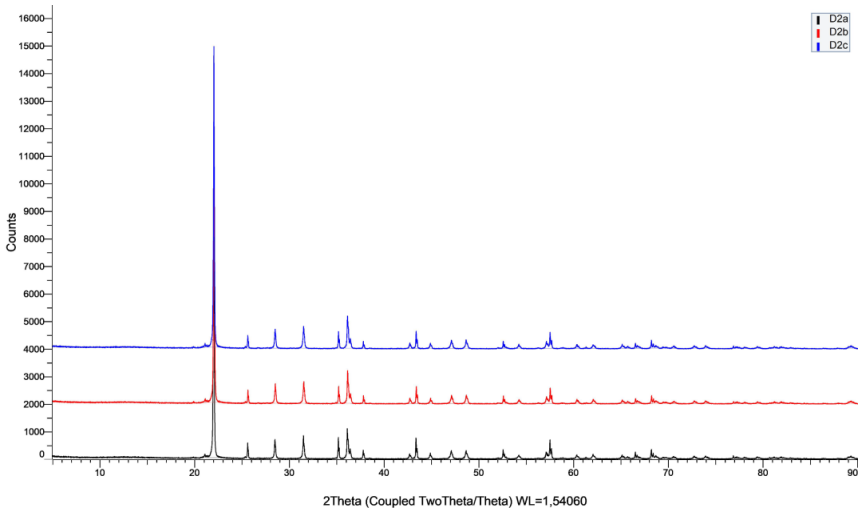

Figure 214: XRD diffraction patterns of D2 samples (10 g, 1600 °C, 120 min).

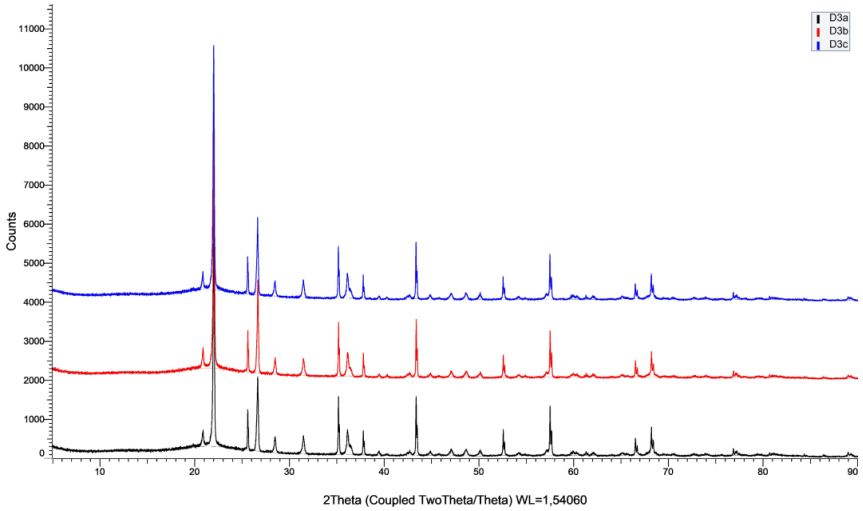

Figure 215: XRD diffraction patterns of D3 samples (10 g, 1700 °C, 0 min).

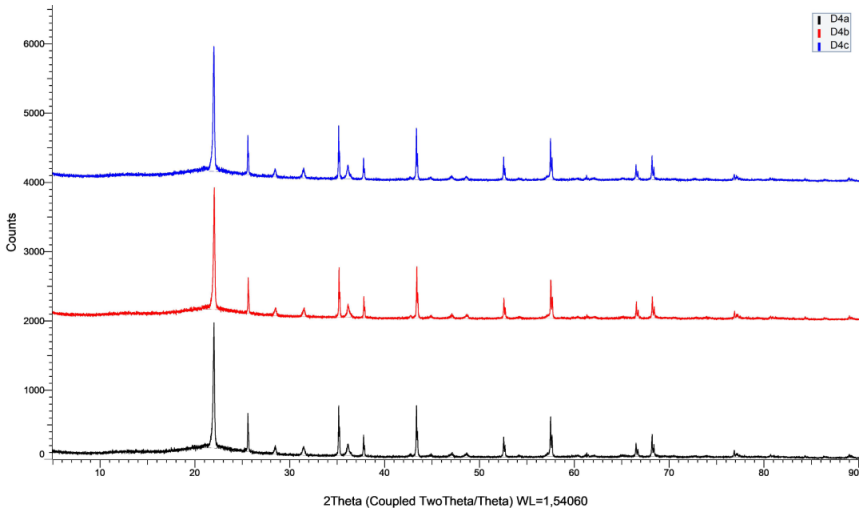

Figure 216: XRD diffraction patterns of D4 samples (10 g, 1700 °C, 15 min).

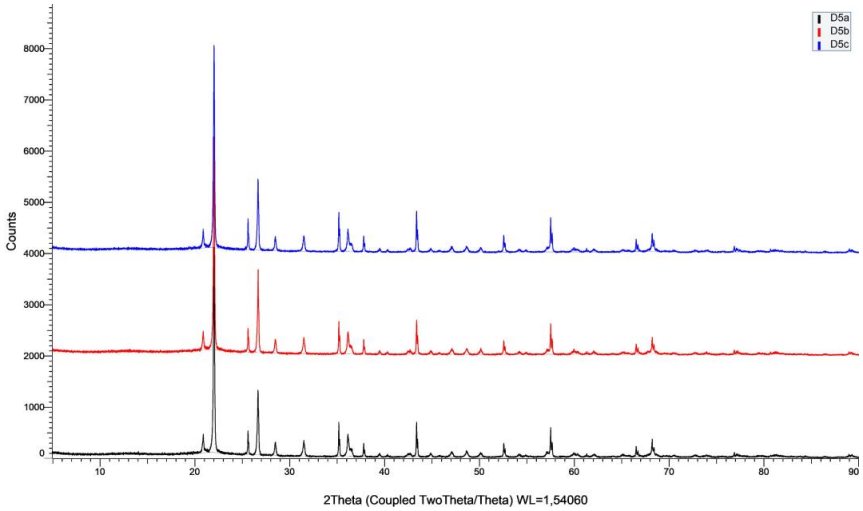

Figure 217: XRD diffraction patterns of D5 samples (10 g, 1600 °C, 15 min).

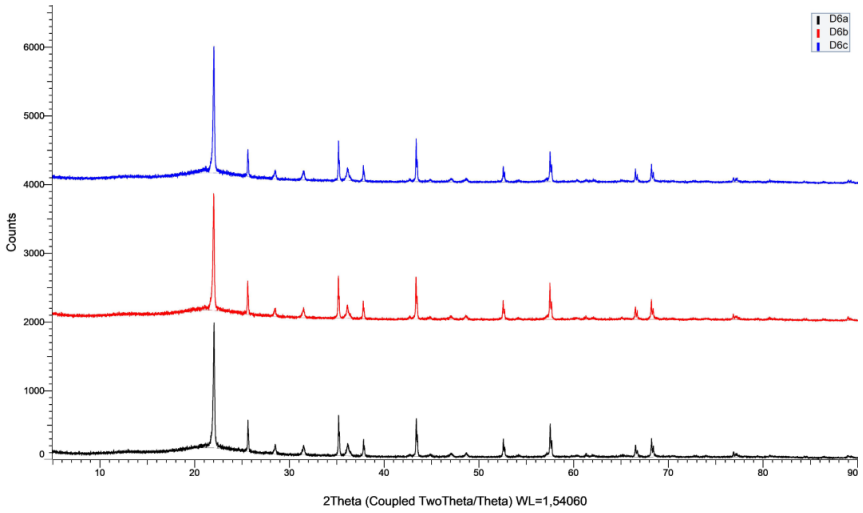

Figure 218: XRD diffraction patterns of D6 samples (10 g, 1700 °C, 30 min).

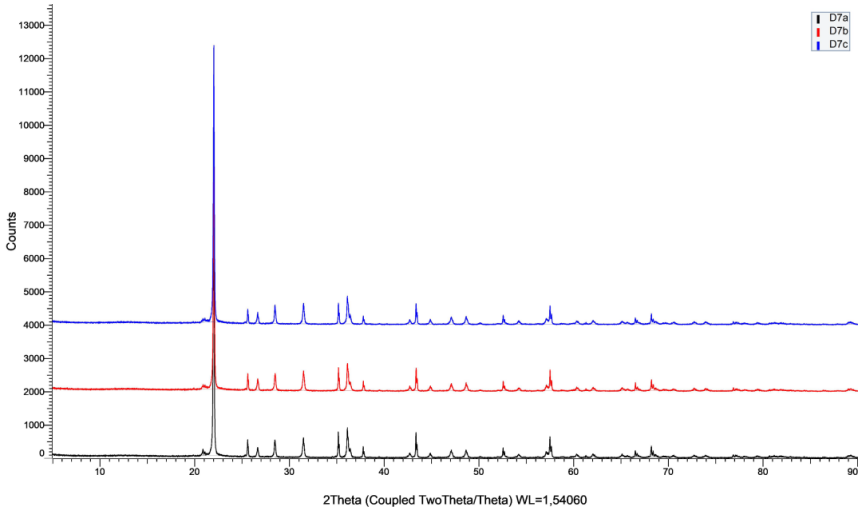

Figure 219: XRD diffraction patterns of D7 samples (10 g, 1600 °C, 30 min).

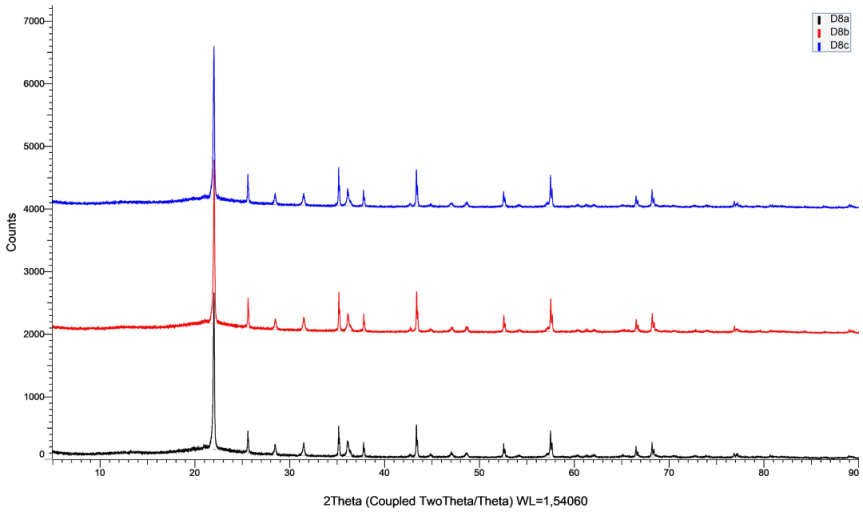

Figure 220: XRD diffraction patterns of D8 samples (10 g, 1700 °C, 45 min).

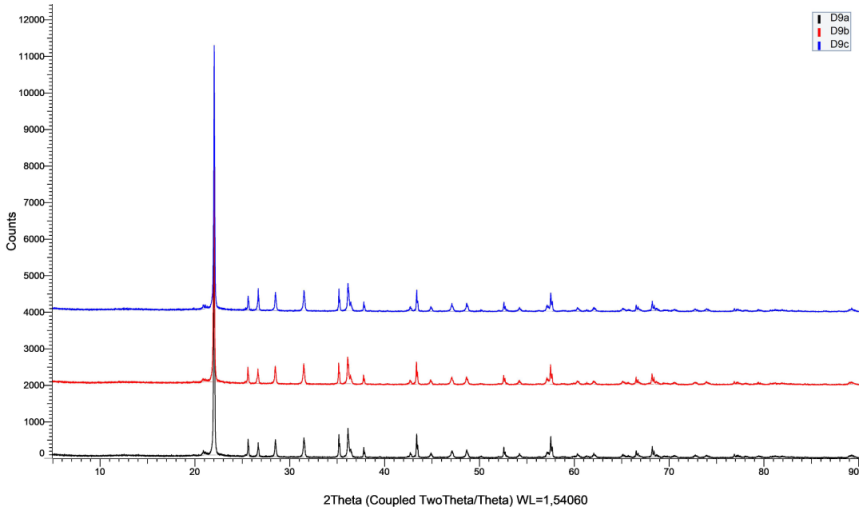

Figure 221: XRD diffraction patterns of D9 samples (10 g, 1600 °C, 45 min).

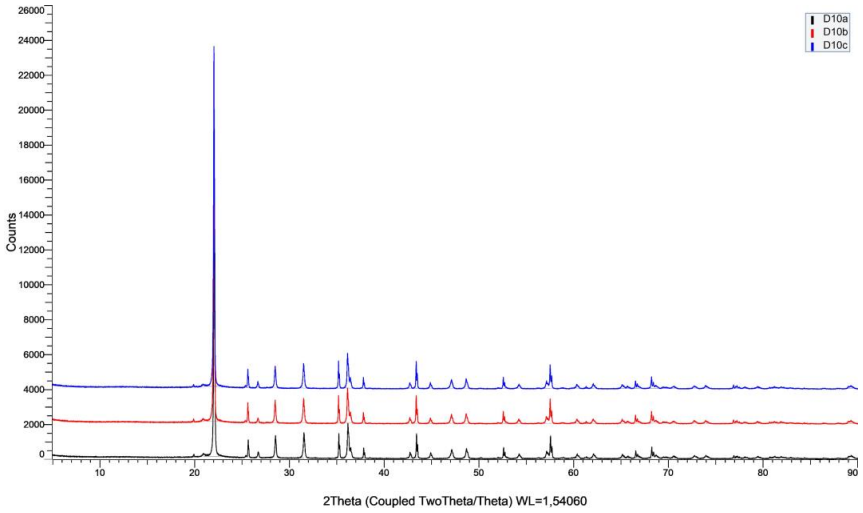

Figure 222: XRD diffraction patterns of D10 samples (10 g, 1600 °C, 60 min).

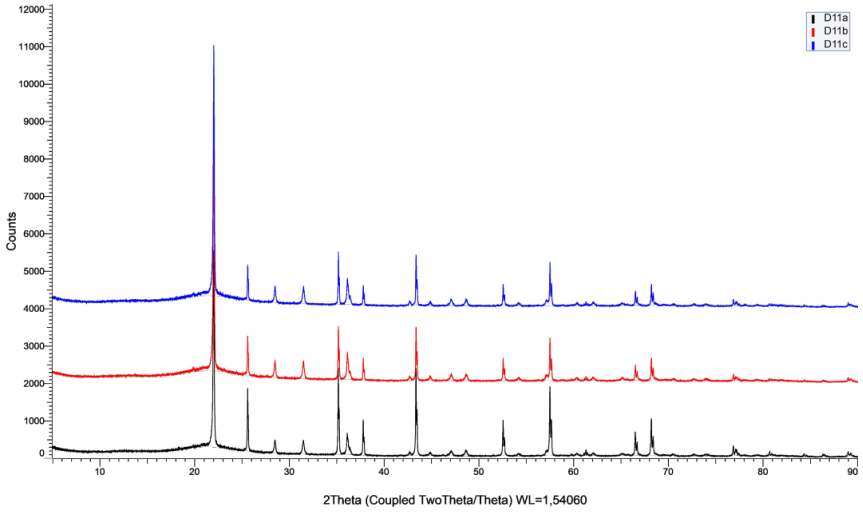

Figure 223: XRD diffraction patterns of D11 samples (10 g, 1700 °C, 60 min).

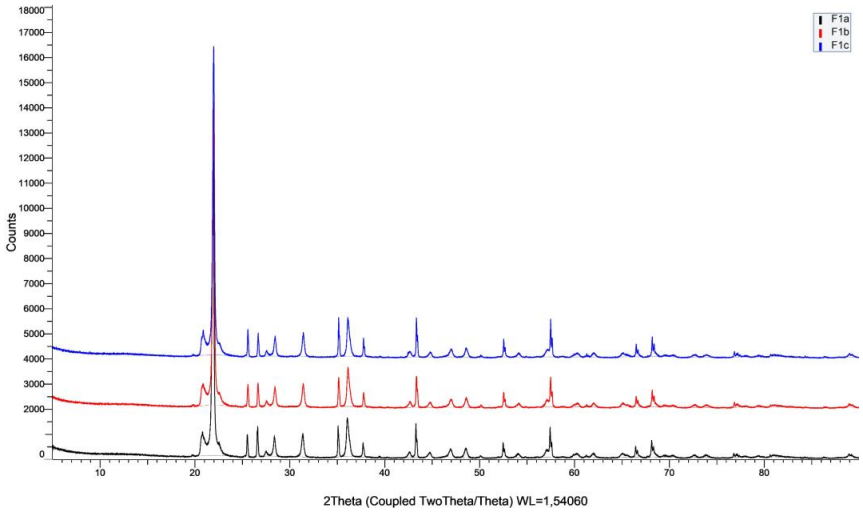

Figure 224: XRD diffraction patterns of F1 samples (10 g, 1600 °C, 0 min).

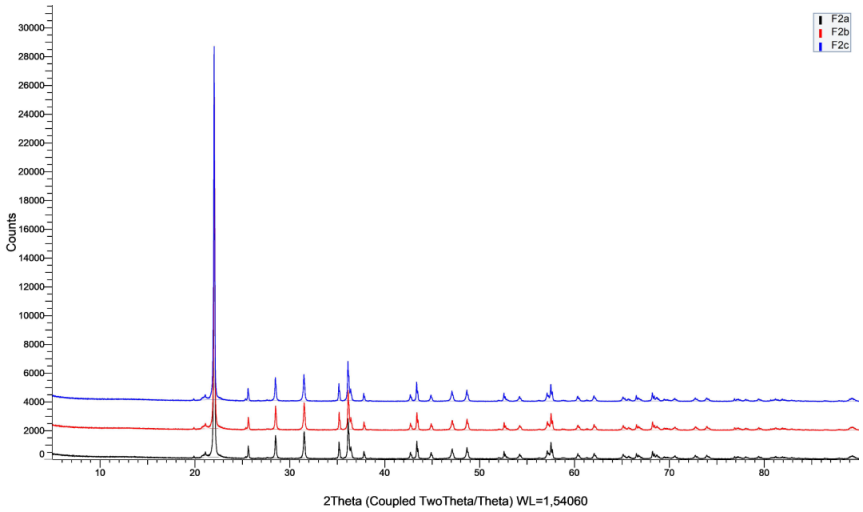

Figure 225: XRD diffraction patterns of F2 samples (10 g, 1600 °C, 120 min).

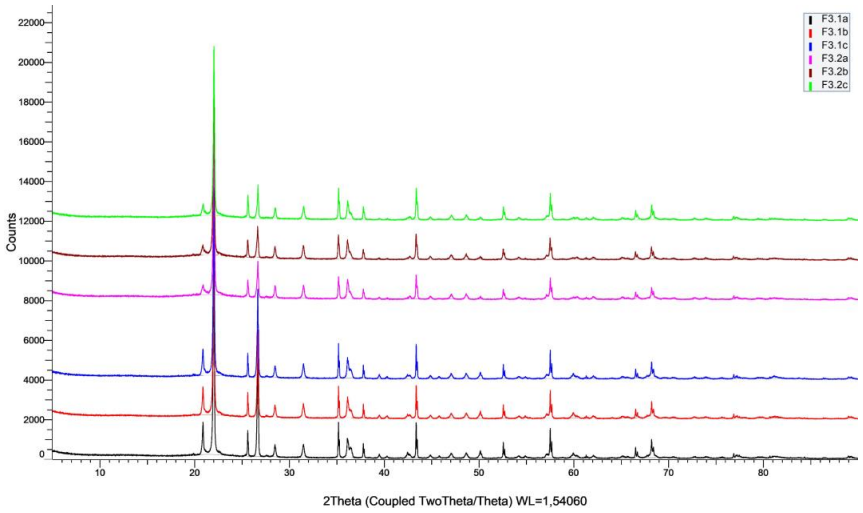

Figure 226: XRD diffraction patterns of F3 samples (10 g, 1700 °C, 0 min).

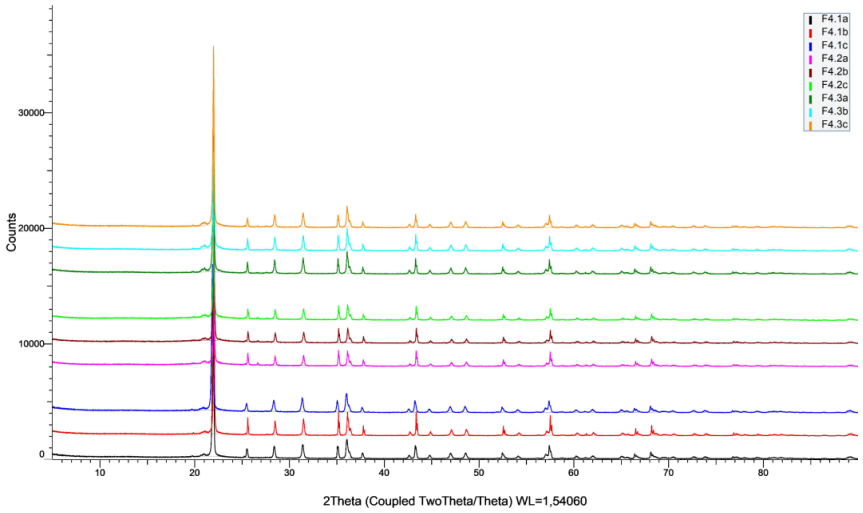

Figure 227: XRD diffraction patterns of F4 samples (10 g, 1700 °C, 15 min).

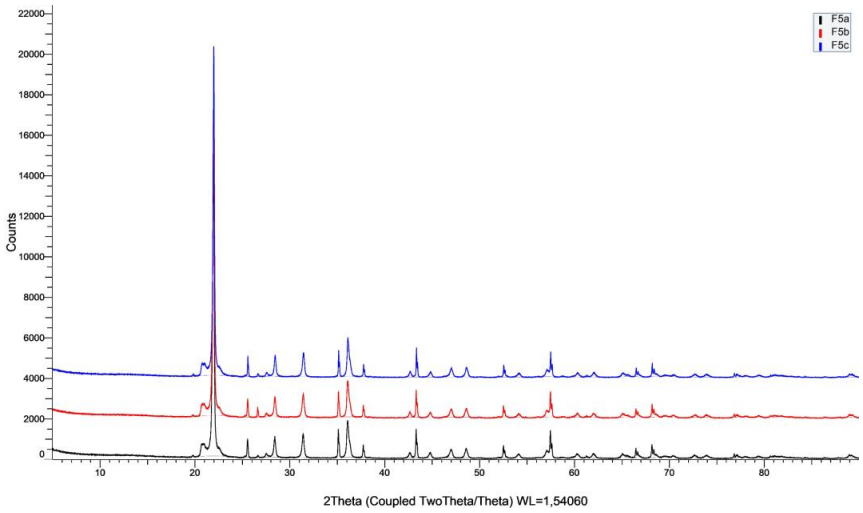

Figure 228: XRD diffraction patterns of F5 samples (10 g, 1600 °C, 15 min).

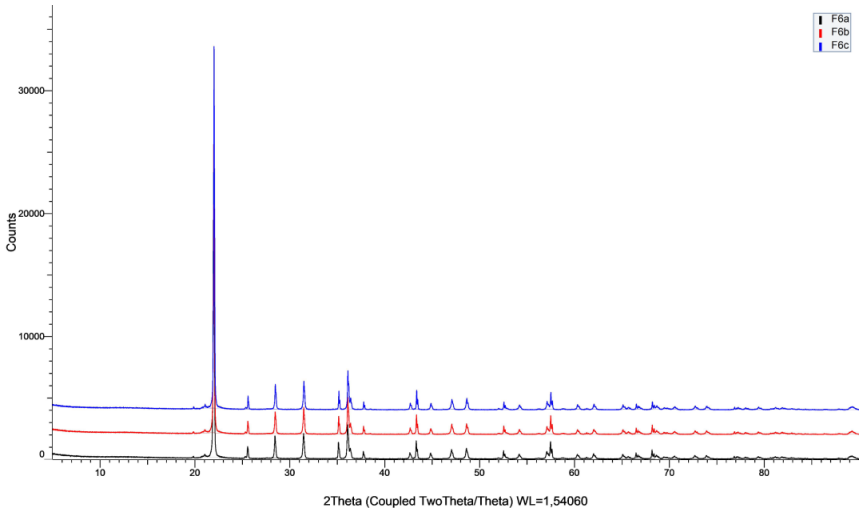

Figure 229: XRD diffraction patterns of F6 samples (10 g, 1700 °C, 30 min).

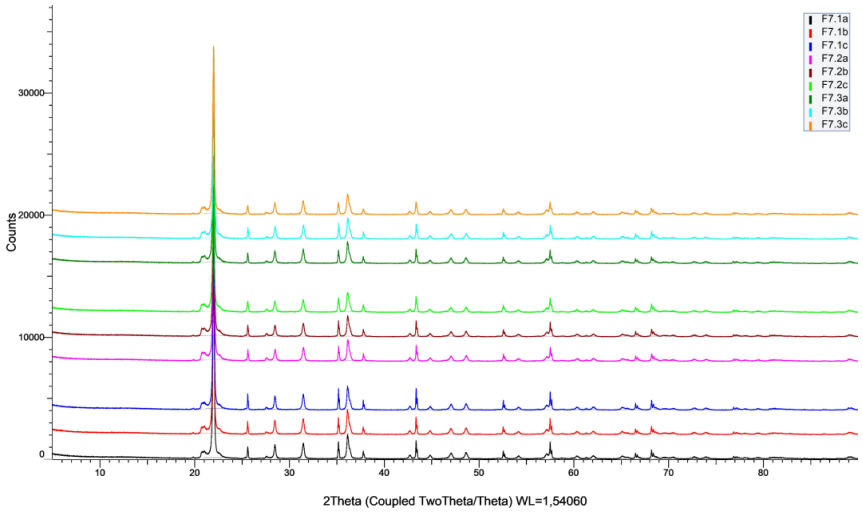

Figure 230: XRD diffraction patterns of F7 samples (10 g, 1600 °C, 30 min).

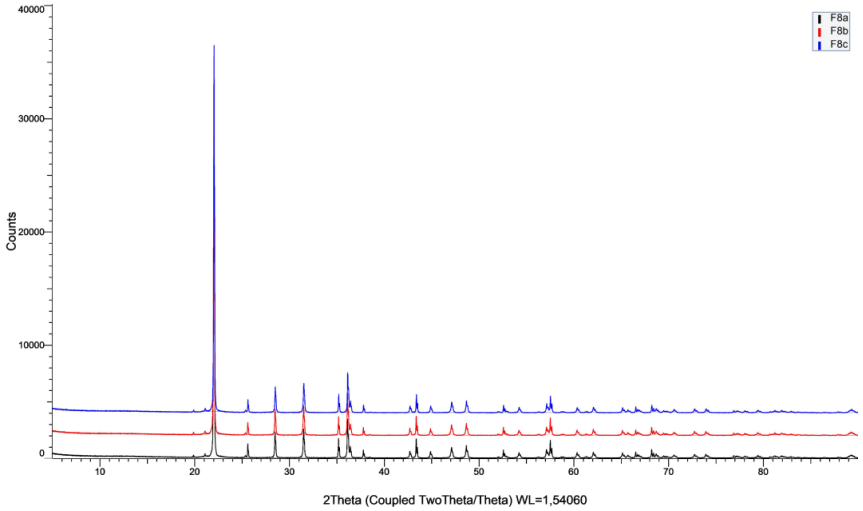

Figure 231: XRD diffraction patterns of F8 samples (10 g, 1700 °C, 45 min).

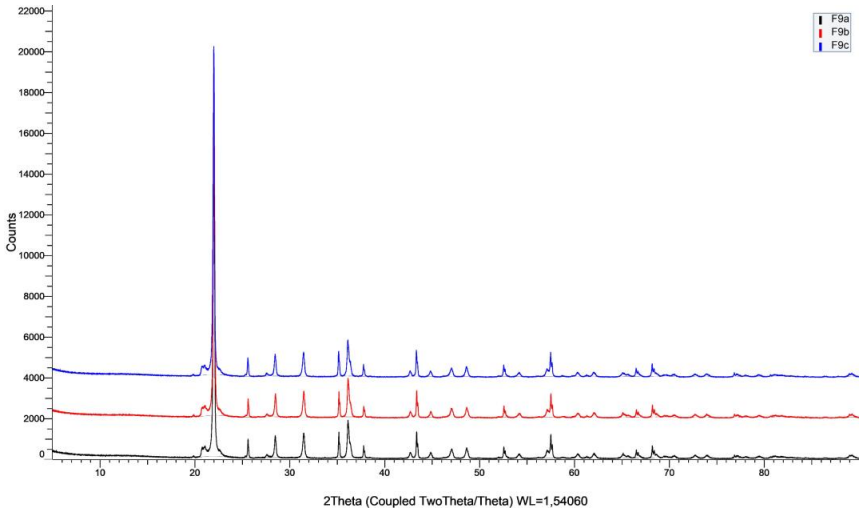

Figure 232: XRD diffraction patterns of F9 samples (10 g, 1600 °C, 45 min).

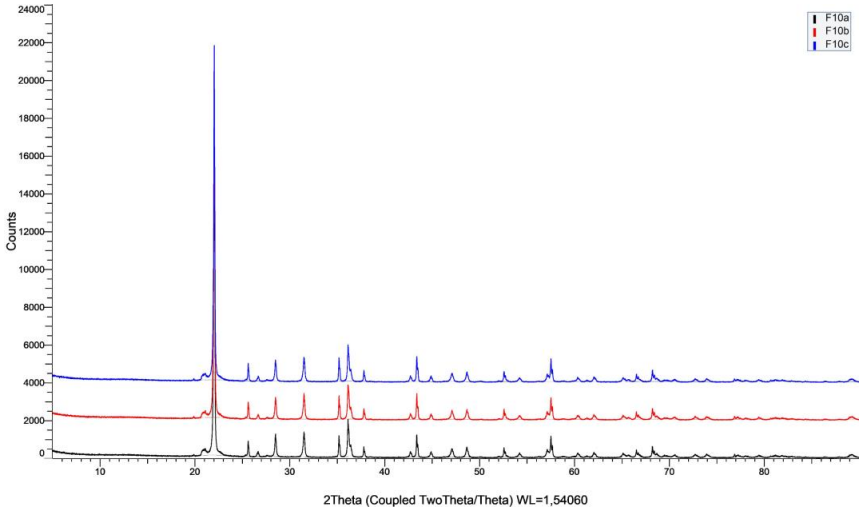

Figure 233: XRD diffraction patterns of F10 samples (10 g, 1600 °C, 60 min).

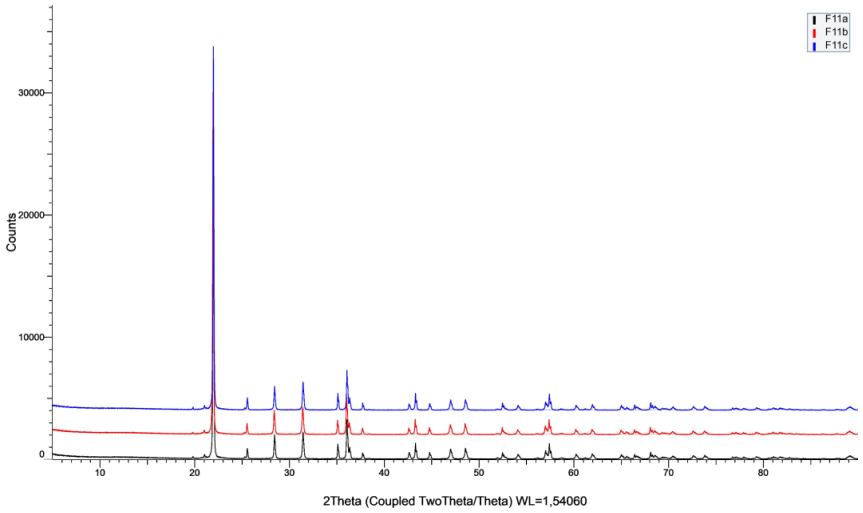

Figure 234: XRD diffraction patterns of F11 samples (10 g, 1700 °C, 60 min).

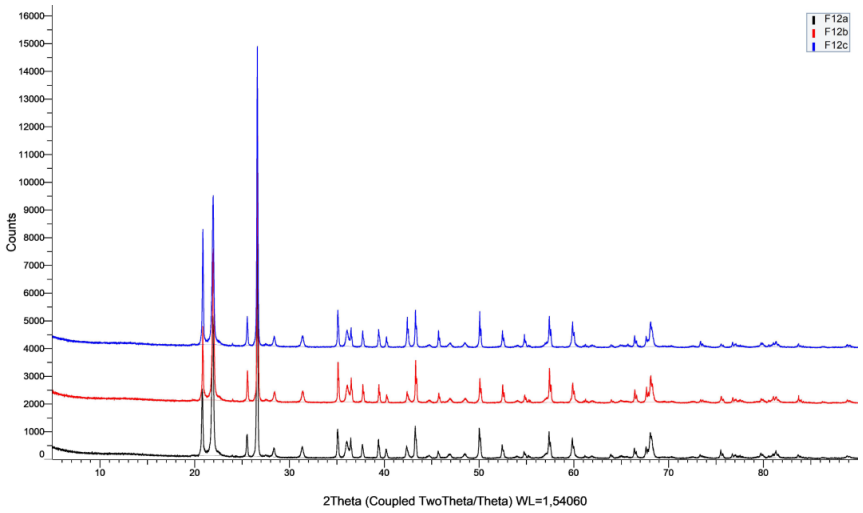

Figure 235: XRD diffraction patterns of F12 samples (100 g, 1600 °C, 0 min).

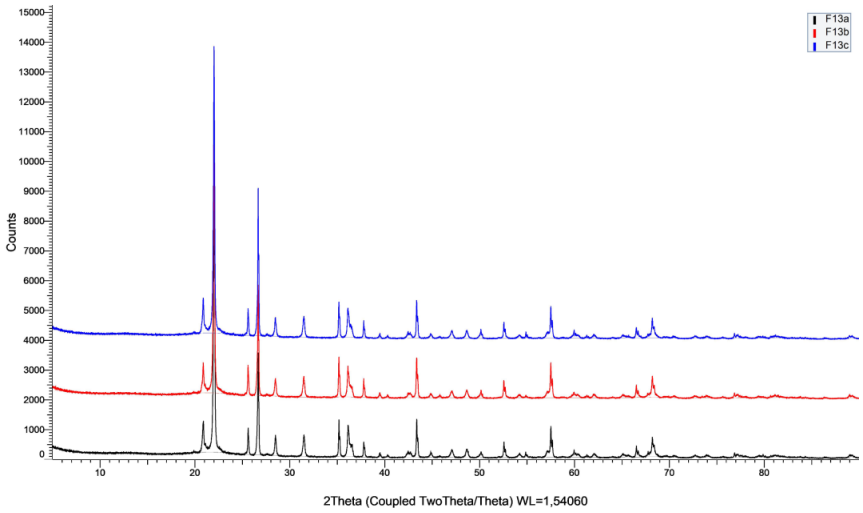

Figure 236: XRD diffraction patterns of F13 samples (100 g, 1700 °C, 0 min).

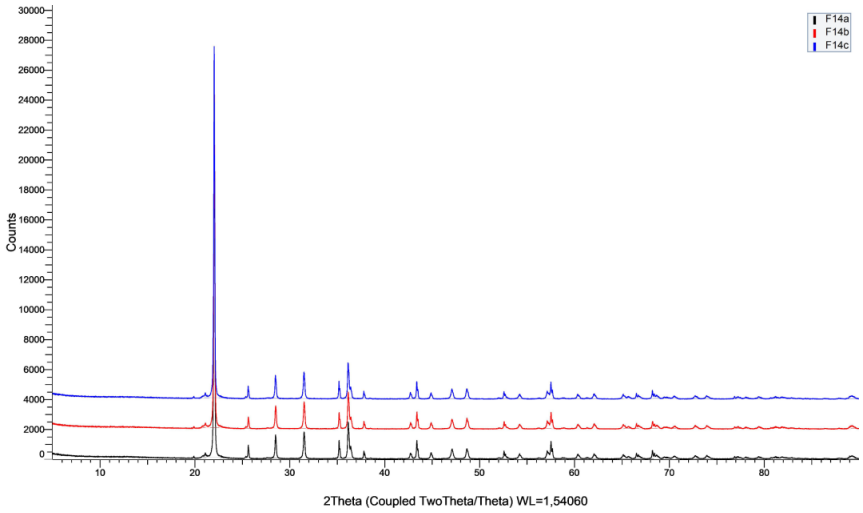

Figure 237: XRD diffraction patterns of F14 samples (100 g, 1700 °C, 15 min).

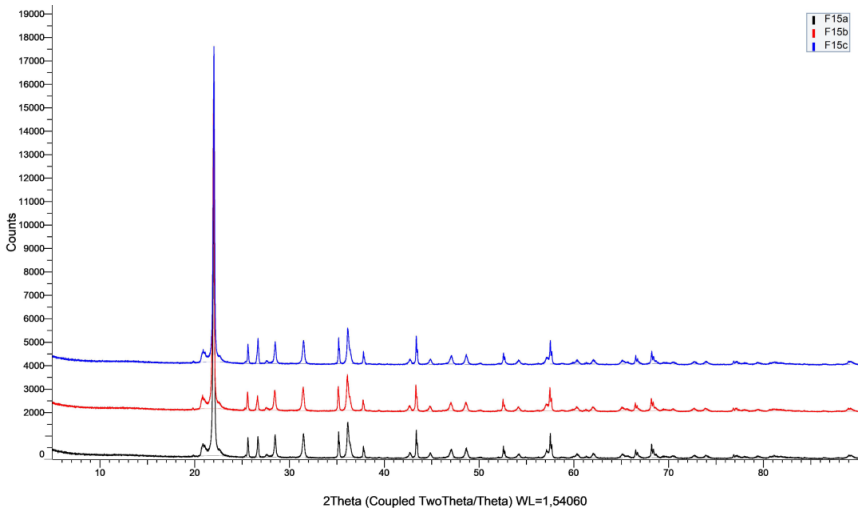

Figure 238: XRD diffraction patterns of F15 samples (100 g, 1600 °C, 15 min).

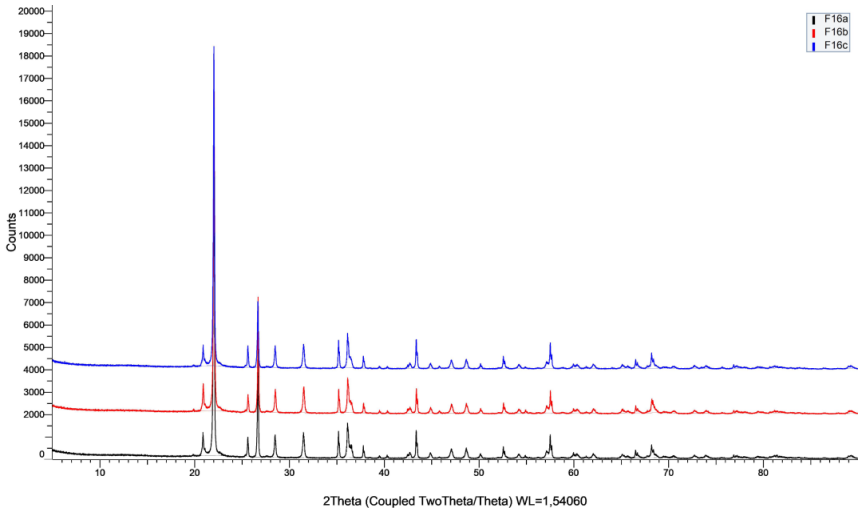

Figure 239: XRD diffraction patterns of F16 samples (100 g, 1600 °C, 30 min).

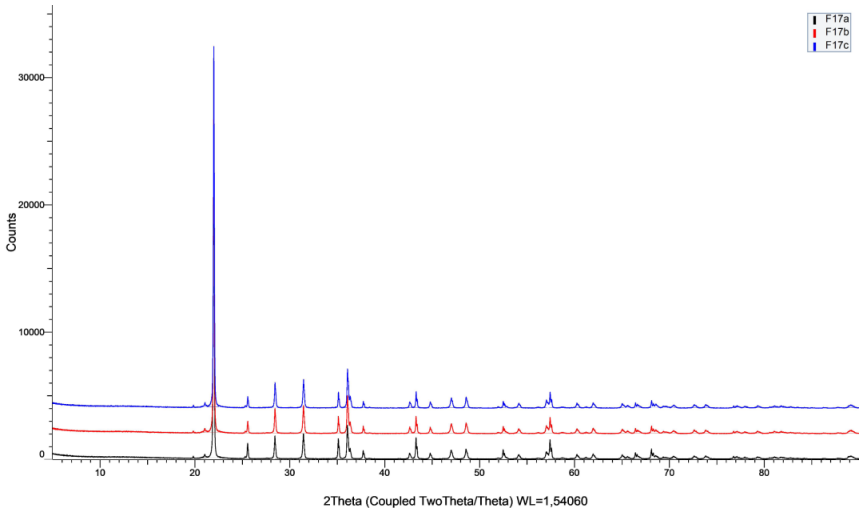

Figure 240: XRD diffraction patterns of F17 samples (100 g, 1700 °C, 30 min).

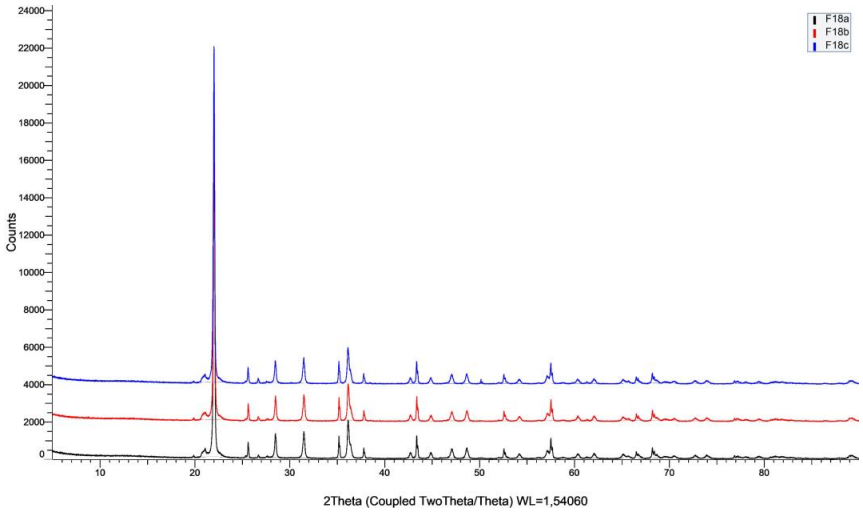

Figure 241: XRD diffraction patterns of F18 samples (100 g, 1600 °C, 45 min).

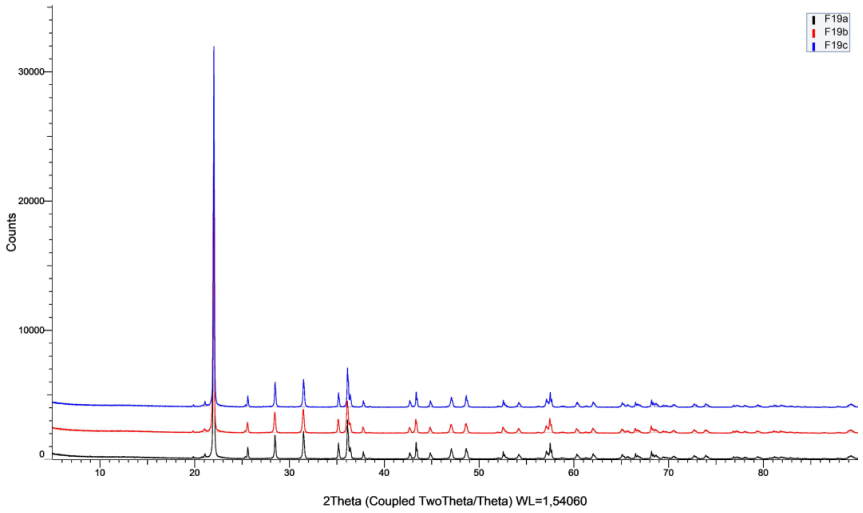

Figure 242: XRD diffraction patterns of F19 samples (100 g, 1700 °C, 45 min).

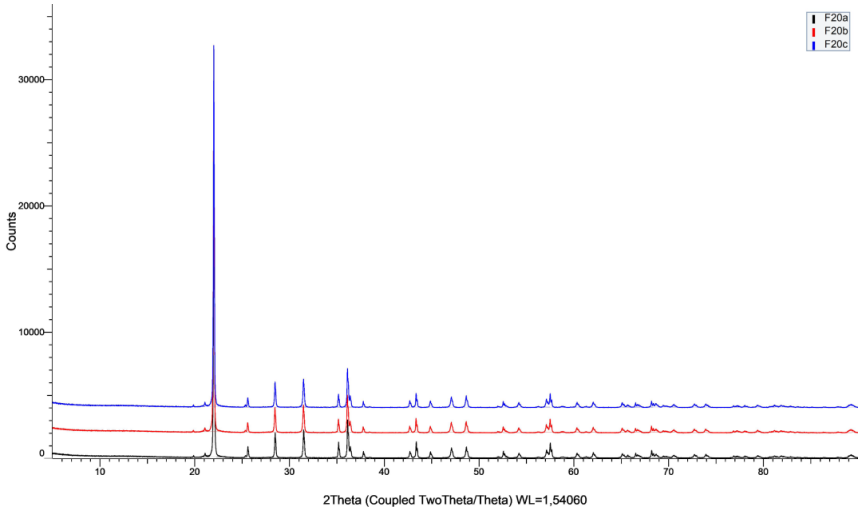

Figure 243: XRD diffraction patterns of F20 samples (100 g, 1700 °C, 60 min).

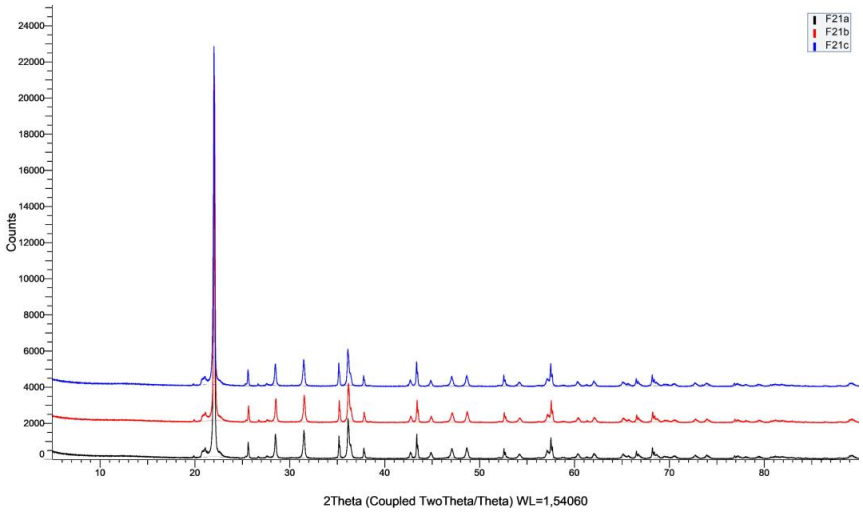

Figure 244: XRD diffraction patterns of F21 samples (100 g, 1600 °C, 60 min).

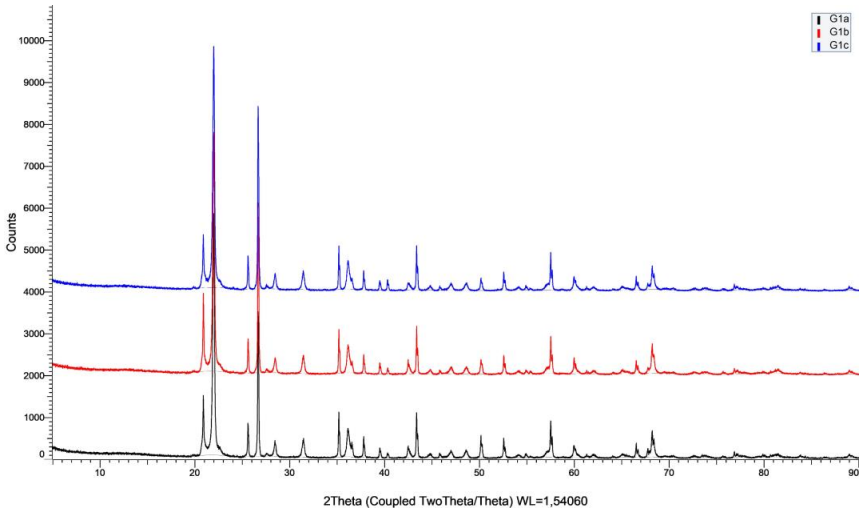

Figure 245: XRD diffraction patterns of G1 samples (10 g, 1600 °C, 0 min).

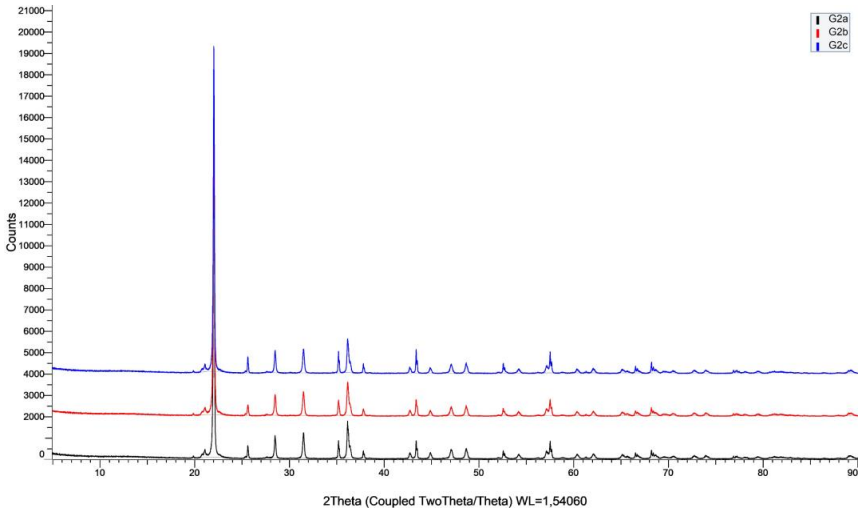

Figure 246: XRD diffraction patterns of G2 samples (10 g, 1600 °C, 120 min).

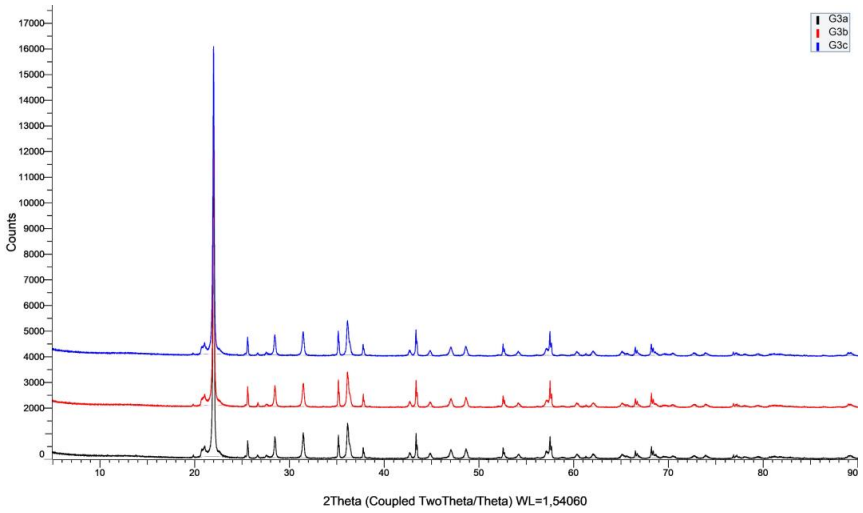

Figure 247: XRD diffraction patterns of G3 samples (10 g, 1700 °C, 0 min).

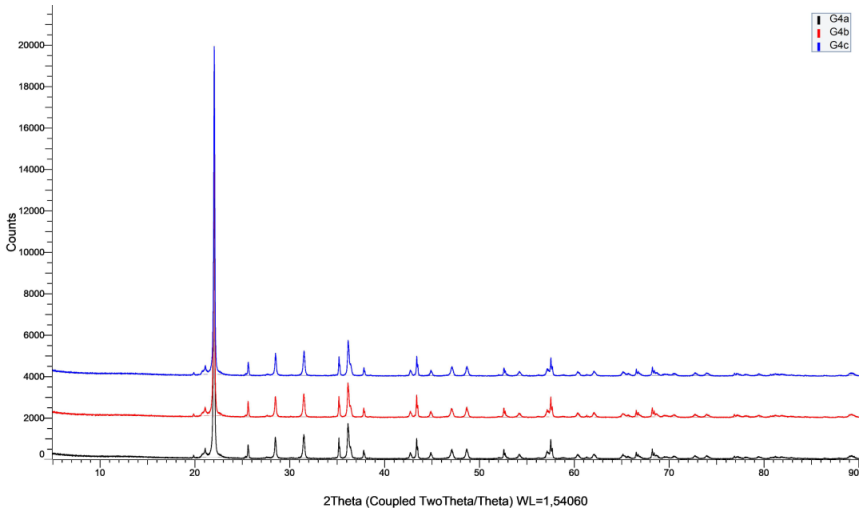

Figure 248: XRD diffraction patterns of G4 samples (10 g, 1700 °C, 15 min).

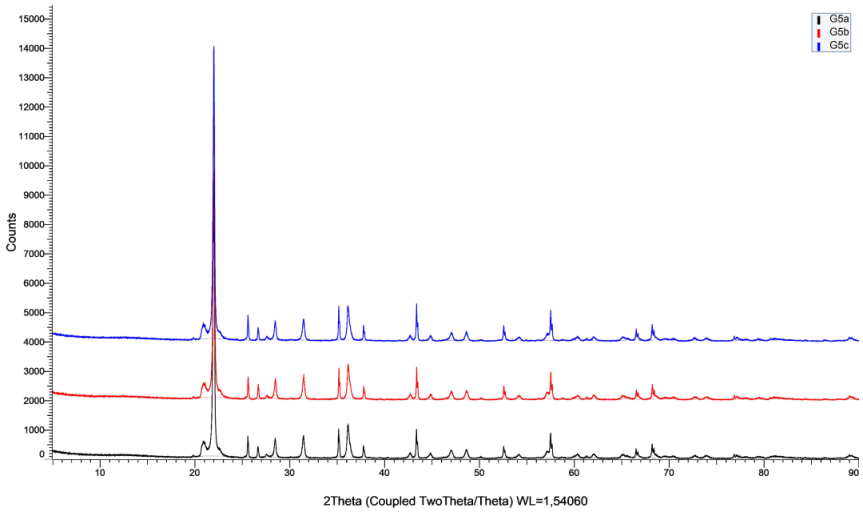

Figure 249: XRD diffraction patterns of G5 samples (10 g, 1600 °C, 15 min).

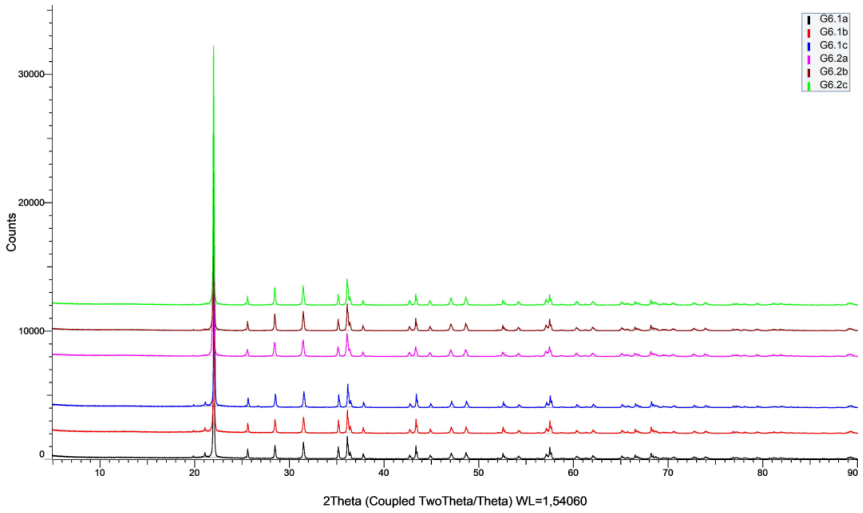

Figure 250: XRD diffraction patterns of G6 samples (10 g, 1700 °C, 30 min).

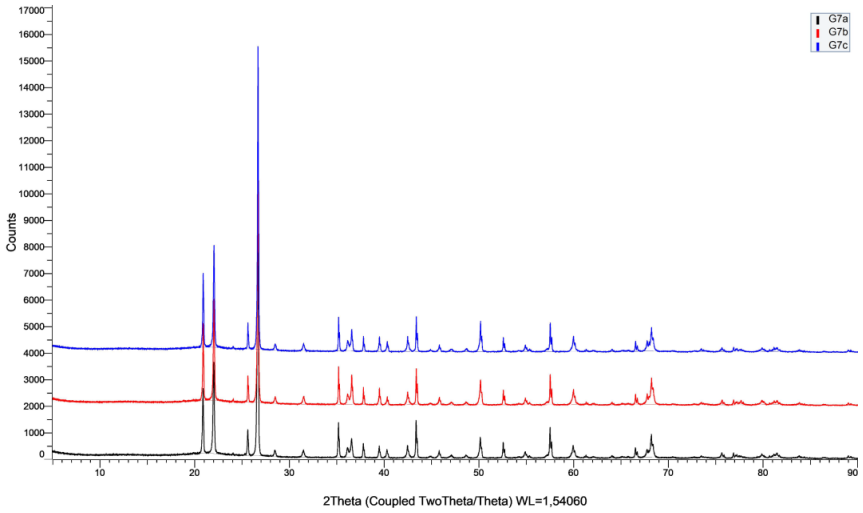

Figure 251: XRD diffraction patterns of G7 samples (10 g, 1600 °C, 30 min).

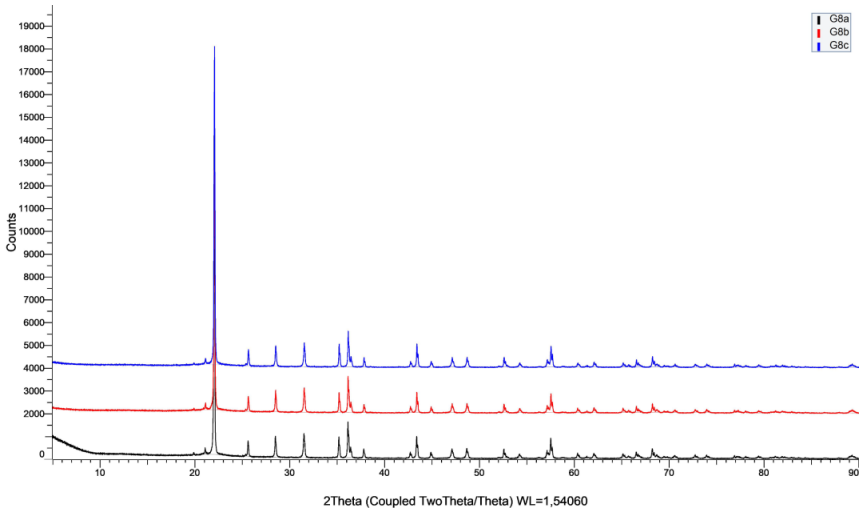

Figure 252: XRD diffraction patterns of G8 samples (10 g, 1700 °C, 45 min).

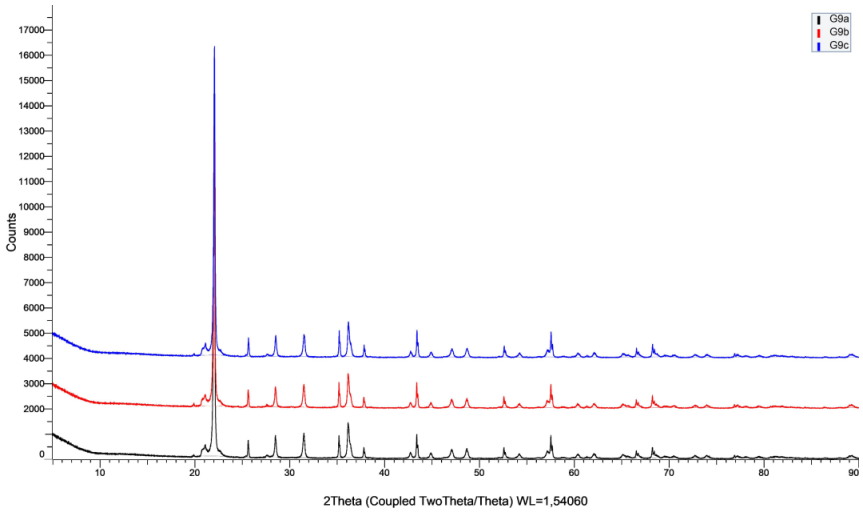

Figure 253: XRD diffraction patterns of G9 samples (10 g, 1600 °C, 45 min).

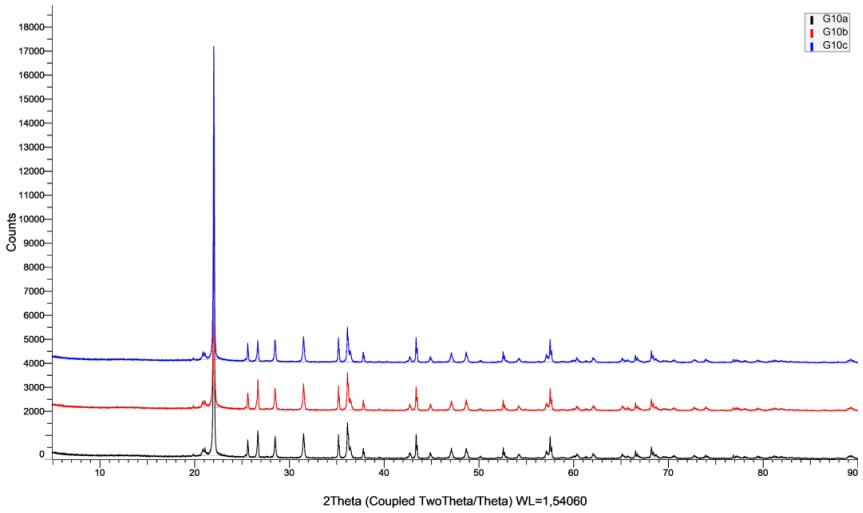

Figure 254 XRD diffraction patterns of G10 samples (10 g, 1600 °C, 60 min).

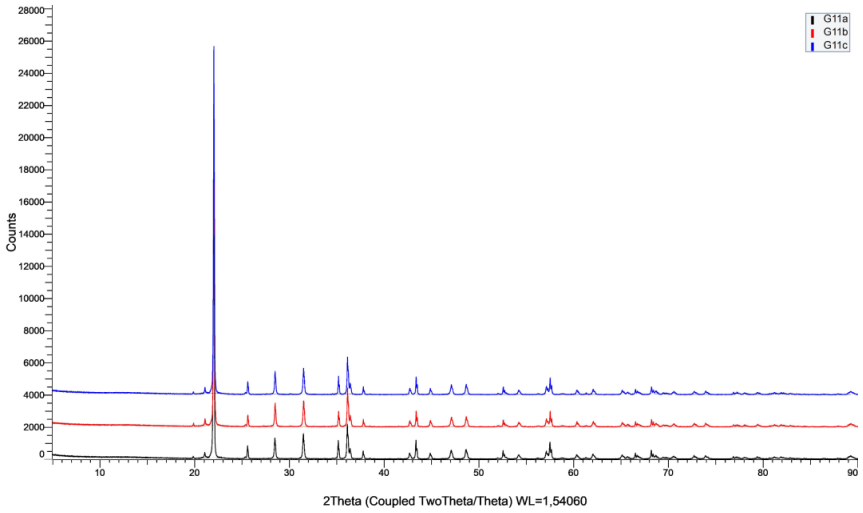

Figure 255: XRD diffraction patterns of G11 samples (10 g, 1700 °C, 60 min).

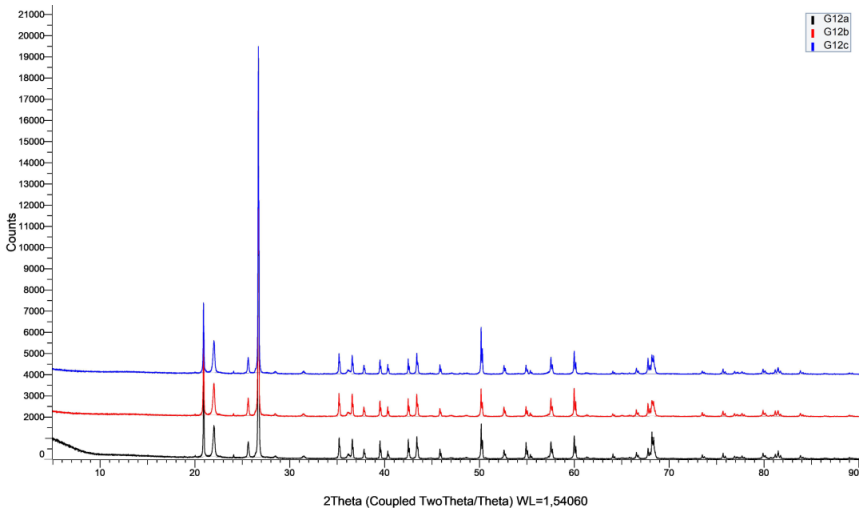

Figure 256: XRD diffraction patterns of G12 samples (100 g, 1600 °C, 0 min).

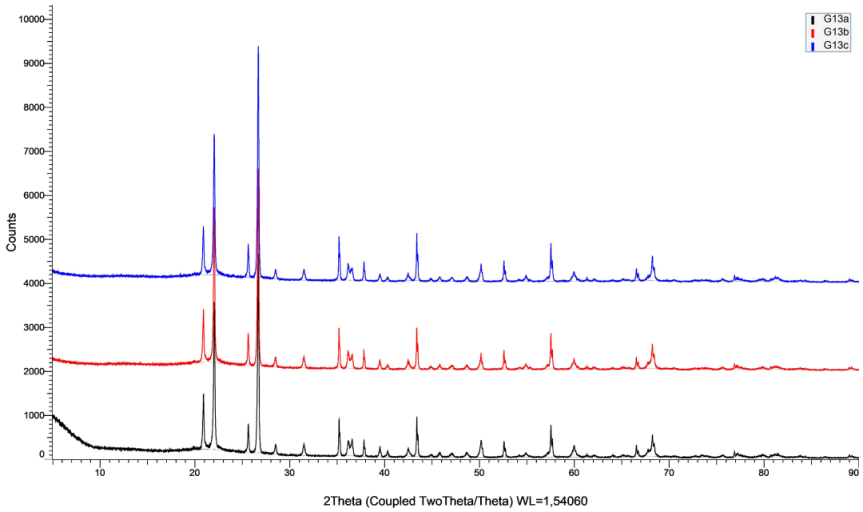

Figure 257: XRD diffraction patterns of G13 samples (100 g, 1700 °C, 0 min).

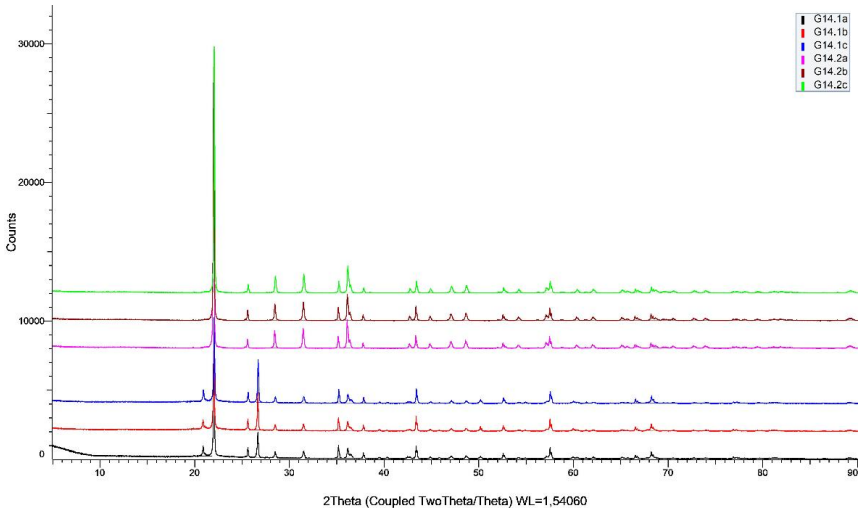

Figure 258: XRD diffraction patterns of G14 samples (100 g, 1700 °C, 15 min).

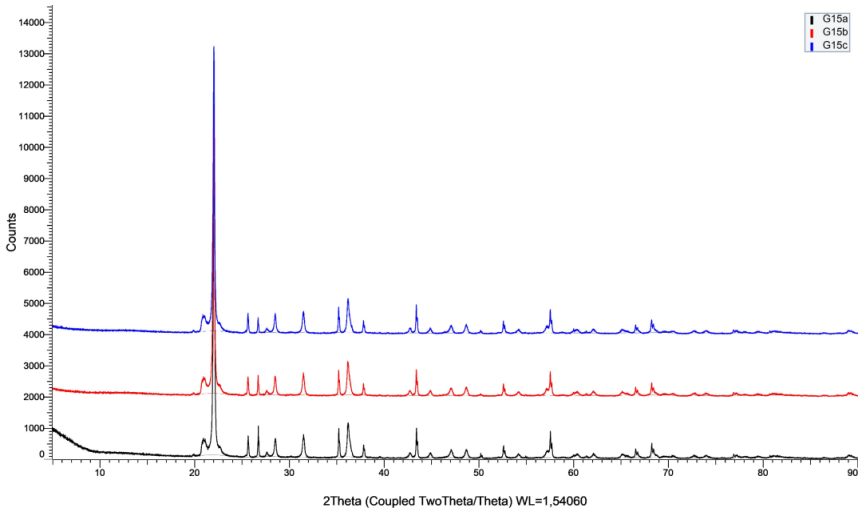

Figure 259: XRD diffraction patterns of G15 samples (100 g, 1600 °C, 15 min).

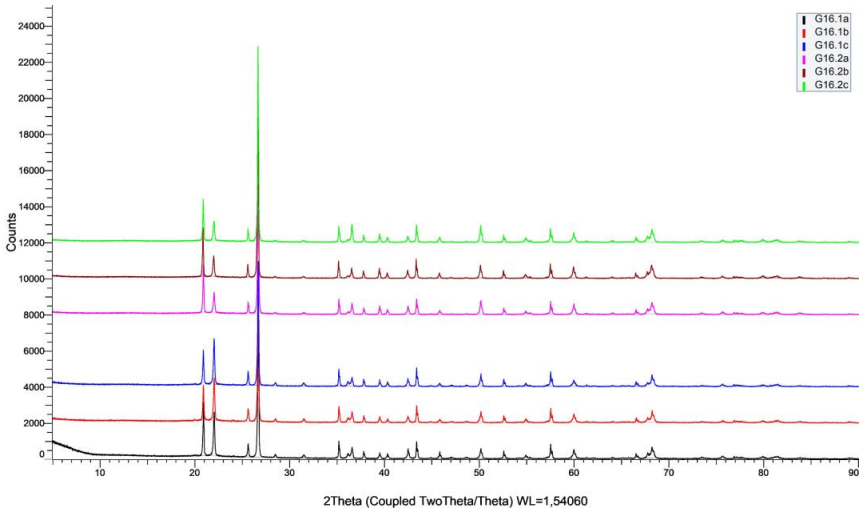

Figure 260: XRD diffraction patterns of G16 samples (100 g, 1600 °C, 30 min).

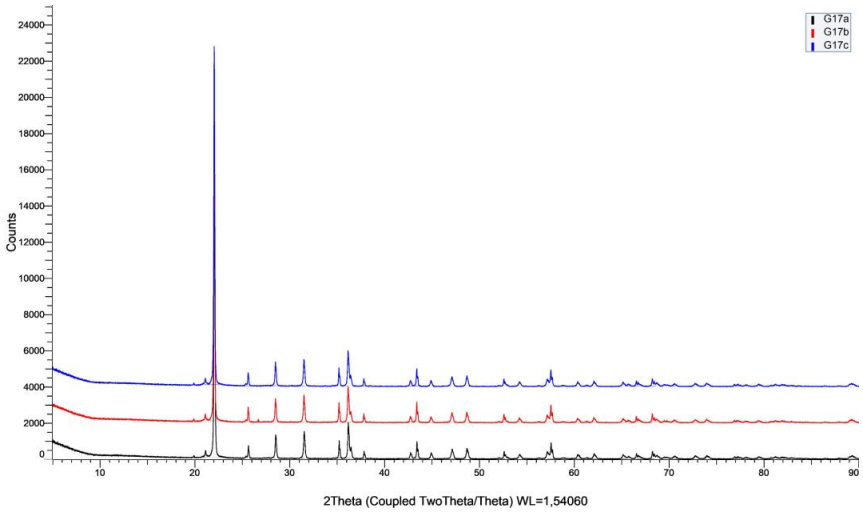

Figure 261: XRD diffraction patterns of G17 samples (100 g, 1700 °C, 30 min).

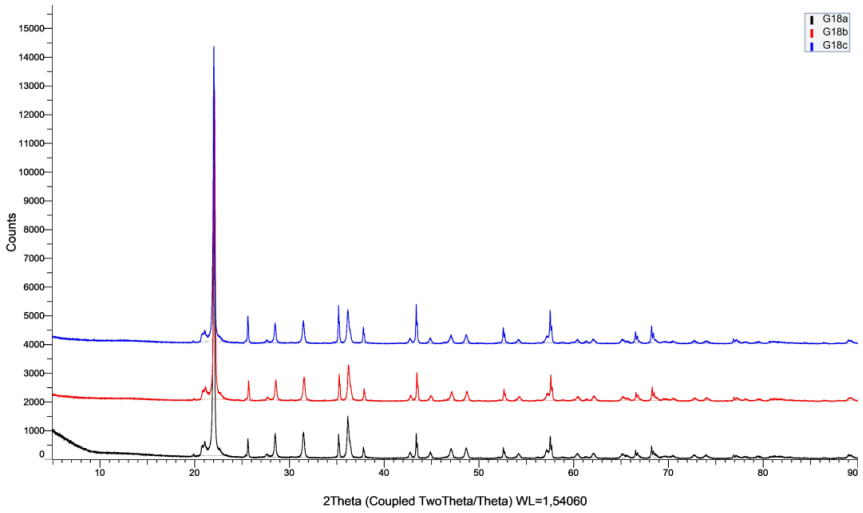

Figure 262: XRD diffraction patterns of G18 samples (100 g, 1600 °C, 45 min).

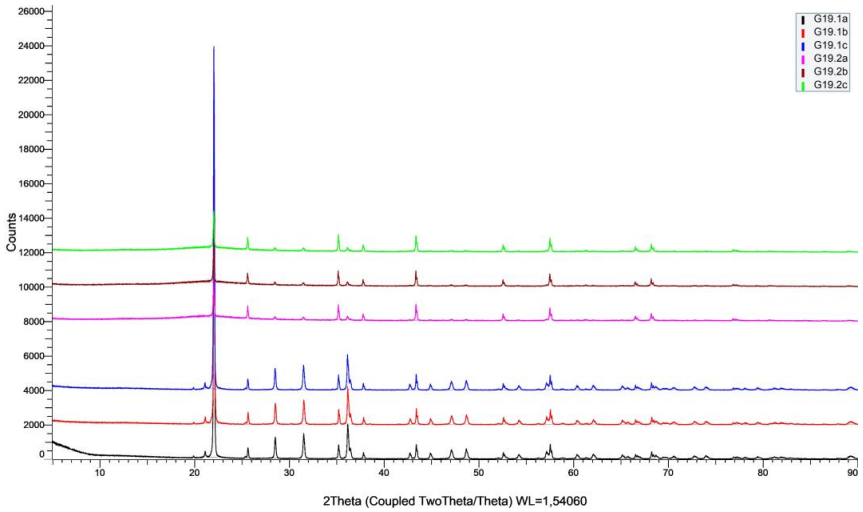

Figure 263: XRD diffraction patterns of G19 samples (100 g, 1700 °C, 45 min).

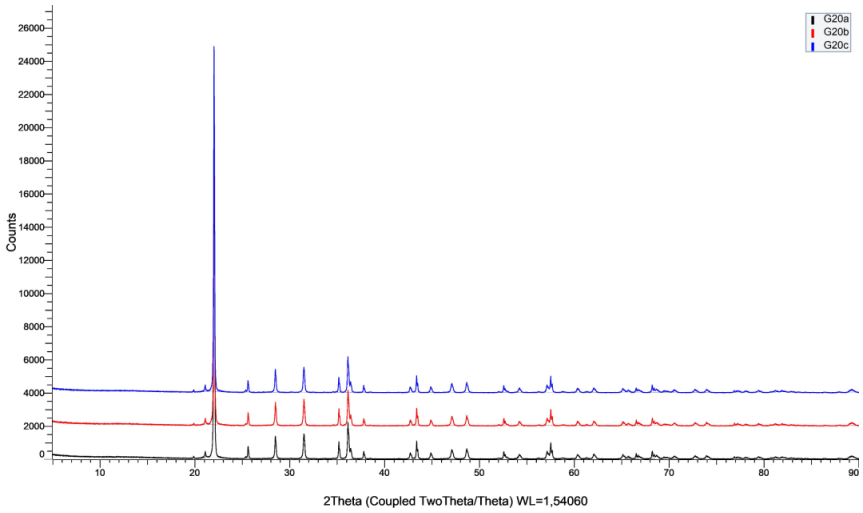

Figure 264: XRD diffraction patterns of G20 samples (100 g, 1700 °C, 60 min).

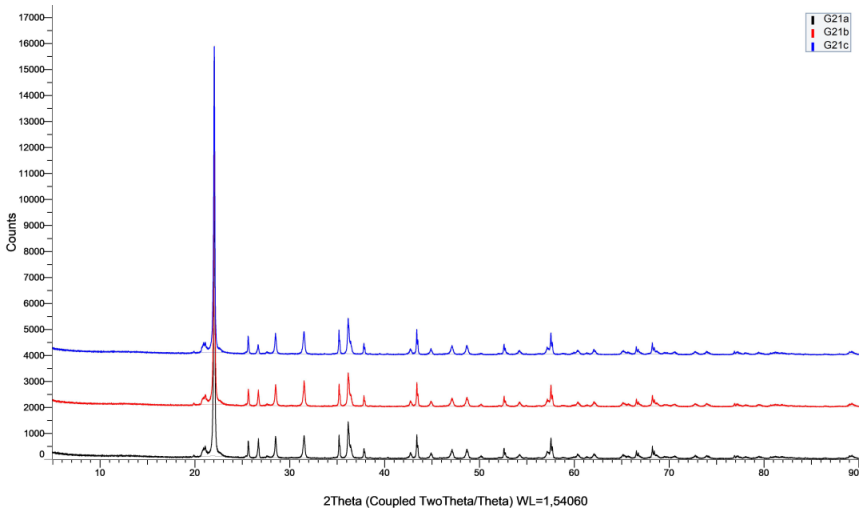

Figure 265: XRD diffraction patterns of G21 samples (100 g, 1600 °C, 60 min).